

**HEAT TRANSPORT THROUGH  
A CORRODING METAL WALL OF  
CONCENTRIC TUBE HEAT EXCHANGER**

**A Thesis  
Submitted to the College of Engineering  
of Al-Nahrain University in Partial Fulfillment  
of the Requirements for the Degree of  
Doctor of Philosophy in  
Chemical Engineering**

**by**

**EMAD YOUSIF MANSOUR ARABO**

**B.Sc. 1994**

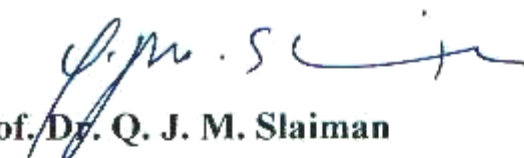
**M.Sc. 1997**

**Thul-Qa'da  
December**

**1426  
2005**

## CERTIFICATION

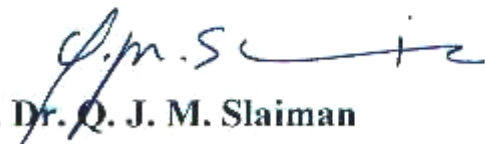
I certify that this thesis titled “**Heat Transport Through a Corroding Metal Wall of Concentric Tube Heat Exchanger**” was prepared by **Emad Yousif Mansour** under my supervision at Al-Nahrain University, College of Engineering, in partial fulfillment of the requirements for the degree of Doctor of Philosophy in Chemical Engineering.

Signature: 

Name: **Prof. Dr. Q. J. M. Slaiman**

(Supervisor)

Date: 28-12-2005

Signature: 

Name: **Prof. Dr. Q. J. M. Slaiman**

(Head of Chemical Engineering Department)

Date: 28-12-2005

## CERTIFICATE

We certify, as an examining committee, that we have read this thesis titled **“Heat Transport Through a Corroding Metal Wall of Concentric Tube Heat Exchanger”**, examined the student **Emad Yousif Mansour** in its content and found it meets the standard of thesis for the degree of Doctor of Philosophy in Chemical Engineering.

Signature:

Name: **Prof. Dr. Q. J. M. Slaiman**  
(Supervisor)

Date: 28-12-2005

Signature:

Name: **Assist. Prof. Dr. Balasim A. Abid**  
(Member)

Date: 27.12.2005

Signature:

Name: **Assist. Prof. Dr. Sami I. J. Al-Rubaiey**  
(Member)

Date: 27.12.2005

Signature:

Name: **Assist. Prof. Dr. Shatha A. Sameh**  
(Member)

Date: 27-12-2005

Signature:

Name: **Assist. Prof. Dr. Cecilia K. Haweel**  
(Member)

Date: 28-12-2005

Signature:

Name: **Prof. Dr. N. B. Nakkash**  
(Chairman)

Date: 28-12-2005

Approval of the College of Engineering

Signature:

Name: **Prof. Dr. Fawzi M. Al-Naima**  
(Dean)

Date: 29/12/2005

## ABSTRACT

Heat transport through a corroded carbon steel pipe in a double pipe heat exchanger in which aerated 0.1 N NaCl solution flowing in the annular space has been investigated. Experiments under isothermal and heat transfer turbulent flow conditions are carried out with Reynolds number range (5000-30000), at three bulk temperatures (30, 40, and 50 °C), and three heat fluxes (15, 30, and 45 kW/m<sup>2</sup>).

Mass transfer rates (corrosion rates) due to diffusion controlled oxygen reduction reaction have been determined by measuring the limiting current density, while rates of heat transfer have been determined by measuring surface temperature. Fouling due to corrosion deposits that form on heat transfer surfaces and its effects on heat and mass transfer processes have been studied through measuring the change of surface temperature and of limiting current density value with time for a period of 200 hours.

The mass transfer data for clean surface (i.e.,  $t=0$ ) have been correlated by the following equations:

$$J_m = 0.514 \text{ Re}^{-0.523} \quad \text{for isothermal conditions, } r_2/r_1=1.75, \text{ and } L/d_e=2$$
$$J_{mf} = 0.287 \text{ Re}^{-0.492} \quad \text{for isothermal and heat transfer conditions, } r_2/r_1=1.75, \\ \text{and } L/d_e=6.7$$

Heat transfer data for clean surface have been correlated by the equation:

$$J_h = 0.058 \text{ Re}^{-0.262} \quad \text{for } r_2/r_1=1.75, \text{ and } L/d_e=6.7$$

Fouling thermal resistance produced from corrosion of heat transfer surfaces has an asymptotic form with an asymptotic fouling thermal resistance range of  $(2.17 \times 10^{-4} - 2.54 \times 10^{-4}) \text{ m}^2 \text{ }^\circ\text{C}/\text{W}$  for 200 hours of exposure time. The asymptotic relation is:

$$R_f = R_f^* [1 - \exp(-bt)]$$

where  $R_f^*$  and  $b$  are functions of Reynolds number and bulk temperature.

Corrosion products forming on heat transfer surfaces have a considerable effect on mass transfer coefficient, which reduces with increasing time and also has asymptotic model. The developed relation is:

$$\% k_m \text{red.} = (\% k_m \text{red.})^* [1 - \exp(-b_m t)]$$

where  $(\% k_m \text{red.})^*$  and  $b_m$  are also functions of Reynolds number and bulk temperature. Relations are obtained between the parameters of the fouling thermal resistance equation and the percentage decrease of mass transfer coefficient equation as follows:

$$R_f^* = 9.35 \times 10^{-5} + 2.7 \times 10^{-6} (\% k_m \text{red.})^*$$

and 
$$b = 0.0065 + 0.157b_m$$

So the effect of corrosion fouling on heat transfer process can be predicted from its effect on mass transfer process (corrosion rate) and vice versa. This means that the heat transfer coefficient at any time can be predicted from mass transfer data, and the mass transfer coefficient can be estimated from heat transfer data.

# CONTENTS

<b>Abstract</b>		i
<b>Contents</b>		iii
<b>Nomenclature</b>		vii
<b>Chapter One</b>	<b>Introduction</b>	1
<b>Chapter Two</b>	<b>Fluid Flow, Heat and Mass Transfer</b>	
2.1	Introduction	3
2.2	Flow Through an Annulus	3
2.3	Friction Factor in an Annulus	6
2.4	Dimensionless Groups of Heat and Mass Transfer	7
2.5	The Boundary Layers	9
2.6	Methods of Supplying Heat Flux	10
2.7	Measurement of Surface Temperature	12
2.8	Heat Transfer Coefficient Correlations for Flow in Annular Space Between Concentric Tubes	13
2.9	Methods of Measuring Mass Transfer Rates	14
2.10	Heat and Mass Transfer Analogy	15
<b>Chapter Three</b>	<b>Electrochemical Corrosion</b>	
3.1	Introduction	17
3.2	Polarization	17
3.2.1	Activation Polarization	17
3.2.2	Concentration (Diffusion or Transport) Polarization	19
3.2.3	Resistance Polarization	21
3.3	Concentration Polarization from Nernst Viewpoint	21
3.4	Limiting Current Density	24
3.5	Mass Transfer Correlations For Flow in Annular Space Between Concentric Pipes Established by Limiting Current Measurement: Literature Review	26
3.6	Anodic and Cathodic Reactions in Corrosion	28
3.7	Oxygen Reduction Reaction	32
3.8	Corrosion Rate Expressions	34
3.9	Corrosion Rate Measurements	35
3.10	Environment Effects on Corrosion Rate	36
3.10.1	Effect of Velocity	36
3.10.2	Effect of Temperature	38
3.10.3	Effect of Chloride Ion	40
3.11	Heat Transfer and Corrosion	42



5.7 Heat Transfer Calculations	90
5.8 Corrosion Fouling Results	94
<b>Chapter Six</b>	<b>Discussion</b>
6.1 Introduction	100
6.2 Cathodic Polarization Region Under Isothermal Conditions	100
6.2.1 Effect of Reynolds Number	100
6.2.2 Effect of Bulk Temperature	104
6.2.3 Effect of Working Electrode Length	107
6.3 Mass Transfer Data Under Isothermal Conditions	111
6.3.1 Effect of Reynolds Number	111
6.3.2 Effect of Bulk Temperature	114
6.3.3 Effect of Working Electrode Length	114
6.3.4 Estimation of Mass Transfer Correlations	116
6.3.5 Estimation of Mass Transfer Correlations	116
6.4 Cathodic Polarization Region Under Heat Transfer Conditions	118
6.4.1 Effect of Reynolds Number	118
6.4.2 Effect of Bulk Temperature	120
6.4.3 Effect of Heat Flux	121
6.5 Mass Transfer Data Under Heat Transfer	124
6.5.1 Estimation of Mass Transfer Correlation	129
6.5.2 Comparison With Other Correlations	130
6.6 Heat Transfer Rate	130
6.6.1 Effect of Reynolds Number	130
6.6.2 Effect of Bulk Temperature	131
6.6.3 Effect of Heat Flux	135
6.6.4 Estimation of Heat Transfer Correlations	137
6.6.5 Comparison With Other Correlations	137
6.7 Analogy Between Heat and Mass Transfer	139
6.8 Corrosion Fouling	139
6.8.1 Effect of Reynolds Number	144
6.8.2 Effect of Bulk Temperature	146
6.8.3 Correlating of Corrosion Fouling Data	147
<b>Chapter Seven</b>	<b>Conclusions and Recommendations</b>
7.1 Conclusions	159
7.2 Recommendations	160
<b>References</b>	161
<b>Appendix A</b>	<b>Calibration of Flowmeter</b>
	A1
<b>Appendix B</b>	<b>Carbon Steel Grades</b>
	B1

## **Appendix C**

C.1 Physical Properties of Water at Atmospheric Pressure	C1
C.2 Electroconductivity of Sodium Chloride Solution	C2
C.3 Solubility of Oxygen	C2
C.4 Diffusivity of Oxygen	C2

## **Appendix D**

D.1 Cathodic Polarization Curves Under Isothermal Conditions	D1
D.2 Cathodic Polarization Curves Under Heat Transfer Conditions	D7

## NOMENCLATURE

$A$	Surface area of specimen	$m^2$
$b$	Reciprocal of time constant	1/hr
$b_m$	Reciprocal of time constant	1/hr
$C$	Concentration	$kg/m^3$
$C_P$	Specific heat	$kJ/kg \cdot ^\circ C$
$D$	Diffusion coefficient	$m^2/s$
$d$	Diameter	m
$d_1$	Inner diameter of annulus (outer diameter of inner tube)	m
$d_2$	Outer diameter of annulus (inner diameter of outer tube)	m
$d_e$	Equivalent diameter	m
$E$	Potential	V
$E_{corr}$	Corrosion potential	mV
$F$	Faraday's constant (96487 Coulombs/equivalent)	
$f$	Friction factor	
$g$	Gravity constant	$m/s^2$
$h$	Heat transfer coefficient	$W/m^2 \cdot ^\circ C$
$I$	Flowing current	Ampere A
$i$	Current density	$A/m^2$
$i_a$	Anodic current density	$A/m^2$
$i_{app}$	Applied current density	$A/m^2$
$i_c$	Cathodic current density	$A/m^2$
$i_{corr}$	Corrosion current density	$A/m^2$
$i_L$	Limiting current density	$A/m^2$
$i_o$	Exchange current density	$A/m^2$
$J_h$	$J$ -factor for heat transfer	
$J_m$	$J$ -factor for mass transfer	
$k$	Thermal conductivity	$W/m \cdot ^\circ C$
$k_m$	Mass transfer coefficient	m/s
$L$	Length of working electrode	m
$M$	Molecular weight of metal	g/mole
$N$	Molar flux	$mole/m^2 \cdot s$
Nu	Nusselt number	
$p$	Pressure	$N/m^2$
$P$	Power	W
Pr	Prandtl number	
$Q_{flow}$	Volumetric flow rate	$m^3/s$
$Q$	Heat transfer rate	W
$q$	Heat flux	$W/m^2$
$r$	Radius	m

$r_1$	Inner radius of annulus (outer radius of inner tube)	m
$r_2$	Outer radius of annulus (inner radius of outer tube)	m
$R$	Gas constant	J/mole.K
$R_t$	Total thermal resistance	$m^2 \text{ }^\circ\text{C/W}$
$R_c$	Convective (clean) thermal resistance	$m^2 \text{ }^\circ\text{C/W}$
$R_f$	Fouling thermal resistance	$m^2 \text{ }^\circ\text{C/W}$
$R_f^*$	Asymptotic Fouling thermal resistance	$m^2 \text{ }^\circ\text{C/W}$
Re	Reynolds number	
Sc	Schmidt number	
Sh	Sherwood number	
$St_h$	Stanton number for heat transfer	
$St_m$	Stanton number for mass transfer	
$T$	Temperature	$^\circ\text{C}$ or K
$T_f$	Film Temperature	$^\circ\text{C}$
$t$	Time	s or hr
$u$	Velocity	m/s
$V$	Applied voltage	Volt V
$w$	Weight loss of metal	g
$x_f$	Thickness of corrosion fouling deposit	mm
$z$	Number of electron transferred	

## Greek Letters

$\alpha$	Thermal diffusivity	$m^2/s$
$\alpha_c$	Symmetry coefficient	
$\beta$	Tafel slope	
$\delta$	Hydrodynamic boundary layer thickness	$\mu\text{m}$
$\delta_d$	Nernst diffusion boundary layer thickness	$\mu\text{m}$
$\delta_m$	Mass boundary layer thickness	$\mu\text{m}$
$\delta_t$	Thermal boundary layer thickness	$\mu\text{m}$
$\eta$	Overpotential	mV
$\theta_d$	Deposition rate	$m^2 \text{ }^\circ\text{C/J}$
$\theta_r$	Removal rate	$m^2 \text{ }^\circ\text{C/J}$
$\mu$	Dynamic viscosity	kg/m.s
$\nu$	Kinematic viscosity	$m^2/s$
$\rho$	Density	$\text{kg}/m^3$

## Subscripts

<i>b</i>	Bulk solution conditions
corr	Corrosion
<i>f</i>	Fouling
<i>f</i>	Film temperature conditions
max	Maximum
<i>s</i>	Surface conditions
<i>c</i>	Clean surface
0	Initial ( $t=0$ )

## Superscripts

<i>A</i>	Activation polarization
<i>C</i>	Concentration polarization
<i>R</i>	Resistance polarization

## Abbreviations

AA%E	Average Absolute Percentage Error
LCDT	Limiting Current Density Technique
SCE	Saturated Calomel Electrode
% $i_L$ red.	Percentage of reduction in limiting current density
% $k_m$ red.	Percentage of reduction in mass transfer coefficient

**CHAPTER ONE**

**INTRODUCTION**

The study of controlled mass transfer electrochemical and corrosion processes is of fundamental importance that allows the provision of the corrosion data for various metals in a process plant. In industrial chemical processes, there are many parts or units involve heat input or extraction such as heat exchangers units, refrigeration units, power plant units, etc. The corrosion process involved in these units is to be under the influence of combined action of mass and heat transfer.

Removing unwanted heat from heat transfer surfaces is done by using cooling fluid. Water is commonly used as cooling fluid in industry. However water is corrosive to most metals and alloys and contributes to most fouling problems. Corrosion shortens the life of the equipment in cooling systems as well as causes various problems such as a reduction of operation efficiency, leakage of products, and pollution from leaked products.

Carbon steel is the most commonly used engineering material. It is cheap; is available in a wide range of standard forms and sizes; can be easily worked and welded; and it has good tensile strength and ductility. Carbon steel is corroded by dissolved oxygen in neutral water, and its surface is covered with corrosion products (rust).

Many heat exchange equipments can be used to input or extract heat to or from a flowing fluid such as double pipe heat exchanger, shell and tube heat exchanger, plate and frame heat exchanger, etc. The double pipe (concentric pipe or annular) heat exchanger was selected in the present work because it is simple, easy to fabricate, and represents a shell and tube heat exchanger in a simplified form.

The present work studies heat transfer through a corroding carbon steel pipe of double pipe heat exchanger under turbulent flow of 0.1 N sodium chloride solution. At first experiments were carried out under isothermal conditions with various controlled conditions of flow and temperature. Then

similar experiments were made under heat transfer conditions at different heat fluxes. The limiting current density technique, which is widely used, was utilized to obtain mass transfer relations. Heat transfer relations were obtained by measuring the surface temperature of the working specimen. The present work deals with the validation of the analogy between mass and heat transfer for the determination of mass and heat transfer coefficients. Fouling due to corrosion products that form on heat transfer surfaces and produces thermal resistance was studied in the present work through its effect on surface temperature. Also the growth of corrosion products on heat transfer surfaces influences the transfer of reactant (dissolved oxygen) to the surface and was studied through its effect on limiting current density.

## **CHAPTER TWO**

# **FLUID FLOW, HEAT AND MASS TRANSFER**

## 2.1 Introduction

When a fluid is flowing through a tube, an annulus, or over a surface, the pattern of the flow will vary with the velocity, the physical properties of the fluid, and the geometry of the surface. Flow at low rates is called laminar or streamline flow, which is characterized by parallel streams not interfering with each other. As the flow rate is increased, the flow is known as turbulent flow and is characterized by the rapid movement of fluid as eddies in random directions across the tube. Most chemical engineering process equipment involves turbulent flow, especially equipment designed for heat and mass transfer.

In order to understand the mechanism of the transfer of material or heat from one phase to another, the flow pattern of the fluid and the distribution of velocity must be studied also.

## 2.2 Flow Through an Annulus

The velocity distribution and the mean velocity of streamline flow of a fluid through an annulus (concentric pipes) of outer radius  $r_2$  and inner radius  $r_1$  is complex (as shown in Fig. 2-1). If the pressure changes by an amount  $dp$  as a result of friction in a length  $dl$  of annulus, the resulting force can be equated to the shearing force acting on the fluid.

Consider the flow of the fluid situated at a distance  $r$  from the centerline of the pipes. The shear force acting on this fluid consists of two parts; one is the drag on its outer surface; this can be expressed in terms of the viscosity of the fluid and the velocity gradient at that radius; the other is the drag occurring at the inner boundary of the annulus; this cannot be estimated at present and will be denoted by the symbol  $\lambda$  for unit length of pipe. Then the force balance [1, 2]:

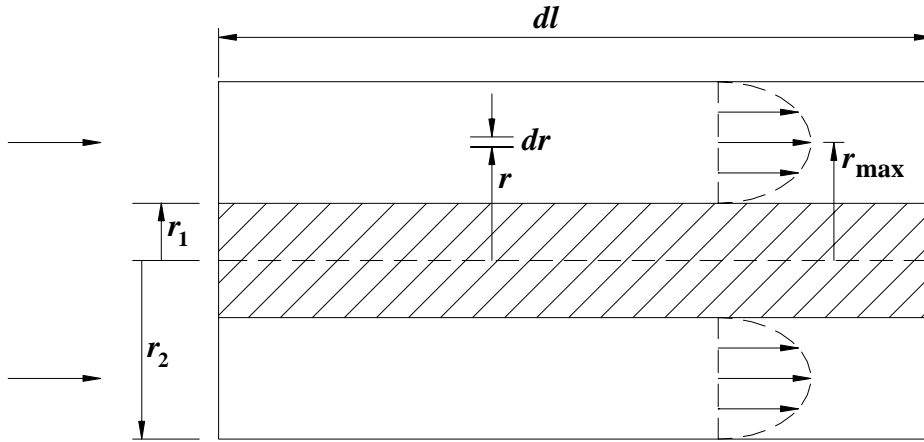


**Figure 2-1** Flow through an annulus [1].

$$\left(\frac{dp}{dl}\right)dl\pi(r^2 - r_1^2) = 2\pi r\mu dl\left(\frac{du_x}{dr}\right) + \lambda dl \quad (2.1)$$

where  $u_x$  is the velocity of the fluid at radius  $r$ .

So

$$du_x = \frac{r^2 - r_1^2}{2\mu r} \left(\frac{dp}{dl}\right)dr - \lambda \frac{dr}{2\pi\mu r} \quad (2.2)$$

Integrating:

$$u_x = \frac{1}{2\mu} \left(\frac{dp}{dl}\right) \left(\frac{r^2}{2} - r_1^2 \ln r\right) - \frac{\lambda}{2\pi\mu} \ln r + c \quad (2.3)$$

where  $c$  is integration constant

Substituting the boundary conditions; at  $r=r_1$ ,  $u_x=0$ , and at  $r=r_2$ ,  $u_x=0$ , in Eq. (2.3) and solving for  $\lambda$  and  $c$ :

$$\lambda = \pi \frac{dp}{dl} \left( \frac{r_2^2 - r_1^2}{2 \ln(r_2/r_1)} - r_1^2 \right) \quad (2.4)$$

$$c = \frac{1}{2\mu} \left( -\frac{dp}{dl} \right) \left( \frac{r_2^2}{2} - \frac{r_2^2 - r_1^2}{2 \ln(r_2/r_1)} \ln r_2 \right) \quad (2.5)$$

Substituting these values of  $\lambda$  and  $c$  in Eq. (2.3) and simplifying:

$$u_x = \frac{1}{4\mu} \left( -\frac{dp}{dl} \right) \left( r_2^2 - r^2 + \frac{r_2^2 - r_1^2}{\ln(r_2/r_1)} \ln \frac{r}{r_2} \right) \quad (2.6)$$

The volumetric flow rate  $Q_{\text{flow}}$  of fluid through a small annulus of inner radius  $r$  and outer radius  $(r+dr)$ , is given by:

$$dQ_{\text{flow}} = 2\pi r dr u_x \quad (2.7)$$

$$\therefore dQ_{\text{flow}} = \frac{\pi}{2\mu} \left( -\frac{dp}{dl} \right) \left( r_2^2 r - r^3 + \frac{r_2^2 - r_1^2}{\ln(r_2/r_1)} r \ln \frac{r}{r_2} \right) dr \quad (2.8)$$

Integrating between the limits  $r=r_1$  and  $r=r_2$  yields:

$$Q_{\text{flow}} = \frac{\pi}{8\mu} \left( -\frac{dp}{dl} \right) \left( r_2^2 + r_1^2 - \frac{r_2^2 - r_1^2}{\ln(r_2/r_1)} \right) (r_2^2 - r_1^2) \quad (2.9)$$

The average velocity is given by:

$$\begin{aligned} u &= \frac{Q_{\text{flow}}}{\pi(r_2^2 - r_1^2)} \\ &= \frac{1}{8\mu} \left( -\frac{dp}{dl} \right) \left( r_2^2 + r_1^2 - \frac{r_2^2 - r_1^2}{\ln(r_2/r_1)} \right) \end{aligned} \quad (2.10)$$

The velocity in the annulus reaches a maximum at some radius  $r=r_{\text{max}}$  which is between  $r_1$  and  $r_2$  as shown in Fig. 2-1. Differentiation of  $u_x$  in Eq. (2.6) with respect to  $r$  yields:

$$\frac{du_x}{dr} = \frac{1}{4\mu} \left( -\frac{dp}{dl} \right) \left( -2r + \frac{r_2^2 - r_1^2}{r \ln(r_2/r_1)} \right) \quad (2.11)$$

Substituting that  $(du_x/dr)=0$  at  $r=r_{\text{max}}$  in Eq. (2.11) results [3]:

$$r_{\text{max}} = \sqrt{\frac{(r_2^2 - r_1^2)}{2 \ln(r_2/r_1)}} \quad (2.12)$$

The above expressions for streamline (laminar) flow in an annulus are exact expressions relating the pressure drop to the velocity. But no exact mathematical analysis of the conditions within a turbulent fluid has yet been developed. For turbulent flow in an annulus, the hydraulic mean diameter (equivalent diameter) may be used in place of the pipe diameter and the formula for circular pipe can then be applied without introducing a large error [1]. This method of approach is entirely empirical.

The equivalent diameter  $d_e$  is defined as four times the cross sectional flow area divided by the wetted perimeter  $d_e = 4 \times \frac{\text{cross sectional area}}{\text{wetted perimeter}}$

For an annulus of inner radius (outer radius of the inner tube)  $r_1$ , and outer radius (inner radius of the outer tube)  $r_2$ :

$$d_e = 4 \times \frac{\pi(r_2^2 - r_1^2)}{2\pi(r_2 + r_1)} = 2(r_2 - r_1) = d_2 - d_1 \quad (2.13)$$

The above  $d_e$  is for pressure drop (fluid flow), which differs from that for heat transfer [2]. The shear stress resisting the flow of fluid acts on both walls of the annulus, while in heat transfer between the annulus and the inner pipe only one wall is involved (i.e. perimeter is different), so  $d_e$  for heat transfer is  $d_e = 4 \times \pi(r_2^2 - r_1^2) / 2\pi r_1 = 2(r_2^2 - r_1^2) / r_1 = (d_2^2 - d_1^2) / d_1$ . However, hydraulic  $d_e$  rather than heat  $d_e$  is more frequently used in literature.

### 2.3 Friction Factor in an Annulus

There is a resistance to flow (or drop in pressure) due to friction of fluids flowing in the different types of ducts. This resistance is expressed by using the concept of friction factor.

For turbulent flow in smooth pipes, the Blasius equation for Fanning friction factor is [2]:  $f = 0.079 \text{Re}^{-0.25}$  (2.14)

Carpenter et al. [4] measured friction factor in annular space in turbulent region:  $f = 0.046 \left( \frac{\rho u d_e}{\mu} \right)^{-0.2} = 0.046 \text{Re}^{-0.2}$  (2.15)

where  $d_e=d_2-d_1$

The distinction between the friction factors at the inner and outer walls of the annulus,  $f_1$  and  $f_2$  respectively, was discussed by Knudsen [5], who presented a method by which the friction factor at both walls of the annulus may be determined for different values of Re and  $r_1/r_2$ . This treatment, based on the work of Rothfus et al. [6] who first defined two distinct annulus friction factors, yields the following expressions for turbulent flow:

$$f_1 = 0.046 \text{Re}^{-0.2} \left( \frac{1 - (r_1/r_2)}{1 - (r_{\max}/r_2)^2} \right)^{0.2} \left( \frac{(r_{\max}/r_2)^2 - (r_1/r_2)^2}{(r_1/r_2)(1 - (r_{\max}/r_2)^2)} \right) \quad (2.16)$$

$$f_2 = 0.079 \text{Re}^{-0.25} \left( \frac{1 - (r_1/r_2)}{1 - (r_{\max}/r_2)^2} \right)^{0.25} \left( \frac{(r_{\max}/r_2)^2 - (r_1/r_2)^2}{(r_1/r_2)(1 - (r_{\max}/r_2)^2)} \right) \quad (2.17)$$

where  $r_{\max}$  is given by Eq. (2.12)

## 2.4 Dimensionless Groups of Heat and Mass Transfer

Many factors influence the value of heat and mass transfer coefficients ( $h$ , and  $k_m$ ), that it is almost impossible to determine their individual effects. By arranging these factors or variables in a series of dimensionless groups, the problem becomes more manageable because the number of groups is significantly less than the number of parameters. Table 2-1 shows the dimensionless groups used in heat and mass transfer.

For forced convection heat and mass transfer, the experimental results can be related by the following relations [1, 7]:

$$\text{Nu} = f(\text{Re}, \text{Pr}) \quad (2.18)$$

$$\text{Sh} = f(\text{Re}, \text{Sc}) \quad (2.19)$$

The reason for these functional forms is the dependence of heat and mass transfer processes on the flow regime, and hence on Reynolds number. The Prandtl number relates the relative rates of diffusion of momentum and

heat, so that the Prandtl number is expected to be a significant parameter in the heat transfer functional form. Also the Schmidt number relates the relative rates of diffusion of momentum and mass, so that the Schmidt number is expected to be a significant parameter in the mass transfer functional form.

Usually these relations are expressed by the following equations [1, 7]:

$$\text{Nu} = c \text{Re}^m \text{Pr}^n \quad (2.20)$$

$$\text{Sh} = c \text{Re}^m \text{Sc}^n \quad (2.21)$$

where  $c$ ,  $m$ , and  $n$  are constants to be determined from experimental data.

Table 2-1 Corresponding dimensionless groups of heat and mass transfer [1, 8].

Heat Transfer	Mass Transfer
Reynolds number $\text{Re} = \frac{\rho u d}{\mu}$	Reynolds number $\text{Re} = \frac{\rho u d}{\mu}$
Prandtl number $\text{Pr} = \frac{C_p \mu}{k} = \frac{\nu}{\alpha}$	Schmidt number $\text{Sc} = \frac{\mu}{\rho D} = \frac{\nu}{D}$
Nusselt number $\text{Nu} = \frac{h d}{k}$	Sherwood number $\text{Sh} = \frac{k_m d}{D}$
Peclet number $\text{Pe}_h = \text{Re Pr} = \frac{d u}{\alpha}$	Peclet number $\text{Pe}_m = \text{Re Sc} = \frac{d u}{D}$
Stanton number $\text{St}_h = \frac{\text{Nu}}{\text{Re Pr}} = \frac{h}{C_p \rho u}$	Stanton number $\text{St}_m = \frac{\text{Sh}}{\text{Re Sc}} = \frac{k_m}{u}$
$J$ -factor $J_h = \text{St}_h \text{Pr}^{2/3}$	$J$ -factor $J_m = \text{St}_m \text{Sc}^{2/3}$

## 2.5 The Boundary Layers

The boundary layers are of considerable interest to chemical engineers because these influence, not only the drag effect of the fluid on the surface, but also the heat or mass transfer rates if a temperature or concentration gradient exists. Three types of boundary layers can be recognized:

- 1- Hydrodynamic (Momentum) boundary layer [9]: is the region adjacent to a solid surface in which viscous (frictional) forces are important. The boundary layer thickness is usually defined as the distance from the surface, where the velocity is zero, to the point where the velocity is 99 percent of the free stream velocity.
- 2- Thermal boundary layer [7]: may be defined as that region where temperature gradients are present in the flow. These temperature gradients would result from a heat exchange between the fluid and the wall.
- 3- Diffusion boundary layer [1, 10]: is defined as that layer in the vicinity of the surface where a concentration gradient exists within a fluid flowing over a surface, and mass transfer will take place. The whole of the resistance to mass transfer can be regarded as lying within this layer.

For laminar flow, the ratios of hydrodynamic boundary layer thickness  $\delta$  to the thermal boundary layer thickness  $\delta_t$ , and to the diffusion boundary layer thickness  $\delta_m$  are given by the following relations [9,10,11]:

$$\frac{\delta}{\delta_t} = \text{Pr}^{1/3} \quad (2.22)$$

$$\frac{\delta}{\delta_m} = \text{Sc}^{1/3} \quad (2.23)$$

The thickness of the diffusion layer is the smallest and the hydrodynamic layer is the greatest, and the diffusion layer lies in the thermal

layer. The building up of these three layers on a surface of a solid body is shown in Fig. 2-2.

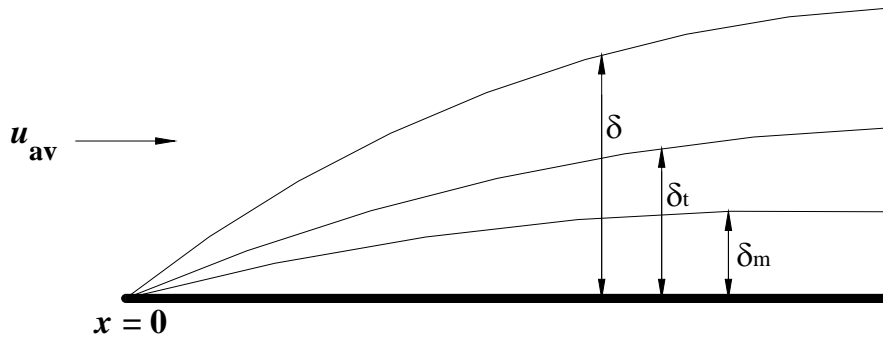


**Figure 2-2** The boundary layers [7, 9, 10].

## 2.6 Methods of Supplying Heat Flux

There are a number of different ways in which the surface of the test section can be heated [12]:

- 1- Electrical resistance heating: this approach uses the electrical resistance of the metal test section to generate heat when an electrical current is passed through it. This type of heating has some limitations and disadvantages. The materials of construction for the test section are limited to those of high electrical resistance, also the high current required limits this use to non-hazardous fluids.
- 2- Indirect electrical heating: two forms are used, the externally heated tube and the internally heated annulus. The externally heated tube uses heating rods or ribbon heating element around the outer circumference of the tube. A disadvantage of this design is the cost of replacing the tube since each test section must be a complete assembly. The center element of the

internally heated annulus is a cartridge type heater. Construction, selection of materials, and replacement of the heating element are the advantages of this design. In general, indirect electrical heating is convenient for simple geometries, but may be restricted to non-hazardous area. Figure 2-3 shows the two types of indirect electrical heating.

- 3- Condensing vapor heating: hot condensing vapors can be used as a constant temperature heating medium by constant pressure operation, or it may be used for constant heat flux operation by keeping the condensate flow rate constant. The condensing vapor presents no problems in hazardous areas and does not limit the design geometry as in the case of electrical heating. The operating temperature range depends on the vapor used.
- 4- Sensible fluid heating: for complex geometries, such as the shell side of shell and tube heat exchangers or plate exchangers, the most attractive heating medium is a sensible heating fluid, usually a liquid. While it is limited to lower heat fluxes and lower temperatures, the sensible heating fluid gives better thermal control than electrical heating or condensing vapors. As with condensing vapors, hot liquids are generally acceptable for hazardous areas. In addition, complex geometries not possible with electrical heating can be handled with sensible fluid heating.

Constant heat flux operation is easily maintained by electrical heating. Operation at constant heating medium temperature is more typical of plant operations, it is best attained with condensing vapors or sensible heating fluids.

Internally heated annulus method was used by the present work, in which the fluid flowing in the annulus of concentric pipe can be heated by a cartridge heater located internally within the inside pipe (hollow rod) providing constant heat flux.

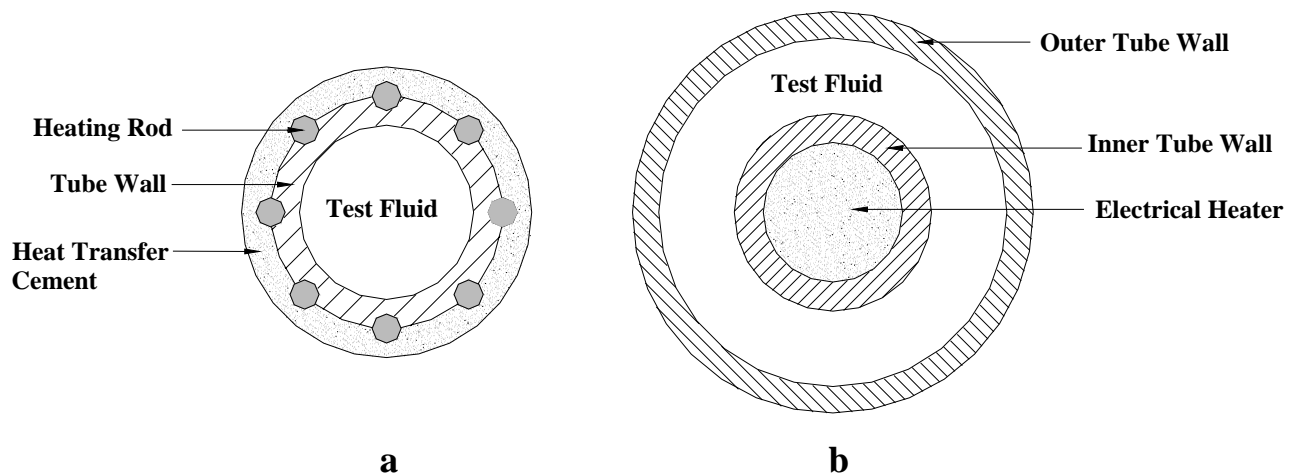


**Figure 2-3** Indirect electrical heating; a) Externally heated tube, b) Internally heated annulus [12].

## 2.7 Measurement of Surface Temperature

The rate at which heat is convected away from a solid surface by a fluid is given by Newton's law of cooling [7, 13, 14]:

$$\frac{Q}{A} = h(T_s - T_b) \quad (2.24)$$

where  $Q$  is the heat transfer rate,  $A$  is the surface area of the test specimen,  $h$  is the heat transfer coefficient,  $T_s$  is the surface temperature, and  $T_b$  is the bulk temperature of a fluid.

When it is desired to obtain heat transfer coefficient  $h$  between fluid and surface by direct measurements, the problem of determining the temperature of the solid surface arises. Using thermocouples does this.

The following two methods are used for installing thermocouples in walls:

- 1- A groove is cut in the part of the outer surface of the working specimen, and the thermocouple is inserted in it. The presence of a thermocouple wire on a surface tends to disturb the flow of the fluid in the zone near the surface, even if the correct surface temperature was measured.

2- A hole is drilled below the surface of the working specimen, from an outer edge to the required point along its length axis. This method does not disturb the surface of the metal and was adopted by the present work.

## 2.8 Heat Transfer Coefficient Correlations for Flow in Annular Space Between Concentric Tubes

In presenting equations for heat transfer correlations in the annulus, one of the difficulties has been to select the best equivalent diameter to use.

Monrad and Pelton [15] presented the following correlation for heat transfer coefficients for water and air in annular space for turbulent flow:

$$\frac{hd_e}{k} = 0.023 \left( \frac{\rho u d_e}{\mu} \right)^{0.8} \left( \frac{C_p \mu}{k} \right)^{0.33} \left( \frac{d_2}{d_1} \right)^{0.5} \quad (2.25)$$

Where  $d_1$  and  $d_2$  are the inside and outside diameter of the annulus respectively,  $d_e$  is the equivalent diameter ( $d_e = d_2 - d_1$ ).

Davis [16] proposed the following equation for turbulent flow based on the inside diameter of the annulus  $d_1$ :

$$\frac{hd_1}{k} = 0.031 \left( \frac{\rho u d_1}{\mu} \right)^{0.8} \left( \frac{C_p \mu}{k} \right)^{0.33} \left( \frac{d_2}{d_1} \right)^{0.15} \left( \frac{\mu}{\mu_s} \right)^{0.14} \quad (2.26)$$

For heating water flowing turbulently upward in the vertical annulus, Carpenter et al. [4] used the equivalent diameter ( $d_e = d_2 - d_1$ ), and recommended:

$$\frac{hd_e}{k} = 0.027 \left( \frac{\rho u d_e}{\mu} \right)^{0.8} \left( \frac{C_p \mu}{k} \right)^{0.33} \left( \frac{\mu}{\mu_s} \right)^{0.14} \quad (2.27)$$

For the laminar flow, Carpenter's results were reasonably well expressed by the following equation [1]:

$$\frac{hd_e}{k} = 1.86 \left[ \left( \frac{\rho u d_e}{\mu} \right) \left( \frac{C_p \mu}{k} \right) \left( \frac{d_1 + d_2}{L} \right) \right]^{1/3} \left( \frac{\mu}{\mu_s} \right)^{0.14} \quad (2.28)$$

where  $L$  is the length of tube.

## 2.9 Methods of Measuring Mass Transfer Rates

Mass transfer coefficients are usually determined experimentally. A large number of techniques have been used but the most widely used are [17, 18]:

- 1- Dissolving wall method: in this method, a specimen is made of or coated with a material that is soluble in the test solution. Typical example of this method is benzoic acid in glycerine/water mixtures, where the solid wall (benzoic acid) is dissolved and the weight loss  $\Delta w$  measured over a period of time  $\Delta t$ , and mass transfer coefficient is calculated by:

$$k_m = \frac{-\Delta w}{AM\Delta t(C_{\text{sat}} - C_b)} \quad (2.29)$$

where  $M$  is the molecular weight,  $A$  is the surface area,  $C_{\text{sat}}$  is the saturation concentration, and  $C_b$  is the bulk concentration. In this technique, the wall geometry is obviously changed and produces an error in measurement.

- 2- Limiting current density technique (LCDT): in this technique, a single electrochemical reaction is driven at such a potential that its rate becomes diffusion controlled. The most common reactions used in literature are the reduction of the ferricyanide ions, and the deposition of copper. This technique will be described in detail in chapter three.
- 3- Analogy with heat transfer: mass transfer coefficients can be obtained from heat transfer data using the analogy between heat and mass transfer. This means that the heat transfer coefficients can also be obtained from mass transfer data by using the analogy.

## 2.10 Heat and Mass Transfer Analogy

The basic mechanisms of mass, heat, and momentum transfer are essentially the same, so the analogy among them can be presented. The analogy between heat and mass transfer is obtained by substituting the analogous dimensionless groups. The Reynolds number appears unchanged in both heat and mass transfer equations. Schmidt number in the mass transfer equations replaces the Prandtl number in the heat transfer equations. Similarly, the Nusselt number in heat transfer is analogous to the Sherwood number in mass transfer. This means that the analogy between heat and mass transfer would differ only in the substitution of the proper dimensionless groups.

The applicable restrictions to the analogy between heat and mass transfer are [10]:

- 1- Same velocity profile
- 2- Analogous mathematical boundary conditions
- 3- Equal eddy diffusivities

The analogy between heat and mass transfer will not be valid if there are additional mechanisms of transfer present in one transfer but not in the other. Examples in which analogies between heat and mass transfer would not be applicable include:

- 1- Viscous heating.
- 2- Chemical reaction.
- 3- A source of heat generation within the flowing fluid such as a nuclear source.
- 4- Absorption or emission of radiant energy.
- 5- Pressure or thermal mass diffusion.

The analogy between heat and mass transfer is often valid even if there is form drag [10, 11], while the analogy between momentum transfer and heat or mass transfer is not valid if there is form drag, so can not be applied to any flow for which separation of the boundary layer occurs, e.g. flow around spheres, cylinders, or flow perpendicular to pipes or tubes.

The analogies are most useful for predicting or correlating mass transfer data and less useful for heat transfer because accurate correlations exist. A large number of analogies are available in literature. Chilton and Colburn analogy [19] has proved useful because it is based on empirical correlations and not on mechanistic assumptions [10]. The Chilton-Colburn analogy is:

$$J_h = J_m = \frac{f}{2} \quad (2.30)$$

## **CHAPTER THREE**

# **ELECTROCHEMICAL CORROSION**

### **3.1 Introduction**

Corrosion is defined as the destructive attack of a metal by chemical or electrochemical reaction with its environment [20]. Corrosion in an aqueous environment is an electrochemical process because corrosion involves the transfer of electrons between a metal surface and an aqueous electrolyte solution. Corrosion results from the tendency of metals to react electrochemically with oxygen, water, and other substances in the aqueous environment [21].

Corrosion can be separated into two partial reactions; oxidation and reduction. Oxidation is the loss of electrons while reduction is the gain of electrons. The electrode at which oxidation occurs is called the anode while the electrode at which reduction occurs is called the cathode. During metallic corrosion these two reactions occur simultaneously and the rate of oxidation equals the rate of reduction [22].

### **3.2 Polarization**

An electrode, which is capable of participating in a perfectly reversible process, is referred to as non-polarisable. In practical processes an electrode shows deviation from equilibrium potential (metal in equilibrium with its ions), and is said to be polarized or to exhibit polarization [22, 23]. The magnitude of this deviation in potential is known as the overpotential or overvoltage  $\eta$ .

#### **3.2.1 Activation Polarization**

Activation overpotential arises due to the phenomena associated with an electrode reaction [23]. The essential feature of any electrode reaction is the electron transfer across the electrode/solution interface, but this process is only one in a sequence of reaction steps. The actual sequence could include

adsorption and desorption of reactants, products and intermediates together with surface diffusion and surface chemical reactions. The rate of reaction will be determined by the slowest step, known as the rate-determining step.

Activation polarization is characterized by slow electrochemical reaction and by low exchange current density  $i_o$ . The surface concentration does not differ much from bulk concentration.

The current density (current per unit area)  $i$ , is given by:

$$i = i_c - i_a \quad (3.1)$$

where  $i_c$  and  $i_a$  are the partial current densities for the cathodic and anodic reactions. For activation polarization, the reaction rate or current density is given by [23, 24]:

$$i = i_o \left\{ \exp \left[ \frac{-\alpha_c z F \eta^A}{RT} \right] - \exp \left[ \frac{(1 - \alpha_c) z F \eta^A}{RT} \right] \right\} \quad (3.2)$$

where

$i_o$  = exchange current density, represents the rate of the forward and reverse reactions at equilibrium.

$F$  = Faraday constant (96487 coulomb/equivalent).

$z$  = number of electrons involved in the rate determining step.

$T$  = absolute temperature.

$\alpha_c$  = symmetry coefficient.

$\eta^A$  = activation polarization.

Eq. (3.2) is known as the Butler-Volmer equation. For appreciable cathodic polarization, the reverse reaction is almost entirely suppressed and the second exponential term is very nearly zero. Consequently:

$$i = i_o \exp \left[ \frac{-\alpha_c z F \eta^A}{RT} \right] \quad (3.3)$$

which can be arranged to [20, 22-25]:

$$\eta^A = \frac{RT}{\alpha_c zF} \ln i_o - \frac{RT}{\alpha_c zF} \ln i \quad (3.4)$$

or

$$\eta^A = \frac{2.3RT}{\alpha_c zF} \log i_o - \frac{2.3RT}{\alpha_c zF} \log i \quad (3.5)$$

or in the form of Tafel equation,  $\eta^A = \beta \log \frac{i}{i_o}$  (3.6)

where Tafel constant is  $\beta = \frac{-2.3RT}{\alpha_c zF}$  (3.7)

Eqs. (3.4-3.6) are used for an overpotential of more than 100 mV in absolute magnitude. Figure 3-1a shows schematic diagram of activation polarization.

### 3.2.2 Concentration (Diffusion or Transport) Polarization

Concentration overpotential is caused by changes in the concentration of species participating in an electrode reaction. When a current passes, a depletion or accumulation of some species occurs in the electrolyte solution adjacent to an electrode. The electrode is thus surrounded by a solution of different composition to that in the bulk, which would cause a shift in the electrode potential away from its equilibrium value [23].

Concentration polarization refers to fast electrochemical reactions that are limited by mass transfer of species to and from the electrode. In other words, concentration polarization [26] occurs when one of the reactants is consumed at an electrode faster than it can be supplied from the bulk of the solution, and the rate of the reaction is limited by diffusion from the solution to the electrode surface. Concentration changes are not a problem in the anodic reaction. Concentration polarization is a factor in determining the rate of the cathodic reaction such as cathodic reduction of oxygen in aqueous solutions. The equation for concentration polarization  $\eta^C$  is given by [20, 22-26]:

$$\eta^c = \frac{2.3RT}{zF} \log\left(1 - \frac{i}{i_L}\right) \quad (3.8)$$

where  $i_L$  is the limiting current density, which represents the maximum rate of a possible reaction for a given system, as shown in Fig. 3-1b, and can be expressed by the following equation for a cathodic partial reaction:

$$i_L = \frac{zFDC_b}{\delta_d} \quad (3.9)$$

where  $D$  is the diffusion coefficient of the reacting ions,  $C_b$  is the concentration of the reacting ions in the bulk solution,  $\delta_d$  is the thickness of the diffusion layer.

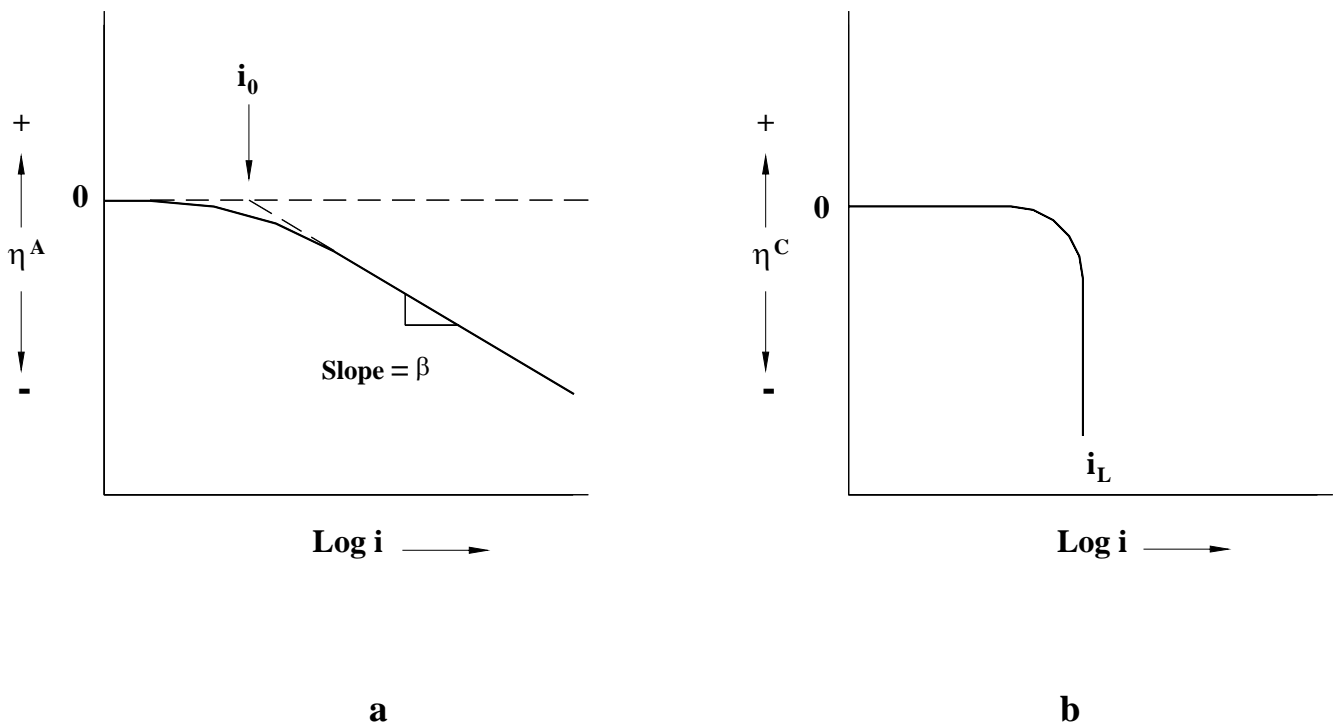


**Figure 3-1** Schematic diagram of cathodic polarization curves;  
a) Activation polarization, b) Concentration polarization.

### 3.2.3 Resistance Polarization

Resistance overpotentials are caused by changes in the solution conductivity and by film formation on the electrodes [23,25]. This means that in addition to the resistivity of the solution, any insulating film deposited either at the cathodic or anodic sites that restricts or completely blocks contact between the metal and the solution will increase the resistance overpotential. This applies particularly to the deposition of  $\text{CaCO}_3$  and  $\text{Mg(OH)}_2$  at the cathodic sites during corrosion in hard waters due to the increase in pH produced by the cathodic process, and since the anodic and cathodic sites are usually close together the calcareous scale will also block the anodic sites, and thus decreases the corrosion rate. The resistance overpotential is defined as:

$$\eta^R = I(R_{\text{soln}} + R_{\text{film}}) \quad (3.10)$$

where  $I$  is the current,  $R_{\text{soln}}$  is the electrical resistance of the solution,  $R_{\text{film}}$  is the resistance formed on the surface of the site.

### 3.3 Concentration Polarization from the Nernst Viewpoint

Nernst proposed an early idea about mass transfer in electrochemical processes. He suggested that mass transfer occurs solely by molecular diffusion through a thin layer of solution adjacent to an electrode. This layer has a linear concentration gradient across it, and the outer edge is assumed to be maintained at the constant bulk concentration by migration and convection. Figure 3-2 shows a schematic diagram of this layer.

The diffusion layer thickness  $\delta_d$  is influenced by the shape of the electrode, the geometry of the system, and by the velocity of the solution or agitation [22, 25]. The molar flux  $N$  across this diffusion layer can be expressed by Fick's first law as [23-25]:

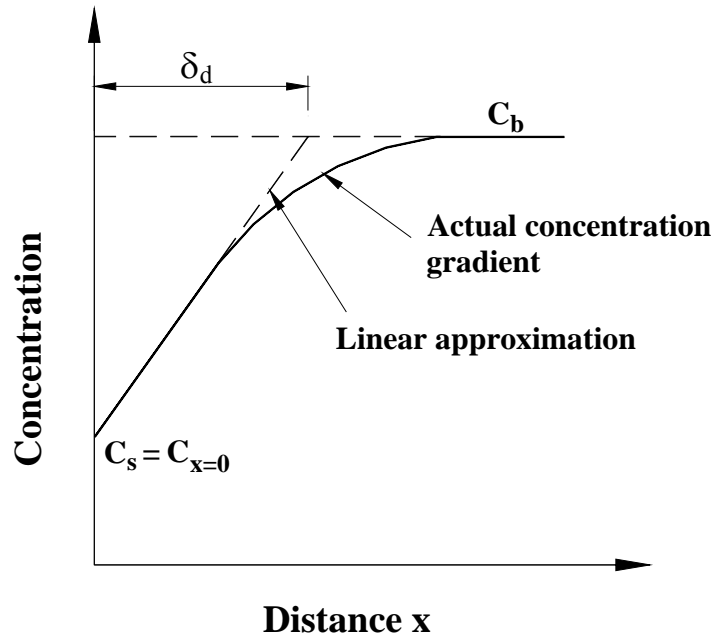


**Figure 3-2** Nernst diffusion layer [24, 25].

$$N = \frac{D}{\delta_d} (C_b - C_s) \quad (3.11)$$

where  $C_s$  is the surface concentration.

The molar flux  $N$  can also be expressed in terms of the current density by Faraday's law so that:

$$N = \frac{i}{zF} = \frac{D}{\delta_d} (C_b - C_s) \quad (3.12)$$

The mass transfer coefficient  $k_m$  can be related by [18, 23, 24, 27]:

$$N = \frac{i}{zF} = k_m (C_b - C_s) \quad (3.13)$$

Comparing Eq. (3.12) with Eq. (3.13) yields:

$$k_m = \frac{D}{\delta_d} \quad (3.14)$$

The concentration gradient will be a maximum when  $C_s = 0$ , and this will correspond with the maximum or limiting current density  $i_L$ . So substituting  $C_s = 0$  in Eqs. (3.12) and (3.13) to obtain:

$$i_L = \frac{zFDC_b}{\delta_d} \quad (3.9)$$

and 
$$i_L = zFk_m C_b \quad (3.15)$$

The Nernst equation written in terms of the concentration polarization of a cathode is [23, 25]:

$$\eta^c = \frac{2.3RT}{zF} \log \frac{C_s}{C_b} \quad (3.16)$$

From Eqs. (3.13) and (3.15), it can be obtained

$$\frac{C_s}{C_b} = 1 - \frac{i}{i_L} \quad (3.17)$$

Substituting this in Eq. (3.16), results

$$\eta^c = \frac{2.3RT}{zF} \log \left( 1 - \frac{i}{i_L} \right) \quad (3.8)$$

which gives the relationship between  $\eta^c$  and  $i$  for a cathodic reaction in which the overpotential is solely due to transport.

The limiting current density in Eq. (3.9) has been derived on the assumption that transport is only by diffusion, but if ionic migration also occurs then for a cathodic process

$$i_L = \frac{zFDC_b}{\delta_d(1 - n_+)} \quad (3.18)$$

where  $n_+$  is the transference number of the cation that is involved in charge transfer. The term  $(1 - n_+)$  can be neglected if ions other than the species involved in the electrode process are responsible for ionic migration.

### 3.4 Limiting Current Density

The limiting current density is defined as the maximum current that can be generated by a given electrochemical reaction at a given reactant concentration under well established hydrodynamic conditions in the steady state.

At a given reaction rate, the distribution of the reacting species in the solution adjacent to the electrode surface is relatively uniform. If the current is increased, the reaction rate will increase, and the region adjacent to the electrode surface will become depleted of reacting species. This means as the current density is increased, the surface concentration of reacting species decreases until it approaches zero at which the current density is called the limiting current density.

The limiting current density  $i_L$  is the rate controlling parameter in concentration polarization. It is usually only significant during reduction (cathodic) processes and is usually negligible during metal dissolution (anodic) reactions. The reason for this is simply that there is an almost unlimited supply of metal atoms for dissolution [22].

The diffusion layer thickness  $\delta_d$  is dependent on the velocity of the solution past the electrode surface [26]. As this velocity increases,  $\delta_d$  decreases and the limiting current density  $i_L$  increases according to Eq. (3.9).

Certain criteria should be met in the choice of electrochemical systems used in limiting current measurements [28]: 1) chemical stability; 2) high solubility; 3) electrode potential sufficiently different from that of hydrogen (or oxygen) to give long, well-defined plateaus; 4) low cost. Therefore, relatively few systems are employed like, deposition of copper, reduction of ferricyanide to ferrocyanide, and reduction of oxygen.

It is possible to determine several different parameters by limiting current measurements [18]:

- 1- The mass transfer coefficient  $k_m$  as a function of flow rate, system geometry, and concentration, by measuring limiting current density and bulk concentration.
- 2- The effective diffusivity of the reactant  $D$  as a function of system geometry, type of flow, and electrolyte composition, by measuring limiting current density, bulk concentration, some bulk solution properties, and flow or rotation velocity.
- 3- The reactant concentration in solution  $C_b$ , by measuring limiting current density in a system of fixed geometry and comparing it with that for a known value of concentration, at fixed flow velocity.

The mass transfer coefficient from the limiting current density measurement is the more easily accessible quantity since one only needs to know the bulk reactant concentration. The mass transfer coefficient is required to be calculated by the present work.

For accurate mass transfer measurements it is desirable to generate a well-defined limiting current plateau, and this implies adequate width and minimum inclination. Adequate width of the plateau is made possible by selecting an electrode reaction with equilibrium potential far removed from the hydrogen and oxygen evolution potential. The inclination of the limiting current plateau is the result of [18]:

- 1- Change in the bulk concentration of reactant, e.g., a decrease in some cases of free convection where a steady state is reached only very slowly.
- 2- Increasing surface roughness, e.g., deposition of metals like copper or zinc, fouling products due to corrosion.
- 3- Nonuniform current distribution, e.g., working with large, non-sectioned electrodes.

### 3.5 Mass Transfer Correlations For Flow in Annular Space Between Concentric Pipes Established by Limiting Current Measurement: Literature Review

First, Lin et al. [29] studied the transfer rates of four electrochemical systems: the cathodic reduction of ferricyanide ion, quinine, and oxygen; and the anodic oxidation of ferrocyanide, in an annular space between two concentric pipes of radius ratio ( $r_1/r_2$ ) of 0.5 at various temperatures and flow rates. The limiting current on the inner pipe was measured. They found that their data for streamline region corresponding to Leveque's equation for mass transfer:

$$\text{Sh} = 1.62(\text{ReSc}d_e / L)^{1/3} \quad (3.19)$$

and with Chilton-Colburn's empirical relation in the turbulent region:

$$J_m = \text{St}_m \text{Sc}^{2/3} = 0.023 \text{Re}^{-0.2} \quad (3.20)$$

Ross and Wragg [30, 31] studied the electrochemical mass transfer in the mass transfer entry region of annuli by measuring the limiting current for the deposition of copper from acidified solution of copper sulphate onto copper cathodes of different lengths. The cathode formed part of the inner wall of an annular flow system and conditions were such that in both streamline and turbulent flow the hydrodynamic conditions were fully developed at the mass transfer section. For streamline flow, the data have been correlated by the equation:

$$\text{Sh} = 1.94(\text{ReSc}d_e / L)^{1/3} \quad (3.21)$$

This for an annulus radius ratio ( $r_1/r_2$ ) of 0.5. For annuli of radius ratios of 0.25 and 0.125, the constant in the correlating equation was found to increase. In the turbulent flow with an annulus radius ratio of 0.5, Ross and Wragg correlated experimental data by the following equation:

$$\text{St}_m = 0.276 \text{Re}^{-0.42} \text{Sc}^{-2/3} (d_e / L)^{1/3} \quad (3.22)$$

Wragg and Ross [32] used the same electrochemical annular system of 0.5 radius ratio to study the rates of mass transfer under conditions of transport control such that both forced and free streamline convective mechanisms were significant in determining the overall mass transfer rate. In this case of free convection with upward forced flow in vertical annulus, the free convection flow is in the same direction as the forced flow. They correlated the experimental data by the equation:

$$\text{Sh} = 1.96 \left\{ \text{Re Sc} d_e / L + 0.04 (\text{Gr}_m \text{Sc} d_e / L)^{0.75} \right\}^{0.319} \quad (3.23)$$

where  $\text{Gr}_m$  is the Grashof number for mass transfer,  $(\text{Gr}_m = gL^3 \Delta\rho / \nu^2 \rho)$ .

Wragg [33] studied combined free and forced convective ionic mass transfer in the case of opposed flow of a vertical annular flow cell. The solution was caused to flow down the cell, to oppose free convection, which is upward. Wragg found that the mass transfer rates decrease with increasing flow, pass through a minimum and then increase to follow typical pure laminar flow behavior.

Newman [34] stated general expression for the average mass transfer rate over length  $L$  for laminar flow in annular channels:

$$\text{Sh} = 1.615 (\phi \text{Re Sc} d_e / L)^{1/3} \quad (3.24)$$

where  $\phi$  is a function of the radius ratio ( $r_1/r_2$ ) as shown in Fig. 3-3. Re and Sh are based on equivalent diameter ( $d_e = d_2 - d_1$ ).

The above correlations and others are listed in Table 3-1 which gives a detailed literature review of mass transfer correlations measured by limiting current density technique for annular flow between two concentric tubes.

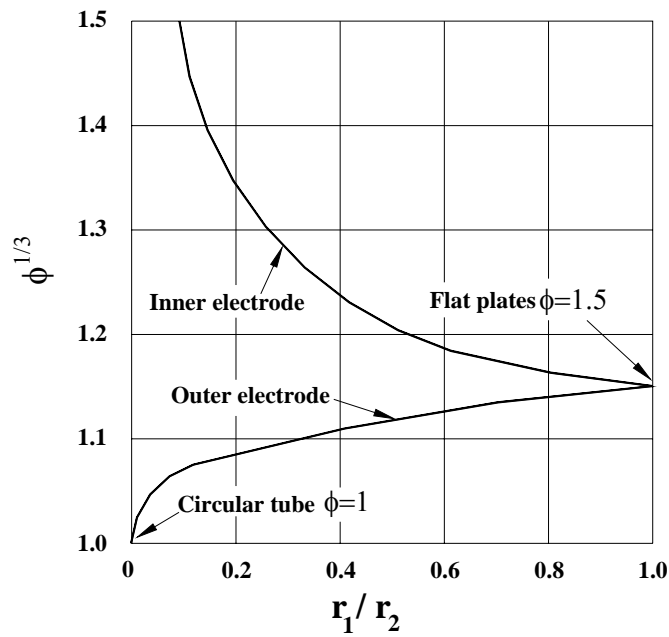


**Figure 3-3**  $\phi$  as a function of the radius ratio ( $r_1/r_2$ ) [34].

### 3.6 Anodic and Cathodic Reactions in Corrosion

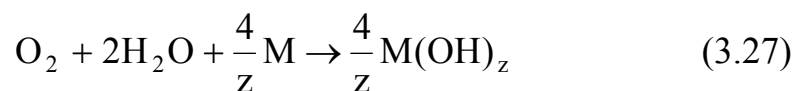
The basic electrochemical reaction of corrosion is the removal of a metal from an anodic site to form an ion in solution, leaving behind excess electrons on the metal [20, 22, 25, 46]:



Simultaneously, electrons are consumed at nearby cathodic sites by a balancing reaction as shown in Fig. 3-4, which for neutral and alkaline solutions is usually the reduction of dissolved oxygen:



Metallic oxide, or hydroxide, deposits are formed thus:



In terms of iron, Fe, the anodic reaction is



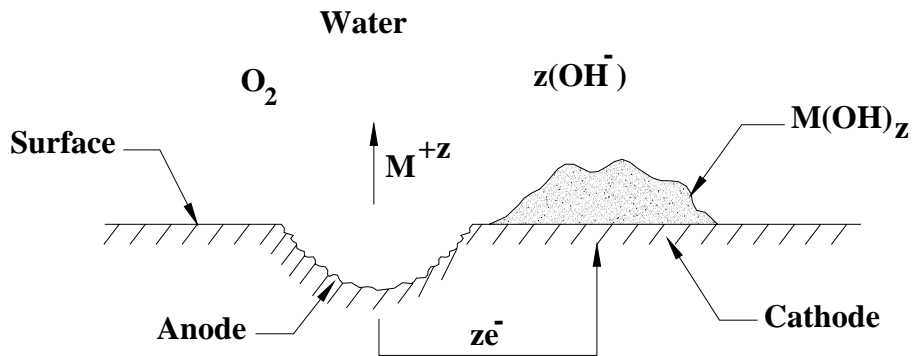
and Eq. (3.27) becomes:  $O_2 + 2H_2O + 2Fe \rightarrow 2Fe(OH)_2$  (3.29)

Table 3-1 Mass transfer correlations for flow in the annular space between two concentric tubes established by limiting current measurement.

	Reference	Reactants	Type of flow	Correlation	Range	Parameters
1	Lin et al. [29]	O <sub>2</sub> , Fe(CN) <sub>6</sub> <sup>-3</sup> , Fe(CN) <sub>6</sub> <sup>-4</sup> , Quinone	Laminar flow  Developed mass transfer in turbulent flow	Sh = 1.62(ReSc <sub>d<sub>e</sub></sub> / L) <sup>1/3</sup>  Sh = 0.023Re <sup>0.8</sup> Sc <sup>1/3</sup>	1.6 × 10 <sup>4</sup> < ReSc <sub>d<sub>e</sub></sub> / L < 1.1 × 10 <sup>6</sup>  300 < Sc < 3000, r <sub>1</sub> /r <sub>2</sub> =0.5  2100 < Re < 30000	Re = ρud <sub>e</sub> / μ  Sh = k <sub>m</sub> d <sub>e</sub> / D
2	Ross & Wragg [30, 31]	Cu <sup>+2</sup>	Laminar flow  Turbulent flow	Sh = 1.94(ReSc <sub>d<sub>e</sub></sub> / L) <sup>1/3</sup>  Sh = 0.276Re <sup>0.58</sup> Sc <sup>1/3</sup> (d <sub>e</sub> / L) <sup>1/3</sup>	1.7 × 10 <sup>4</sup> < ReSc <sub>d<sub>e</sub></sub> / L < 9 × 10 <sup>7</sup>  r <sub>1</sub> /r <sub>2</sub> =0.5  3000 < Re < 17000	Re = ρud <sub>e</sub> / μ  Sh = k <sub>m</sub> d <sub>e</sub> / D
3	Wragg & Ross [32]	Cu <sup>+2</sup>	Combined free and forced convection	Sh = 1.96 $\left\{ \begin{array}{l} \text{ReSc}_{d_e} / L + 0.04 \\ (\text{Gr}_m \text{Sc}_{d_e} / L)^{0.75} \end{array} \right\}^{1/3}$	1.3 × 10 <sup>7</sup> < Gr <sub>m</sub> Sc <sub>d<sub>e</sub></sub> / L < 1.1 × 10 <sup>9</sup> 7 × 10 <sup>3</sup> < ReSc <sub>d<sub>e</sub></sub> / L < 2.5 × 10 <sup>5</sup>	Gr <sub>m</sub> = gL <sup>3</sup> Δρ / νρ <sup>2</sup>
4	Newman [34]	O <sub>2</sub>	Laminar flow	Sh = 1.615(φ ReSc <sub>d<sub>e</sub></sub> / L) <sup>1/3</sup>		φ, Fig. 3-3
5	Bazan & Arvia [35]	Cu <sup>+2</sup>	Developing flow in laminar region	Sh = 0.647Re <sub>L</sub> <sup>1/2</sup> Sc <sup>1/3</sup>		Re <sub>L</sub> = ρuL / μ
6	Bazan & Arvia [36]	Fe(CN) <sub>6</sub> <sup>-3</sup>	Developing flow in laminar region	Sh = 0.525Re <sub>d</sub> <sup>1/2</sup> Sc <sup>1/3</sup> (L/d <sub>e</sub> ) <sup>3/4</sup>		Re <sub>d</sub> = ρud <sub>e</sub> / μ

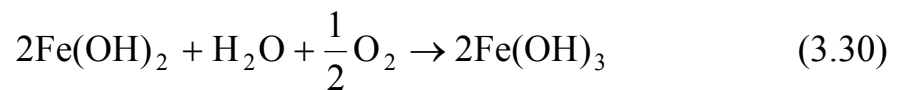
Table 3-1 Continued

	Reference	Reactants	Type of flow	Correlation	Range	Parameters
7	Coeuret et al. [37, 38]	$\text{Fe}(\text{CN})_6^{-3}$	Developing flow in laminar region	$\text{Sh} = 0.45 \text{Re}_{d_1}^{0.53} \text{Sc}^{1/3}$	$25 < \text{Re}_{d_1} < 225$  $\text{Sc}=1230$	$\text{Re}_{d_1} = \rho u d_1 / \mu$
8	Carbin & Gabe [39, 40]	$\text{Cu}^{+2}$	Developing flow in laminar region	$\text{Sh} = 3.93 \text{Re}_d^{0.32} \text{Sc}^{1/3} (d_e / L)^{0.35}$	$6 \times 10^4 < \text{Re}_d \text{Sc} < 10^6$  $\text{Sc}=750, 1680$	$\text{Re}_d = \rho u d_e / \mu$
9	Regner & Rousar [41]	$\text{Fe}(\text{CN})_6^{-4}$	Tangential inflow	$\text{Sh} = 0.24 \text{Re}_d^{0.78} \text{Sc}^{1/3} (d_e / L)^{0.5} (A / A_1)^{1/3}$	$48 < \text{Re}_d < 500$  $1.3 < L / d_e < 12$	$A = \pi(r_2^2 - r_1^2)$ $A_1 = \text{flow entrance area}$
10	Jagannadharajo & Rao [42]	$\text{Fe}(\text{CN})_6^{-4}$	Mass transfer to the wall of a fluidized bed (annulus)	$\varepsilon J_m = 0.43 \text{Re}_p^{-0.38}$	$200 < \text{Re}_p < 23000$  $2.67 < r_2 / r_1 < 4$	$\varepsilon = \text{porosity}$ $d_p = \text{particle dia.}$ $u = \text{superficial vel.}$ $\text{Re}_p = u d_p / \nu(1 - \varepsilon)$
11	Krishna et al. [43-45]	$\text{Fe}(\text{CN})_6^{-3}$	Mass transfer to the wall of a fluidized bed (annulus)	$J_m = 0.0113 [(d_e / d_p)(r_2 / r_{\max})(1 - \varepsilon)]^{0.44}$ for $\varepsilon > 0.87$ $J_m = 0.029 [(d_e / d_p)(r_2 / r_{\max})(1 - \varepsilon)^2]^{0.44}$  for $\varepsilon < 0.87$	$200 < \text{Re}_p < 23000$  $1.6 < r_2 / r_1 < 53$	$\text{Re}_p = u d_p / \nu(1 - \varepsilon)$



**Figure 3-4** Schematic representation of anodic and cathodic areas on surface subjected to corrosion [22, 46].

Ferrous hydroxide  $\text{Fe}(\text{OH})_2$  precipitates from solution and composes a layer next to the iron surface. The colour of  $\text{Fe}(\text{OH})_2$  is normally green to greenish black. However, this compound is unstable in oxygenated solutions and is oxidized to the ferric hydroxide  $\text{Fe}(\text{OH})_3$  :



Ferric hydroxide  $\text{Fe}(\text{OH})_3$  is orange to red brown in colour and comprises most of ordinary rust. Rusting applies to the corrosion of iron or iron base alloys. Nonferrous metals corrode but do not rust.

Other common cathodic reaction in metallic corrosion is the reduction of hydrogen ions to hydrogen, which becomes important in solution of decreasing pH and predominates in strongly acid environments:



Also oxygen reduction reaction occurs in acid solution:



It has been noticed that anodic reaction is rapid in most media, while cathodic reaction is much slower. Thus corrosion is said to be under cathodic

control. So in most cases of corrosion in which transport of the cathodic reactant (e.g., dissolved O<sub>2</sub>) is rate determining, the anodic curve intersects the cathodic curve at  $i_L$  [25], then

$$i_{\text{corr}} = i_L \quad \text{at } E_{\text{corr}} \quad (3.33)$$

where  $i_{\text{corr}}$  is the corrosion rate per unit area (or corrosion current density). Any factor that increases  $i_L$  will result in a corresponding increase in  $i_{\text{corr}}$ .

### 3.7 Oxygen Reduction Reaction

When hydrogen ions are available only in limited quantity (neutral or alkaline solutions), the most common cathodic reaction leading to metallic corrosion is the reduction of dissolved oxygen, and the transport of oxygen to the metal surface will be more significant than activation controlled electron transfer.

The transport of oxygen from the atmosphere to the metal/solution interface involves the following steps [25]:

- 1- Transfer of oxygen across the atmosphere/solution interface.
- 2- Transport through the solution by natural and forced convection to the diffusion layer.
- 3- Transport across the static solution at the metal/solution interface (the diffusion layer) by diffusion.

Steps 1 and 2 are fairly rapid compared with step 3, which is normally the rate determining.

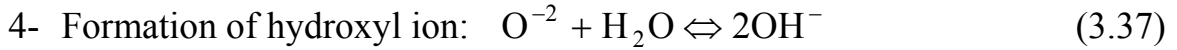
Expressing by chemical equations, the oxygen reduction reaction is consisted of the following interconnected reactions [47, 48]:

- 1- Diffusion of oxygen from the solution toward the cathode:

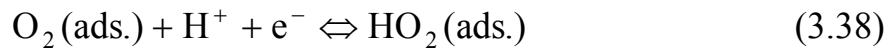


- 2- Adsorption of oxygen and dissociation of molecules into atoms:





But an easier path is provided by hydrogen peroxide  $\text{H}_2\text{O}_2$ , as an intermediate without the need for breaking the oxygen-oxygen bond (dissociation O atoms). Thus, a hydrogen ion (from water dissociation) and an electron are together added successively to oxygen of the  $\text{O}_2$  molecule to form  $\text{H}_2\text{O}_2$ , which then acquires two more electrons before splitting up into two  $\text{OH}^-$  ions, according to:



The initiating reaction (3.38) is known to be slow and may determine the rate of the overall reaction:



Jovancicevic and Bockirs [49] studied the pathways of oxygen on iron in neutral solutions. They found that the formation of hydrogen peroxide  $\text{H}_2\text{O}_2$  is an intermediate in the reduction pathway but only 1 % of the total oxygen goes to peroxide and 99 % goes directly to form hydroxyl ion on bare iron. Anastasijevic et al. [50] observed that 86 % of the flux of oxygen reduces by dissociated O atoms. Zecevic et al. [51] investigated the oxygen reduction in near neutral solution on iron. In their experiments very little peroxide was formed.

### 3.8 Corrosion Rate Expressions

Corrosion rates have been expressed in a variety of ways in the literature [22, 52]:

- 1- Weight loss in grams or milligrams, and percent weight change of materials after exposure to the corrosion environment. Both of these expressions are poor because they don't take into considerations the effects of sample shape and exposure time.
- 2- Weight loss per unit area per unit time. Milligrams per square decimeter per day (mdd), grams per square meter per hour (gmh), and grams per square meter per day (gmd) are used in literature. These expressions include the effect of the exposed area and the duration of exposure. Thus,

e.g.:

$$\text{gmh} = \frac{w}{At} \quad (3.41)$$

where  $w$  is the loss in weight in grams,  $A$  is the area of specimen in  $\text{m}^2$ ,  $t$  is the exposure time in hr.

- 3- Expression of corrosion rates in terms of penetration, like inches penetration per month, millimeters penetration per year, and mils (milli inches) penetration per year (mpy). So that

$$\text{mpy} = \frac{534w}{\rho At} \quad (3.42)$$

where  $w$  is weight loss in mg,  $\rho$  is density of specimen in  $\text{g/cm}^3$  (for iron and steel  $\rho = 7.9 \text{ g/cm}^3$ ),  $A$  is the area of specimen in  $\text{in}^2$ ,  $t$  is exposure time in hr. mpy is preferred, since the corrosion rate of practically useful materials varies between 1 and 200 mpy. Thus, using this expression, it is possible to present corrosion data using small whole numbers and avoiding decimals.

- 4- The corrosion rate can be expressed in terms of corrosion current density  $i_c$ , which can be calculated using Faraday's law:

$$i_c = zFN = \frac{zFw}{AMt} \quad (3.43)$$

where  $N$  is the molar flux of the metal reacted due to corrosion,  $w$  is the weight loss,  $z$  is the number of electrons associated with metal corrosion (for iron  $z=2$ ),  $M$  is the molecular weight of metal.

### 3.9 Corrosion Rate Measurements

Measurements of corrosion rate can be made by the following methods [52-54]:

- 1- The weight loss of the metal, which gives a complete indication of the amount of corrosion.
- 2- The growth of corrosion product film, which gives an indirect indication of the amount of corrosion. This can be related directly to amount of corrosion only if there is no loss of corrosion products into the aqueous environment, and provided that its chemical composition is known.
- 3- Mass transfer measurements, i.e. measurement of the transfer of the cathode reactant (dissolved oxygen in water).
- 4- Electrochemical methods include measurements of corrosion current and corrosion potential. Two most commonly used electrochemical measurements are: 1) galvanostatic, in which the current is specified at some definite value, then is increased or decreased (either discontinuously at regular intervals, or continuously at a slow controlled rate), the potential corresponding to each current value being recorded; 2) potentiostatic, in which the potential is controlled, being raised or lowered continuously or in steps, the current corresponding to different values of the potential is recorded. Potentiostatic method was employed during the present work.

### **3.10 Environment Effects on Corrosion Rate**

Frequently in the process industries, it is desirable to change process variables. This change has an effect on corrosion rate of the metals utilized in the process. Some of the most common environmental variables are discussed below.

#### **3.10.1 Effect of Velocity**

The effect of velocity on corrosion rate is complex and depends on the characteristics of the metal and the environment to which it is exposed [22]. If a metal is corroding under cathodic control, the velocity of the solution will be significant when diffusion of the cathodic reactant is rate controlling [25].

A review of literature dealing with the corrosion of iron and steel when velocity or fluid flow is a variable shows many contradictions, and can be summarized as follows:

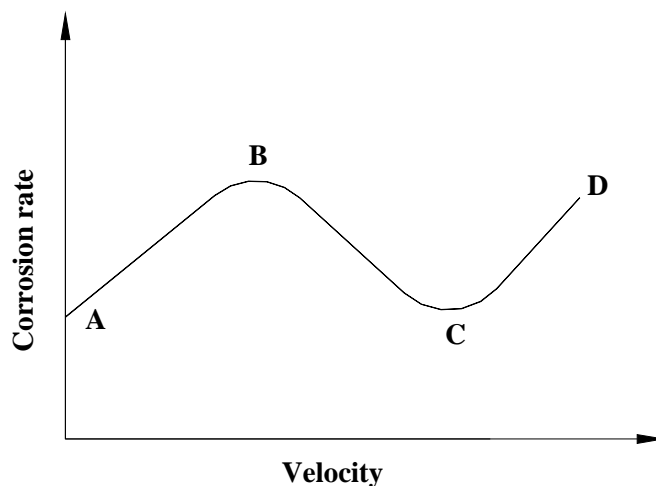
- 1- Friend [55] observed the corrosion rate of iron in a natural water decreases with increasing velocity until above 2.4 m/s it was almost zero. Evans [56] indicated that greater turbulence due to high velocities results in more uniform oxygen concentration and mostly delays the initiation of corrosion on a previously uncorroded surface.
- 2- Speller and Kendall [57] found the rate is low under laminar flow conditions, rapidly increasing in the transition range, and more slowly increasing under turbulent flow conditions. Whitman [58] stated that the corrosion rates should increase at higher flow rates due to an increase in oxygen diffusion and breaking down of the protective films on the metal surfaces. Cox and Roetheli [59] obtained data for steel specimens in aerated natural water by varying the rotational speed of the specimen and the oxygen content in the water, and found that corrosion rate increased with the increased oxygen content (up to 6 ppm) and increased peripheral velocity (up to 0.4 m/s). Mahato et al. [53] carried out corrosion tests of

steel pipe in natural water at 66°C at a series of four flow rates and at varied test durations up to 25 days. They found that the corrosion rate increases with velocity increase for the same corresponding test duration, and interpreted this as higher Reynolds numbers should decrease the resistance factor in the so-called damped turbulence zone, thus increasing the rate of oxygen transfer to the cathodic area.

- 3- Cohn [60] showed that in natural water pipe corrosion increased with velocity up to 1.4 m/s and then decreased with further increase of flow. Butler and Stroud [61] studied the corrosion rate of mild steel tubes by high purity water and observed that the corrosion rate increased with increasing speed of flow to a maximum value at about 1 m/s, any further increase resulted in a decreased corrosion rate.
- 4- Roetheli and Brown [62] reported that the corrosion rates increased to a maximum, as the rotational velocities of their steel specimens in oxygenated water increased, then decreased to a very low value and increased again to a somewhat higher value at very high velocities.

Figure 3-5 shows these four cases; case 1 is represented by part BC; case 2 by AB or CD; case 3 by ABC; and case 4 by ABCD part. The lack of agreement amongst the investigators is almost related to the impossibility of making adequate hydrodynamic comparison between the various experiments recorded.

**Figure 3-5**  
Schematic diagram showing the effect of velocity on corrosion rate.



### 3.10.2 Effect of Temperature

In contrast to the influence of velocity, whose primary effect is to increase the corrosion rates of electrode processes that are controlled by the diffusion of reactants, temperature changes have the greatest effect when the rate-determining step is the activation process [25]. In general, if diffusion rates are doubled for a certain increase in temperature, activation processes may be increased by 10-100 times, depending on the magnitude of the activation energy.

For corrosion processes governed by dissolved oxygen reduction reaction which is controlled by concentration polarization because of the low solubility of oxygen, especially in concentrated salt solution, the effect of temperature is complex since there are two conflicting factors; a decrease in oxygen concentration, and an increase in the diffusion coefficient of oxygen.

In a closed system from which oxygen cannot escape, there is a linear increase in corrosion rate with temperature increase due to the increase in diffusion coefficient (Fig. 3-6). In an open system, allowing dissolved oxygen to escape, the rate increases with temperature to about 80°C and then falls to a very low value at the boiling point. The falling off of corrosion rate above 80°C is due to the decrease in oxygen solubility, which at that temperature becomes more significant than the increase in diffusion coefficient [20].

Speller and Kendal [57] noted that the specific corrosion rate ( $\text{mg}/\text{dm}^2\text{s}$  Fe corroded per ppm of dissolved  $\text{O}_2$ ) increased with the increase in temperature over a range of 16-77°C. Their study was limited to the investigation of the initial corrosion rate at various temperatures and flow rates, and neglected the role of the corrosion products that deposit on the corroding surface with passage of time.

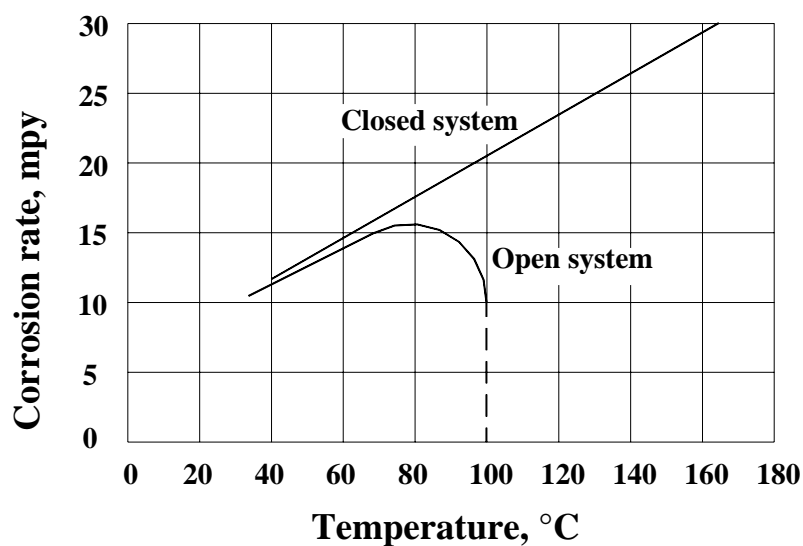


**Figure 3-6** Effect of temperature on corrosion of iron in water containing dissolved oxygen [20].

Butler and Ison [63] studied the effect of temperature on the corrosion of mild steel pipe between 25 and 55°C for a flow velocity of 2 m/s and varying periods of exposure up to 70 days. For periods between 5 to 18 days they found more corrosion at 25°C than at 40°C, but after about 18 days, the amount of corrosion increased with increasing temperature.

Mahato et al. [64] made corrosion tests of mild steel pipe by the continuous flow of aerated natural water at velocities of 0.14-0.82 m/s and at temperatures of 52, 66, and 77°C over periods up to 40 days using weight loss measurements. At 52°C they found that the amount of corrosion increases with the increase in velocity up to 0.55 m/s, while the results at 0.82 m/s are below those at 0.55 m/s. They interpreted this as follows: with increase in Reynolds number, the rate of replenishment of O<sub>2</sub> increases with an increase in the corrosion rate, but at the same time, due to higher shear and impact forces, the compactness of corrosion product will increase and the corrosion rate will decrease due to the higher resistance to the mass transfer. At 77°C they observed that the amount of corrosion decreases with increase

of flow and explained that to the resistance of corrosion product that is greater at higher flow rates. Their results showed that at lower velocities (0.14 and 0.27 m/s), the corrosion rate at 77° C is higher than at 52° C and the latter is higher than at 66° C. After about 10 days, at 0.55 m/s the 66° C curve crosses the 52° C curve. But at 0.82 m/s the results for the initial period at 52° C are higher than those at 66 and 77° C, the results at 66 and 77° C ultimately surpass those at 52° C after about 5 and 12 days periods.

### **3.10.3 Effect of Chloride Ion**

One of the main aggressive ions present in natural waters is chloride. The amount present may range from a negligible quantity, as in rain water and certain surface supplies, to about 30000 ppm (3%) sodium chloride as in sea water or brackish waters [65].

The effect of sodium chloride concentration on corrosion of iron in air-saturated water at room temperature is shown in Fig. 3-7. The corrosion rate first increases with salt concentration, reaching a maximum at about 3% NaCl, then decreases [20]. The value falling below that for distilled water when saturation is reached (26%).

Oxygen solubility in water decreases continuously with sodium chloride concentration, explaining the falling off of corrosion at the higher sodium chloride concentrations. The initial rise appears to be related to a change in the protective nature of the diffusion-barrier rust film that forms on corroding iron. In distilled water having low conductivity, anodes and cathodes must be located relatively near each other. Consequently, OH<sup>-</sup> ions forming at cathodes are always in the proximity of Fe<sup>+2</sup> ions forming at nearby anodes, resulting in a film of Fe(OH)<sub>2</sub> adjacent and adherent to the metal surface. This provides an effective diffusion-barrier film.

In sodium chloride solutions, the conductivity is greater, hence additional anodes and cathodes can operate much farther one from the other. At such cathodes, NaOH does not react immediately with  $\text{FeCl}_2$  formed at anodes, instead, these substances diffuse into the solution and react to form  $\text{Fe(OH)}_2$  away from the metal surface, so any  $\text{Fe(OH)}_2$  formed does not provide a protective barrier layer on the metal surface. Hence iron corrodes more rapidly in dilute sodium chloride because more dissolved oxygen can reach cathodic areas. Above 3% NaCl, the continuing decreased solubility of oxygen becomes more important than any change in the diffusion-barrier layer, hence corrosion decreases.

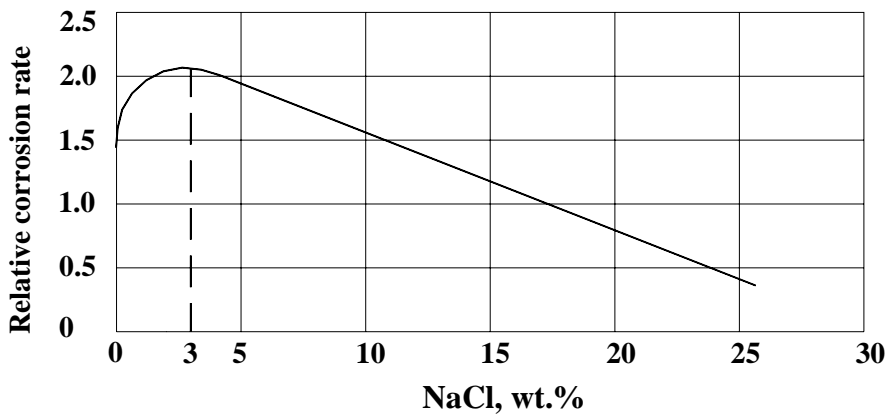


**Figure 3-7** Effect of sodium chloride concentration on corrosion of iron in aerated solutions at room temperature [20].

Wormwell [66], using rotating cylinders of mild steel, found that for 100 days or more, the corrosion rate in 0.5 N sodium chloride solution at peripheral velocity of 0.003 m/s is three times, and that at 0.35 m/s twelve times, the rate in stagnant solution. Then Wormwell et al. [67] observed that at peripheral velocity of 10 m/s, the corrosion rate over a period of a week increased considerably when the sodium chloride concentration was raised from 0.001 to 0.5 N.

McAllister et al. [68] studied the rate of corrosion and fouling in condenser tubes of different alloys using river water (contaminated with sea

water) as the cooling medium, it appeared that the rate of corrosion fouling increases with increase of chloride ion concentration.

Butler and Stroud [65] studied the corrosion of mild steel tubes, through which chloride solutions (25, 250, 2500 ppm NaCl) flowing at velocities up to 2 m/s, at temperatures up to 55°C, and test periods from 3 days to 10 weeks. They expressed the influence of chloride concentration on the corrosion rate in the form [corrosion rate = a (concentration)<sup>b</sup>, where a and b are constants].

Recently, Bahar [69] showed that, carbon steel in stationary aerated water, the limiting current density increases with increasing NaCl concentration up to 3.5%, and the corrosion potential becomes more negative.

### **3.11 Heat Transfer and Corrosion**

The previous sections have assumed isothermal conditions, but in many practical situations corrosion reactions have to be considered when the electrode is acting as a heater or a cooler, like corrosion of heat exchangers, which in many cases is controlled by the rate of diffusion processes. There is no common opinion about the influence of heat transfer on the corrosion rate in diffusion control, and little agreement as to whether the different corrosion rates are due to the heat flux itself, to the changed surface temperature, or to some other causes such as uneven surface deposit.

Ross [70] reviewed this subject comprehensively and suggested that heat transfer might affect:

- 1- The rate of corrosion reaction by influencing the temperature of the corroding surface.
- 2- The solubility and diffusivity of chemical species involved in the corrosion reaction; in particular, the effect of the temperature distribution on the solubility of oxygen in water.

3- The solubility of the deposit of corrosion products attached to the corroding surface. This could control the removal of the corrosion products at the water/deposit interface. Ross pointed out that heat transfer could change the stability of the product layer on the surface. Thus, if the corrosion products have a tendency to go into solution at the temperatures encountered at the deposit/metal interface then the deposit will tend to be loosened from the surface, and spalling of the deposit occurs. If the solubility of the deposit does not encourage its dissolution then the deposit will be more likely to remain attached to the surface.

Porter et al. [71] studied the rate of dissolution of copper in 50% phosphoric acid in the range of 20-65°C in the absence of heat flux and in the presence of either positive or negative heat fluxes up to 75 kW/m<sup>2</sup>. The limiting current density was found to be proportional to the surface/bulk concentration difference, the diffusivity and the kinematic viscosity. It was concluded that heat flux alters the mass transfer rate of a diffusion-controlled reaction mainly because it alters the surface/solution interface temperature.

According to Zarubin [72] corrosion rate under heat transfer is consistent with that under isothermal conditions at some mean temperature of a given temperature drop, and with increasing liquid flow velocity this mean temperature shifts from the metal temperature to the solution temperature.

Ashford et al. [73] monitored the corrosion rate of mild steel in oxygenated and deoxygenated 100 ppm sodium chloride solutions at temperatures between 200 and 350°C at heat fluxes of 110-260 kW/m<sup>2</sup>. In deoxygenated solutions, corrosion rates were low and a thin magnetic film was found on both heated and unheated surface. In oxygenated solutions, severe corrosion occurred at heated surface forming a thick laminated oxide scale.

Parshin et al. [74] investigated the cathode reduction of oxygen on a rotating heat emitting copper disc electrode in limiting diffusion current

regime in aerated 0.05 N H<sub>2</sub>SO<sub>4</sub>. Under natural aeration, the rate of oxygen diffusion to the heat-emitting disc is essentially higher than that under isothermal conditions at the same temperature of the disc surface, which is due to the decreasing of oxygen solubility with increasing liquid temperature. At constant concentration of the oxidizer (oxygen) in liquid, the diffusion rate under laminar flow and heat transfer is equal to that under isothermal conditions at a temperature corresponding to that of the middle of the diffusion layer. Heat transfer from the disc at a temperature drop higher than some critical value ( $\Delta T_{cr} = T_s - T_b = 15 \text{ to } 20 \text{ }^\circ\text{C}$ ) facilitates the disturbance of laminar flow. This means that at identical disc rotation velocities, mass transfer under isothermal conditions can occur under laminar flux, while mass transfer under heat transfer can occur under turbulent flow, which is the reason for the increase of the reduction rate of oxygen.

AL-Mashta [75] reported that the limiting current density under heat transfer is higher than under isothermal conditions for cross flow of carbon steel cylinder. Also AL-Auasi [76] observed that the heat flux through the pipe wall enhances the corrosion rate for all values of Reynolds number.

## **3.12 Fouling of Heat Transfer Surfaces**

### **3.12.1 Introduction**

The term “fouling” originally a descriptive expression used in the oil industry, became established in the literature to mean any undesirable deposit on heat transfer surfaces which increases the resistance to heat transmission [77, 78].

Fouling is one of the most important issues facing the heat exchanger designer. It can degrade the performance of heat exchangers by as much as 80% and can sometimes cause complete failure [79]. Heat transfer designers increase heat transfer surface area to overcome the loss in performance. Often

this over surfacing accounts for more than half of the required clean area, and thus increasing the cost of equipment.

Newton's law of cooling is given by:

$$\frac{Q}{A} = h(T_s - T_b) \quad (2.24)$$

Can be written as: 
$$q = \frac{(T_s - T_b)}{R_t} \quad (3.44)$$

where  $R_t=1/h$  is the total thermal resistance, and  $q=Q/A$  is the heat flux.

The effect of the fouling deposit is to add a fouling thermal resistance  $R_f$  to the convective thermal resistance  $R_c$  at the heat transfer surface, so the total thermal resistance  $R_t$  is given by [79-81]:

$$R_t = R_c + R_f \quad (3.45)$$

or 
$$\frac{1}{h} = \left(\frac{1}{h}\right)_c + R_f \quad (3.46)$$

from Eq. (3.44), at any time  $t$  :

$$R_t = \frac{T_s - T_b}{q} \quad (3.47)$$

for clean surface at  $t=0$

$$R_c = \frac{T_{s,0} - T_b}{q} \quad (3.48)$$

Substituting Eqs. (3.47) and (3.48) in Eq. (3.45) yields:

$$\frac{T_s - T_b}{q} = \frac{T_{s,0} - T_b}{q} + R_f \quad (3.49)$$

$$\therefore R_f = \frac{T_s - T_{s,0}}{q} \quad (3.50)$$

### 3.12.2 Types of Fouling

Fouling is commonly classified by the immediate cause or mechanisms of the process involved. Five categories are needed to describe the fouling of solid-fluid interfaces [77-79, 82]:

- 1- Particulate fouling; involves the deposition of particles suspended in the fluid stream onto the heat transfer surface, e.g. sand, mud, clay, dust etc.
- 2- Precipitation (scaling) fouling; involves the crystallization of inverse solubility salts (such as  $\text{CaCO}_3$ ,  $\text{CaSO}_4$ ,  $\text{Na}_2\text{SO}_4$  in water) from a liquid solution onto heat transfer surface. This mechanism is most severe in applications involving boiling but also occurs in single-phase heat transfer equipment.
- 3- Chemical reaction fouling; comprising the fouling originated by a chemical reaction at the heat transfer surface, namely polymerization, cracking and coking of hydrocarbons at high temperatures.
- 4- Corrosion fouling; involves a chemical reaction between the material of heat transfer surface and the fluid stream to produce corrosion products which, in turn, foul the surface.
- 5- Biological fouling; involves the accumulation and growth of biological organisms at the heat transfer surface. Slime formation in cooling tower is a typical case.

### 3.12.3 Fouling Curves

Fouling is usually considered to be the difference between two simultaneous processes, a deposition process and a removal process. Three types of fouling curves are found experimentally (Fig. 3-8) [79, 82]:

- 1- A linear increase of fouling resistance  $R_f$  with time, this occurs if either removal rate is negligible, or deposition rate and removal rate are constant with deposition rate being predominant.
- 2- A rate of deposition that falls off with increasing time, or the removal rate increases with time.
- 3- An asymptotic behavior where the value of  $R_f$  finally becomes constant independent of time, in other words the deposition rate and removal rate

ultimately become equal resulting in an asymptotic form of the fouling time curve.

The asymptotic mode is of greatest practical importance. The linear and falling rate modes may be the early stages of asymptotic behavior, for this reason, a fouling experiment must be carried for very long period of time before it can be classified.

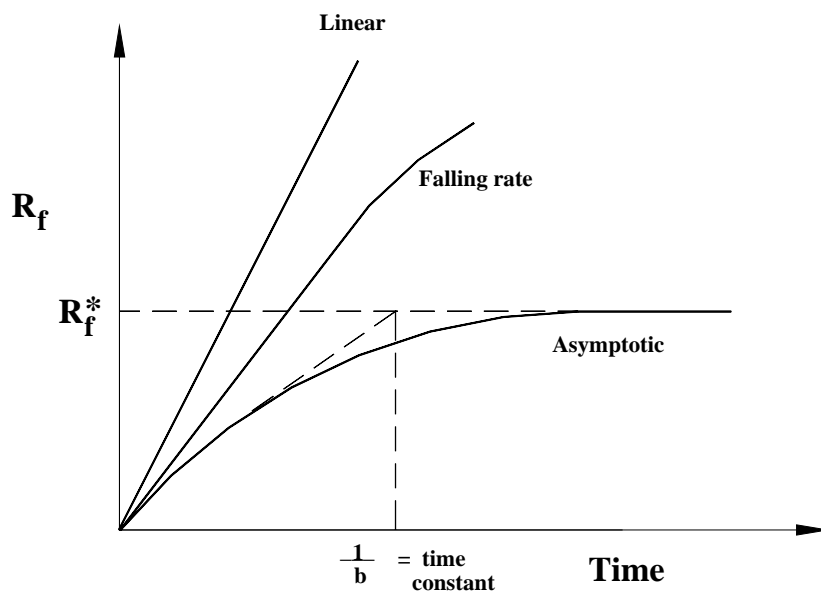


**Figure 3-8** Types of fouling curves [79, 82].

### 3.12.4 Basic Fouling Model

The first real attempt to derive a general fouling model was by Kern and Seaton [83] who found experimentally a typical fouling pattern in which after an initial period of fast fouling build up, the fouling resistance (or the fouling thickness) tended to remain nearly constant, and they expressed the net fouling rate as the difference between a deposition and a removal process:

$$\frac{dR_f}{dt} = \theta_d - \theta_r \quad (3.51)$$

where  $\theta_d$  is the rate of deposition,  $\theta_r$  is the rate of removal,  $t$  is the time.

Kern and Seaton considered further that  $\theta_d$  is independent of time or  $R_f$ , whereas  $\theta_r$  depends directly on the actual value of  $R_f$ :

$$\theta_d = \left( \frac{dR_f}{dt} \right)_{t=0} = \text{constant} \quad (3.52)$$

$$\theta_r = bR_f \quad (3.53)$$

under these conditions, the integration of Eq. (3.51) yields:

$$R_f = \frac{\theta_d}{b} [1 - \exp(-bt)] \quad (3.54)$$

or can be written as:

$$R_f = R_f^* [1 - \exp(-bt)] \quad (3.55)$$

where  $R_f^* = \frac{\theta_d}{b}$  is the asymptotic fouling resistance for  $t = \infty$  as shown in Fig. 3-8. The quantity  $1/b$  is defined as the time constant of the fouling curve, i.e., the time required for 63% of the asymptotic fouling level to be reached. It may also be interpreted as the mean residence time for an element of fouling material at the heating surface [82].

This basic model of Kern and Seaton constitutes the fundamentals behind most models that have appeared in the literature which differ essentially on the fundamental dependence of  $\theta_d$  and  $\theta_r$  [78].

### 3.12.5 Corrosion Fouling

The corrosion products formed on a heat transfer surface as a result of corrosion of that surface can introduce a resistance to heat transfer and affect the fluid friction characteristic of the surface. This type of fouling is called corrosion fouling [80, 84, 85].

The term “in situ” corrosion fouling has been used to describe fouling caused by corrosion products formed at the heat transfer surface. While “ex

situ ” corrosion fouling is used to describe fouling due to corrosion products formed elsewhere in the system and then deposited on heat transfer surfaces either by precipitation or by particulate fouling mechanisms, depending on whether the corrosion products are soluble or insoluble at the bulk fluid conditions. In spite of the usefulness of this classification, it is probably to call “ in situ ” corrosion fouling just corrosion fouling.

Example of systems at which fouling corrosion can occur include:

- 1- Heat exchangers handling natural waters (frequently this entails corrosion fouling in combination with some other category of fouling).
- 2- Water-cooled components of electrical and electronic equipment.
- 3- Cooling system of water-cooled internal combustion engines.
- 4- Domestic and commercial hot water-heating systems.

In all these situations, the corrosion products formed on exposure to flowing oxygenated water can introduce a significant resistance to heat transfer.

Oxygen transport to the surface involves three steps [46, 86]; convective transport from the bulk of the water to the interface between the corrosion products and the flowing water; diffusion through the corrosion products; and the reaction with the metal according to Eq. (3.27) as shown in Fig. 3-9. Mahato et al. [53] proposed model based on two series resistances to diffusion. Dissolved oxygen in the flowing turbulent water must diffuse through some form of fluid film (damped turbulence layer) and then through a porous corrosion product to reach the reaction zone.

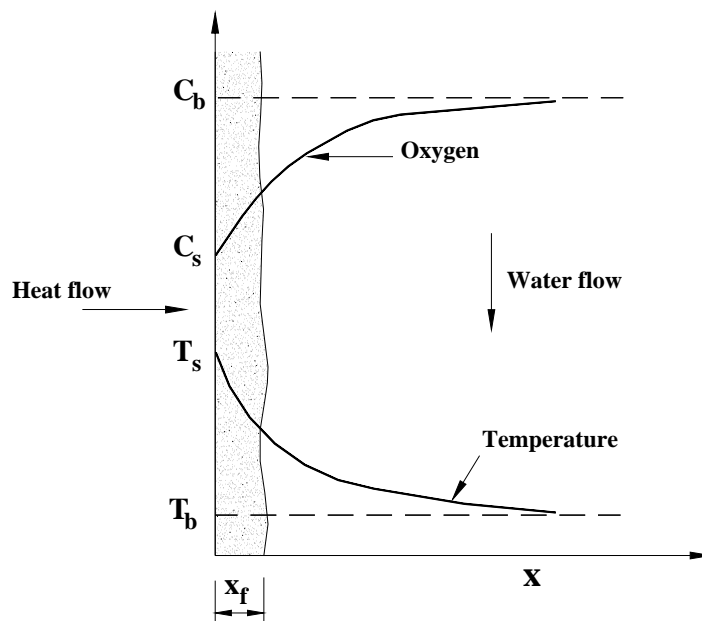


**Figure 3-9** Overview of corrosion fouling [46, 86]

### 3.12.6 Literature Review of Corrosion Fouling

Corrosion fouling has not attracted as much attention as have other categories of fouling, probably because it was not widely recognized until about 1960 that the products of corrosion processes can affect heat transfer at a corroding system. Although there is an extensive literature on the corrosion of metals exposed to oxygenated water, most of it deals with the material damage associated with corrosion and the composition of the corrosion products. This information is clearly important in understanding the corrosion process, but it does not provide direct information on corrosion fouling.

McAllister et al. [68] reported quantitative data on the rates of fouling and corrosion in condenser tubes (concentric tube heat exchanger type) using river water, contaminated with sea water, as the cooling medium for 3 to 4 months test period. Alloys tested were; 90-10 copper-nickel, aluminum-brass, admiralty-brass, 304 stainless steel, and others. They found that the heat transfer resistance was approximately linear with time, and the increasing in

the river water chloride ion concentration, accompanied by a simultaneous increase in hardness, increases the rate of fouling. The change in the river water velocity did not alter the initial net rate of fouling, but after 20 days the net rate of fouling decreased for the tube velocity of 3.5 m/s, while for velocity of 2.4 m/s there was little decrease in comparison with velocity of 1.2 m/s.

Somerscales and Kassemi [80] carried out tests of corrosion fouling on specimens of 1010 carbon steel in the form of an electrically heated wire suspended in a bath of distilled water. The wire was heated electrically and the measured electrical resistance was used to determine its temperature and its power dissipation. Distilled water maintained at a constant temperature and saturated with atmospheric oxygen was continuously circulated through the test cell. They found that as time proceeds, the deposit thermal resistance  $R_f$  increases and then tends to approach a constant value. The average value of this final constant deposit thermal resistance is  $2.8 \times 10^{-4} \text{ m}^2 \text{ }^\circ\text{C} / \text{W}$  for six specimens and test duration of 166-483 hr.

Somerscales et al. [87] observed that the corrosion fouling of 6061 aluminum to be affected by the pH of the water. At pH =7, there was a rapid initial increase in the fouling thermal resistance, followed by a very small change in this quantity for the remainder of the duration of exposure. At pH =10, the initial rapid increase also was observed, but subsequently there was a steady increase in the fouling thermal resistance. At pH =7, there is initial corrosion, but after a sufficient time of exposure (a few hours), the corrosion products, which have a low solubility, decreases the rate of diffusion of oxygen to the metal/deposit interface. At pH =10, the higher solubility of the corrosion products permits the oxygen to penetrate to the deposit/metal interface and thereby to support the corrosion process.

The above experimental investigations and others of “in situ” aqueous corrosion fouling are summarized in Table 3-2.

Table 3-2 Previous experimental investigations of “in situ” aqueous corrosion fouling.

	Reference	System	Material	Water Velocity m/s	Water Temp. °C	Specimen Surface Temp., °C	Water Character	Duration of Test	Deposit Composition & Appearance	Factors Affecting $R_f$	$R_f=f(t)$ $m^2\text{ }^\circ\text{C}/\text{W}$
1	McAllister et al. [68]	Concentric tube, counter flow heat exchanger	90-10 Cu-Ni Aluminum-Brass Admiralty-Brass 304 Stainless Steel	1.2 2.4 3.5		46	River water and sea water pH ~ 7	130 days	Cuprous oxide and sulphides and iron oxides	Decreases with increase in water velocity	$R_f=mt$ $m=3.24 \times 10^{-6}$ ( $u=1.2$ ) $m=2.91 \times 10^{-6}$ ( $u=2.4$ ) $m=7.74 \times 10^{-7}$ ( $u=3.5$ ) ( $m$ for 90-10 Cu-Ni) $t$ in days
2	Griess et al. [88]	Electrically heated duct	6061 Al X8001Al	7.6 10.1 12.8- 13.7		204-354	Distilled water pH= 5 pH=6 (adjusted with $\text{HNO}_3$ )	300-500 hr	Boehmite $\text{Al}_2\text{O}_3 \cdot \text{H}_2\text{O}$ Uniform deposit with some pitting		$R_f = at^p e^{-b/T_s}$ $p=0.778$ $b=4600 \text{ K}$ $a=78$ (pH=5) $a=211$ (pH=5.7-7) $t$ in hours
3	Gutzeit [89]	Concentric tube, parallel flow steam condenser	Admiralty brass Al	1.8 and variable	41	71-77	Cooling tower water pH=7 Hardness 200-750 ppm (as $\text{CaCO}_3$ )	2-4 months	Discoloration in admiralty brass	Decreases with increase in water velocity	$R_f=mt$ $m=2.82 \times 10^{-7}$ (Admir.) $m=2.73 \times 10^{-7}$ (Al) $t$ in days
4	Ritter & Suito [90]	Flow parallel to electrical rod	Cu alloy 706  Ti	0.61 1.22 1.83  0.61 1.22 1.83	13-21  13-21	41-62  30-60	Sea water pH=8 Salinity 0.035 ppm  Oxygen 90% sat.	600-2000 hr  600-2000 hr	Corrosion products and silt  Corrosion products and silt, cemented by biological materials	Decreases with increase in water velocity	$R_f=mt$ $m=1.76 \times 10^{-7}$ ( $u=0.61$ ) $m=1.2 \times 10^{-7}$ ( $u=1.22$ ) $m=5.28 \times 10^{-8}$ ( $u=1.83$ ) $t$ in hours
5	Somerscales & Kassemi [80, 87]	Flow across U shaped wire	1010 C steel  6061 Al	$2.3 \times 10^{-3}$  $2.3 \times 10^{-3}$	24  24	28-35  28-35	Distilled water pH=6.7 air sat.  Distilled water pH=10 air sat.	240 hr  240 hr	Iron oxide, outer(red) Inner (black)  Aluminum oxide Very hard and tenacious black oxide	$\text{O}_2$ conc. Fluid velocity  pH	$R_f=e^{mt}$

## **CHAPTER FOUR**

### **EXPERIMENTAL WORK**

## **4.1 Introduction**

In this work, experiments have been carried out to study the influence of corrosion on the heat transfer process of shell side of 1019 AISI carbon steel pipe in concentric tube heat exchanger induced by 0.1 N sodium chloride solution flowing in the annular space. Experiments were performed under turbulent flow conditions of Reynolds number in the range of 5000-30000 at three bulk temperatures 30, 40, and 50°C, and three heat fluxes 15, 30, and 45 kW/m<sup>2</sup>. The effect of time on corrosion rate and subsequently on the process of heat transport was introduced through the experiments of corrosion fouling.

Hence, the experiments involved in the present work can be classified into four categories:

- 1- Isothermal electrochemical experiments, using limiting current density technique (LCDT).
- 2- Electrochemical experiments under heat flux supply, using limiting current density technique.
- 3- Heat transfer experiments, by measuring surface temperature.
- 4- Corrosion fouling experiments, by measuring surface temperature and by using limiting current density technique.

## **4.2 The Apparatus**

The apparatus used in this work consists mainly of five parts; the flow system, the electrochemical corrosion cell, the electrical circuit, heat flux supply unit, and finally surface temperature measuring unit.

## **4.2.1 The Flow System**

The flow system as shown in Figs. 4-1 and 4-2 is composed of the following items:

### **4.2.1.1 Electrolyte Reservoir**

A glass container of 30 liters in volume was used to prepare the electrolytic solution, and then to pump it to the system.

### **4.2.1.2 Heater and Thermostat**

A stainless steel heater (Techone TE-8J type, 5 A, 1000 W) was used to obtain the required temperature in the electrolyte reservoir. The heater was combined with thermostat to control the temperature within an accuracy of  $\pm 0.1^\circ\text{C}$ .

### **4.2.1.3 Pump**

A centrifuge PVC pump (Hanning PS 40-731 type,  $P_{\max}=1.1$  bar,  $Q_{\text{flow}(\max)}=24$  m<sup>3</sup>/hr, 800 W) was used to obtain the required flowrate to circulate the solution from the electrolyte reservoir to the test section.

### **4.2.1.4 Flowmeter**

A PVC liquid flowmeter (range 300-3000 l/hr) was used to measure the flowrate of the solution through the system. The flowmeter was calibrated for its entire capacity range at different working temperatures. The calibration results are presented in Appendix (A).

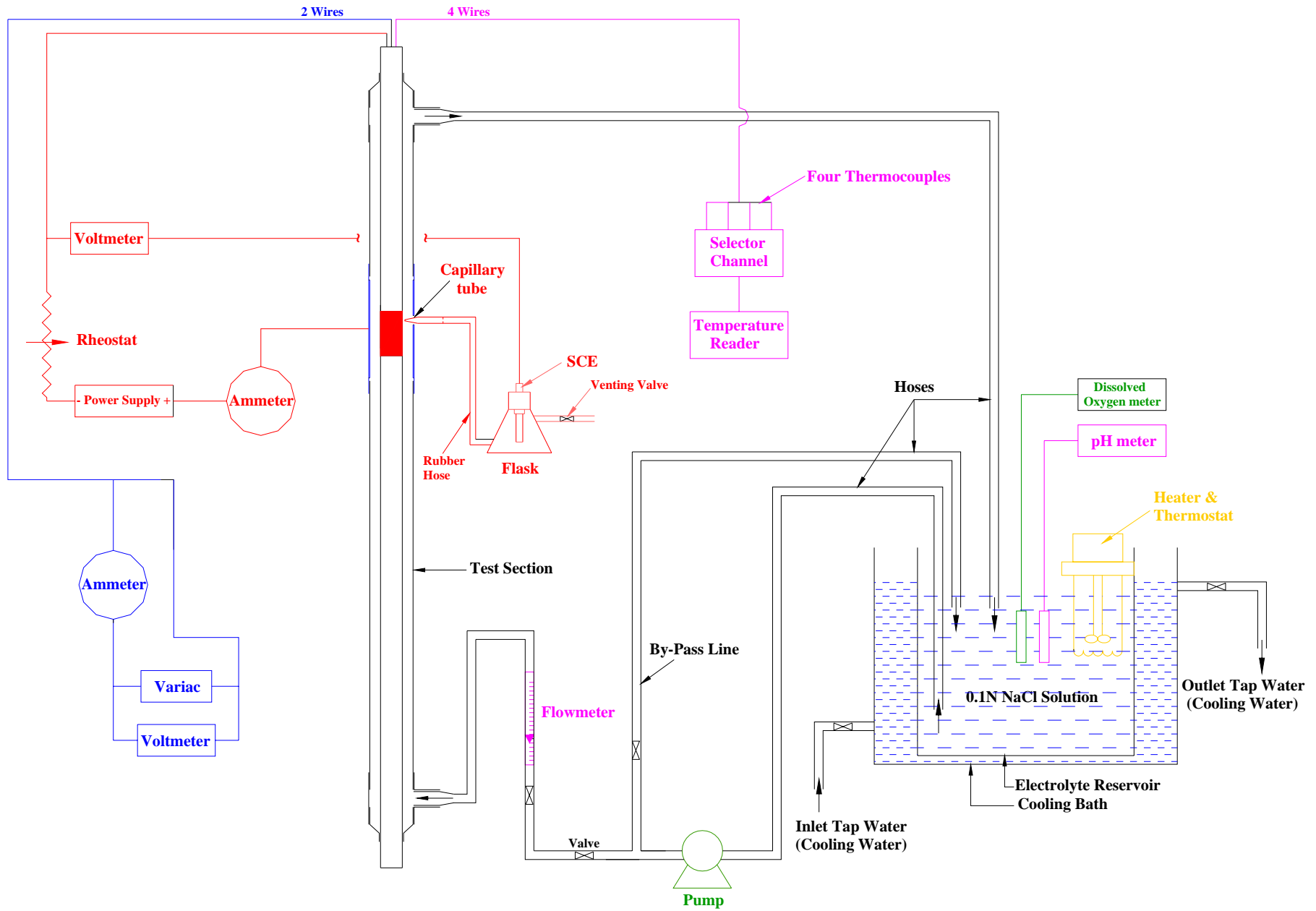
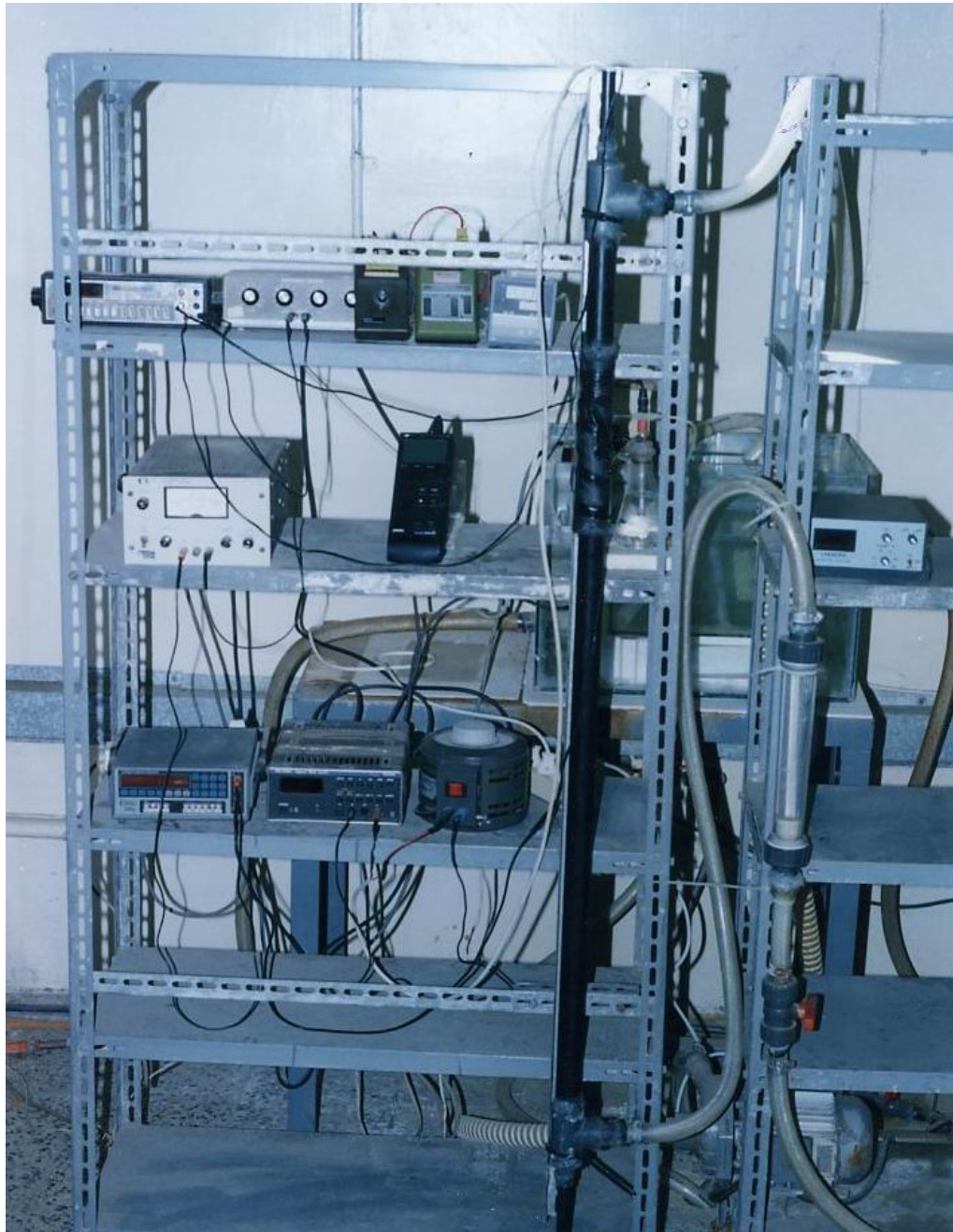


Figure 4-1 Diagram of Experimental Apparatus



**Figure 4-2** Picture of experimental rig.

#### **4.2.1.5 Test Section**

The test section was mounted vertically and the electrolyte was pumped vertically upwards through the test section in order to ensure that the test section is full of flowing working solution. The test section consisted of an outer PVC tube, connected at both ends to PVC fittings that served to inlet and outlet of the solution, and also these fittings hold the inner PVC tube concentrically within the outer tube.

The carbon steel cathode section on which the mass transfer and heat transfer took place formed part of the inner tube, and was situated at such a distance from the test section entrance to ensure fully developed flow conditions. Seventy equivalent diameters were allowed as an entrance length [29, 30]. Twenty equivalent diameters were allowed as an exit length to avoid disturbance at the outlet.

Part of the outer tube was graphite and acted as anode in the electrolysis cell and was situated concentrically opposite to cathode section. Details of duct section are shown in Fig. 4-3.

Many auxiliary components were used in the flow system, like PVC hoses, valves, fittings, etc. as shown in Figs. 4-1 and 4-2.

### **4.2.2 Electrochemical Cell**

#### **4.2.2.1 Working Electrode**

The working electrode was cylindrical bar of 20 mm in diameter of two lengths 3 and 10 cm. The diameter of the working electrode was the same as the outer diameter of the inner PVC tube. At both ends of the working electrode, there were increments of smaller diameter that served to insert the

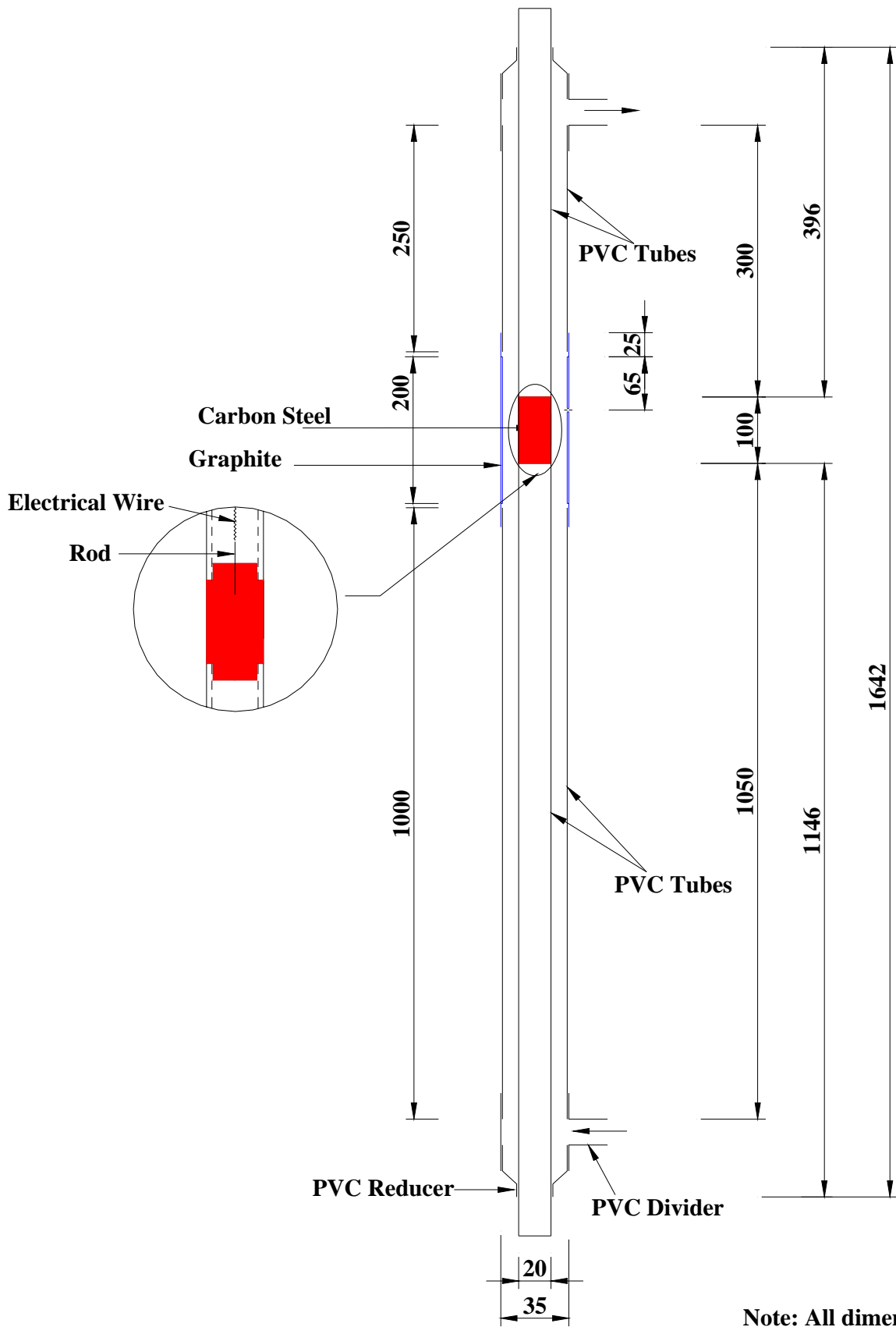


**Figure 4-3a** Schematic diagram of test section using 3 cm working electrode

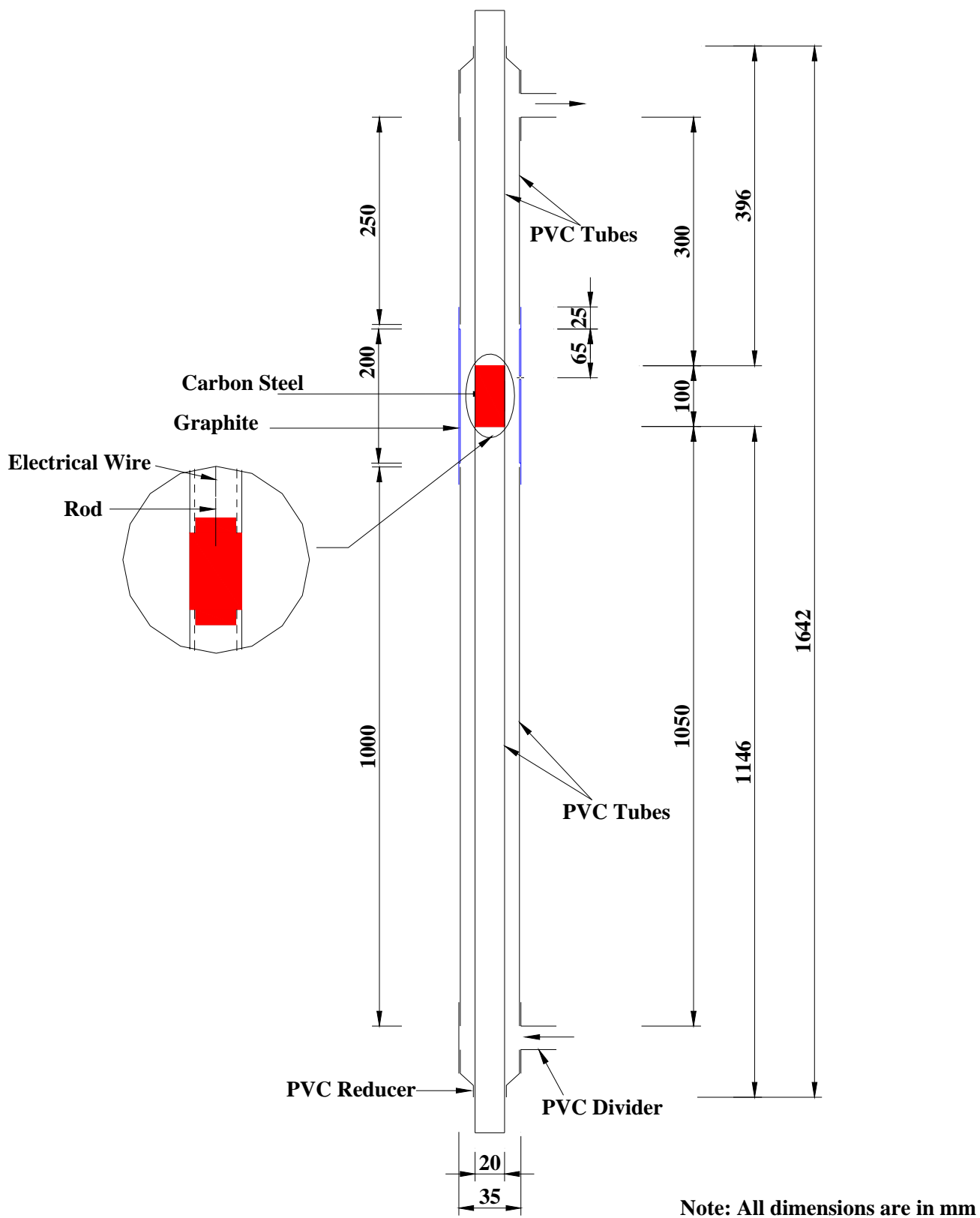


**Figure 4-3b** Schematic diagram of test section using 10 cm working electrode

working electrode within the inner PVC tube so that the working electrode formed part of the inner tube. Details of this electrode are shown in Fig. 4-4.

The material of working electrode was carbon steel (1019 AISI type) according to American Iron and Steel Institute (see Appendix B). The analysis of specimen was performed by Engineering Inspection Department / Al-Daura Oil Refinery / Baghdad.

A hole of 2.5 mm in diameter was drilled in each specimen at its centerline through a length of 5 mm from the upper edge of 3 cm working electrode, or 15 mm from the upper edge of 10 cm working electrode. A metallic rod of 2.5 mm in diameter and of sufficient length was inserted in this hole and mounted in place by using epoxy. An electrical wire was connected to this rod, which used as a connection to the electrical circuit.

#### **4.2.2.2 Counter Electrode**

High conductivity graphite (carbon) electrode was used as a counter electrode. The graphite electrode was cylindrical tube in shape of 35 mm inner diameter and 20 cm long as shown in Fig. 4-5. The inner diameter of the counter electrode was the same as the inner diameter of the outer PVC tube.

At both ends of the counter electrode, there were increments of larger inner diameter to insert the graphite electrode within the outer PVC tube, so that the graphite electrode formed part of the outer tube.

The counter electrode (anode) surface area was made larger than that of the working electrode (cathode) to make the current density at the anode smaller than that at the cathode, and the process at the anode has no noticeable effect on the shape of the applied potential-current curve [27, 28]. For 3 cm working electrode, the ratio of surface area of anode to cathode was 11.7, and for 10 cm working electrode was 3.5, which in both two cases is sufficient to achieve the condition.

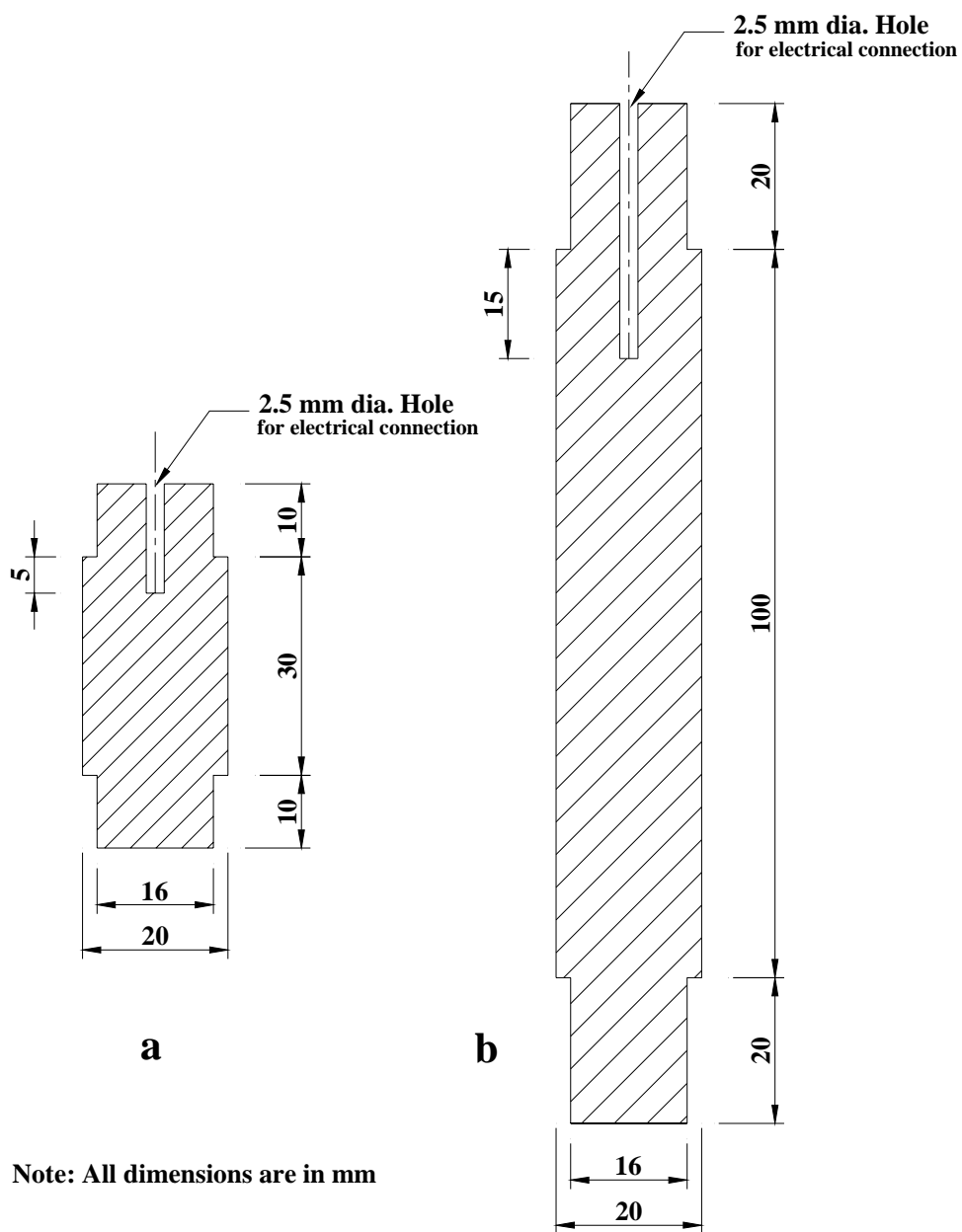


**Figure 4-4** Working Electrode (Carbon Steel)  
 a) L=3 cm, b) L=10 cm

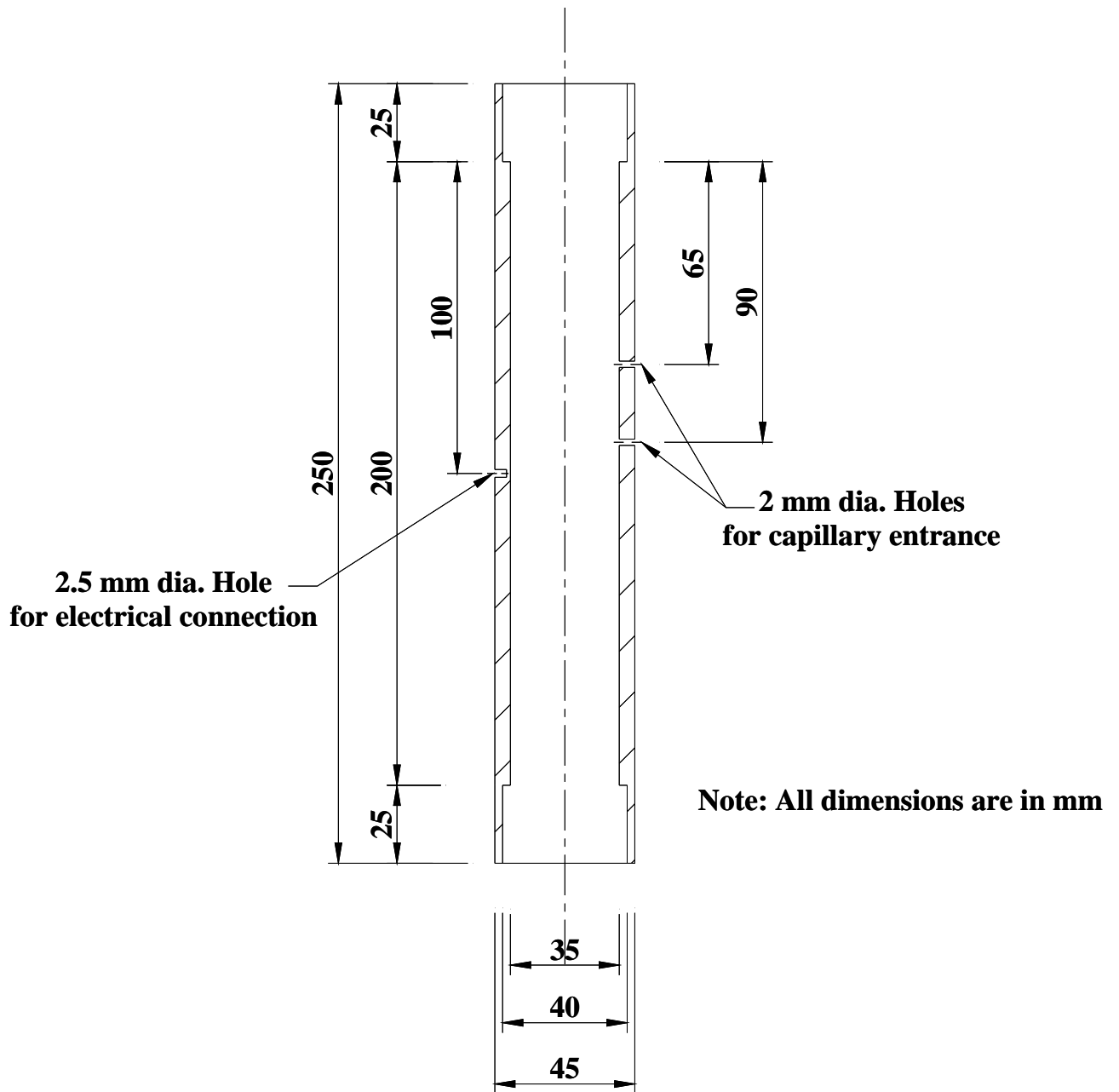


**Figure 4-5 Counter Electrode (Graphite)**

Also as shown in Fig. 4-5, there are two holes of 2 mm in diameter to allow the capillary entering through it to the cathode surface. The lower was used when utilizing 3 cm working electrode and the upper when utilizing 10 cm working electrode. When one hole was used the other one was closed using RTV (Room Temperature Vulcanizing) silicone and so on. Also there is a hole of 2.5 mm in diameter in the middle of the graphite electrode length extending in radial direction from outside of the graphite to a distance of 4 mm in its wall. A metallic rod of 2.5 mm in diameter was inserted in this hole and connected to an electrical wire. The electrical wire was turned entirely and fixed firmly around the graphite length to ensure uniform current distribution around the anode, and then was covered by electrical insulating tape. Presence of inner and outer PVC pipes in the test section provided electrical insulation of counter electrode from working electrode.

#### **4.2.2.3 Reference Electrode**

The reference electrode employed through out the experiments was the saturated calomel electrode (SCE). All potentials were measured with reference to this electrode through a capillary, the tip of the capillary was placed about 1 mm away from the cathode surface close to its upper edge [29, 74, 91, 92]. Concentration boundary layer thickness ranges from (10-100)  $\mu\text{m}$  [92], so the capillary tip was well outside the mass transfer boundary layer. When 3 cm working electrode was used, the tip of capillary was placed 5 mm from its upper edge, and 15 mm from the upper edge when 10 cm working electrode was used.

The opening at tip of the capillary was about (0.7-1) mm in diameter. The capillary was passed in straight line through a hole of 2 mm diameter in the graphite in order to reach cathode surface. A rubber hose or tube of 3 mm

inside diameter was used to connect between the end of the capillary and a 250 ml conical flask, which was used as a reservoir to put the SCE in it.

Calomel electrode is available as a compact ready-made unit as shown in Fig. 4-6.

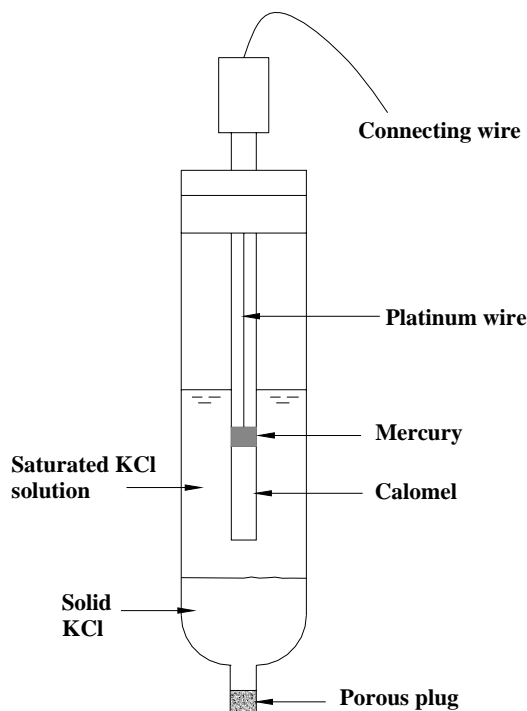


**Figure 4-6** Saturated Calomel Electrode (SCE) [23].

### 4.2.3 Electrical Cell

The electrical cell as shown in Fig. 4-7 consisted of the following devices:

- 1- DC power supply (6290A Hewlett-Packard HP type, max. range 40 V, 5 A).
- 2- Rheostat (variable resistance box), (model 236A Phipps & Bird, max. range 5 M $\Omega$ ).
- 3- Two digital multimeters, (1905a Thurlby type, and 2830 B+K Precision type, max. range 2000 mA, 1000 V).

The DC power supply was used to obtain a constant applied voltage of 6 V between the electrodes. The potential of the working electrode was monitored using voltmeter, while the current was observed with the aid of ammeter. The value of the potential was changed using the rheostat, and the steady state corresponding current was noted. Series values of potential and current were recorded. This method of obtaining potential and current is known as “potentiostatic method” [52, 54].

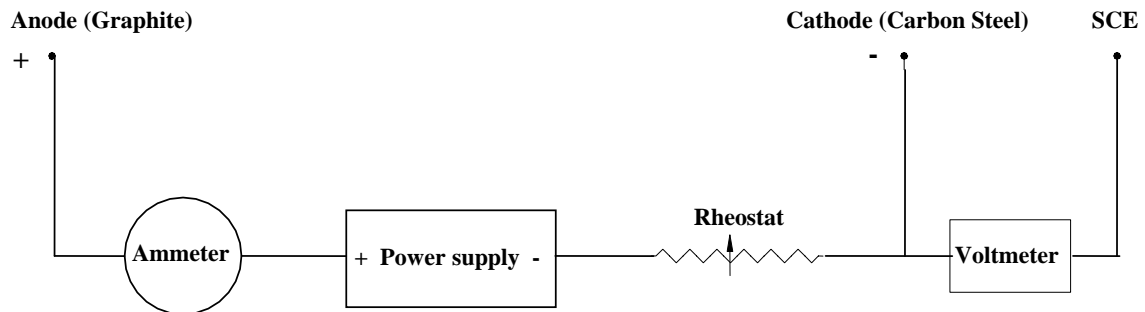


**Figure 4-7** Electrical circuit.

#### 4.2.4 Heat Flux Supply Unit

When experiments on 10 cm working electrode specimens were done under heat transfer, a heat flux supply unit must be introduced and some modifications on 10 cm working electrode specimen were made. The heat flux supply unit and details of heat transfer working electrode are shown in Figs. 4-8 and 4-9 respectively. The heat flux supply unit consisted of the following items:

- 1- Cartridge steel heater of 10 mm in diameter, 10 cm in length, 220 V, and 300 W was used. The 10 cm working electrode was drilled at its

centerline through its entire length with a hole of 10 mm in diameter, and the cartridge heater was inserted in this hole.

- 2- Variac (HSN 0103 type, 0-250 V, 5 A) was used to control and adjust the electrical voltage, this means to control the electrical power, supplied to steel heater.
- 3- Two digital multimeters (PM 2522 Philips type, and 1905a Thurlby type, max. range 2000 mA, 1000 V). The voltage supplied by the variac was monitored by voltmeter, while the current passed through this unit was measured by ammeter.

The power was estimated from Ohm's law,  $P = IV = I^2R = V^2 / R$ , where  $I$  is the flowing current in Ampere (A),  $V$  is the applied voltage in Volt (V), and  $R$  is the electrical resistance of steel heater in Ohm ( $\Omega$ ). This power is equal to the heat flow rate to the system (i.e.  $Q=P$ ).

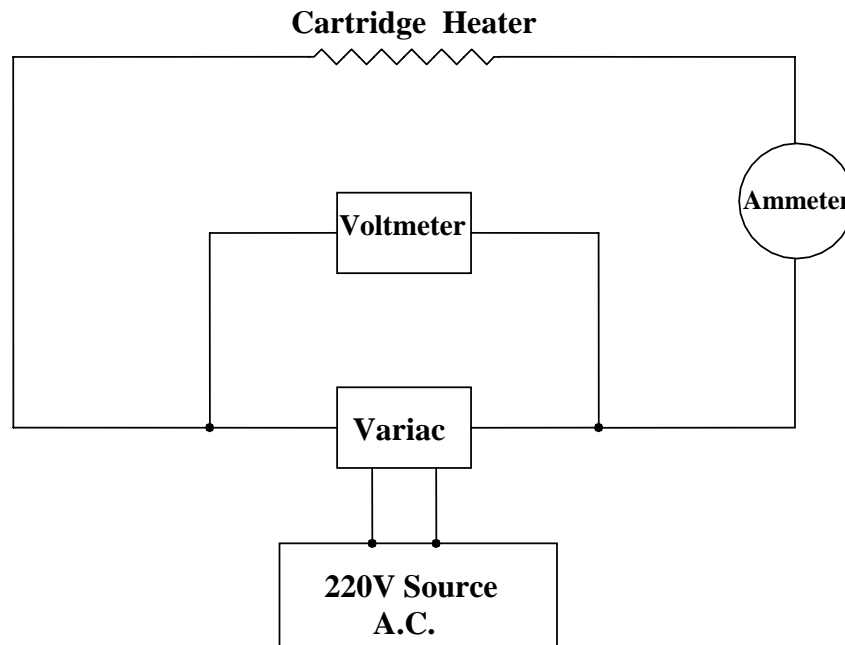


**Figure 4-8** Heat flux supply unit.

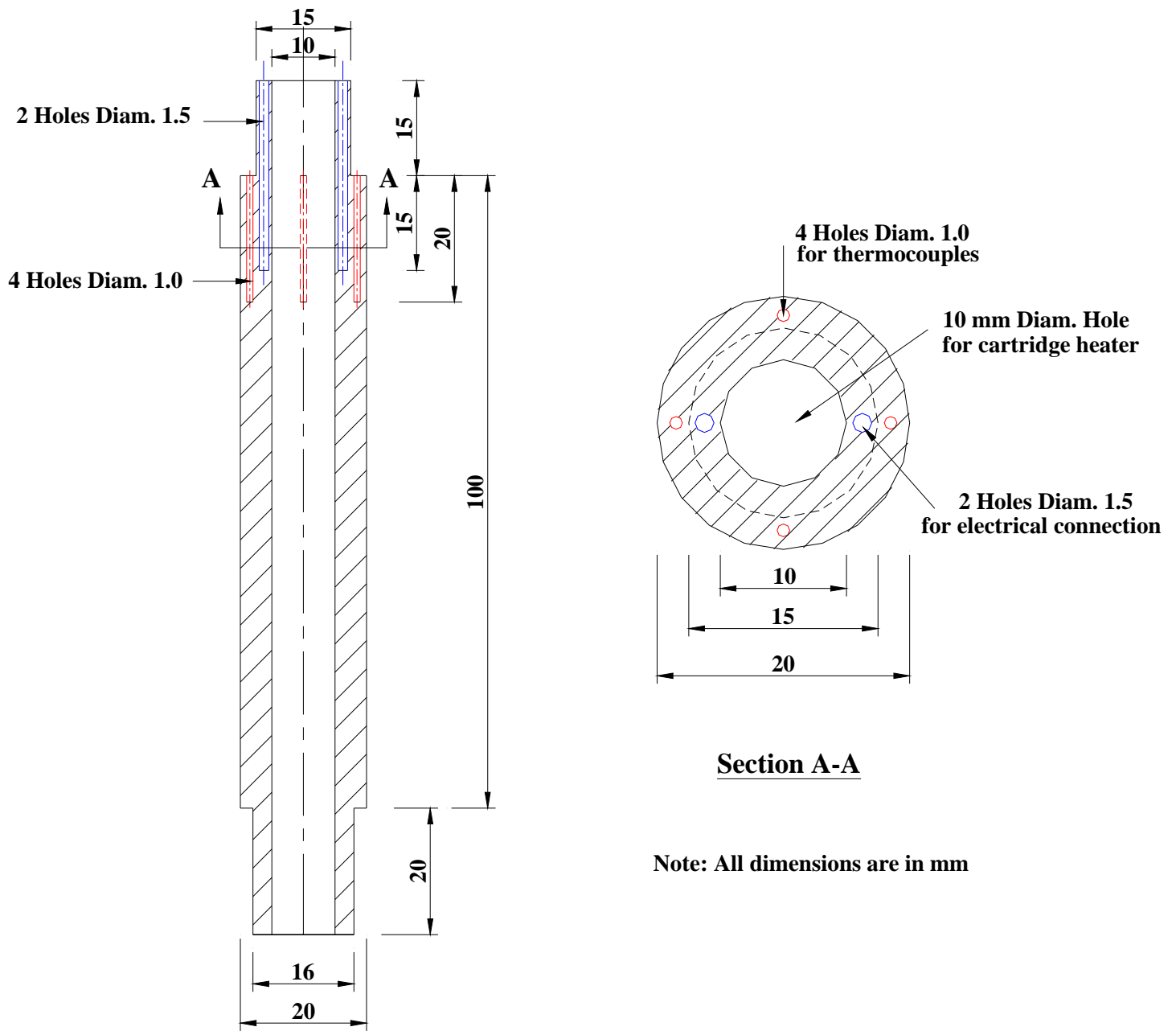


**Figure 4-9** Heat Transfer Working Electrode (Carbon Steel)

## **4.2.5 Surface Temperature Measuring Unit**

To study a process under heat transfer conditions, it is necessary to obtain the surface temperature of the specimen. This was accomplished by using:

- 1- Four copper-constantan (type K) thermocouples, (RS model, 1 mm wires diameter, point welded joint about 1 mm diameter).
- 2- Selector channel (Type K), to change the reading to various locations in carbon steel surface.
- 3- Digital temperature reader (Rex-C900 model, type K).

For 10 cm working electrode, four holes of 1 mm in diameter were drilled 1 mm below the specimen surface to a distance of 20 mm from its upper edge [12, 93-95] as shown in Fig. 4-9. These four holes were arranged every 90°. The four thermocouples were mounted in these holes and epoxided (using epoxy) in place.

The thermocouples were calibrated before use in a water bath using a thermometer. The accuracy of them was found to be of  $\pm 0.1^\circ \text{C}$ .

## **4.3 Experimental Program**

### **4.3.1 Specimen Preparation**

Prior to each experiment, the carbon steel surface was treated with increasing fine grades of emery paper (180, 320, 400, and 600). Then washed by tap water followed by distilled water, dried with clean tissue paper, and degreased with ethanol to remove any dirt, oil or grease. Finally dried by acetone and then with clean tissue to avoid water deposited films [52].

### **4.3.2 Electrolyte Preparation**

Sodium chloride 0.1 N was used as an electrolyte. This electrolyte was prepared from Analar sodium chloride (purity of NaCl > 99.8 wt%). The presence of NaCl increases the electroconductivity of the solution, so the cathode potential was not appreciably influenced by the resistance drop in the bulk of the solution because this drop was small and the potential was measured close to the cathode surface by using capillary [91]. Increasing the conductivity of the solution is one of the reasons for using NaCl solution.

The electroconductivity of the solution was measured using a digital electroconductivity meter (Acon Con 6 series Type). Appendix (C.2) lists the values of the solution electroconductivity at different temperatures.

The pH of the solution was measured before each test by digital pH meter (Chemtrix 60A Type). The pH meter was calibrated before use using buffer solutions (pH = 4, 7, and 9). The value of pH of the solution was 7.0 with negligible variation during the test run.

The solubility of O<sub>2</sub> (dissolved oxygen concentration) in 0.1 N NaCl solution was measured by using dissolved oxygen meter (model 810A plus, Orion). Appendix (C.3) lists the value of dissolved oxygen concentration in 0.1 N NaCl solution at different temperatures. The dissolved oxygen content was close to the saturated conditions throughout the test duration.

### **4.3.3 Experimental Procedure**

#### **4.3.3.1 Cathodic Polarization Experiments Under Isothermal Conditions**

Thirty liters of 0.1 N NaCl solution were prepared in the reservoir. The combined unit of heater and thermostat was adjusted to the desired temperature and switched on. The electrolyte was circulated through the by-pass line until the desired temperature was reached.

During this operation, the test section components were mounted in their positions, this includes inserting the working electrode in the other two parts of inner PVC tubes to form part of the inner tube. Then the whole inner tube was inserted in the outer tube (that contains graphite electrode). The RTV (Room Temperature Vulcanizing) silicone was used to prevent leakage from upstream and downstream ends of the duct. Then the capillary of the reference electrode was adjusted in place with the aid of RTV silicone also.

Whenever the desired temperature of solution was reached and the RTV silicone was vulcanized, the working, counter, and reference electrodes were connected to the electrical circuit and the latter was switched on. The valve leading to the duct was opened. The flowrate was adjusted to the required value by another valve close to the flowmeter.

Finally the specimen (working electrode) was cathodically polarized from a potential of nearly  $-1.4$  V (vs. SCE) to the corrosion potential  $E_{\text{corr}}$  where  $i_{\text{app}}=0$ . The potential and current were recorded during the run in steps of 30-40 mV [30], and two minutes were allowed for steady state to be reached after each potential increment [71].

Experiments under isothermal conditions were done for two lengths of working electrodes, 3 and 10 cm, at three different bulk temperatures 30, 40, and 50° C, and at Re from 5000-30000.

#### **4.3.3.2 Cathodic Polarization and Heat Transfer Experiments Under Heat Transfer Conditions**

During experiments under heat transfer conditions, the electrolyte reservoir was introduced inside another larger glass bath of 90 liters capacity, forming like jacketed vessel as shown in Fig. 4-1. Since there is little increase of electrolyte reservoir temperature during the run under heat flux supply, the

tap water was flowing in the jacket and controlled by inlet and outlet valves to maintain the electrolyte reservoir temperature within the desired one.

Cartridge steel heater was inserted in its position in carbon steel specimen and fixed by using epoxy. Also the four thermocouples were inserted in their holes and epoxied in place to ensure enough firmness. To prevent heat leakages from specimen ends, the two incremental ends of 10 cm working electrode were isolated by fiber glass. Then the working electrode was mounted in its position in the test section.

Following the same procedure under isothermal conditions, except that as the electrolyte solution entered the test section, the heat flux supply unit was turned on, and adjusted to the desired heat flux by variac. Also the surface temperature-measuring unit was switched on, and the four readings of thermocouples were recorded. The average value of these readings was taken as the surface temperature.

Experiments under heat transfer conditions were done for 10 cm working electrode, at three different temperatures 30, 40, and 50°C, at Re from 5000-30000, and for three heat fluxes 15, 30, and 45 kW/m<sup>2</sup>.

Surface temperature measuring experiments can be performed simultaneously with cathodic polarization experiments or can be done alone. No appreciable variation in results was observed.

#### **4.3.3.3 Corrosion Fouling Experiments**

The same procedure illustrated above was repeated for fouling experiments. At the beginning of fouling experiment ( $t=0$ ), the values for cathodic polarization and surface temperature were recorded. These values represent a clean surface where no corrosion products formed. During the polarization no free corrosion occurs, except at low currents near corrosion potential, because the specimen will be cathodically protected. At the end of

the first readings, the electrical circuit was switched off and the specimen was allowed to corrode freely under the influence of corrosive solution 0.1N NaCl. This means that corrosion products began forming.

At the beginning of fouling experiments, the cathodic polarization and surface temperature results were taken every (4-8) hours for the first 48 hours, and every (14-20) hours for the remaining experimental time. The corrosion fouling experiment continued for 200 hours. The electrical circuit was switched on whenever cathodic polarization results were recorded, and then switched off after accomplishing the results, and so on.

Corrosion fouling experiments were carried out using 10 cm working electrode, at three different temperatures 30, 40, and 50°C, at Re 5000, 10000, and 15000, and for 15 kW/m<sup>2</sup> heat flux.

# **CHAPTER FIVE**

## **RESULTS**

## 5.1 Introduction

This chapter displays the experimental results obtained by the present work, like limiting current densities, corrosion potentials, and surface temperatures. At first, results under isothermal conditions are presented, and then under heat transfer conditions, and finally corrosion fouling results.

Also this chapter includes mass and heat transfer calculations in order to evaluate mass and heat transfer coefficients, Sherwood number, Nusselt number, and other dimensionless groups.

The effects of various variables on experimental results are stated, like the effect of increasing bulk temperature, Reynolds number, and heat flux.

## 5.2 Cathodic Polarization Curve

Typical cathodic potential-current curve for the behavior of carbon steel in air saturated 0.1 N NaCl solution is shown in Fig. 5-1. The curve ABCD is called the cathodic region of polarization curve, where AB is the secondary reaction (hydrogen evolution) region, BCD is the interest reaction (oxygen reduction reaction) region, and D is the corrosion potential  $E_{\text{corr}}$ .

The limiting current density of oxygen reduction  $i_L$  is determined from the plateau BC in Fig. 5-1.  $i_1$  is the final limiting value of oxygen reduction reaction, while  $i_2$  refers to final stage of hydrogen evolution reaction [96].

The limiting current plateau is not absolutely flat, thus the method given by Gabe and Makanjoula [97] will be adopted to find the limiting current density value:

$$i_L = \frac{i_1 + i_2}{2} \quad (5.1)$$

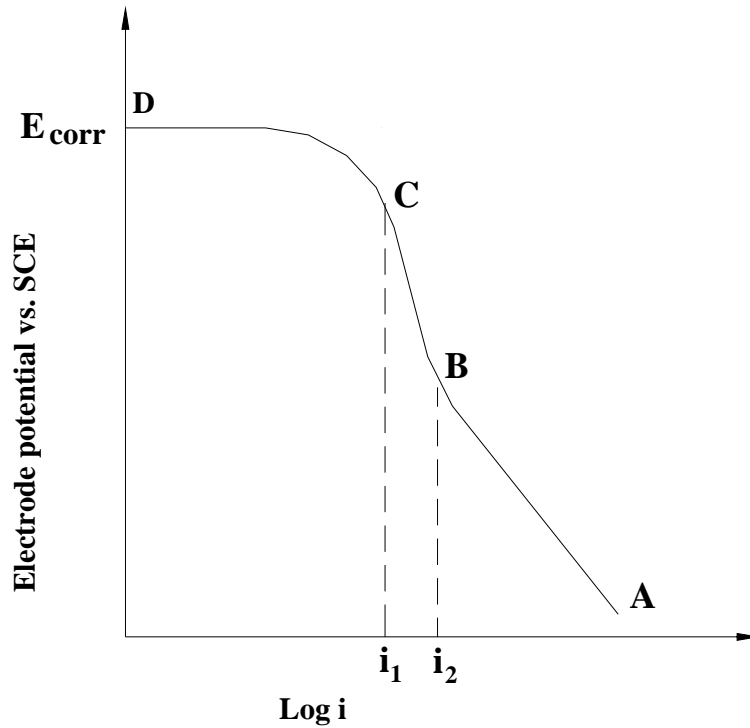


**Figure 5-1** Typical cathodic region of polarization curve of carbon steel in air saturated 0.1N NaCl solution.

### 5.3 Cathodic Polarization Results Under Isothermal Conditions

The cathodic polarization curves were obtained from experimental data by plotting cathode potential versus current density on semi-log paper. These curves are presented in Appendix (D.1) for isothermal conditions at different temperatures (30, 40, and 50°C) and for different Re values (5000-30000) obtained from two working electrode lengths ( $L=3$  and  $L=10$  cm). An example of these curves is shown in Fig. 5-2.

The limiting current density values  $i_L$  and the values of corrosion potential  $E_{\text{corr}}$  were obtained from cathodic polarization curves and are shown in Tables 5-1 to 5-3 for working electrode lengths of 3 and 10 cm under isothermal conditions at various bulk temperatures and Reynolds numbers.

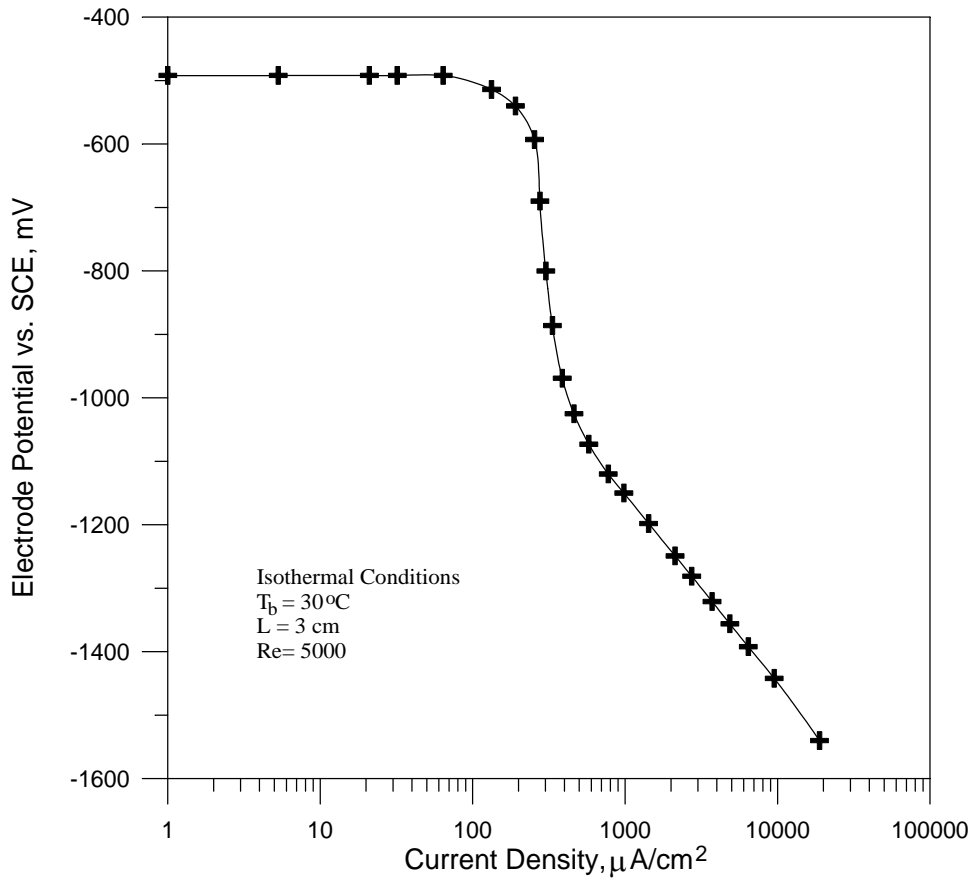


**Figure 5-2** Cathodic polarization curve for  $L=3 \text{ cm}$ ,  $Re = 5000$ , and  $T_b = 30^\circ\text{C}$  under isothermal conditions.

Table 5-1 The limiting current densities and corrosion potentials under isothermal conditions at  $T_b = 30^\circ\text{C}$ ,  $L = 3$  and  $10 \text{ cm}$ .

Re	$L=3 \text{ cm}$		$L=10 \text{ cm}$	
	$i_L$ $\mu\text{A}/\text{cm}^2$	$E_{\text{corr}}$ (vs. SCE) mV	$i_L$ $\mu\text{A}/\text{cm}^2$	$E_{\text{corr}}$ (vs. SCE) mV
5000	312.5	- 492	207.5	- 508
10000	416.5	- 490	319.0	- 490
15000	520.0	- 488	370.0	- 486
20000	597.0	- 487	422.5	- 470

Table 5-2 The limiting current densities and corrosion potentials under isothermal conditions at  $T_b = 40^\circ\text{C}$ ,  $L = 3$  and 10 cm.

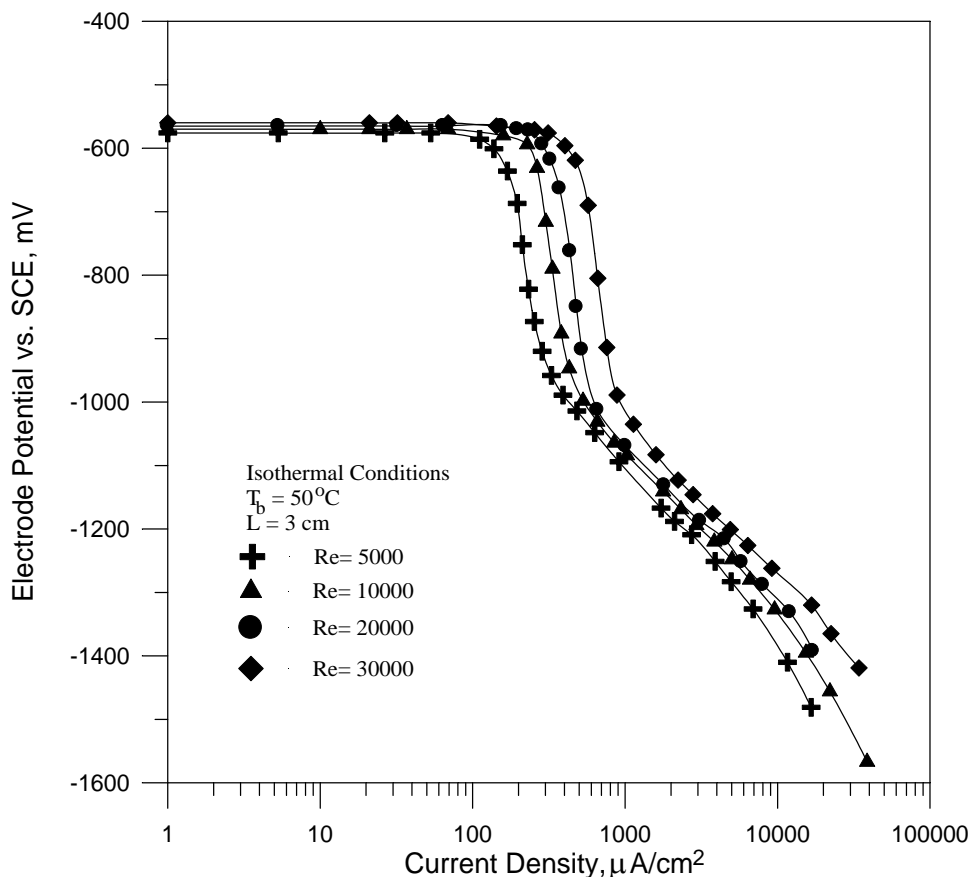
Re	$L=3$ cm		$L=10$ cm	
	$i_L$ $\mu\text{A}/\text{cm}^2$	$E_{\text{corr}}$ (vs. SCE) mV	$i_L$ $\mu\text{A}/\text{cm}^2$	$E_{\text{corr}}$ (vs. SCE) mV
5000	270.5	- 552	194.0	- 545
10000	379.5	- 550	290.0	- 544
15000	456.0	- 545	320.0	- 541
20000	510.0	- 539	364.0	- 536
25000	582.0	-536	426.5	-531

Table 5-3 The limiting current densities and corrosion potentials under isothermal conditions at  $T_b = 50^\circ\text{C}$ ,  $L = 3$  and 10 cm.

Re	$L=3$ cm		$L=10$ cm	
	$i_L$ $\mu\text{A}/\text{cm}^2$	$E_{\text{corr}}$ (vs. SCE) mV	$i_L$ $\mu\text{A}/\text{cm}^2$	$E_{\text{corr}}$ (vs. SCE) mV
5000	250.5	- 576	176.0	- 581
10000	347.5	- 570	266.5	- 576
15000	420.0	- 566	301.0	- 572
20000	480.5	- 565	355.5	- 570
25000	560.0	- 561	395.0	- 567
30000	666.0	- 560	451.0	- 558

From these Tables (5-1 to 5-3), the following can be observed:

- 1- At constant bulk temperature, the limiting current density increases with increasing velocity (or Re) and the corrosion potential becomes less negative (more noble), as shown in Figs. 5-3 and 5-4.
- 2- At constant Reynolds number, the limiting current density decreases with increasing bulk temperature, and the corrosion potential shifts to more negative values, as shown in Figs. 5-5 and 5-6.
- 3- At constant bulk temperature and Reynolds number, the limiting current density decreases with increasing working electrode length from 3 to 10 cm as shown in Figs. 5-7 and 5-8, while Corrosion potential values remain approximately close.



**Figure 5-3** Cathodic polarization curves showing the effect of Re for  $L=3\text{ cm}$  and  $T_b=50^\circ\text{C}$  under isothermal conditions.

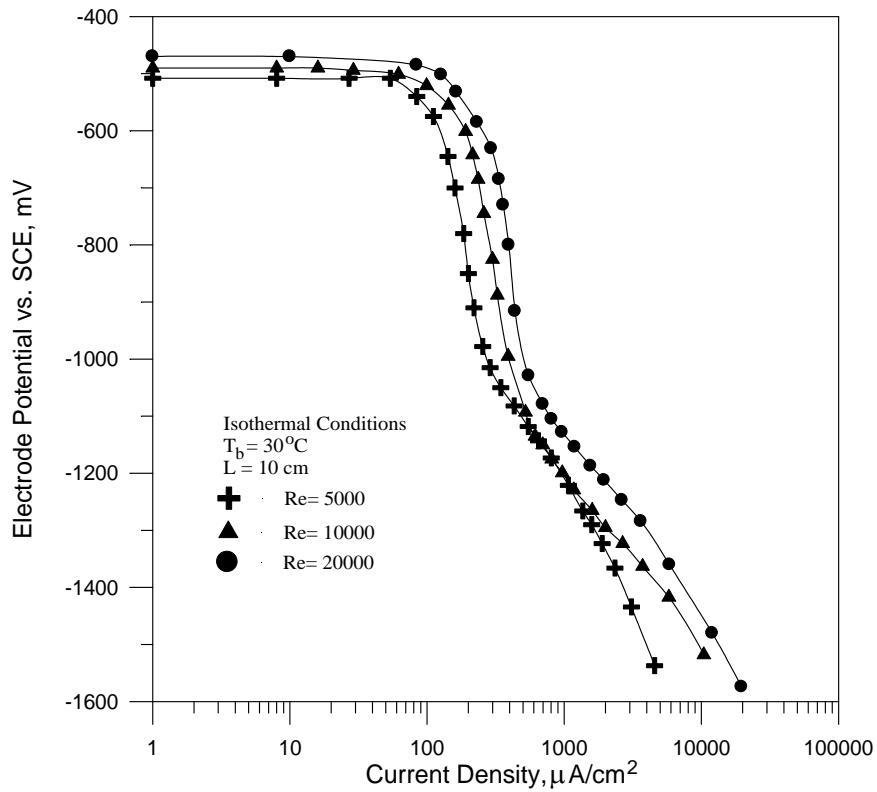


**Figure 5-4** Cathodic polarization curves showing the effect of Re for  $L=10\text{ cm}$  and  $T_b = 30^\circ\text{C}$  under isothermal conditions.

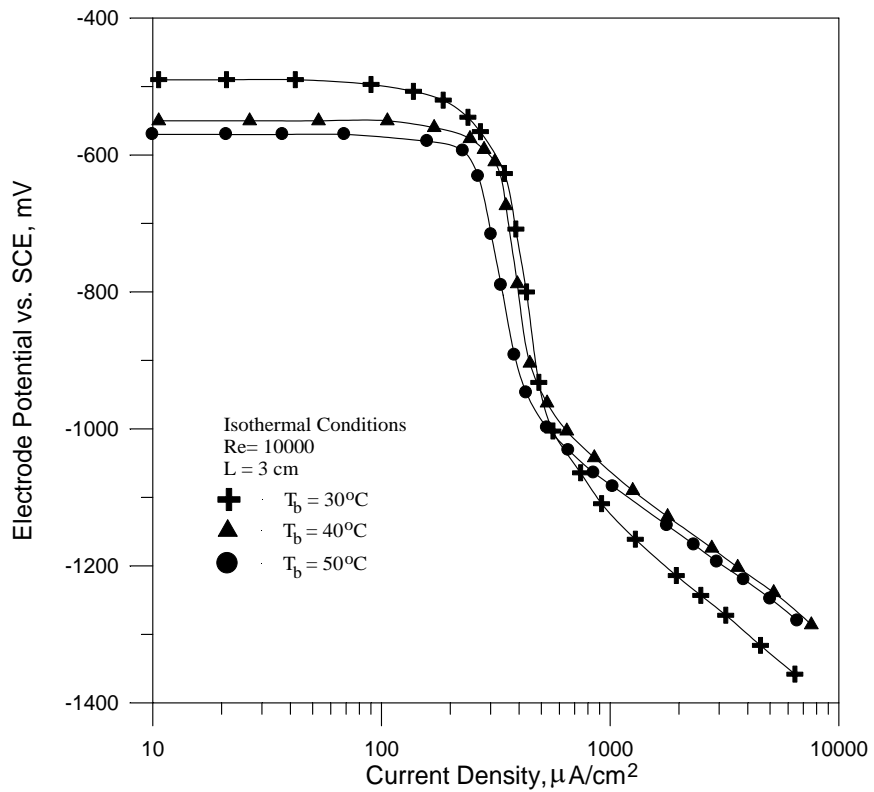


**Figure 5-5** Cathodic polarization curves showing the effect of bulk temperature for  $\text{Re} = 10000$ , and  $L=3\text{ cm}$  under isothermal conditions.

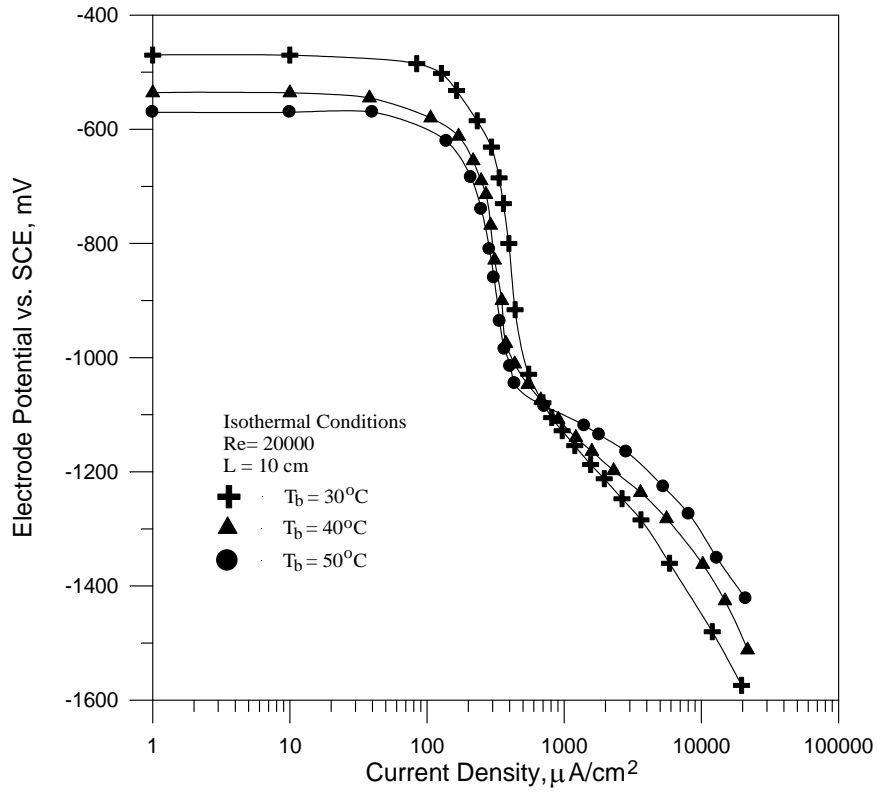


**Figure 5-6** Cathodic polarization curves showing the effect of bulk temperature for  $\text{Re} = 20000$ , and  $L = 10$  cm under isothermal conditions.

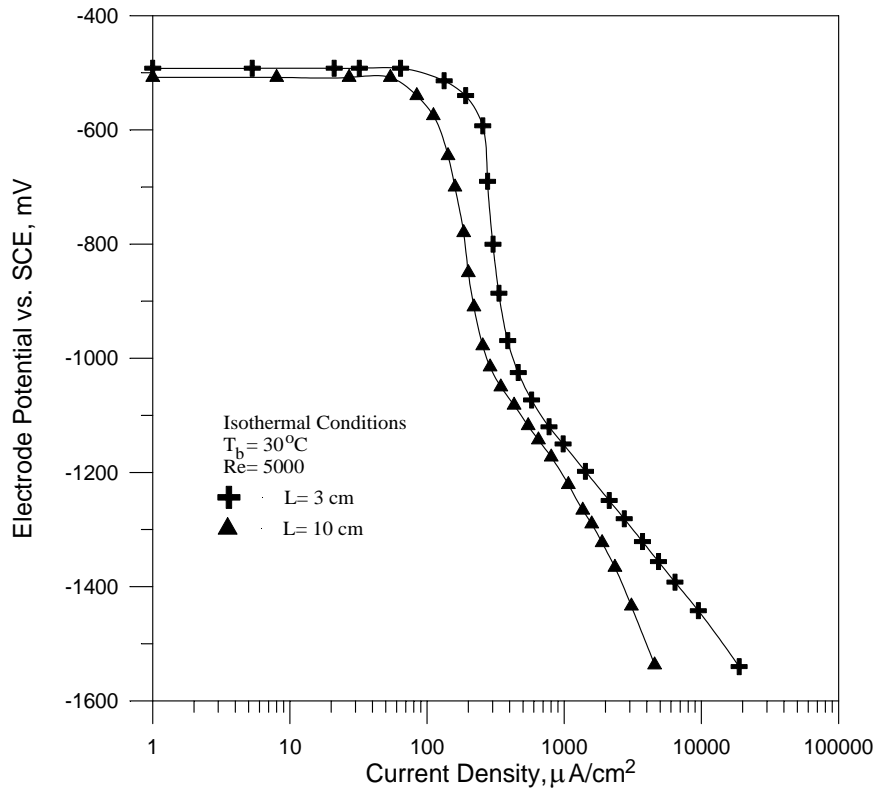


**Figure 5-7** Cathodic polarization curves showing the effect of electrode length for  $\text{Re} = 5000$ , and  $T_b = 30^\circ\text{C}$  under isothermal conditions.

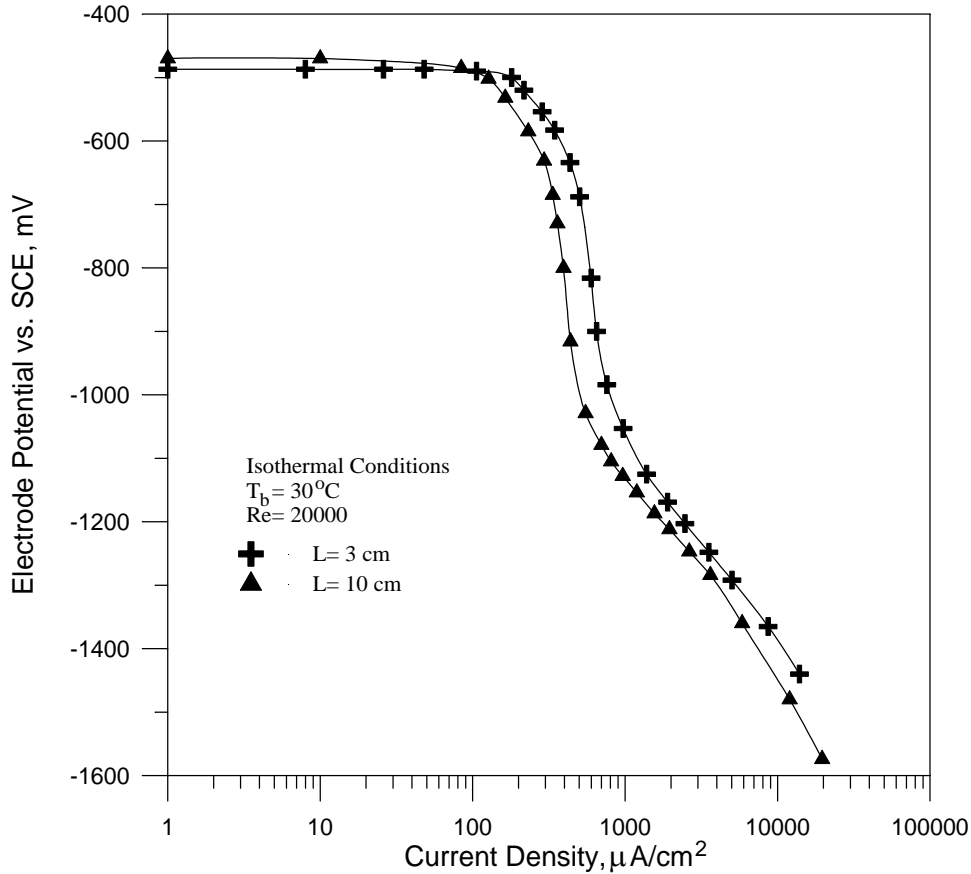


**Figure 5-8** Cathodic polarization curves showing the effect of electrode length for  $Re = 20000$ , and  $T_b = 30^\circ C$  under isothermal conditions.

#### 5.4 Mass Transfer Calculations Under Isothermal Conditions

From the limiting current density data of oxygen reduction, the mass transfer coefficient  $k_m$  is calculated from Eq. (3.15):

$$k_m = \frac{i_L}{zFC_b} \quad (5.2)$$

where  $i_L$  = limiting current density

$F$  = Faraday's constant (96487 Coulombs/equivalent)

$z$  = No. of electrons transferred ( $z = 4$  for oxygen reduction)

$C_b$  = bulk concentration of oxygen in solution

Then a number of mass transfer dimensionless groups can be calculated as presented in Table 2-1:

$$\text{Schmidt No. : } Sc = \frac{\mu}{\rho D} \quad (5.3)$$

$$\text{Sherwood No. : } Sh = \frac{k_m d_e}{D} \quad (5.4)$$

$$\text{Stanton No. : } St_m = \frac{Sh}{Re Sc} = \frac{k_m}{u} \quad (5.5)$$

$$J\text{-factor : } J_m = St_m Sc^{2/3} \quad (5.6)$$

where  $D$  is the diffusion of oxygen in solution,  $d_e$ = equivalent diameter  $= (d_2 - d_1) = 35 - 20 = 15 \text{ mm} = 0.015 \text{ m}$ . The physical properties required to perform the above calculations, i.e.,  $C_b$ ,  $D$ ,  $\mu$ , and  $\rho$  are presented in Appendix (C).

The results of mass transfer calculations under isothermal conditions are given in Tables 5-4 to 5-9.

Table 5-4 Mass transfer calculations under isothermal conditions at  $T_b = 30^\circ \text{C}$ , and  $L = 3 \text{ cm}$ .

Re	$k_m \times 10^5 \text{ (m/s)}$	Sc	Sh	$St_m \times 10^5$	$J_m \times 10^3$
5000	3.45	339.43	218.65	12.94	6.30
10000	4.60	339.43	291.42	8.62	4.20
15000	5.75	339.43	363.84	7.18	3.49
20000	6.60	339.43	417.71	6.18	3.01

Table 5-5 Mass transfer calculations under isothermal conditions at  $T_b = 40^\circ \text{C}$ , and  $L = 3 \text{ cm}$ .

Re	$k_m \times 10^5 \text{ (m/s)}$	Sc	Sh	$St_m \times 10^5$	$J_m \times 10^3$
5000	3.53	218.93	175.43	16.13	5.86
10000	4.96	218.93	246.12	11.31	4.11
15000	5.95	218.93	295.73	9.06	3.29
20000	6.66	218.93	330.75	7.60	2.76
25000	7.60	218.93	377.45	6.94	2.52

Table 5-6 Mass transfer calculations under isothermal conditions at  $T_b = 50^\circ\text{C}$ , and  $L = 3\text{ cm}$ .

Re	$k_m \times 10^5$ (m/s)	Sc	Sh	$St_m \times 10^5$	$J_m \times 10^3$
5000	3.71	156.07	156.27	20.11	5.83
10000	5.15	156.07	216.78	13.95	4.04
15000	6.22	156.07	262.01	11.24	3.26
20000	7.11	156.07	299.76	9.642	2.80
25000	8.29	156.07	349.35	8.990	2.61
30000	9.86	156.07	415.48	8.909	2.58

Table 5-7 Mass transfer calculations under isothermal conditions at  $T_b = 30^\circ\text{C}$ , and  $L = 10\text{ cm}$ .

Re	$k_m \times 10^5$ (m/s)	Sc	Sh	$St_m \times 10^5$	$J_m \times 10^3$
5000	2.29	339.43	145.18	8.59	4.18
10000	3.53	339.43	223.20	6.60	3.21
15000	4.09	339.43	258.88	5.11	2.49
20000	4.67	339.43	295.62	4.37	2.13

Table 5-8 Mass transfer calculations under isothermal conditions at  $T_b = 40^\circ\text{C}$ , and  $L = 10\text{ cm}$ .

Re	$k_m \times 10^5$ (m/s)	Sc	Sh	$St_m \times 10^5$	$J_m \times 10^3$
5000	2.53	218.93	125.82	11.57	4.20
10000	3.79	218.93	188.07	8.65	3.14
15000	4.18	218.93	207.53	6.36	2.31
20000	4.75	218.93	236.07	5.43	1.97
25000	5.57	218.93	276.60	5.09	1.85

Table 5-9 Mass transfer calculations under isothermal conditions at  $T_b = 50^\circ\text{C}$ , and  $L = 10\text{ cm}$ .

Re	$k_m \times 10^5$ (m/s)	Sc	Sh	$St_m \times 10^5$	$J_m \times 10^3$
5000	2.61	156.07	109.80	14.13	4.10
10000	3.95	156.07	166.25	10.70	3.10
15000	4.46	156.07	187.78	8.05	2.33
20000	5.26	156.07	221.78	7.13	2.07
25000	5.85	156.07	246.42	6.34	1.84
30000	6.68	156.07	281.35	6.03	1.75

From mass transfer calculations Tables (5-4 to 5-9), the following items can be indicated:

- 1- At constant bulk temperature, with increasing Reynolds number the mass transfer coefficient and hence the Sherwood number increase, while Stanton number and mass transfer  $J$ -factor decrease with increasing Reynolds number.
- 2- At constant Reynolds number, with increasing bulk temperature, mass transfer coefficient, and Stanton number increase, while Sherwood number decreases. No appreciable effect is observed on  $J$ -factor.
- 3- At constant temperature, the Schmidt number is constant. It is significantly affected by temperature because as the bulk temperature rises, viscosity decreases and diffusion coefficient increases significantly. So Schmidt number decreases with increase in temperature (see Eq. 5.3).
- 4- At constant bulk temperature and Reynolds number, the increase of working electrode length from 3 to 10 cm, leads to decrease mass transfer coefficient, Sherwood number, Stanton number, and  $J$ -factor.

## 5.5 Cathodic Polarization Results Under Heat Transfer Conditions

Cathodic polarization curves under heat transfer conditions for working electrode length of 10 cm are given in Appendix (D.2). These polarization curves are for different heat fluxes ( $q=15, 30, \text{ and } 45 \text{ kW/m}^2$ ), at different Reynolds numbers ( $Re=5000 \text{ to } 30000$ ), and at bulk temperatures ( $T_b= 30, 40, \text{ and } 50 \text{ }^\circ\text{C}$ ). The values of limiting current density and corrosion potential for working electrode length of 10 cm under heat transfer conditions are given in Tables 5-10 to 5-12.

Table 5-10 The limiting current densities and corrosion potentials under heat transfer conditions at  $T_b = 30^\circ\text{C}$ , and  $L = 10 \text{ cm}$ .

Re	$q=15 \text{ kW/m}^2$		$q=30 \text{ kW/m}^2$		$q=45 \text{ kW/m}^2$	
	$i_L$ $\mu\text{A/cm}^2$	$E_{\text{corr}}$ , mV (vs. SCE)	$i_L$ $\mu\text{A/cm}^2$	$E_{\text{corr}}$ , mV (vs. SCE)	$i_L$ $\mu\text{A/cm}^2$	$E_{\text{corr}}$ , mV (vs. SCE)
5000	250.5	- 555	253.0	- 551	274.0	- 563
10000	359.5	- 530	399.5	- 527	371.0	- 545
15000	392.0	- 501	429.5	- 517	452.5	- 529
20000	453.5	- 491	482.0	- 485	496.5	- 525

Table 5-11 The limiting current densities and corrosion potentials under heat transfer conditions at  $T_b = 40^\circ\text{C}$ , and  $L = 10 \text{ cm}$ .

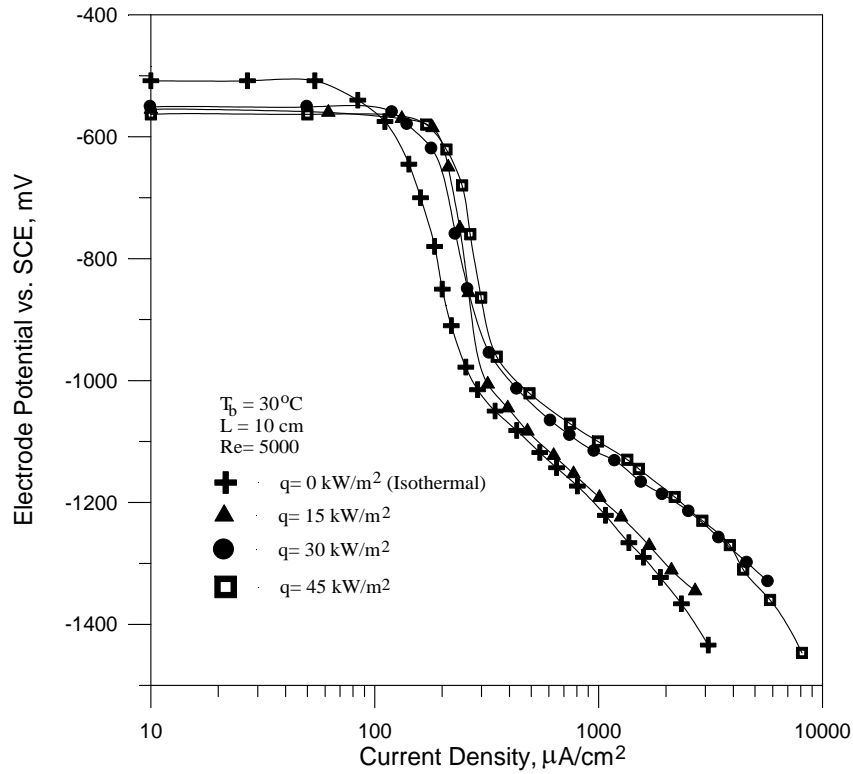
Re	$q=15 \text{ kW/m}^2$		$q=30 \text{ kW/m}^2$		$q=45 \text{ kW/m}^2$	
	$i_L$ $\mu\text{A/cm}^2$	$E_{\text{corr}}$ , mV (vs. SCE)	$i_L$ $\mu\text{A/cm}^2$	$E_{\text{corr}}$ , mV (vs. SCE)	$i_L$ $\mu\text{A/cm}^2$	$E_{\text{corr}}$ , mV (vs. SCE)
5000	214.5	- 579	246.0	- 581	251.0	- 592
10000	323.0	- 567	357.5	- 570	365.0	- 585
15000	348.0	- 563	380.5	- 568	411.5	- 574
20000	393.5	- 561	416.5	- 564	443.0	- 561
25000	435.0	-557	450.5	-560	481.0	-560

Table 5-12 The limiting current densities and corrosion potentials under heat transfer conditions at  $T_b = 50^\circ\text{C}$ , and  $L = 10\text{ cm}$ .

Re	$q=15\text{ kW/m}^2$		$q=30\text{ kW/m}^2$		$q=45\text{ kW/m}^2$	
	$i_L$ $\mu\text{A/cm}^2$	$E_{\text{corr}}$ , mV (vs. SCE)	$i_L$ $\mu\text{A/cm}^2$	$E_{\text{corr}}$ , mV (vs. SCE)	$i_L$ $\mu\text{A/cm}^2$	$E_{\text{corr}}$ , mV (vs. SCE)
5000	204.5	- 601	217.5	- 620	226.5	- 623
10000	286.5	- 595	298.5	- 607	313.5	- 610
15000	324.5	- 589	356.5	- 596	369.0	- 590
20000	375.0	- 575	398.0	- 581	400.0	- 586
25000	418.0	- 566	423.5	- 570	459.0	- 572
30000	461.5	- 561	471.5	- 563	479.5	- 567

Tables 5-10 to 5-12 show that at constant bulk temperature and Reynolds number, the limiting current density increases with increasing heat flux, and the corrosion potential shifts to more negative (less noble) values.

By comparing these tables with Tables 5-1 to 5-3 for 10 cm working electrode under isothermal conditions (zero heat flux) shows that the limiting current density under heat transfer conditions is higher than under identical isothermal conditions. The corrosion potential under heat transfer is generally more negative than that under identical isothermal conditions as shown in Figs. 5-9 and 5-10.



**Figure 5-9** Cathodic polarization curves showing the effect of heat flux at  $T_b = 30^\circ\text{C}$ ,  $\text{Re} = 5000$ , and  $L = 10\text{ cm}$ .

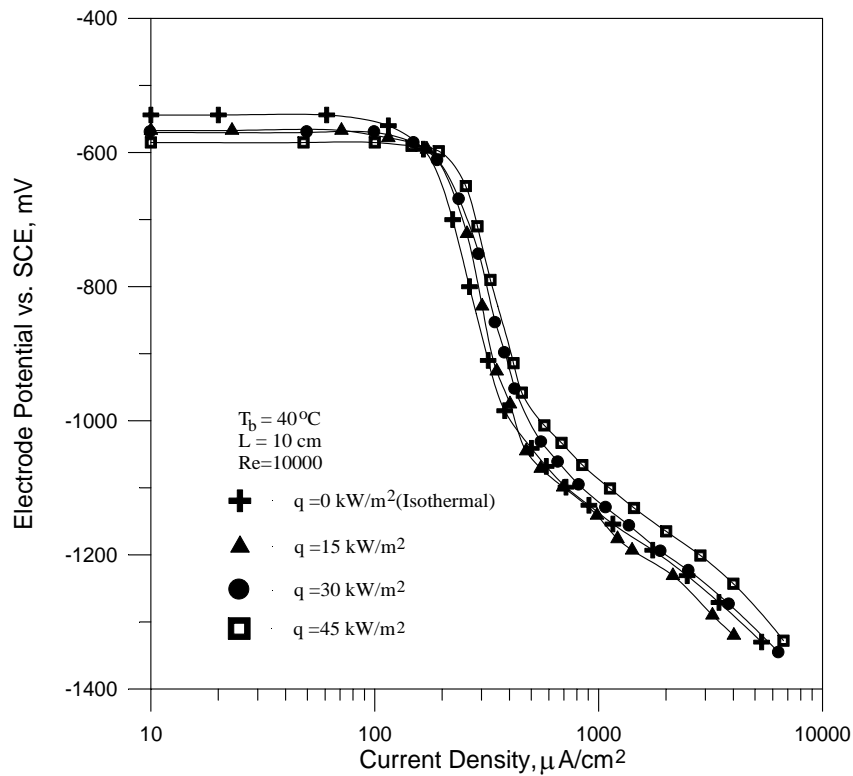


**Figure 5-10** Cathodic polarization curves showing the effect of heat flux at  $T_b = 40^\circ\text{C}$ ,  $\text{Re} = 10000$ , and  $L = 10\text{ cm}$ .

## 5.6 Mass Transfer Calculations Under Heat Transfer Conditions

The results of mass transfer calculations under heat transfer conditions are given in Tables 5-13 to 5-21.

Table 5-13 Mass transfer calculations under heat transfer conditions at  $T_b = 30^\circ\text{C}$ ,  $L = 10\text{ cm}$ , and  $q=15\text{ kW/m}^2$ .

Re	$k_m \times 10^5$ (m/s)	Sh	$St_m \times 10^5$	$Sc_f$	$J_{mf} \times 10^3$
5000	2.77	175.27	10.38	297.19	4.62
10000	3.97	251.54	7.44	316.16	3.45
15000	4.33	274.28	5.41	324.08	2.55
20000	5.01	317.31	4.69	328.80	2.24

Table 5-14 Mass transfer calculations under heat transfer conditions at  $T_b = 30^\circ\text{C}$ ,  $L = 10\text{ cm}$ , and  $q=30\text{ kW/m}^2$ .

Re	$k_m \times 10^5$ (m/s)	Sh	$St_m \times 10^5$	$Sc_f$	$J_{mf} \times 10^3$
5000	2.80	177.02	10.48	262.63	4.30
10000	4.42	279.52	8.27	294.14	3.66
15000	4.75	300.51	5.93	308.43	2.71
20000	5.33	337.25	4.99	316.81	2.32

Table 5-15 Mass transfer calculations under heat transfer conditions at  $T_b = 30^\circ\text{C}$ ,  $L = 10\text{ cm}$ , and  $q=45\text{ kW/m}^2$ .

Re	$k_m \times 10^5$ (m/s)	Sh	$St_m \times 10^5$	$Sc_f$	$J_{mf} \times 10^3$
5000	3.03	191.71	11.35	230.73	4.27
10000	4.10	259.58	7.68	270.87	3.22
15000	5.00	316.61	6.25	291.13	2.74
20000	5.49	347.39	5.14	303.38	2.32

Table 5-16 Mass transfer calculations under heat transfer conditions at  $T_b = 40^\circ\text{C}$ ,  $L = 10\text{ cm}$ , and  $q=15\text{ kW/m}^2$ .

Re	$k_m \times 10^5$ (m/s)	Sh	$St_m \times 10^5$	$Sc_f$	$J_{mf} \times 10^3$
5000	2.80	139.11	12.79	197.94	4.34
10000	4.22	209.48	9.63	210.00	3.40
15000	4.54	225.69	6.92	214.77	2.48
20000	5.14	255.20	5.87	217.42	2.12
25000	5.68	282.11	5.19	218.76	1.88

Table 5-17 Mass transfer calculations under heat transfer conditions at  $T_b = 40^\circ\text{C}$ ,  $L = 10\text{ cm}$ , and  $q=30\text{ kW/m}^2$ .

Re	$k_m \times 10^5$ (m/s)	Sh	$St_m \times 10^5$	$Sc_f$	$J_{mf} \times 10^3$
5000	3.21	159.54	14.67	173.87	4.57
10000	4.67	231.85	10.66	193.96	3.57
15000	4.97	246.77	7.56	203.25	2.61
20000	5.44	270.11	6.21	207.87	2.18
25000	5.88	292.16	5.37	211.29	1.91

Table 5-18 Mass transfer calculations under heat transfer conditions at  $T_b = 40^\circ\text{C}$ ,  $L = 10\text{ cm}$ , and  $q=45\text{ kW/m}^2$ .

Re	$k_m \times 10^5$ (m/s)	Sh	$St_m \times 10^5$	$Sc_f$	$J_{mf} \times 10^3$
5000	3.28	162.78	14.97	153.56	4.29
10000	4.77	236.71	10.88	179.58	3.46
15000	5.37	266.87	8.18	192.78	2.73
20000	5.78	287.30	6.60	199.56	2.25
25000	6.28	311.94	5.74	203.67	1.99

Table 5-19 Mass transfer calculations under heat transfer conditions at  $T_b = 50^\circ\text{C}$ ,  $L = 10\text{ cm}$ , and  $q=15\text{ kW/m}^2$ .

Re	$k_m \times 10^5$ (m/s)	Sh	$St_m \times 10^5$	$Sc_f$	$J_{mf} \times 10^3$
5000	3.03	127.58	16.42	131.95	4.26
10000	4.24	178.73	11.50	139.65	3.10
15000	4.80	202.44	8.68	142.71	2.37
20000	5.55	233.94	7.53	144.98	2.08
25000	6.19	260.77	6.71	146.13	1.86
30000	6.83	287.90	6.17	147.00	1.72

Table 5-20 Mass transfer calculations under heat transfer conditions at  $T_b = 50^\circ\text{C}$ ,  $L = 10\text{ cm}$ , and  $q=30\text{ kW/m}^2$ .

Re	$k_m \times 10^5$ (m/s)	Sh	$St_m \times 10^5$	$Sc_f$	$J_{mf} \times 10^3$
5000	3.22	135.69	17.46	117.53	4.19
10000	4.42	186.22	11.98	130.67	3.08
15000	5.28	222.40	9.54	135.34	2.51
20000	5.89	248.29	7.99	138.83	2.14
25000	6.27	264.20	6.80	140.75	1.84
30000	6.98	294.14	6.31	142.15	1.72

Table 5-21 Mass transfer calculations under heat transfer conditions at  $T_b = 50^\circ\text{C}$ ,  $L = 10\text{ cm}$ , and  $q=45\text{ kW/m}^2$ .

Re	$k_m \times 10^5$ (m/s)	Sh	$St_m \times 10^5$	$Sc_f$	$J_{mf} \times 10^3$
5000	3.35	141.30	18.19	104.58	4.04
10000	4.64	195.57	12.58	121.18	3.08
15000	5.46	230.20	9.87	129.15	2.52
20000	5.92	249.54	8.03	133.24	2.09
25000	6.80	286.34	7.37	135.87	1.95
30000	7.10	299.13	6.41	137.74	1.71

It is obvious from these Tables (5-13 to 5-21), that at constant bulk temperature and Reynolds number, the increase in heat flux leads to increase mass transfer coefficient, Sherwood number, and Stanton number. No considerable effect on mass transfer  $J$ -factor  $J_{mf}$  evaluated at film temperature  $T_f$ , which is given in the next section, is observed. Also by comparing these tables with Tables (5-7 to 5-9) for 10 cm working electrode under isothermal conditions (zero heat flux) shows that mass transfer coefficient, Sherwood number, and Stanton number under heat transfer conditions are higher than those under isothermal conditions. While  $J$ -factor value remains close to its value under isothermal conditions.

## 5.7 Heat Transfer Calculations

The surface temperature of working electrode was measured by using four thermocouples located around the specimen, and the average values are listed in the tables. The heat transfer coefficient was calculated from Eq. (2.24) according to Newton's law of cooling:

$$h = \frac{q}{T_s - T_b} \quad (5.7)$$

Then the following heat transfer dimensionless groups were estimated as illustrated in Table 2-1:

$$\text{Prandtl No. : } \Pr = \frac{C_p \mu}{k} \quad (5.8)$$

$$\text{Nusselt No. : } \text{Nu} = \frac{h d_e}{k} \quad (5.9)$$

$$\text{Stanton No. : } \text{St}_h = \frac{\text{Nu}}{\text{Re Pr}} = \frac{h}{C_p \rho u} \quad (5.10)$$

$$\text{J-factor : } J_h = \text{St}_h \Pr^{2/3} \quad (5.11)$$

Film temperature is calculated by:

$$T_f = \frac{T_s + T_b}{2} \quad (5.12)$$

The physical properties required to perform the heat transfer calculations, i.e.,  $\mu$ ,  $\rho$ ,  $C_p$ ,  $k$ , and Pr are given in Appendix (C). The surface temperature results and heat transfer calculations are given in Tables 5-22 to 5-30.

Table 5-22 Surface temperature results and heat transfer calculations at  $T_b = 30^\circ\text{C}$  (Pr=5.448),  $L = 10\text{ cm}$ , and  $q=15\text{ kW/m}^2$ .

Re	$T_s, ^\circ\text{C}$	$T_f, ^\circ\text{C}$	$h, \text{W/m}^2 \cdot ^\circ\text{C}$	Nu	$\text{St}_h \times 10^3$	$J_h \times 10^3$
5000	37.6	33.8	1973.7	48.22	1.770	5.480
10000	34.6	32.3	3260.9	79.66	1.462	4.527
15000	33.4	31.7	4411.8	107.78	1.319	4.083
20000	32.7	31.4	5555.6	135.72	1.246	3.857

Table 5-23 Surface temperature results and heat transfer calculations at  $T_b = 30^\circ\text{C}$  (Pr=5.448),  $L = 10\text{ cm}$ , and  $q=30\text{ kW/m}^2$ .

Re	$T_s, ^\circ\text{C}$	$T_f, ^\circ\text{C}$	$h, \text{W/m}^2 \cdot ^\circ\text{C}$	Nu	$\text{St}_h \times 10^3$	$J_h \times 10^3$
5000	43.6	36.8	2205.9	53.89	1.978	6.125
10000	38.1	34.1	3703.7	90.48	1.661	5.142
15000	35.8	32.9	5172.4	126.36	1.546	4.788
20000	34.5	32.3	6666.7	162.87	1.495	4.628

Table 5-24 Surface temperature results and heat transfer calculations at  $T_b = 30^\circ\text{C}$  ( $\text{Pr}=5.448$ ),  $L = 10\text{ cm}$ , and  $q=45\text{ kW/m}^2$ .

Re	$T_s, ^\circ\text{C}$	$T_f, ^\circ\text{C}$	$h, \text{W/m}^2 \cdot ^\circ\text{C}$	Nu	$\text{St}_h \times 10^3$	$J_h \times 10^3$
5000	49.9	40.0	2261.3	55.24	2.028	6.279
10000	42.1	36.1	3719.0	90.86	1.668	5.163
15000	38.6	34.3	5232.6	127.83	1.564	4.843
20000	36.6	33.3	6818.2	166.57	1.529	4.733

Table 5-25 Surface temperature results and heat transfer calculations at  $T_b = 40^\circ\text{C}$  ( $\text{Pr}=4.369$ ),  $L = 10\text{ cm}$ , and  $q=15\text{ kW/m}^2$ .

Re	$T_s, ^\circ\text{C}$	$T_f, ^\circ\text{C}$	$h, \text{W/m}^2 \cdot ^\circ\text{C}$	Nu	$\text{St}_h \times 10^3$	$J_h \times 10^3$
5000	47.4	43.7	2027.0	48.49	2.220	5.933
10000	44.5	42.3	3333.3	79.74	1.825	4.878
15000	43.4	41.7	4411.8	105.54	1.611	4.304
20000	42.8	41.4	5357.1	128.16	1.467	3.920
25000	42.5	41.3	6000.0	143.54	1.314	3.512

Table 5-26 Surface temperature results and heat transfer calculations at  $T_b = 40^\circ\text{C}$  ( $\text{Pr}=4.369$ ),  $L = 10\text{ cm}$ , and  $q=30\text{ kW/m}^2$ .

Re	$T_s, ^\circ\text{C}$	$T_f, ^\circ\text{C}$	$h, \text{W/m}^2 \cdot ^\circ\text{C}$	Nu	$\text{St}_h \times 10^3$	$J_h \times 10^3$
5000	53.8	46.9	2173.9	52.01	2.381	6.363
10000	48.4	44.2	3571.4	85.44	1.956	5.226
15000	46.1	43.1	4918.0	117.66	1.795	4.798
20000	45.0	42.5	6000.0	143.54	1.643	4.390
25000	44.2	42.1	7142.9	170.88	1.564	4.181

Table 5-27 Surface temperature results and heat transfer calculations at  $T_b = 40^\circ\text{C}$  (Pr=4.369),  $L = 10$  cm, and  $q=45$  kW/m<sup>2</sup>.

Re	$T_s, ^\circ\text{C}$	$T_f, ^\circ\text{C}$	$h, \text{W/m}^2 \cdot ^\circ\text{C}$	Nu	$St_h \times 10^3$	$J_h \times 10^3$
5000	60.0	50.0	2250.0	53.83	2.464	6.585
10000	52.2	46.1	3688.5	88.24	2.020	5.398
15000	48.7	44.4	5172.4	123.74	1.888	5.046
20000	47.0	43.5	6428.6	153.79	1.760	4.704
25000	46.0	43.0	7500.0	179.43	1.643	4.390

Table 5-28 Surface temperature results and heat transfer calculations at  $T_b = 50^\circ\text{C}$  (Pr=3.586),  $L = 10$  cm, and  $q=15$  kW/m<sup>2</sup>.

Re	$T_s, ^\circ\text{C}$	$T_f, ^\circ\text{C}$	$h, \text{W/m}^2 \cdot ^\circ\text{C}$	Nu	$St_h \times 10^3$	$J_h \times 10^3$
5000	57.7	53.9	1948.1	45.66	2.546	5.966
10000	54.8	52.4	3125.0	73.24	2.042	4.785
15000	53.7	51.9	4054.1	95.02	1.766	4.138
20000	52.9	51.5	5172.4	121.23	1.690	3.960
25000	52.5	51.3	6000.0	140.63	1.569	3.675
30000	52.2	51.1	6818.2	159.80	1.485	3.480

Table 5-29 Surface temperature results and heat transfer calculations at  $T_b = 50^\circ\text{C}$  (Pr=3.586),  $L = 10$  cm, and  $q=30$  kW/m<sup>2</sup>.

Re	$T_s, ^\circ\text{C}$	$T_f, ^\circ\text{C}$	$h, \text{W/m}^2 \cdot ^\circ\text{C}$	Nu	$St_h \times 10^3$	$J_h \times 10^3$
5000	63.7	56.9	2189.8	51.32	2.862	6.706
10000	58.2	54.1	3658.5	85.75	2.391	5.602
15000	56.4	53.2	4687.5	109.86	2.042	4.785
20000	55.1	52.6	5882.4	137.87	1.922	4.504
25000	54.4	52.2	6818.2	159.80	1.783	4.176
30000	53.9	52.0	7692.3	180.29	1.676	3.926

Table 5-30 Surface temperature results and heat transfer calculations at  $T_b = 50^\circ\text{C}$  ( $\text{Pr}=3.586$ ),  $L = 10\text{ cm}$ , and  $q=45\text{ kW/m}^2$ .

Re	$T_s, ^\circ\text{C}$	$T_f, ^\circ\text{C}$	$h, \text{W/m}^2 \cdot ^\circ\text{C}$	Nu	$\text{St}_h \times 10^3$	$J_h \times 10^3$
5000	69.9	60.0	2261.3	53.00	2.956	6.925
10000	62.1	56.1	3719.0	87.16	2.431	5.695
15000	58.8	54.4	5113.6	119.85	2.228	5.220
20000	57.2	53.6	6250.0	146.48	2.042	4.785
25000	56.2	53.1	7258.1	170.11	1.898	4.446
30000	55.5	52.8	8181.8	191.76	1.783	4.176

From these Tables (5-22 to 5-30), the following can be observed:

- 1- At a particular heat flux and constant bulk temperature, increasing Reynolds number will decrease surface temperature, increase heat transfer coefficient and Nusselt number, and decrease Stanton number and heat transfer  $J$ -factor.
- 2- At a particular heat flux and constant Reynolds number, increasing bulk temperature will increase surface temperature, slightly decrease heat transfer coefficient and Nusselt number, increase Stanton number, and less increase in  $J$ -factor was observed.
- 3- At constant bulk temperature and Reynolds number, increasing heat flux will increase the surface temperature, heat transfer coefficient, Nusselt number, Stanton number, and  $J$ -factor.

## 5.8 Corrosion Fouling Results

During corrosion fouling experiments, the surface temperature was measured using four thermocouples, and the limiting current density and corrosion potential values were obtained from cathodic polarization curve. At the beginning of fouling experiments, the surface temperature and polarization data were recorded every (4-8) hours up to two days, and then

every (14-20) hours were recorded. The reason of that is at the beginning there is a rapid increase of fouling effects with time. Each experiment lasted 200 hours (8.33 days) continuously, in which the effect of 0.1 N NaCl solution on 10 cm carbon steel pipe under heat flux ( $q=15 \text{ kW/m}^2$ ) was studied.

The results of five experiments are shown in Tables 5-31 to 5-35. In these tables the average surface temperature  $T_s$  of four thermocouple readings, the increase in surface temperature with respect to initial value at  $t=0$  ( $T_s - T_{s,0}$ ), heat transfer coefficient  $h$ , fouling thermal resistance  $R_f$ , limiting current density  $i_L$ , mass transfer coefficient  $k_m$ , and corrosion potential  $E_{\text{corr}}$  are listed.  $h$  is calculated using Eq. (5.7),  $R_f$  using Eq. (3.50), and  $k_m$  is calculated using Eq. (5.2).

Table 5-31 Corrosion fouling results at  $\text{Re} = 5000$ ,  $T_b = 30^\circ \text{C}$ ,  $L = 10 \text{ cm}$ , and  $q=15 \text{ kW/m}^2$ .

$t$ hr	$T_s$ $^\circ \text{C}$	$T_s - T_{s,0}$ $^\circ \text{C}$	$h$ $\text{W/m}^2 \text{ }^\circ \text{C}$	$R_f \times 10^4$ $\text{m}^2 \text{ }^\circ \text{C/W}$	$i_L$ $\mu \text{A/cm}^2$	$k_m \times 10^5$ m/s	$E_{\text{corr}}$ , mV (vs. SCE)
0	37.6	0.0	1973.7	0.00	250.5	2.77	-555
4	37.9	0.3	1898.7	0.20	164.0	1.81	-610
11	38.7	1.1	1724.1	0.73	138.5	1.53	-650
17	39.3	1.7	1612.9	1.13	125.5	1.39	-671
24	39.9	2.3	1515.2	1.53	115.0	1.27	-683
31	40.1	2.5	1485.1	1.67	110.0	1.22	-685
37	40.2	2.6	1470.6	1.73	108.0	1.19	-691
48	40.3	2.7	1456.3	1.80	106.0	1.17	-725
58	40.5	2.9	1428.6	1.93	104.0	1.15	-739
67	40.6	3.0	1415.1	2.00	103.5	1.14	-760
80	40.9	3.3	1376.1	2.20	100.0	1.11	-771
100	41.1	3.5	1351.4	2.33	98.0	1.08	-774
120	41.2	3.6	1339.3	2.40	95.0	1.05	-774
140	41.4	3.8	1315.8	2.53	94.0	1.04	-776
160	41.5	3.9	1304.3	2.60	94.0	1.04	-778
180	41.6	4.0	1293.1	2.67	91.0	1.01	-780
200	41.6	4.0	1293.1	2.67	90.0	0.99	-780

Table 5-32 Corrosion fouling results at  $Re = 10000$ ,  $T_b = 30^\circ C$ ,  $L = 10$  cm,  
and  $q=15$  kW/m<sup>2</sup>.

$t$ hr	$T_s$ °C	$T_s - T_{s,0}$ °C	$h$ W/m <sup>2</sup> °C	$R_f \times 10^4$ m <sup>2</sup> °C/W	$i_L$ μA/cm <sup>2</sup>	$k_m \times 10^5$ m/s	$E_{corr}$ , mV (vs. SCE)
0	34.6	0.0	3260.9	0.00	359.5	3.97	-530
6	34.9	0.3	3061.2	0.20	239.5	2.65	-567
11	35.5	0.9	2727.3	0.60	215.0	2.38	-618
18	35.9	1.3	2542.4	0.87	193.0	2.13	-621
25	36.4	1.8	2343.8	1.20	183.0	2.02	-668
32	36.9	2.3	2173.9	1.53	176.0	1.95	-663
48	37.1	2.5	2112.7	1.67	171.0	1.89	-681
68	37.4	2.8	2027.0	1.87	169.0	1.87	-701
80	37.6	3.0	1973.7	2.00	164.5	1.82	-710
100	37.8	3.2	1923.1	2.13	162.0	1.79	-721
120	38.0	3.4	1875.0	2.27	159.0	1.76	-725
140	38.1	3.5	1851.9	2.33	154.0	1.70	-730
160	38.2	3.6	1829.3	2.40	150.0	1.66	-730
180	38.3	3.7	1807.2	2.47	148.0	1.64	-733
200	38.4	3.8	1785.7	2.53	147.0	1.63	-736

Table 5-33 Corrosion fouling results at  $Re = 15000$ ,  $T_b = 30^\circ C$ ,  $L = 10$  cm,  
and  $q=15$  kW/m<sup>2</sup>.

$t$ hr	$T_s$ °C	$T_s - T_{s,0}$ °C	$h$ W/m <sup>2</sup> °C	$R_f \times 10^4$ m <sup>2</sup> °C/W	$i_L$ μA/cm <sup>2</sup>	$k_m \times 10^5$ m/s	$E_{corr}$ , mV (vs. SCE)
0	33.4	0.0	4411.8	0.00	392.0	4.33	-501
5	33.6	0.2	4166.7	0.13	291.0	3.22	-550
10	34.0	0.6	3750.0	0.40	264.0	2.92	-585
18	34.4	1.0	3409.1	0.67	239.0	2.64	-592
27	35.1	1.7	2941.2	1.13	225.5	2.49	-606
32	35.2	1.8	2884.6	1.20	218.0	2.41	-647
48	35.8	2.4	2586.2	1.60	212.0	2.34	-653
68	36.2	2.8	2419.4	1.87	201.0	2.22	-659
80	36.3	2.9	2381.0	1.93	198.5	2.19	-662
105	36.5	3.1	2307.7	2.07	193.5	2.14	-679
120	36.6	3.2	2272.7	2.13	190.0	2.10	-679
140	36.7	3.3	2238.8	2.20	189.0	2.09	-688
170	36.7	3.3	2238.8	2.20	186.0	2.06	-690
180	36.8	3.4	2205.9	2.27	182.0	2.01	-690
200	36.8	3.4	2205.9	2.27	181.0	2.00	-691

Table 5-34 Corrosion fouling results at  $Re = 15000$ ,  $T_b = 40^\circ C$ ,  $L = 10$  cm,  
and  $q=15$  kW/m<sup>2</sup>.

$t$ hr	$T_s$ °C	$T_s - T_{s,0}$ °C	$h$ W/m <sup>2</sup> °C	$R_f \times 10^4$ m <sup>2</sup> °C/W	$i_L$ μA/cm <sup>2</sup>	$k_m \times 10^5$ m/s	$E_{corr}$ , mV (vs. SCE)
0	43.4	0.0	4411.8	0.00	348.0	4.54	-563
4	43.6	0.2	4166.7	0.13	275.0	3.59	-599
8	43.8	0.4	3947.4	0.27	252.0	3.29	-630
12	44.0	0.6	3750.0	0.40	232.0	3.03	-640
18	44.2	0.8	3571.4	0.53	223.0	2.91	-666
26	44.8	1.4	3125.0	0.93	210.0	2.74	-681
34	45.3	1.9	2830.2	1.27	202.0	2.64	-692
50	45.8	2.4	2586.2	1.60	197.0	2.57	-715
66	46.0	2.6	2500.0	1.73	192.0	2.51	-735
82	46.2	2.8	2419.4	1.87	185.0	2.42	-750
100	46.3	2.9	2381.0	1.93	180.0	2.35	-769
114	46.5	3.1	2307.7	2.07	176.0	2.30	-773
122	46.5	3.1	2307.7	2.07	175.0	2.28	-778
140	46.6	3.2	2272.7	2.13	174.0	2.27	-781
164	46.6	3.2	2272.7	2.13	173.0	2.26	-785
180	46.7	3.3	2238.8	2.20	172.0	2.25	-786
200	46.7	3.3	2238.8	2.20	170.0	2.22	-786

Table 5-35 Corrosion fouling results at  $Re = 15000$ ,  $T_b = 50^\circ C$ ,  $L = 10$  cm,  
and  $q=15$  kW/m<sup>2</sup>.

$t$ hr	$T_s$ °C	$T_s - T_{s,0}$ °C	$h$ W/m <sup>2</sup> °C	$R_f \times 10^4$ m <sup>2</sup> °C/W	$i_L$ μA/cm <sup>2</sup>	$k_m \times 10^5$ m/s	$E_{corr}$ , mV (vs. SCE)
0	53.7	0.0	4054.1	0.00	324.5	4.80	-589
5	53.9	0.2	3846.2	0.13	259.0	3.83	-631
10	54.1	0.4	3658.5	0.27	239.0	3.54	-659
16	54.3	0.6	3488.4	0.40	218.0	3.23	-678
24	54.6	0.9	3260.9	0.60	207.0	3.06	-696
30	55.0	1.3	3000.0	0.87	195.5	2.89	-720
40	55.6	1.9	2678.6	1.27	189.0	2.80	-731
56	56.0	2.3	2500.0	1.53	184.0	2.72	-744
80	56.3	2.6	2381.0	1.73	178.0	2.64	-781
98	56.4	2.7	2343.8	1.80	174.0	2.58	-788
120	56.6	2.9	2272.7	1.93	170.0	2.52	-790
142	56.7	3.0	2238.8	2.00	169.0	2.50	-793

Table 5-35 Continued

$t$ hr	$T_s$ °C	$T_s - T_{s,0}$ °C	$h$ W/m <sup>2</sup> °C	$R_f \times 10^4$ m <sup>2</sup> °C/W	$i_L$ μA/cm <sup>2</sup>	$k_m \times 10^5$ m/s	$E_{\text{corr}}$ , mV (vs. SCE)
160	56.8	3.1	2205.9	2.07	168.0	2.49	-797
182	56.8	3.1	2205.9	2.07	167.0	2.47	-801
200	56.8	3.1	2205.9	2.07	167.0	2.47	-803

From the tables above, the following can be concluded:

- 1- The surface temperature  $T_s$ ,  $(T_s - T_{s,0})$ , and  $R_f$  increase with time, while limiting current density  $i_L$ , heat transfer coefficient  $h$ , and mass transfer coefficient  $k_m$  decrease, and corrosion potential  $E_{\text{corr}}$  shifts to more negative values.
- 2- At constant bulk temperature, increasing Reynolds number leads to decrease  $T_s$ ,  $(T_s - T_{s,0})$ , and  $R_f$ , increase in  $i_L$ ,  $h$ ,  $k_m$ , and corrosion potential (less negative) at all times.
- 3- At constant Reynolds number, increasing bulk temperature leads to increase  $T_s$  and  $k_m$ , decrease  $(T_s - T_{s,0})$ ,  $h$ ,  $R_f$ ,  $i_L$ , and corrosion potential (more negative) at all times.

Figures 5-11 and 5-12 show the increase in surface temperature and the decrease in limiting current density with time.

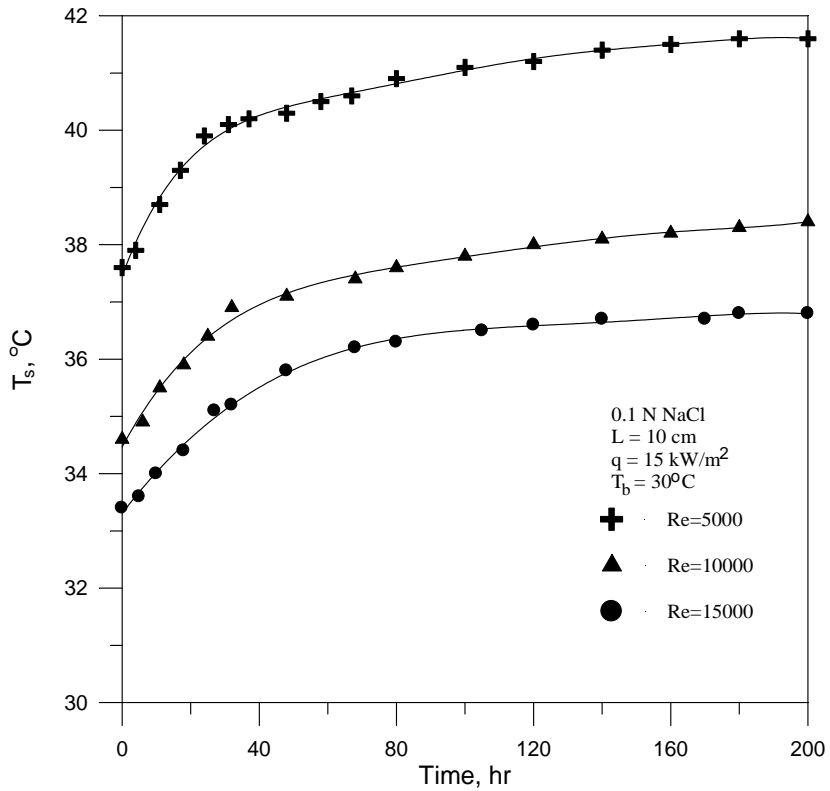


**Figure 5-11** Variation of surface temperature with time.

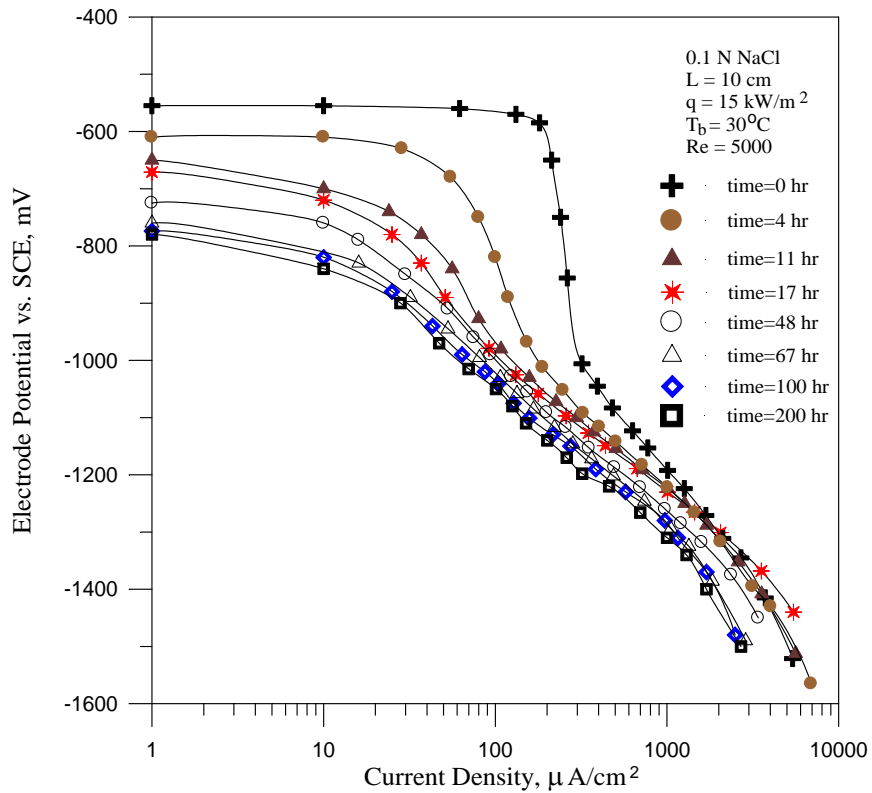


**Figure 5-12** Variation of cathodic polarization curve with time.

# **CHAPTER SIX**

## **DISCUSSION**

## **6.1 Introduction**

Chapter five presented the effect of velocity, bulk temperature, electrode length, and heat flux on limiting current density, corrosion potential, mass and heat transfer dimensionless groups, and on corrosion fouling. The behavior of carbon steel under the influence of these variables will be discussed in details in this chapter.

A number of correlations for heat and mass transfer are presented in this chapter that relate the experimental data obtained by the present work. Also a comparison was made between these correlations and the others that are found in the literature for annular flow in concentric tube heat exchanger.

During this chapter, it is hoped to present satisfactory explanations giving further insight into the role of the corrosion products that deposit on heat transfer surfaces and their effect on heat and mass transfer processes.

## **6.2 Cathodic Polarization Region Under Isothermal Conditions**

### **6.2.1 Effect of Reynolds Number**

It is shown in Figs. 6-1 and 6-2 for isothermal conditions that increasing Reynolds number (or velocity) at constant bulk temperature tends to increase the limiting current density for working electrode lengths of 3 and 10 cm respectively.

This behavior is consistent with the fact that velocity increases the corrosion rate if the process is under concentration polarization. This behavior is anticipated as the increasing in velocity (or Re) past the metal surface tends to decrease the thickness of diffusion boundary layer  $\delta_d$  (viscous layer adjacent to metal surface) [22, 25, 26, 53], and thus increase the diffusion and corrosion rates according to Eq. (3.9):

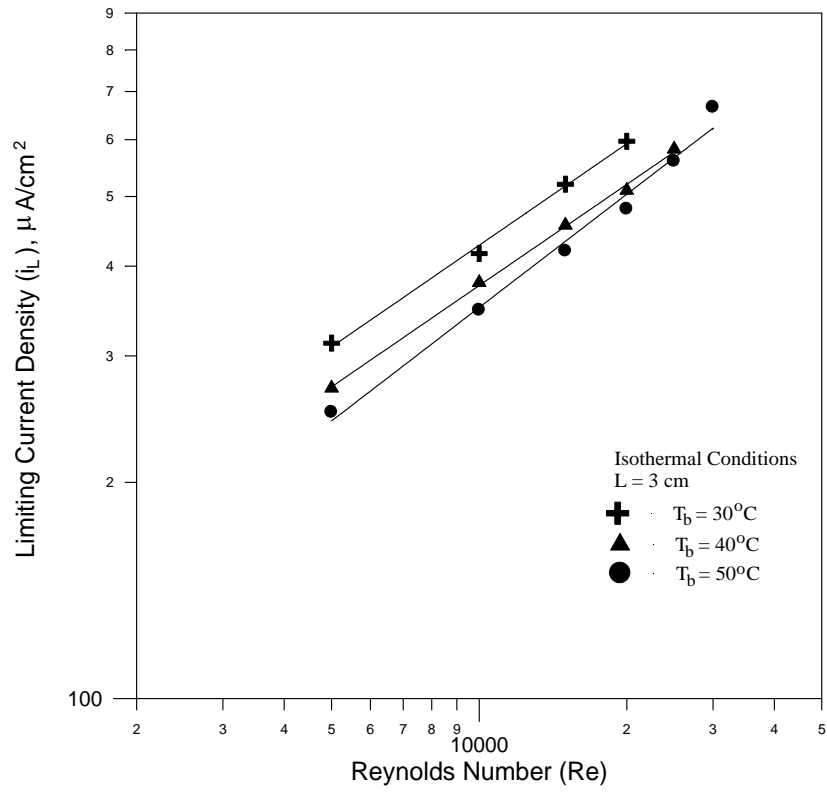


**Figure 6-1** Variation of limiting current density with Re for  $L=3$  cm under isothermal conditions.

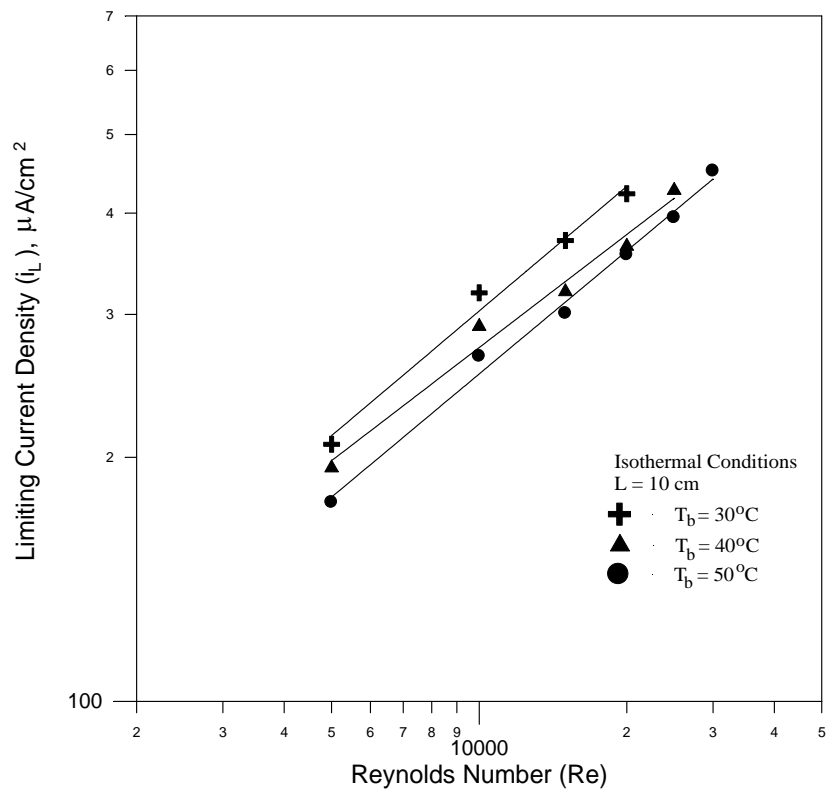


**Figure 6-2** Variation of limiting current density with Re for  $L=10$  cm under isothermal conditions.

$$i_L = \frac{zFDC_b}{\delta_d} \quad (3.9)$$

in which the limiting current (corrosion rate) is inversely proportional to the diffusion layer thickness. This means that increasing velocity (or Re) facilitates the passage of oxygen from the bulk of the solution through the diffusion boundary layer to the metal surface and increases the corrosion rate.

Figure 6-3 aids to understand the effect of Reynolds number on corrosion of carbon steel with diffusion controlled cathodic oxygen reduction. The limiting current density  $i_L$  is the most significant parameter in a corrosion reaction in which oxygen is the cathodic reactant and that any factor that increases  $i_L$ , as in this case velocity, will increase the corrosion rate, since:

$$i_{\text{corr}} = i_L \quad \text{at } E_{\text{corr}} \quad (3.33)$$

Figures 6-4 and 6-5 for working electrode lengths of 3 and 10 cm respectively show that the corrosion potential becomes less negative (or more noble) with increasing velocity (or Re) at a particular bulk temperature under isothermal conditions, and a linear relation exists between corrosion potential and Reynolds number.

Also this behavior can be understood with the aid of Fig. 6-3. The corrosion potential of carbon steel in neutral media is determined from the rate of anodic dissolution (mass transfer independent process) and the rate of cathodic reduction of oxygen (mass transfer process). So as the velocity or Reynolds number increases, the limiting current density increases shifting the intersection point (corrosion potential  $E_{\text{corr}}$ ) between the cathodic oxygen reduction curve and anodic iron dissolution curve to more positive potential value. This behavior was observed by many investigators [26, 53, 61, 98].

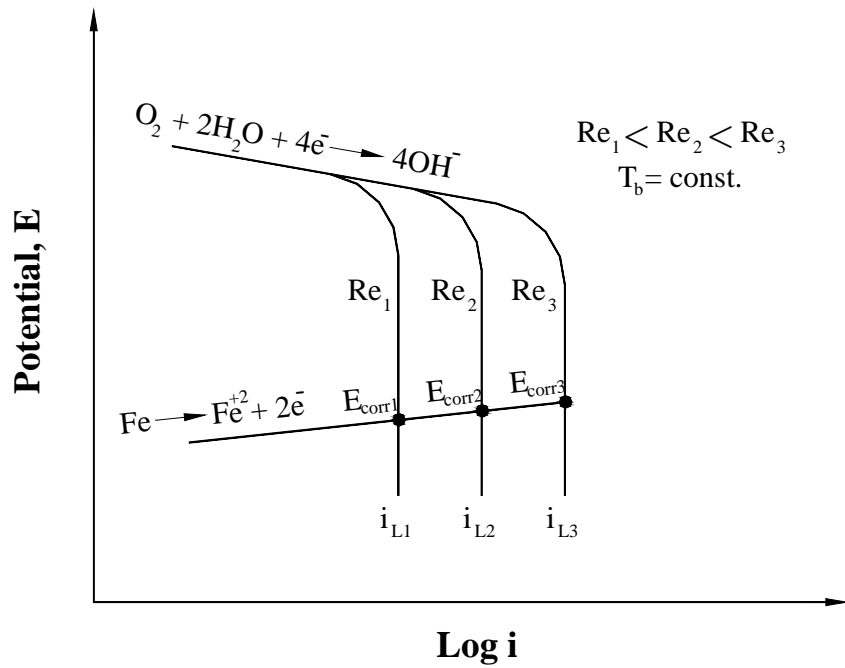


Figure 6-3 The effect of Reynolds number on corrosion of carbon steel.

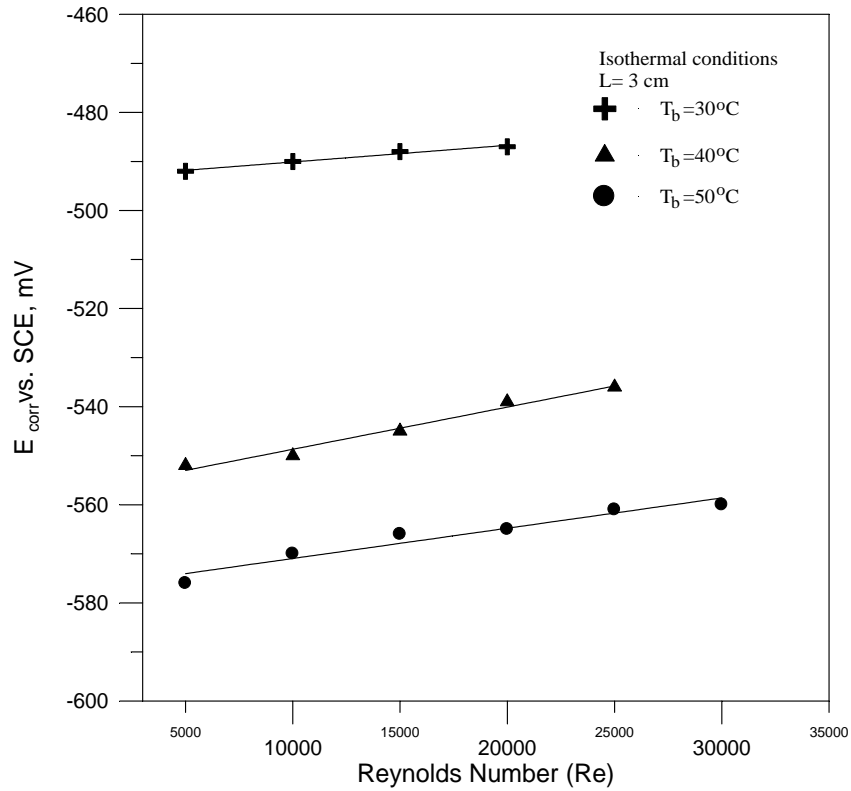
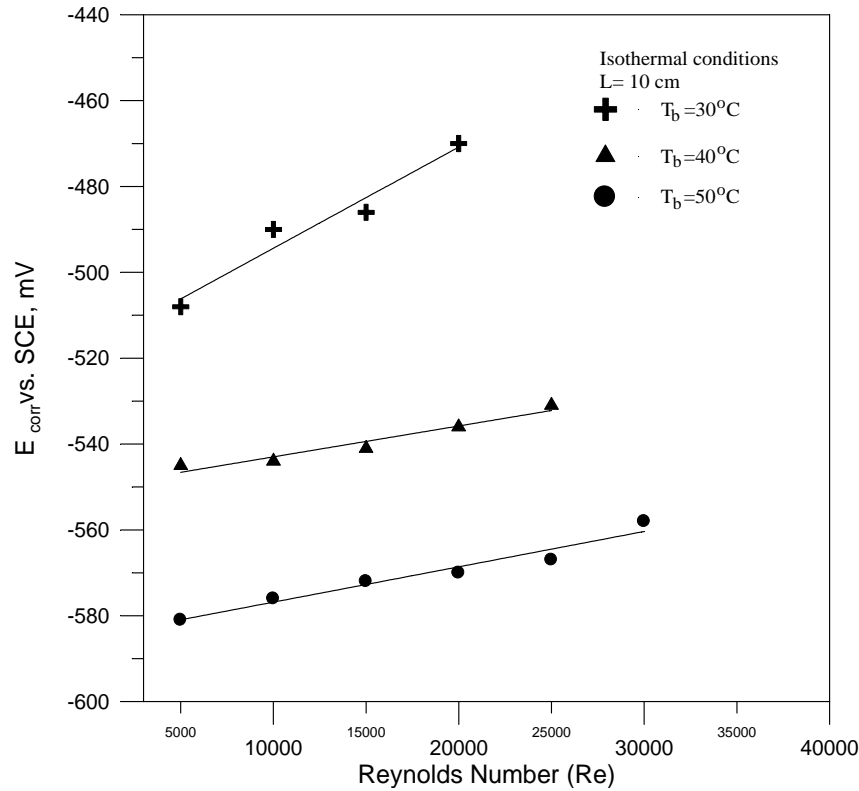


Figure 6-4 Variation of corrosion potential with Re for  $L=3$  cm under isothermal conditions.



**Figure 6-5** Variation of corrosion potential with Re for  $L=10$  cm under isothermal conditions.

### 6.2.2 Effect of Bulk Temperature

The effect of bulk temperature on limiting current density  $i_L$  for working electrode lengths of 3 and 10 cm under isothermal conditions are shown in Figs. 6-6 and 6-7 respectively. From these figures, it can be observed that the limiting current density decreases with increasing bulk temperature at a specified Reynolds number.

Upon studying the effect of temperature on limiting current density (or corrosion rate), various situations have to be taken into account which usually act in a conflicting way and as follows:

- 1- Increasing temperature is accompanied by an increase in diffusion coefficient of oxygen  $D$ , see Appendix (C.4), and this leads to increase

the diffusion rate of oxygen and increase the limiting current density according to Eq. (3.9).

- 2- Increasing temperature, decreases the oxygen solubility (oxygen concentration)  $C_b$  in the solution, see Appendix (C.3), and this leads to decrease the limiting current density according to Eq. (3.9).
- 3- Increasing temperature at constant Reynolds number, leads to decrease the quantity (or flow rate) of solution passes to working electrode. For example at  $Re = 5000$ , and  $T_b=30, 40, \text{ and } 50 \text{ }^\circ\text{C}$  the flowrates are 622, 511, and 430 l/hr respectively. As explained in section 6.2.1, this leads to increase the diffusion layer thickness  $\delta_d$ , so the limiting current density decreases according to Eq. (3.9).

Points 2 and 3 mentioned above are predominant with respect to point 1, hence the limiting current and corrosion rate decrease with increasing bulk temperature at constant Reynolds number. This decrease in corrosion rate was observed by other investigators [63, 64].

Also it is observed in Figs. 6-4 and 6-5 or Tables 5-1 to 5-3, that the corrosion potential shifts to less noble (more negative) value with increasing bulk temperature.

This behavior can be explained with the aid of Fig. 6-8. Corrosion potential values  $E_{\text{corr}}$  obey the mixed potential theory, i.e., they are affected by both anodic and cathodic processes. The anodic (activation controlled) is stimulated by increasing bulk temperature to a greater extent [25], in comparison to that of cathodic (concentration controlled) process, which shows a decrease in limiting current. This will lead to a fall in  $E_{\text{corr}}$  with increasing bulk temperature.

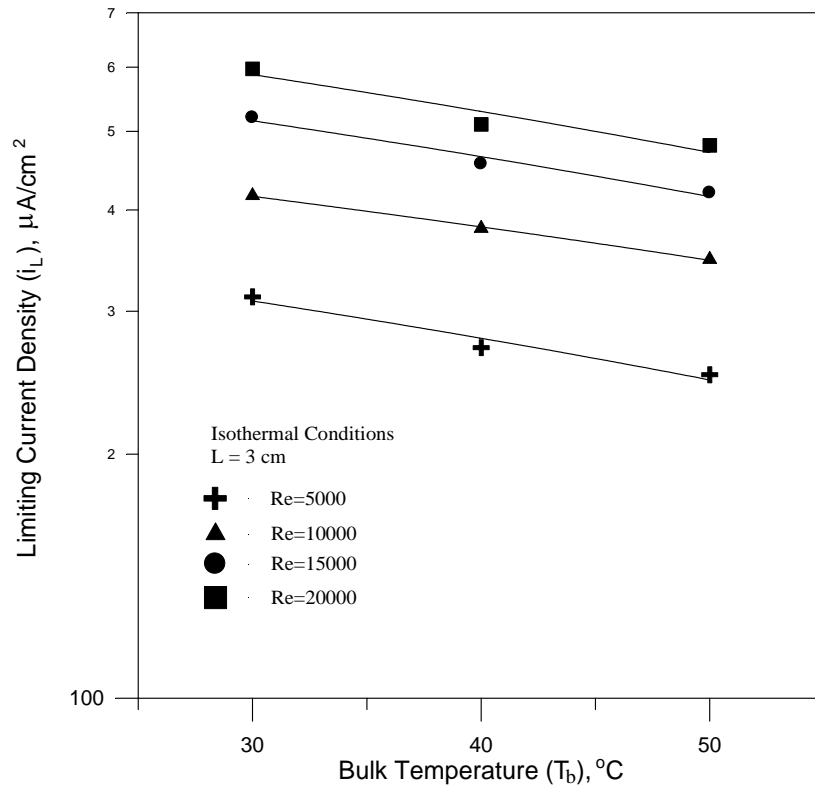


**Figure 6-6** Variation of limiting current density with bulk temperature for  $L=3$  cm under isothermal conditions.

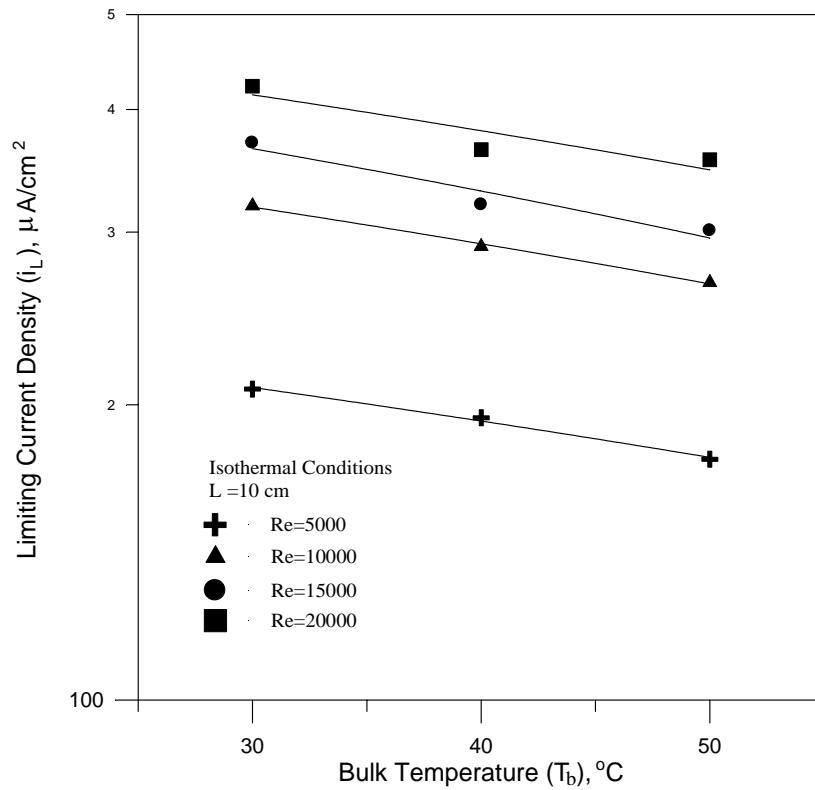


**Figure 6-7** Variation of limiting current density with bulk temperature for  $L=10$  cm under isothermal conditions.

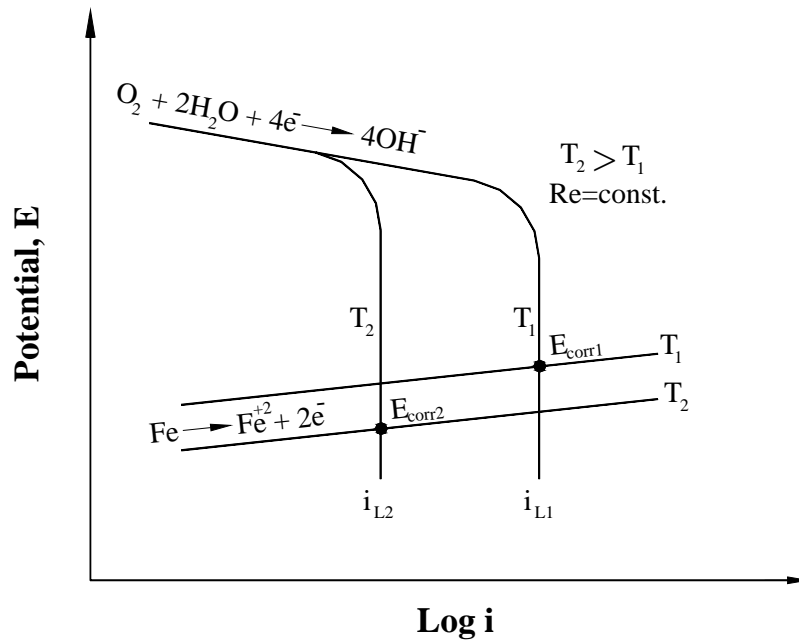


**Figure 6-8** The effect of bulk temperature on corrosion of carbon steel.

### 6.2.3 Effect of Working Electrode Length

The limiting current density  $i_L$  of oxygen reduction decreases with increasing working electrode length from 3 to 10 cm for a particular bulk temperature under isothermal conditions as shown in Figs. 6-9 to 6-11.

The mass transfer rate tends to an infinite value at the upstream edge of the working electrode (corresponding to zero mass transfer boundary layer thickness) where fresh solution is brought in contact with the electrode, then the mass transfer rate decreases with increasing distance along the electrode since the solution in the diffusion layer has been depleted by the electrode reaction further upstream.

It will be remembered that the velocity profile was fully developed before entering to the cathode electrode and the decrease in mass transfer rate is therefore due only to the developing concentration boundary layer.

At 3 cm working electrode length ( $L/d_e=2$ ) the mass transfer boundary layer thickness is small because at this length the mass transfer region was not fully developed (in the mass transfer entry region), and according to Eq. (3.9) the smaller mass transfer boundary layer thickness  $\delta_d$  the greater limiting current and corrosion rate. While at 10 cm working electrode length ( $L/d_e=6.7$ ) the concentration boundary layer was fully developed and its thickness is greater than that at 3 cm working electrode length, so the limiting current will be smaller.

Von Shaw et al. [99] indicated that mass transfer entry region length in circular tubes ranges from 2 diameters (i.e.  $L/d=2$ ) to 0.5 as the Reynolds number ranges from 5000 to 75000. Beyond this short entry region, the mass transfer rate approaches a constant value corresponding to fully developed mass transfer and becomes independent of the transfer length. Berger and Hau [92] found that the distance from the entrance where Stanton number reaches a value of 5% higher than the asymptotic one to vary from  $L/d = 5$  for  $Re=10000$  to  $L/d = 1$  for  $Re=100000$ .

The effect of working electrode length on corrosion potential  $E_{\text{corr}}$  can be deduced from Tables 5-1 to 5-3. At constant bulk temperature and Reynolds number, the increase in working electrode length from 3 to 10 cm has slight effect on corrosion potential value.

The influence of electrode length on corrosion potential can be explained with the aid of Fig. 6-12, i.e. with the aid of mixed potential theory. Increasing electrode length yields to decrease the oxygen reduction process and iron dissolution process, so the corrosion potentials will be approximately within similar potential range for 3 and 10 cm electrode length.

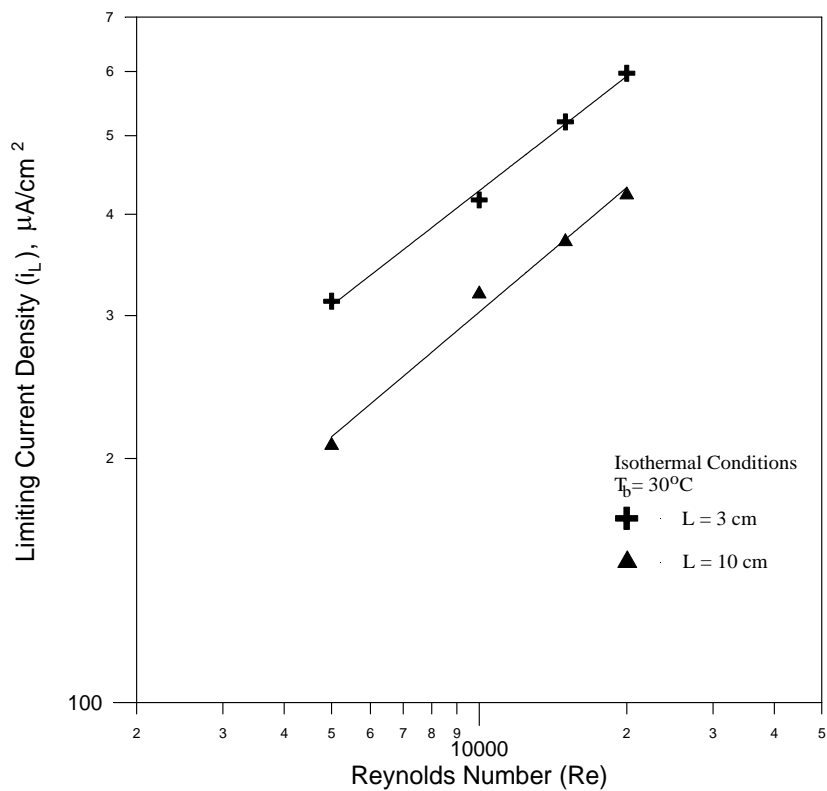


**Figure 6-9** Effect of working electrode length on limiting current density at  $T_b = 30^\circ\text{C}$  under isothermal conditions.

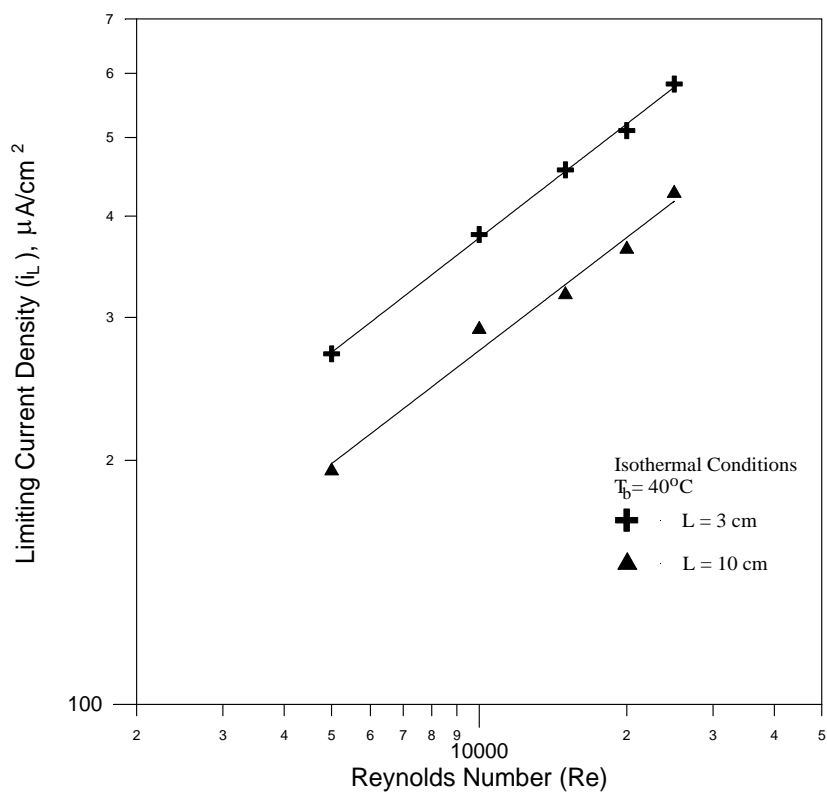


**Figure 6-10** Effect of working electrode length on limiting current density at  $T_b = 40^\circ\text{C}$  under isothermal conditions.

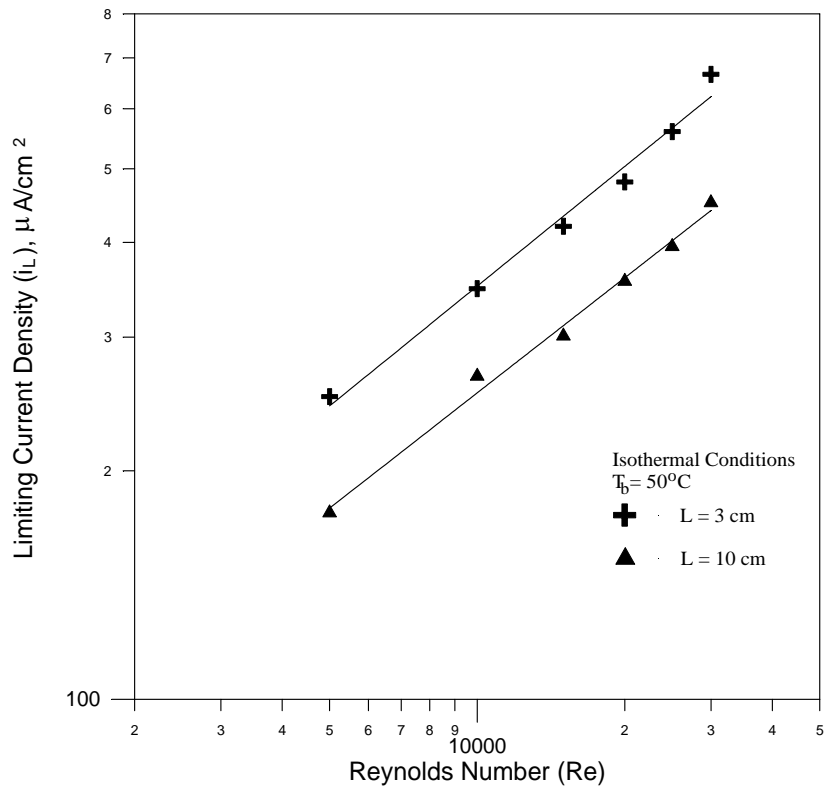


**Figure 6-11** Effect of working electrode length on limiting current density at  $T_b = 50^\circ\text{C}$  under isothermal conditions.

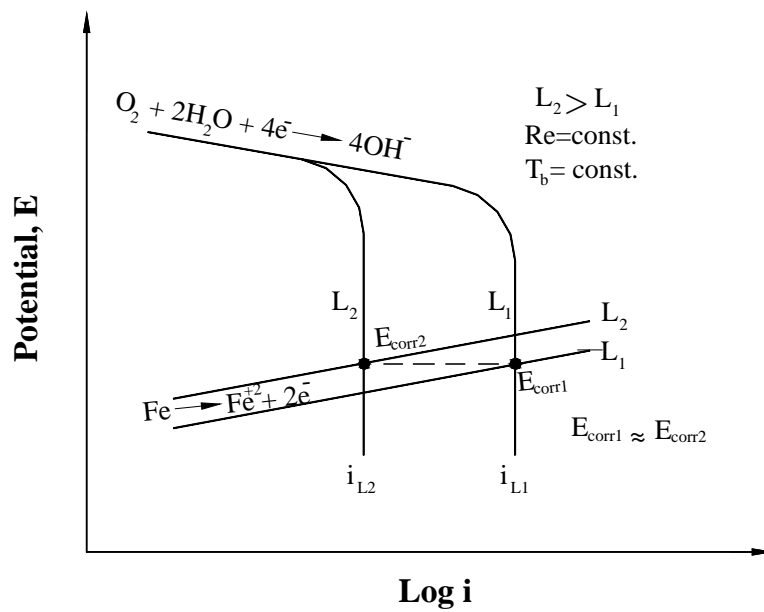


**Figure 6-12** The effect of working electrode length on corrosion of carbon steel.

## 6.3 Mass Transfer Data Under Isothermal Conditions

### 6.3.1 Effect of Reynolds Number

It is worthy here to observe the effect of Reynolds number (or velocity) on mass transfer data. From Tables 5-4 to 5-9 or Figs. 6-13 and 6-14 it can be noticed that increasing Reynolds number increases the mass transfer coefficient  $k_m$ . The increase in  $k_m$  can be explained due to the fact that increasing turbulence with increasing Reynolds number leads to decrease the thickness of the diffusion boundary layer  $\delta_d$  and hence  $k_m$  increases according to Eq. (3.14):

$$k_m = \frac{D}{\delta_d} \quad (3.14)$$

An increase in  $k_m$  with Re at a particular bulk temperature (a particular Schmidt number Sc) will tend to increase Sherwood number Sh according to Eq. (5.4), and as shown in Figs. 6-15 and 6-16 for working electrode lengths of 3 and 10 cm respectively. This means that an increase in Sh can also be attributed to the decrease in diffusion boundary layer with Re increase.

The variation of Stanton number  $St_m$  with Re is shown in Figs. 6-17 and 6-18. It is obvious that  $St_m$  decreases with increase in Re for all temperatures. Increasing Re is accompanied by an increase in mass transfer coefficient  $k_m$  and average velocity  $u$ , but the increase in average velocity is higher than the increase in mass transfer coefficient. Hence Stanton number will decrease according to Eq. (5.5) [30, 92].

Also since the Schmidt number Sc is constant at a particular temperature, the mass transfer  $J$ -factor  $J_m$  calculated by Eq. (5.6) will decrease with increase in Re as shown in Figs. 6-19 and 6-20. This is in accordance with the usual trend of  $J_m$  with Re [19, 29, 30, 100].

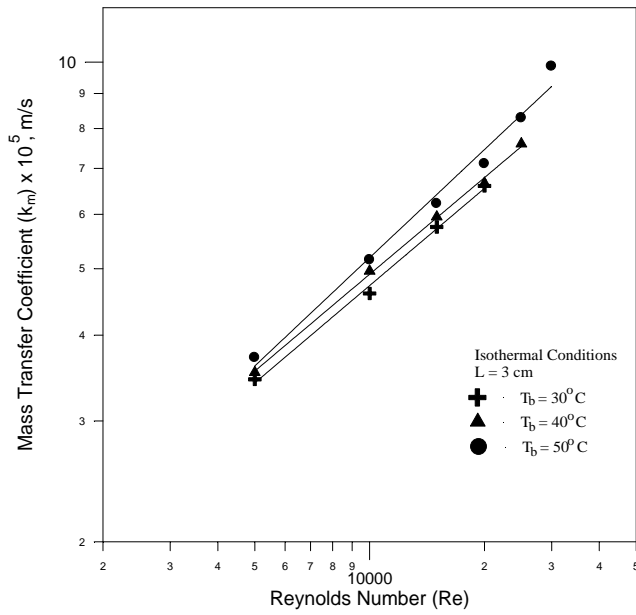


**Figure 6-13** Variation of mass transfer coefficient with  $Re$  for  $L=3 \text{ cm}$ .

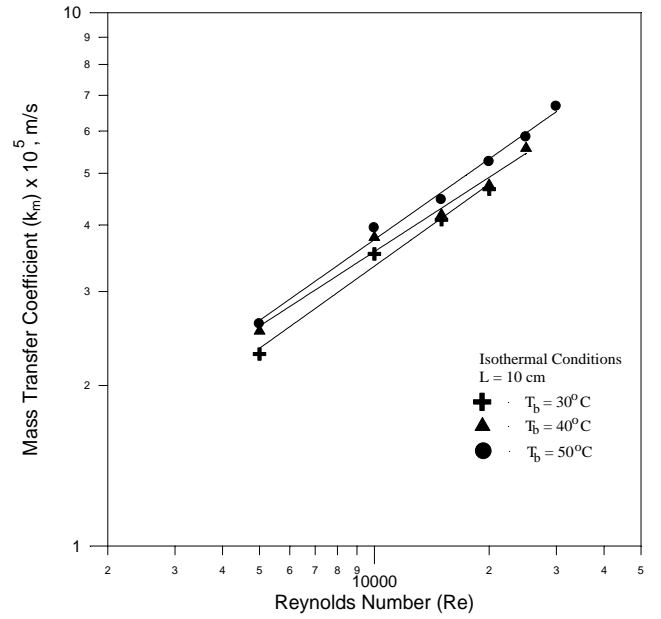


**Figure 6-14** Variation of mass transfer coefficient with  $Re$  for  $L=10 \text{ cm}$ .

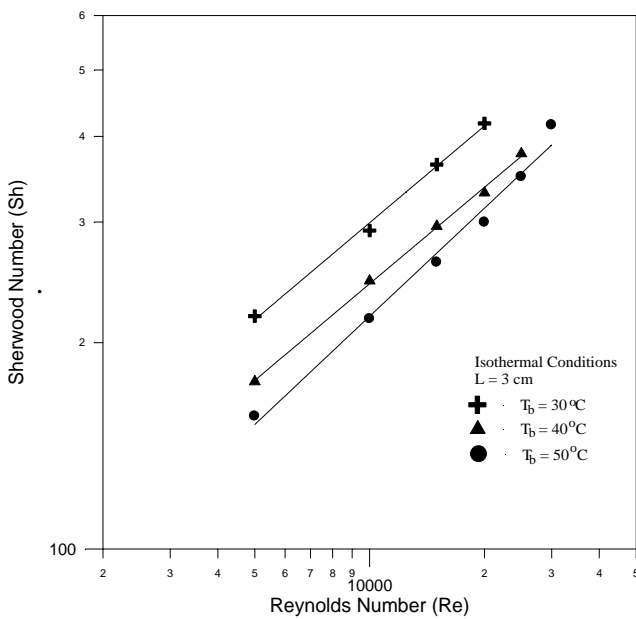


**Figure 6-15** Variation of Sherwood number with  $Re$  for  $L=10 \text{ cm}$ .

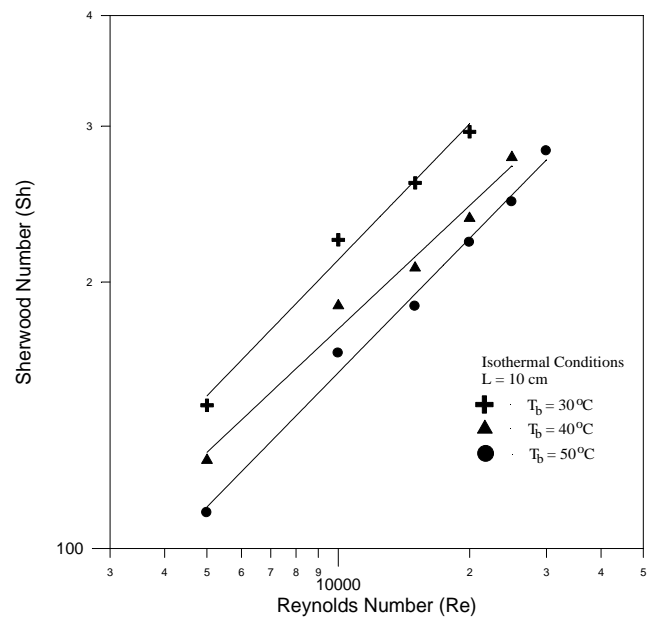


**Figure 6-16** Variation of Sherwood number with  $Re$  for  $L=10 \text{ cm}$ .

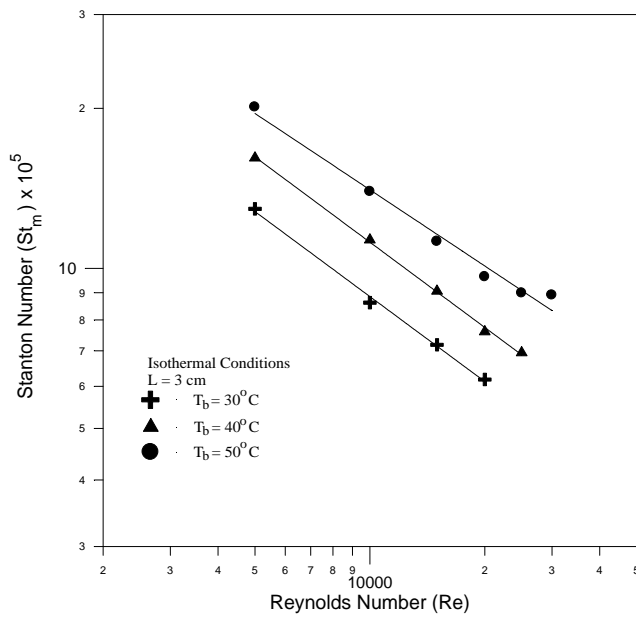


**Figure 6-17** Variation of Stanton number with  $Re$  for  $L=3$  cm.

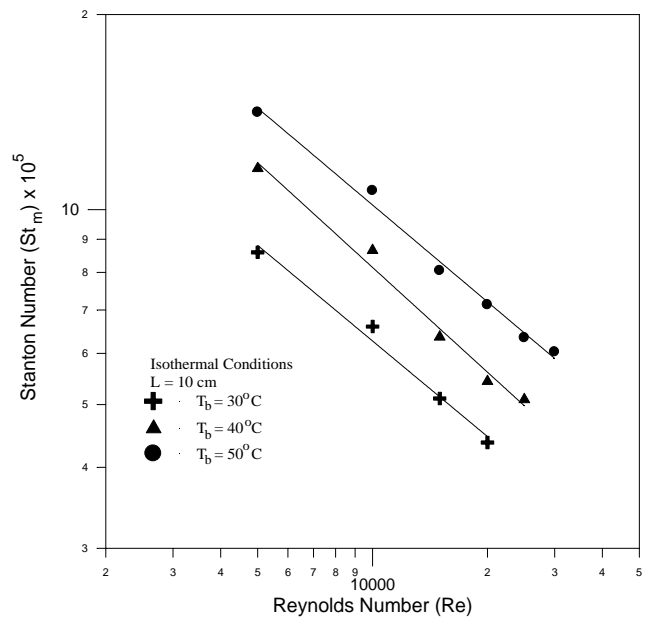


**Figure 6-18** Variation of Stanton number with  $Re$  for  $L=10$  cm.

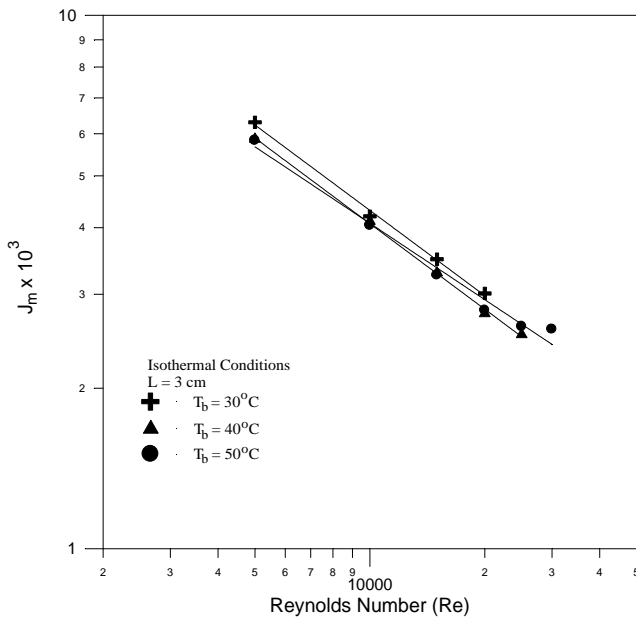


**Figure 6-19** Variation of  $J_m$ -factor with  $Re$  for  $L=3$  cm.

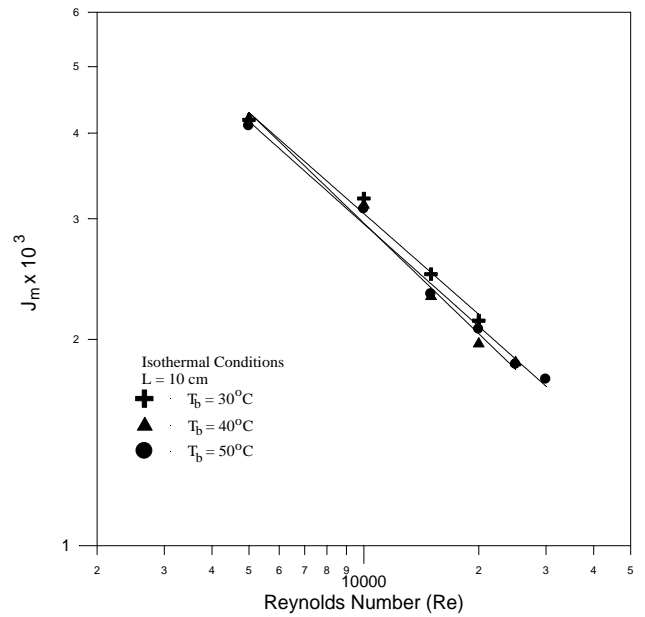


**Figure 6-20** Variation of  $J_m$ -factor with  $Re$  for  $L=10$  cm.

### 6.3.2 Effect of Bulk Temperature

Increasing bulk temperature increases the diffusion coefficient of oxygen  $D$  and also increases the diffusion layer thickness  $\delta_d$  (as illustrated in section 6.2.2), and these two factors determine the value of mass transfer coefficient  $k_m$  according to Eq. (3.14). So the increase in  $k_m$  with increasing bulk temperature at constant Reynolds number can be interpreted as that the increase in  $D$  is higher than the accompanied increase in  $\delta_d$ .

From Eqs. (3.14) and (5.4) for  $k_m$  and Sh respectively, it can be obtained:

$$\text{Sh} = \frac{d_e}{\delta_d} \quad (6.1)$$

Hence Sherwood number decreases with increasing bulk temperature via increasing diffusion boundary layer  $\delta_d$ . While the value of Stanton number  $St_m$  at particular Reynolds number increases with increasing bulk temperature via increasing of mass transfer coefficient and decreasing average velocity. Simultaneous increase in Stanton number and decrease in Schmidt number yields no considerable effect on  $J$ -factor for mass transfer.

### 6.3.3 Effect of Working Electrode Length

As previously mentioned in section (6.2.3) that increasing electrode length from 3 to 10 cm leads to developing concentration boundary layer and to increase its thickness, so the mass transfer coefficient, Sherwood number, Stanton number, and  $J$ -factor for mass transfer decrease when comparison is made at the same bulk temperature and Reynolds number as shown in Tables 5-4 to 5-9 or Figs. 6-21 and 6-22.

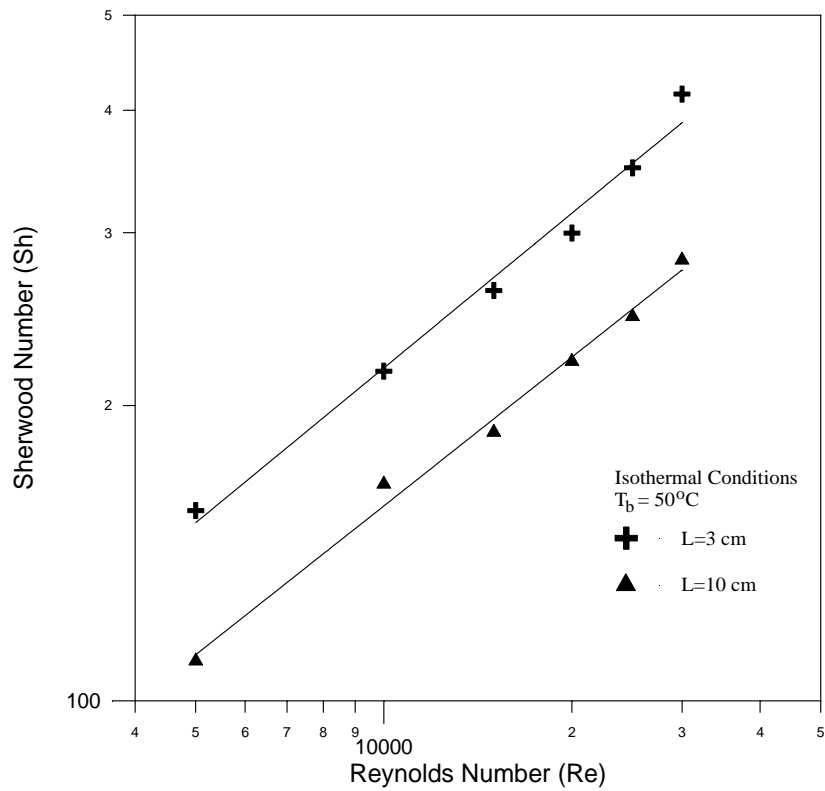


**Figure 6-21** Effect of working electrode length on Sherwood number at  $T_b = 50^\circ\text{C}$  under isothermal conditions.

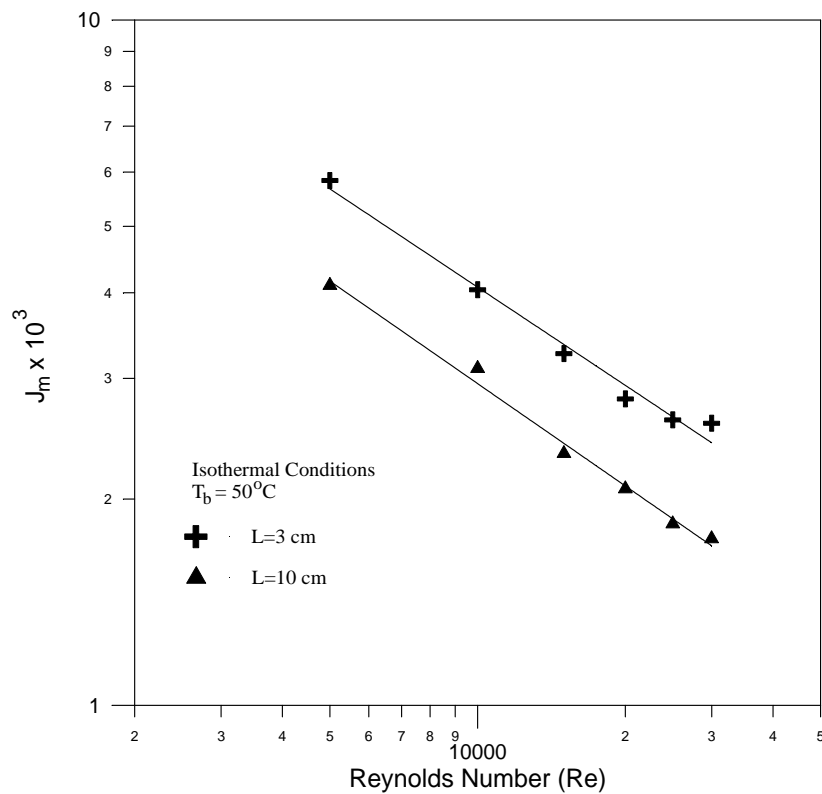


**Figure 6-22** Effect of working electrode length on  $J$ -factor for mass transfer at  $T_b = 50^\circ\text{C}$  under isothermal conditions.

### 6.3.4 Estimation of Mass Transfer Correlations

As stated previously in section (2.4) that mass transfer process depends on the flow regime, and hence on Reynolds number  $Re$ , and also depends on the relative rates of diffusion of momentum and mass, i.e. on Schmidt number  $Sc$ . So in mass transfer correlations, the experimental data of  $J_m$ ,  $St_m$ , or  $Sh$ , are related to  $Re$  and  $Sc$ .

Using regression technique, the mass experimental data given in Tables 5-4 to 5-9 for isothermal conditions and for the whole range of Reynolds number and bulk temperature (or  $Sc$ ) can be correlated by the following equations:

For  $L = 3$  cm:

$$J_m = 0.514 Re^{-0.523} \quad (6.2)$$

or  $St_m = 0.514 Re^{-0.523} Sc^{-2/3} \quad (6.3)$

or  $Sh = 0.514 Re^{0.477} Sc^{1/3} \quad (6.4)$

The coefficient of correlation for these three equations is 0.994.

and for  $L = 10$  cm:

$$J_m = 0.298 Re^{-0.5} \quad (6.5)$$

or  $St_m = 0.298 Re^{-0.5} Sc^{-2/3} \quad (6.6)$

or  $Sh = 0.298 Re^{0.5} Sc^{1/3} \quad (6.7)$

The coefficient of correlation for these three equations is 0.993.

### 6.3.5 Comparison With Other Correlations

The experimental mass transfer results obtained in the present work are compared with previous correlations. Unfortunately few correlations are available in literature for relating mass transfer data for turbulent flow in annular space between concentric tubes. Lin et al. correlation [29] given in

Eq. (3.20) is used for fully developed mass transfer profile, and Ross and Wragg correlation [30] given in Eq. (3.22) which correlated data in the mass transfer entry region and fully developed region. Comparison of the present correlation with Ross and Wragg correlation is shown in Fig. 6-23 for working electrode length of 3 cm, and with Lin et al. and Ross and Wragg correlations is shown in Fig. 6-24 for working electrode length of 10 cm.

Ross and Wragg correlation shows close agreement with experimental results for low Reynolds number and the deviation increases with increasing Reynolds number for the two working electrode lengths, 3 and 10 cm. This is due to the fact that Ross and Wragg correlation is for Re range of 3000-17000. Lin et al. correlation shows great deviation from experimental results and from Ross and Wragg correlation.

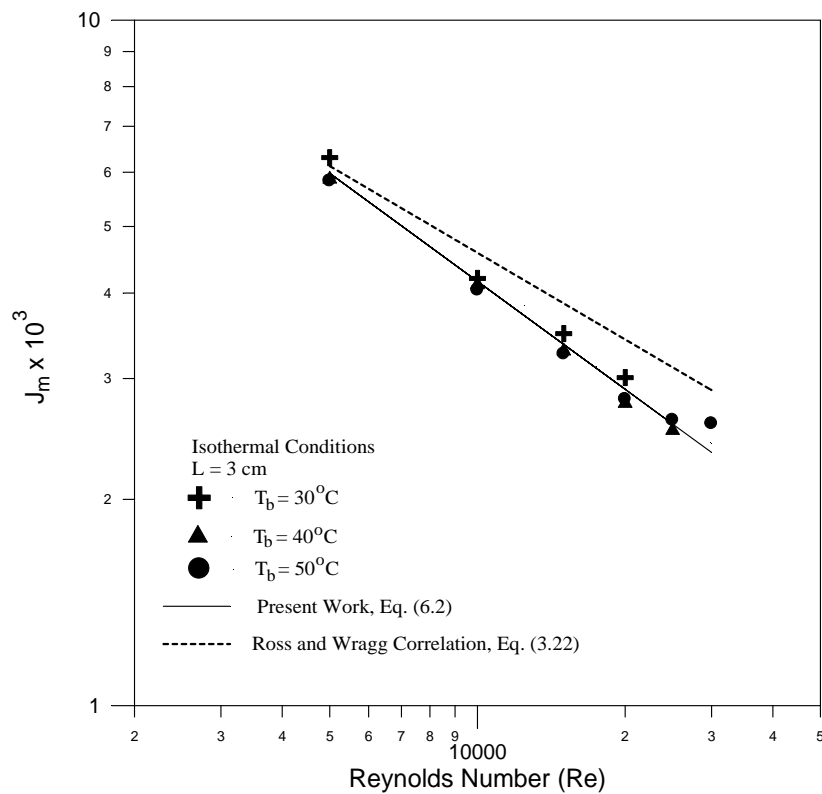


**Figure 6-23** Comparison of experimental  $J_m$  with other correlation for  $L=3$  cm.

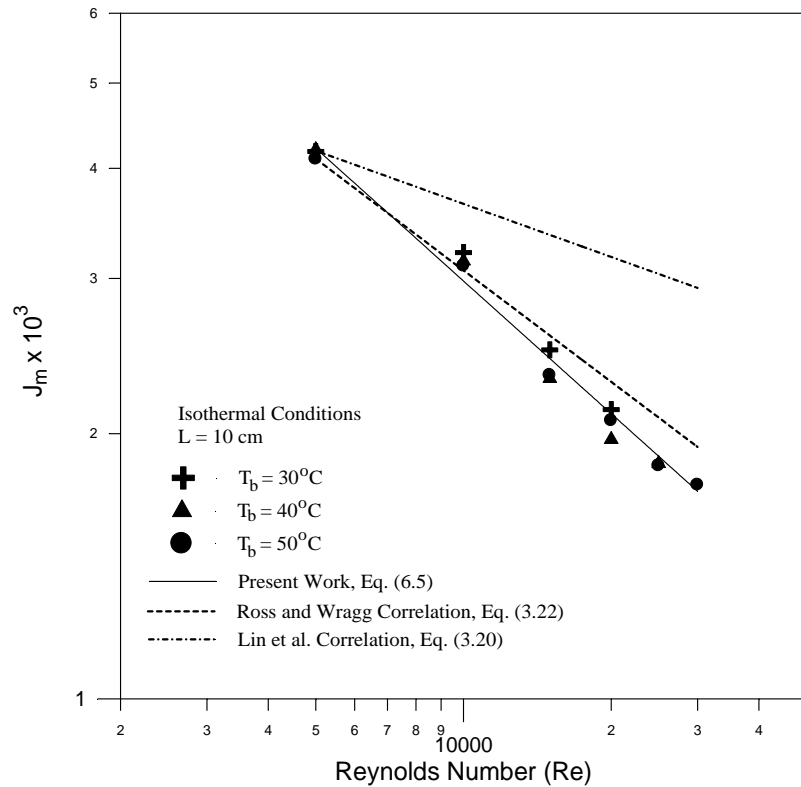


**Figure 6-24** Comparison of experimental  $J_m$  with other correlations for  $L=10$  cm.

## 6.4 Cathodic Polarization Region Under Heat Transfer Conditions

### 6.4.1 Effect of Reynolds Number

The same effect of Reynolds number (or velocity) could be observed on limiting current density under a particular heat flux as that for isothermal condition. This means that increasing Reynolds number under a constant bulk temperature and a particular heat flux will increase limiting current density as presented in Tables 5-10 to 5-12 and as shown in Figs. 6-25 to 6-27 for working electrode length of 10 cm, and heat fluxes of 15, 30, and 45 kW/m<sup>2</sup>. This behavior may also be attributed to decreasing diffusion boundary layer thickness with increasing Reynolds number.

Noticing Tables 5-10 to 5-12 or Figs. 6-28 to 6-30 shows that corrosion potential becomes less negative (more noble) with increasing Reynolds

number. This behavior is similar to that of isothermal conditions and can be explained by the same manner illustrated in section (6.2.1).

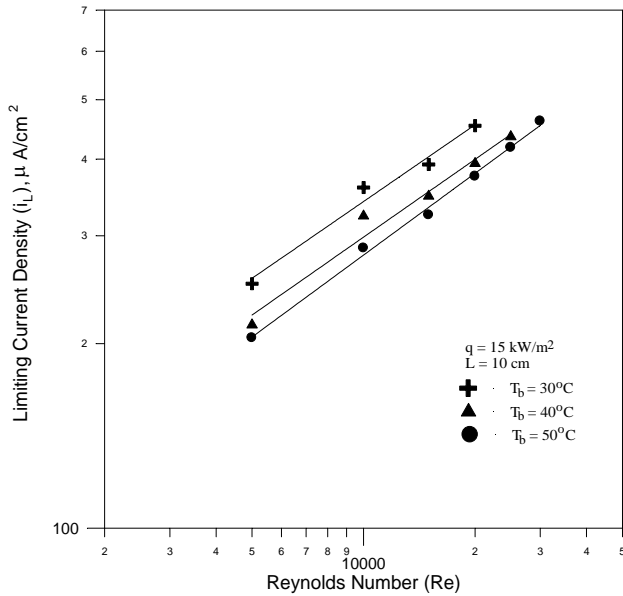


**Figure 6-25** Variation of  $i_L$  with Re for  $L=10$  cm and  $q=15$  kW/m<sup>2</sup>.

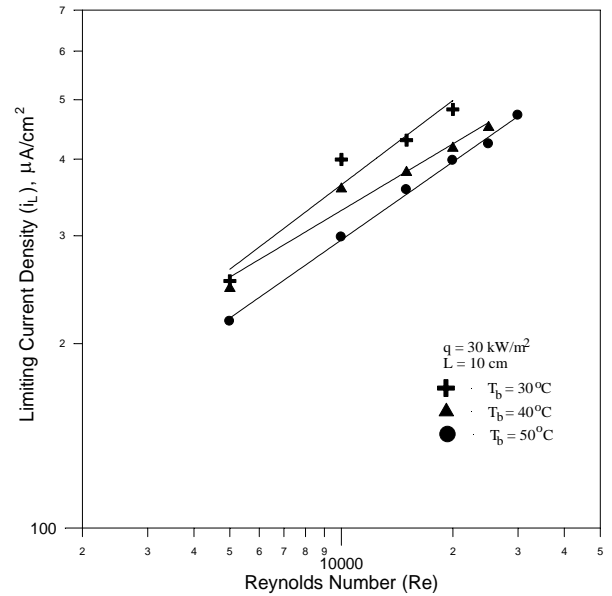


**Figure 6-26** Variation of  $i_L$  with Re for  $L=10$  cm and  $q=30$  kW/m<sup>2</sup>.

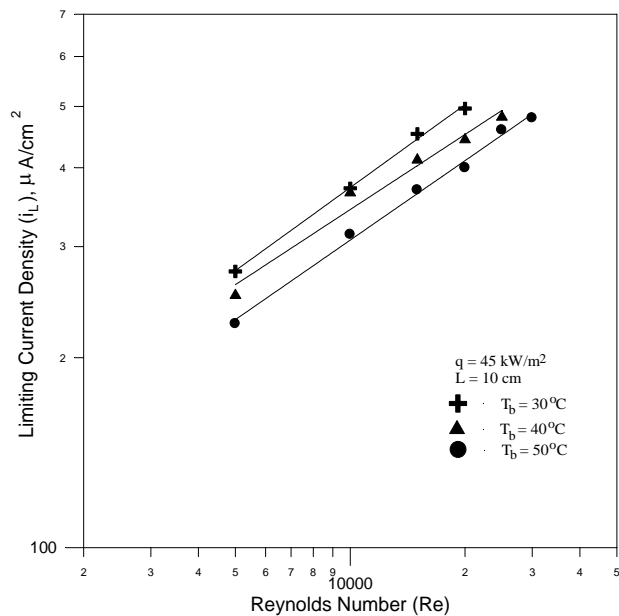


**Figure 6-27** Variation of  $i_L$  with Re for  $L=10$  cm and  $q=45$  kW/m<sup>2</sup>.

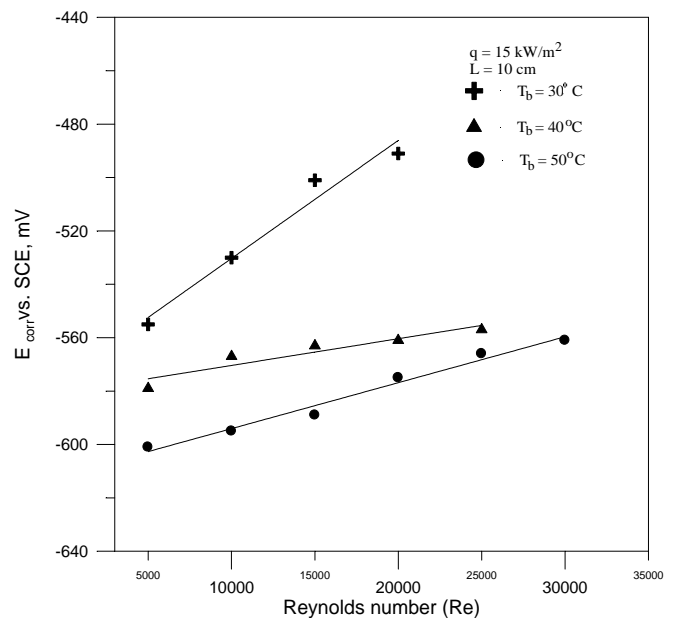


**Figure 6-28** Variation of  $E_{\text{corr}}$  with Re for  $L=10$  cm and  $q=15$  kW/m<sup>2</sup>.

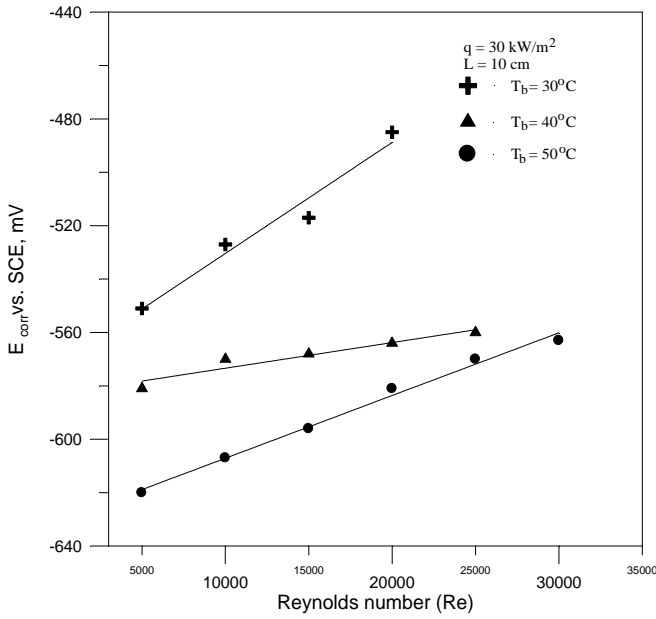


**Figure 6-29** Variation of  $E_{\text{corr}}$  with Re for  $L=10$  cm and  $q=30$  kW/m<sup>2</sup>.

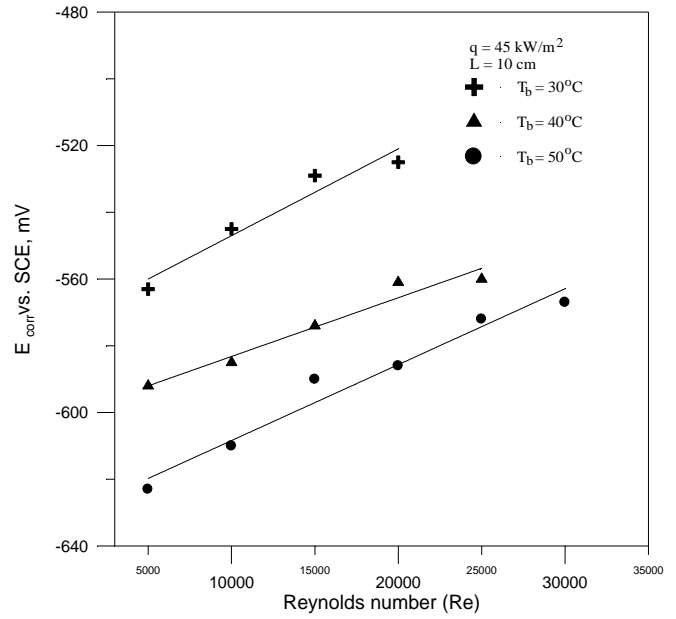


**Figure 6-30** Variation of  $E_{\text{corr}}$  with Re for  $L=10$  cm and  $q=45$  kW/m<sup>2</sup>.

### 6.4.2 Effect of bulk temperature

At a specified heat flux and Reynolds number, increasing bulk temperature will decrease the limiting current density of oxygen reduction as illustrated in Figs. 6-25 to 6-27. This effect is similar to that under isothermal conditions and can be explained by the same viewpoints illustrated in section (6.2.2).

The corrosion potential value moves to more negative region with increasing bulk temperature. As mentioned previously that  $E_{\text{corr}}$  values obey the mixed potential theory. The anodic region (an activation controlled process) is stimulated by increasing bulk temperature to greater extent than the cathodic process (a mass transfer process), thus the corrosion potential falls with increasing bulk temperature. Figure 6-8 is helpful to explain this behavior.

### 6.4.3 Effect of Heat Flux

The limiting current density  $i_L$  under heat transfer is greater than under isothermal conditions when compared at the same bulk temperature and Reynolds number. Also the limiting current density increases with increase in heat flux from 15 to 30 and 45 kW/m<sup>2</sup> as shown in Figs. 6-31 to 6-33.

In the presence of heat flux, a temperature difference between the metal surface and liquid bulk is developed through a thermal boundary layer  $\delta_t$ . The diffusion boundary layer  $\delta_d$  lies in the thermal boundary layer, so that the temperature gradient exists also within the diffusion boundary layer.

Increasing temperature within the diffusion layer to that at liquid bulk temperature by supplying heat flux leads to:

- 1- Increase diffusivity coefficient of oxygen within this layer and this leads to increase the limiting current of oxygen reduction and corrosion rate.
- 2- Decrease oxygen concentration within this layer, which would increase the concentration difference between the bulk liquid and the diffusion layer, i.e. that another concentration driving force will be developed and this leads to increase the corrosion rate.

Hence corrosion rate increases with supplying heat flux as observed by many authors [71-76].

Comparing corrosion potential under heat transfer conditions with that under isothermal shows that  $E_{\text{corr}}$  under heat transfer is more negative (less noble) than that under isothermal conditions at identical Reynolds number and bulk temperature of flow. The surface temperature in the presence of heat flux is higher than that under isothermal conditions. Hence supplying heat flux leads to enhance anodic and cathodic processes so that  $E_{\text{corr}}$  moves to more negative value as illustrated in Fig. 6-37.

Also increasing heat flux from 15 to 30, and 45 kW/m<sup>2</sup> is accompanied by an increase in surface temperature and  $E_{\text{corr}}$  falls according to this as shown in Figs. 6-34 to 6-36. This means that it is the surface temperature that has a determined role in changing  $E_{\text{corr}}$ .

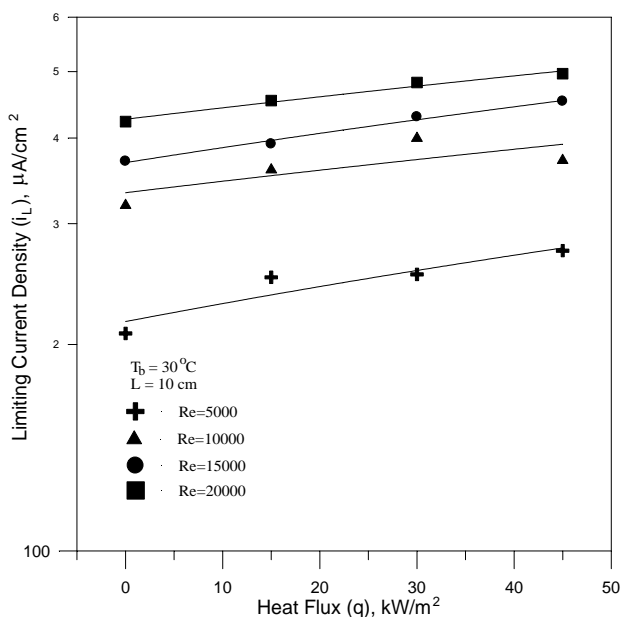


**Figure 6-31** Variation of  $i_L$  with heat flux for  $L=10$  cm, and  $T_b=30^\circ\text{C}$ .

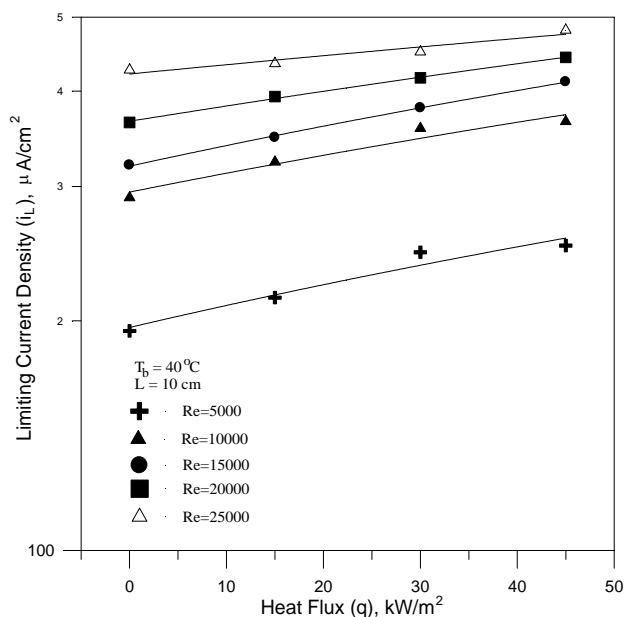


**Figure 6-32** Variation of  $i_L$  with heat flux for  $L=10$  cm, and  $T_b=40^\circ\text{C}$ .

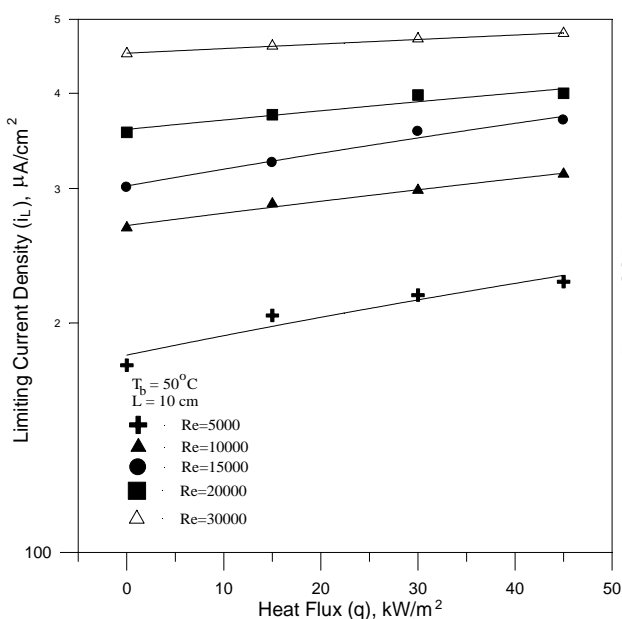


**Figure 6-33** Variation of  $i_L$  with heat flux for  $L=10$  cm, and  $T_b=50^\circ\text{C}$ .

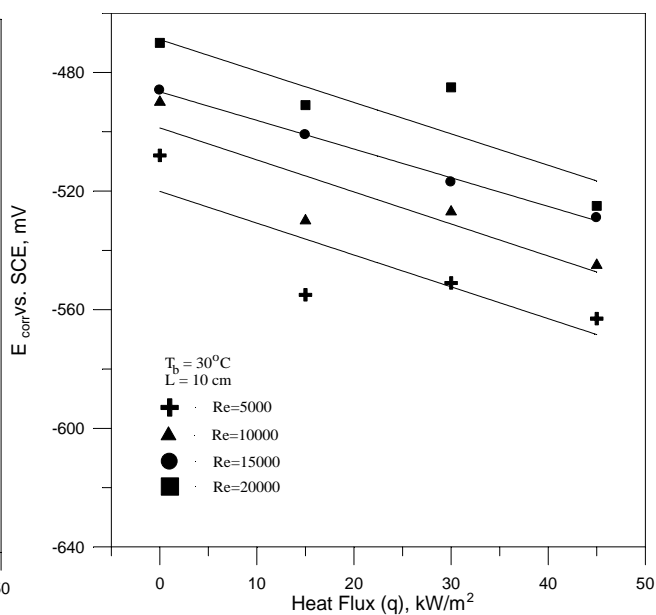


**Figure 6-34** Variation of  $E_{\text{corr}}$  with heat flux for  $L=10$  cm, and  $T_b=30^\circ\text{C}$ .

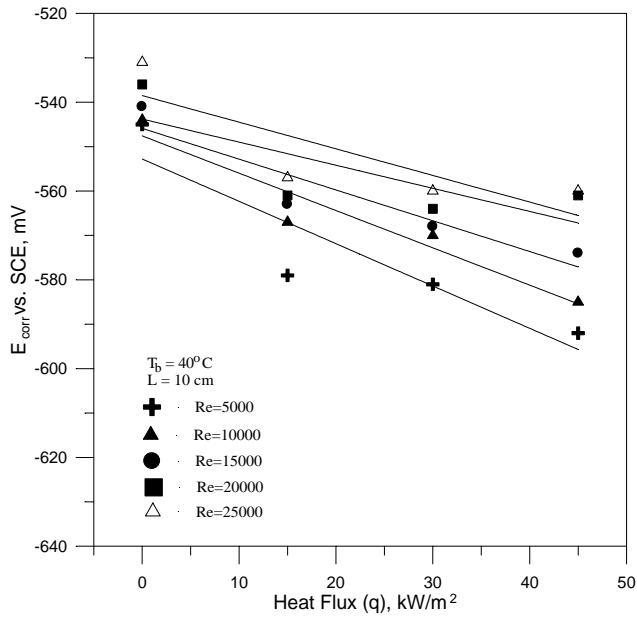


**Figure 6-35** Variation of  $E_{\text{corr}}$  with heat flux for  $L=10$  cm, and  $T_b=40^\circ\text{C}$ .

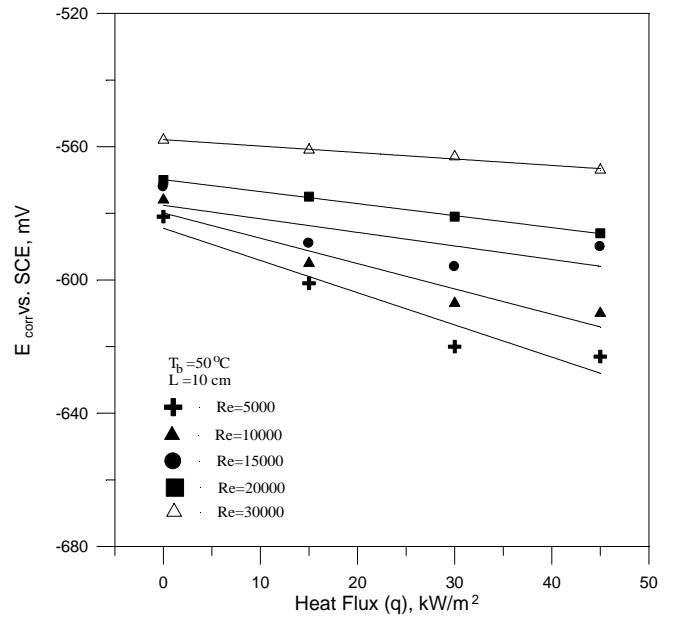


**Figure 6-36** Variation of  $E_{\text{corr}}$  with heat flux for  $L=10$  cm, and  $T_b=50^\circ\text{C}$ .

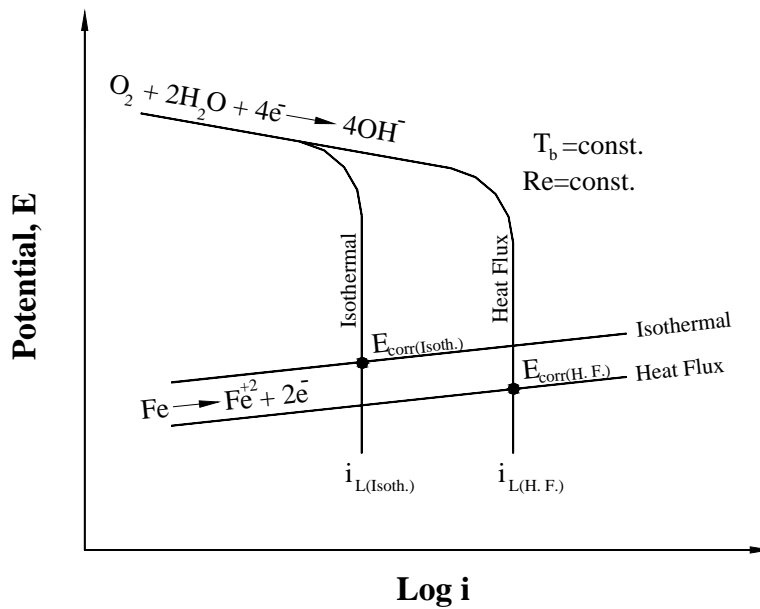


**Figure 6-37** The effect of heat flux on corrosion of carbon steel.

## 6.5 Mass Transfer Data Under Heat Transfer

The effect of increasing Reynolds number on  $k_m$ , Sh,  $St_m$ , and  $J_{mf}$  at constant bulk temperature and at a specified heat flux, can be discussed in the same manner for isothermal conditions mentioned in section (6.3.1). This means that  $k_m$ , Sh will increase with increasing Reynolds number, while  $St_m$ , and  $J_{mf}$  will decrease as shown in Figs. 6-38 to 6-41 or Tables 5-13 to 5-21.

In general increasing bulk temperature at constant Reynolds number and heat flux leads to increase  $k_m$ , and  $St_m$ , and decrease Sh, but no appreciable effect on  $J_{mf}$  was observed as shown in Figs 6-38 to 6-41 or Tables 5-13 to 5-21. This behavior is similar to that under isothermal conditions mentioned and discussed in section (6.3.2).

Comparing Tables 5-7 to 5-9 for mass transfer result under isothermal conditions with Tables 5-13 to 5-21 under heat transfer conditions shows that the values of  $k_m$ , Sh, and  $St_m$  are greater under heat transfer than that under isothermal ( $q=0 \text{ kW/m}^2$ ) and these values increase with increase heat flux from 15 to 30 and 45  $\text{kW/m}^2$  at specified Reynolds number and bulk temperature. The increase in  $k_m$  with heat flux as shown in Figs. 6-42 and 6-43 is due to the increase in limiting current density or corrosion rate that is directly proportional to  $k_m$ . Increasing  $k_m$  also leads to increase Sh and  $St_m$  which are also directly proportional to  $k_m$  and  $i_L$ .

The mass transfer  $J$ -factor  $J_{mf}$  evaluated at film temperature  $T_f$  as shown in Figs. 6-44 and 6-45 remains approximately constant with increase heat flux and similar to the value under isothermal conditions ( $q=0 \text{ kW/m}^2$ ). This is due to the fact that ( $J_{mf} = St_m Sc_f^{2/3}$ ) implies two parameters,  $St_m$  which increases with heat flux as mentioned above, and  $Sc_f$  which decreases with heat flux due to increase boundary layer temperature (film temperature), so these two conflicting values produce negligible change in  $J$ -factor.

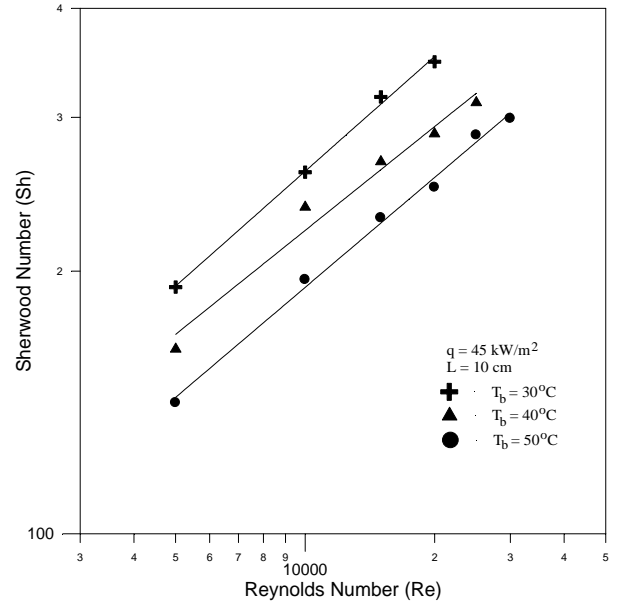
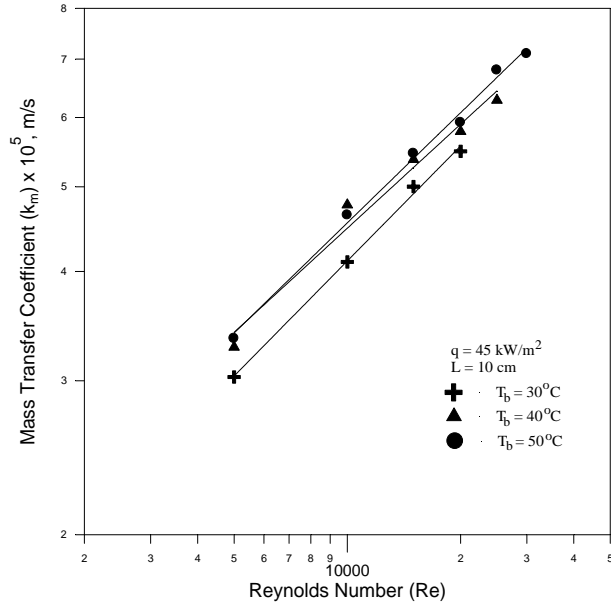
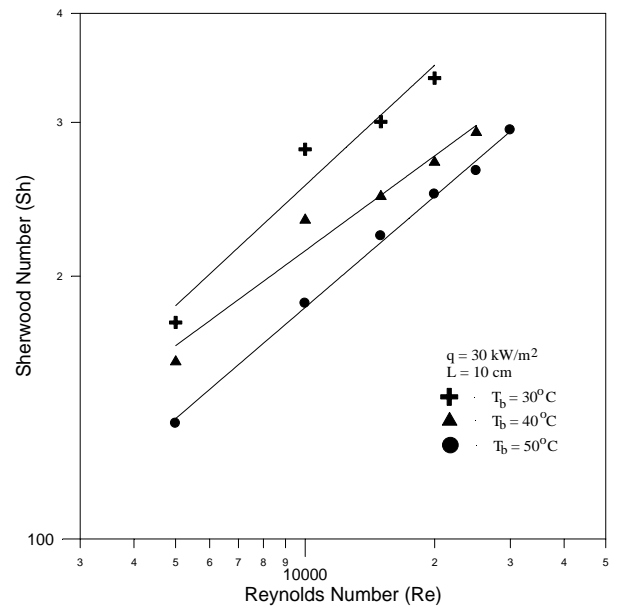
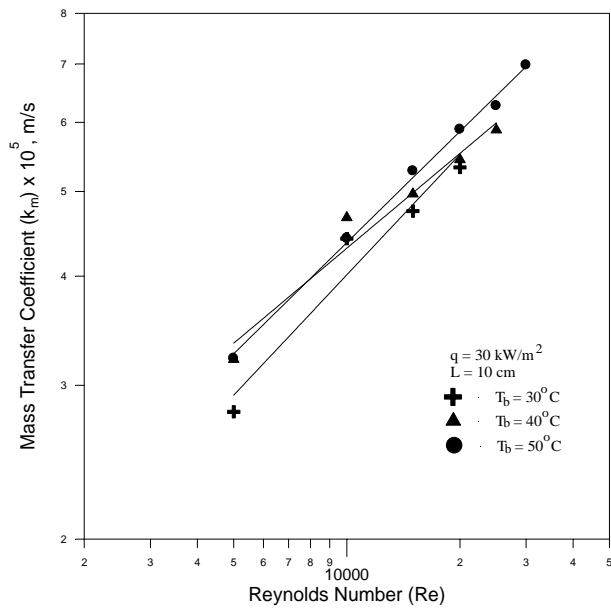
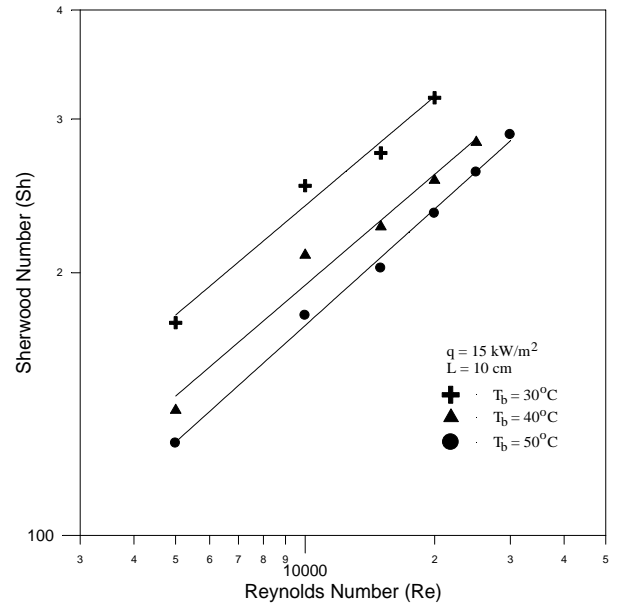
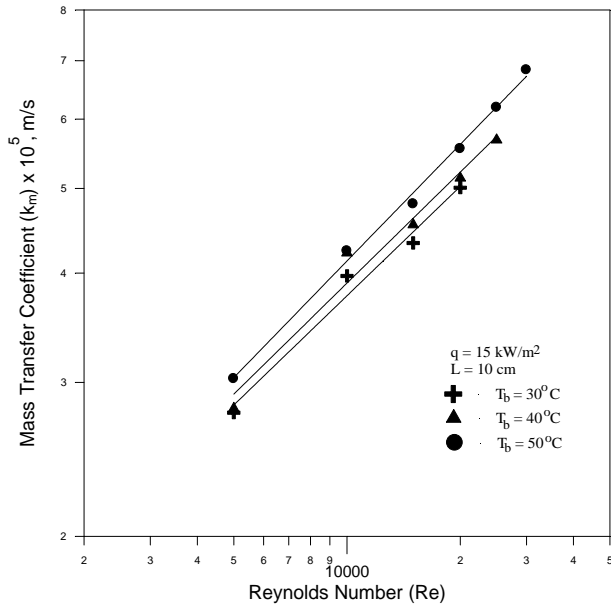


**Figure 6-38** Variation of  $k_m$  with Re under heat transfer conditions.

**Figure 6-39** Variation of Sh with Re under heat transfer conditions.

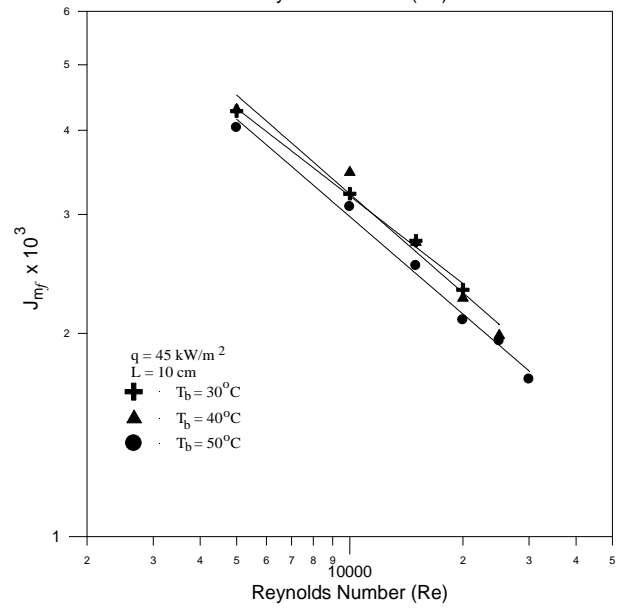
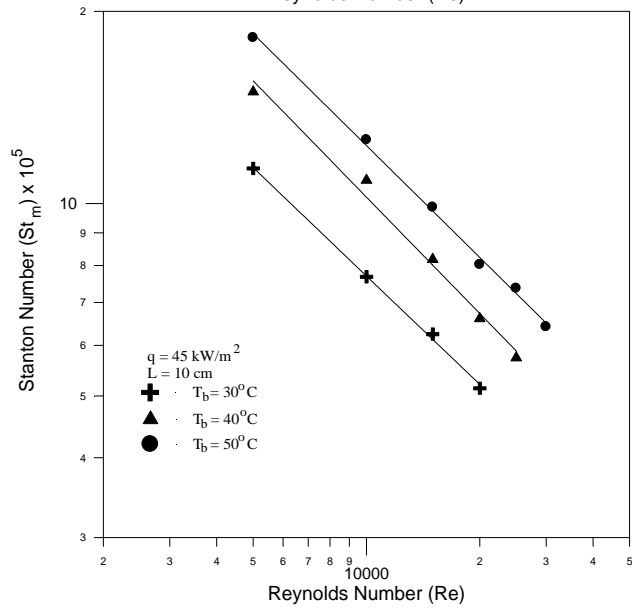
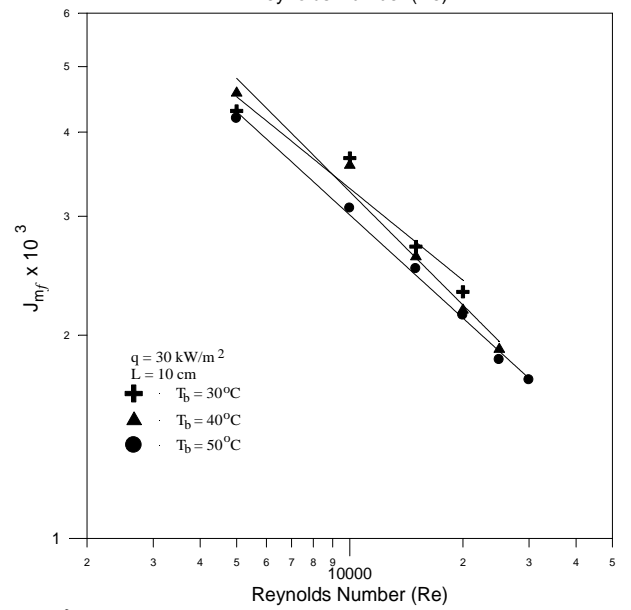
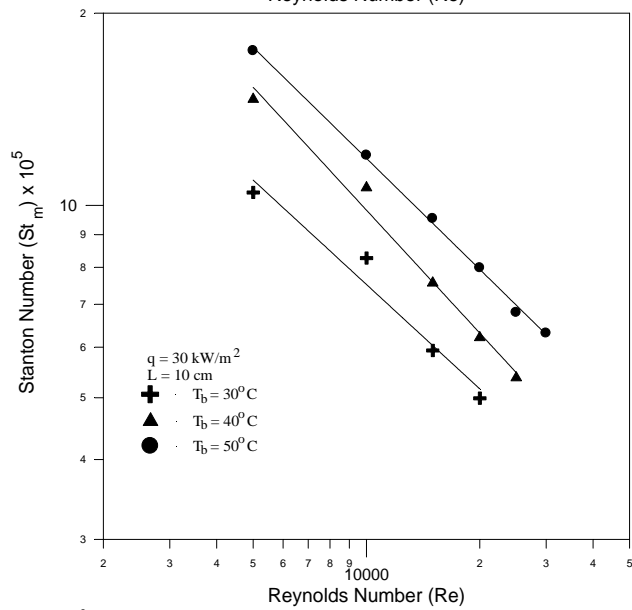
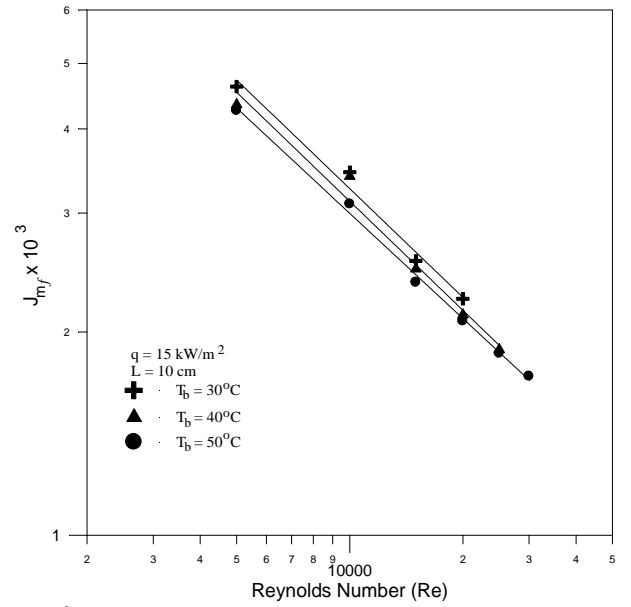
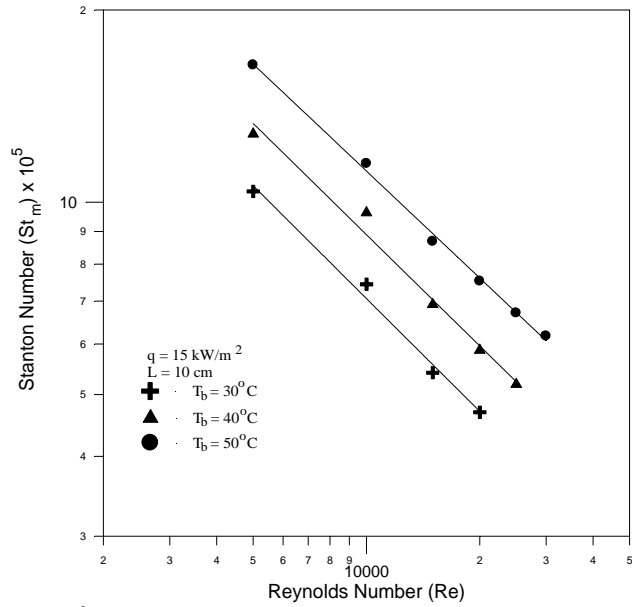


**Figure 6-40** Variation of  $St_m$  with Re under heat transfer conditions.

**Figure 6-41** Variation of  $J_{mf}$  with Re under heat transfer conditions.

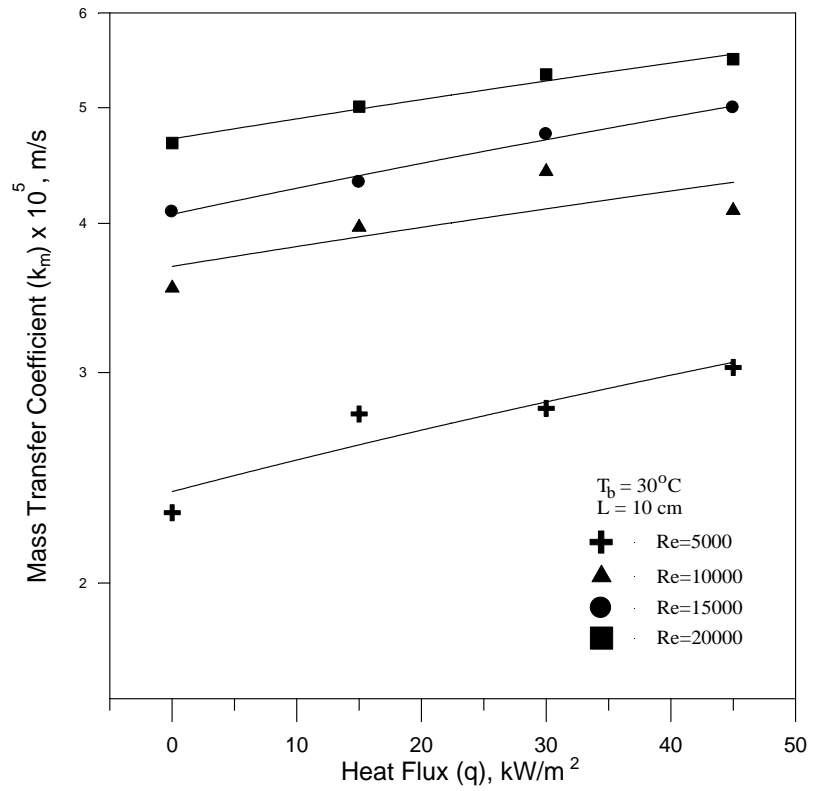


**Figure 6-42** Variation of  $k_m$  with heat flux at  $T_b = 30^\circ\text{C}$ .

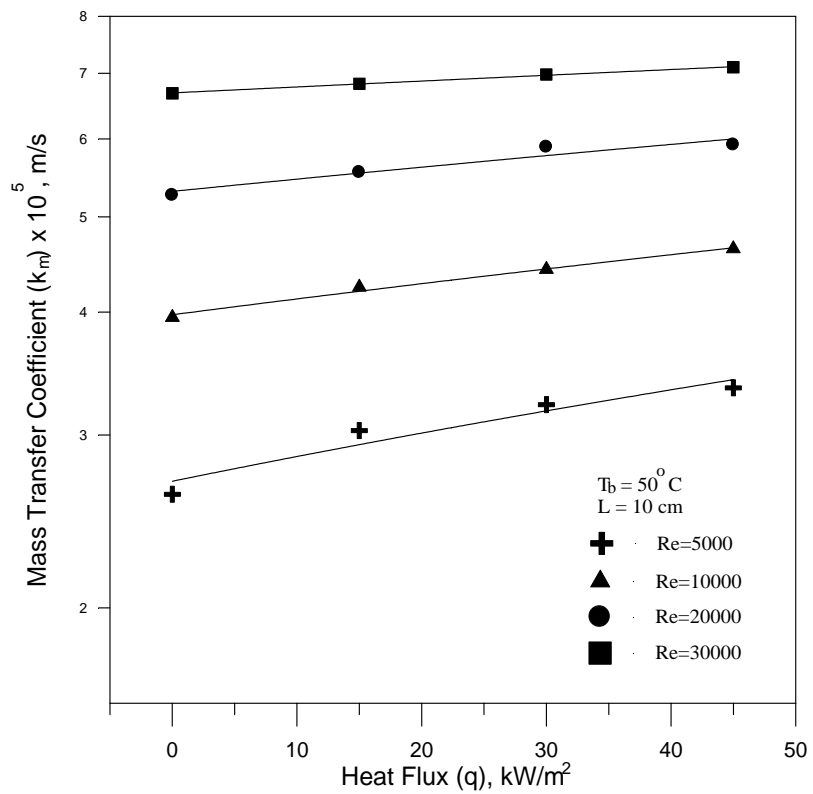


**Figure 6-43** Variation of  $k_m$  with heat flux at  $T_b = 50^\circ\text{C}$ .

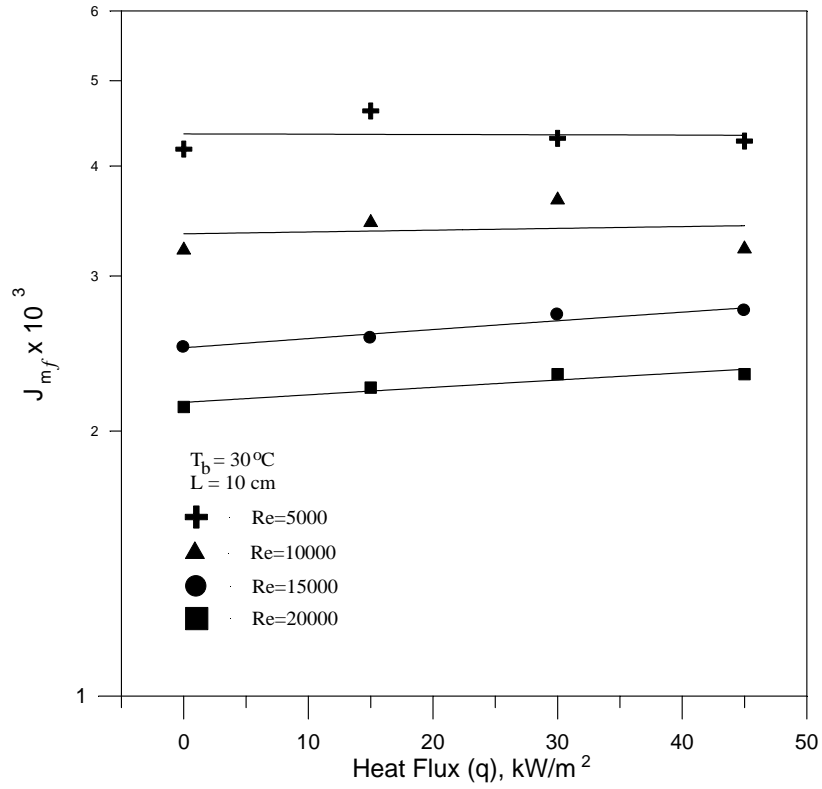


**Figure 6-44** Variation of  $J_{mf}$  with heat flux at  $T_b = 30^\circ\text{C}$ .

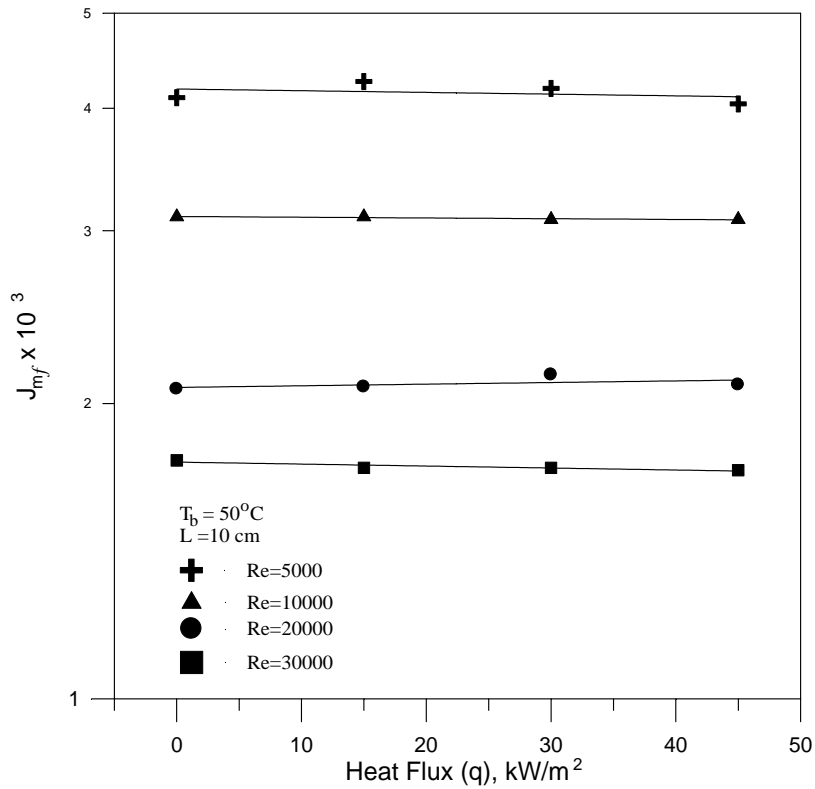


**Figure 6-45** Variation of  $J_{mf}$  with heat flux at  $T_b = 50^\circ\text{C}$ .

### 6.5.1 Estimation of Mass Transfer Correlations

As stated previously that the reason of using  $J_{mf}$  instead of  $J_m$  is the  $Sc_f$  term, which decreases with increasing heat flux (increasing film temperature), hence the value of  $J_{mf}$  remains approximately constant with increase in heat flux. In other words, rather than of obtaining a relation between  $J_m$  and Re for each particular heat flux, and then three relations can be obtained for the three heat fluxes. It is possible to obtain one correlation relating  $J_{mf}$  to Re taking the effect of the three fluxes into consideration.

Using regression technique, the experimental data given in Tables 5-13 to 5-21 for working electrode length of 10 cm, for whole range of Reynolds number (5000-30000), three bulk temperatures (30, 40, and 50 °C), and three heat fluxes (15, 30, and 45 kW/m<sup>2</sup>), can be related by:

$$J_{mf} = 0.284 \text{ Re}^{-0.489} \quad (6.8)$$

or

$$\text{St}_m = 0.284 \text{ Re}^{-0.489} \text{ Sc}_f^{-2/3} \quad (6.9)$$

The coefficient of correlation for these two equations is 0.981.

Also the mass data under isothermal conditions ( $q=0$  kW/m<sup>2</sup>), and under heat transfer conditions (15, 30, and 45 kW/m<sup>2</sup>), for working electrode length of 10 cm can be combined by one equation:

$$J_{mf} = 0.287 \text{ Re}^{-0.492} \quad (6.10)$$

or

$$\text{St}_m = 0.287 \text{ Re}^{-0.492} \text{ Sc}_f^{-2/3} \quad (6.11)$$

The coefficient of correlation for these two equations is 0.981. Under isothermal conditions  $Sc_f$  is equal to Sc evaluated at bulk temperature, and hence  $J_{mf}$  means  $J_m$ .

## 6.5.2 Comparison With Other Correlations

No correlation is available in the literature for mass transfer under the influence of heat flux for annular flow in two concentric tubes. But since mass transfer data under isothermal conditions and heat transfer conditions can be included in one equation as illustrated in previous section. So the same literature correlations used for isothermal can be used here for comparison and as shown in Fig. 6-46.

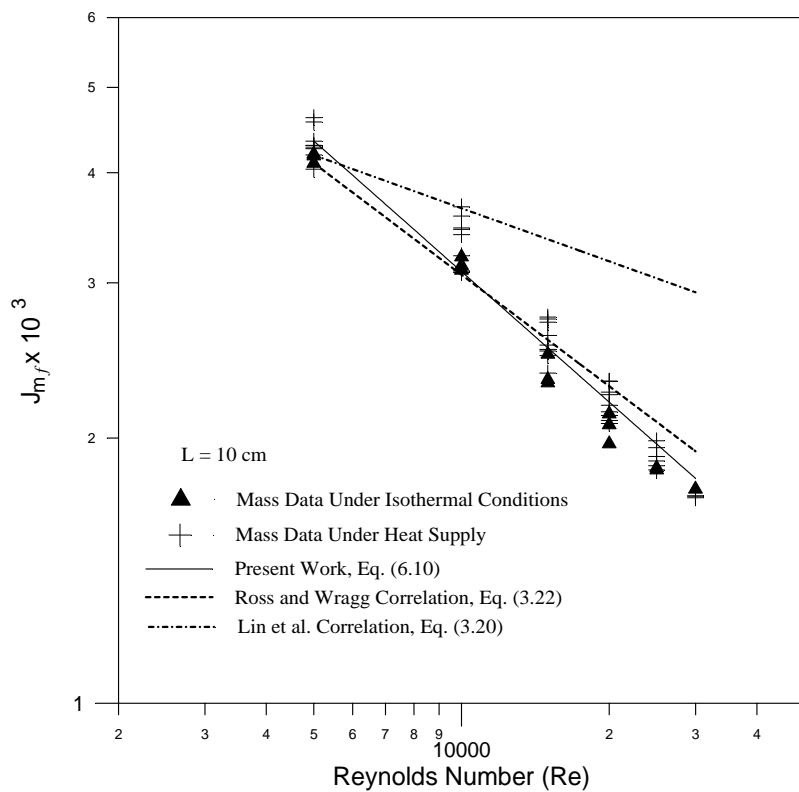


**Figure 6-46** Comparison of experimental  $J_{mf}$  with other correlations for  $L=10$  cm under isothermal and heat transfer conditions.

## 6.6 Heat Transfer Rate

### 6.6.1 Effect of Reynolds Number

The effect of Reynolds number (or velocity) on heat transfer coefficient  $h$ , Nusselt number  $Nu$ , Stanton number  $St_h$ , and  $J$ -factor  $J_h$  is tabulated in

Tables 5-22 to 5-30. Increasing Reynolds number at constant bulk temperature and certain heat flux will increase  $h$ . Increasing Reynolds number will increase the turbulence allowing transfer of low temperature fluid towards the surface leading to higher rate of heat transfer. Increasing velocity will thin the thermal boundary layer  $\delta_t$  in a similar fashion to that of diffusion layer, so  $h$  will increase according to [9, 71]:

$$h = \frac{k}{\delta_t} \quad (6.12)$$

where  $k$  is the thermal conductivity of the solution.

Nusselt number according to Eq. (5.9), which is directly proportional to  $h$ , will be increased as shown in Figs. 6-47 to 6-49. But this increase in heat transfer coefficient or Nusselt number is less than the corresponding increase in velocity or Reynolds number so that the Stanton number will decrease at constant temperature (constant Prandtl number) according to Eq. (5.10) as shown in Figs. 6-50 to 6-52. Also  $J$ -factor will be decreased according to Eq. (5.11).

### 6.6.2 Effect of Bulk Temperature

It is illustrated in Figs. 6-47 to 6-49 that an increase in bulk temperature at constant Reynolds number and heat flux will slightly decrease the Nusselt number. Substituting Eq. (6.12) in Eq. (5.9) to obtain:

$$\text{Nu} = \frac{d_e}{\delta_t} \quad (6.13)$$

This means that Nusselt number depends on thermal boundary layer thickness. Increasing temperature at constant Reynolds number leads to decrease the flow rate, i.e. decrease the velocity, of passing solution to carbon steel specimen and this leads to increase the thermal boundary layer thickness.

Hence, Nusselt number will be decreased. In other words, this slight increase in heat transfer coefficient and Nusselt number with decreasing bulk temperature can be interpreted to greater quantity of cold fluid reached heat transfer surface than hotter one.

This slight decrease in Nu has less effect than Prandtl number Pr which decrease with increase bulk temperature, so the Stanton number  $St_h$  will be increased with bulk temperature according to Eq. (5.10), and less increase in  $J$ -factor  $J_h$  was observed as illustrated in Tables 5-22 to 5-30.

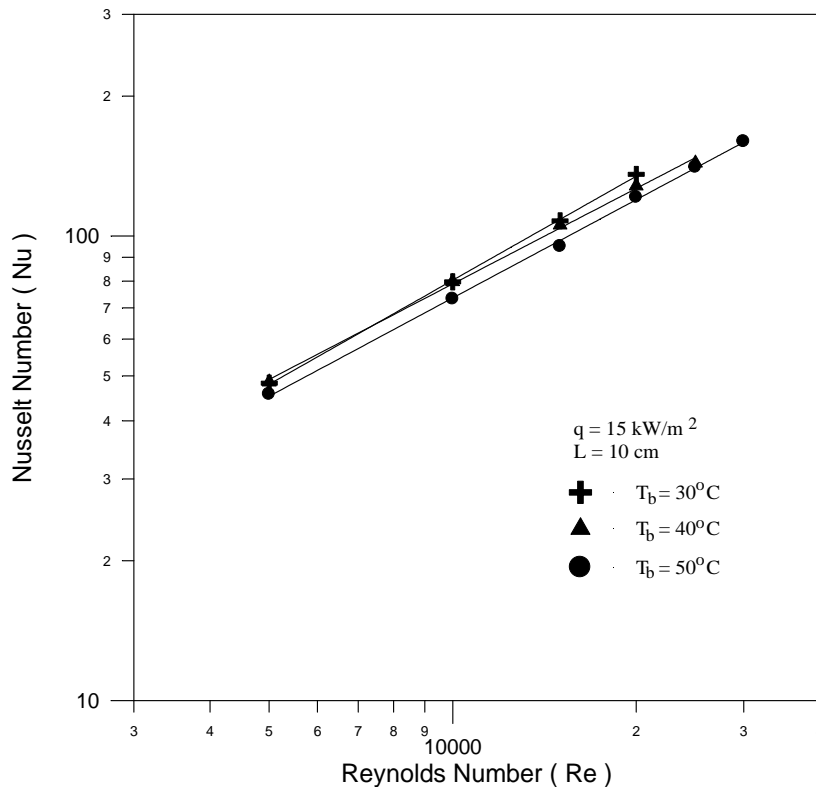


**Figure 6-47** Variation of Nusselt number with Reynolds number for  $L=10$  cm, and  $q=15$  kW/m<sup>2</sup>.

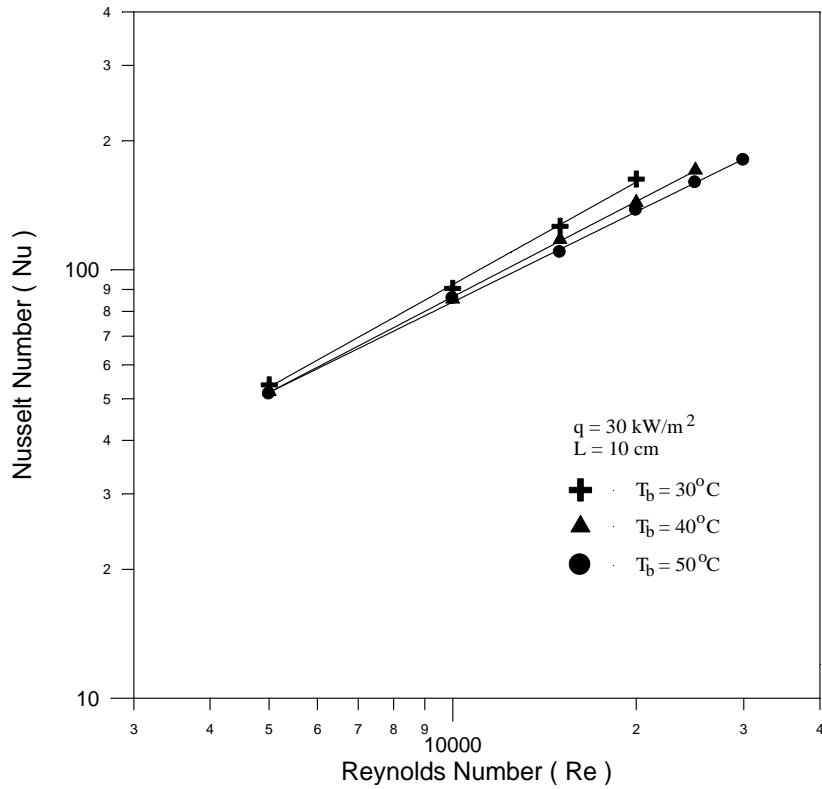


**Figure 6-48** Variation of Nusselt number with Reynolds number for  $L=10 \text{ cm}$ , and  $q=30 \text{ kW/m}^2$ .

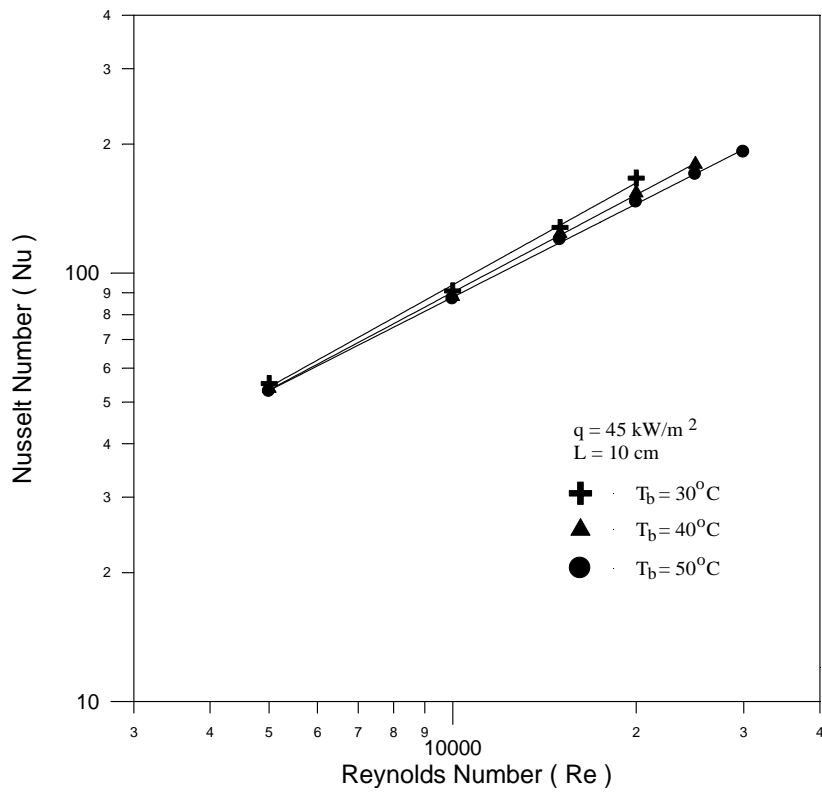


**Figure 6-49** Variation of Nusselt number with Reynolds number for  $L=10 \text{ cm}$ , and  $q=45 \text{ kW/m}^2$ .

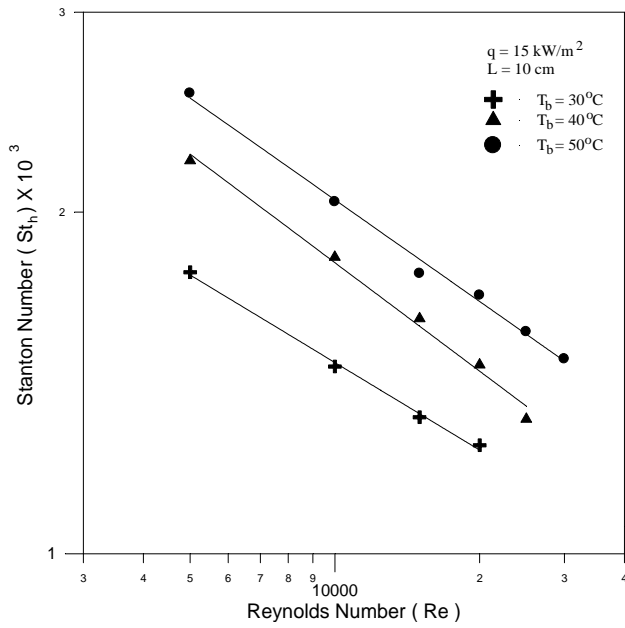


**Figure 6-50** Variation of  $St_h$  with  $Re$  for  $L=10$  cm, and  $q=15$  kW/m<sup>2</sup>.

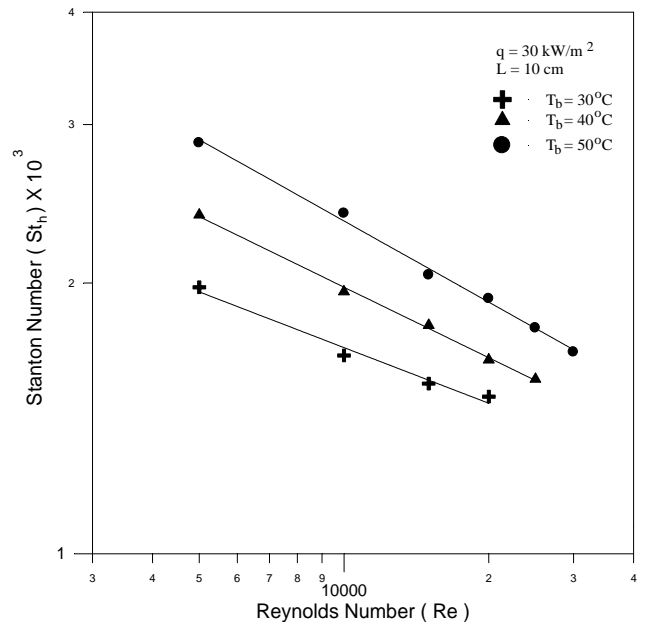


**Figure 6-51** Variation of  $St_h$  with  $Re$  for  $L=10$  cm, and  $q=30$  kW/m<sup>2</sup>.

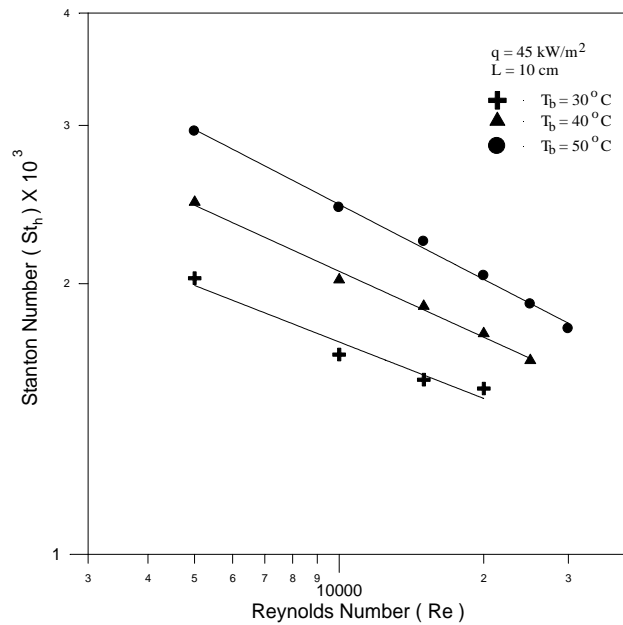


**Figure 6-52** Variation of  $St_h$  with  $Re$  for  $L=10$  cm, and  $q=45$  kW/m<sup>2</sup>.

### 6.6.3 Effect of Heat Flux

The increase in heat flux at constant Reynolds number and bulk temperature leads to increase the thermal conductivity within the thermal boundary layer, and this will lead slightly to decrease the thermal boundary layer thickness adjacent to heat transfer surface. This means that the perpendicular distance at which temperature gradient exists between the surface and bulk will be decreased. Hence slight increase in heat transfer coefficient, Nusselt number, Stanton number, and  $J$ -factor with increase heat flux was observed as shown in Tables 5-22 to 5-30 or Figs. 6-53 to 6-55 for Nusselt number.

Allen and Eckert [101] showed that at low Reynolds number, the heat transfer coefficient was little affected by heat rate, while at higher Re the effect of heating rate was increased.

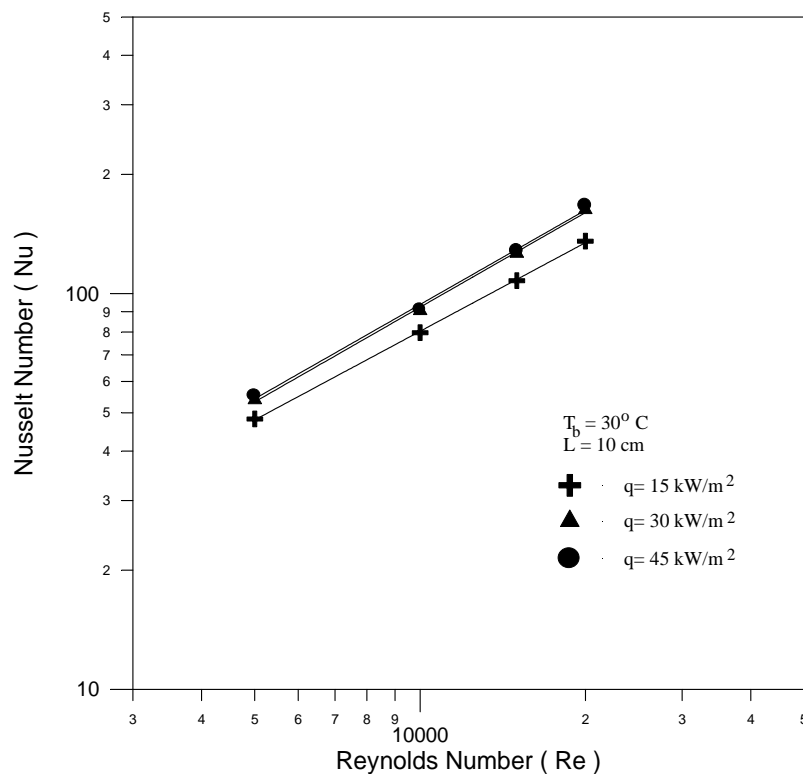


**Figure 6-53** Variation of Nusselt number with Reynolds number showing the effect of heat flux at  $T_b = 30^\circ\text{C}$ .

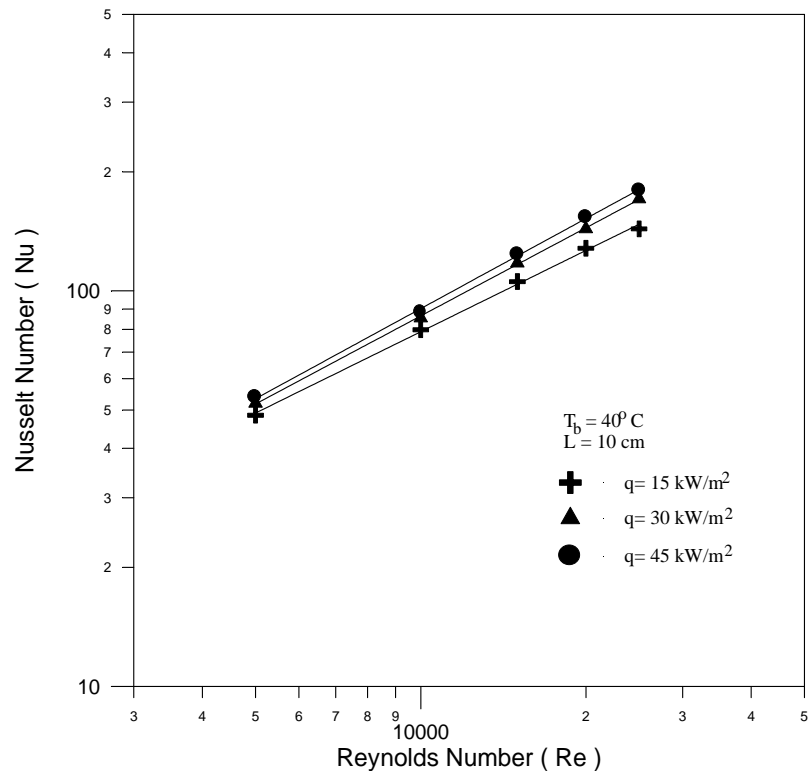


**Figure 6-54** Variation of Nusselt number with Reynolds number showing the effect of heat flux at  $T_b = 40^\circ\text{C}$ .

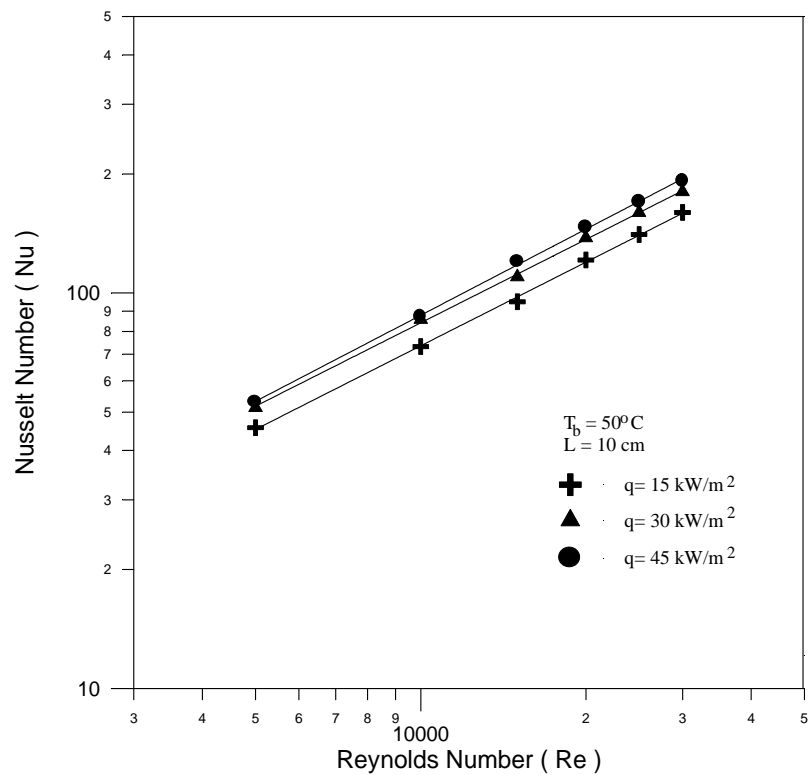


**Figure 6-55** Variation of Nusselt number with Reynolds number showing the effect of heat flux at  $T_b = 50^\circ\text{C}$ .

#### 6.6.4 Estimation of Heat Transfer Correlations

The heat transfer process depends on Reynolds and Prandtl numbers [1, 7]. Hence the heat experimental data ( $Nu$ ,  $St_h$ , and  $J_h$ ) given in Tables 5-22 to 5-30 can be correlated in terms of  $Re$  and  $Pr$  using regression technique:

$$Nu = 0.058 Re^{0.738} Pr^{1/3} \quad (6.14)$$

or 
$$St_h = 0.058 Re^{-0.262} Pr^{-2/3} \quad (6.15)$$

or 
$$J_h = 0.058 Re^{-0.262} \quad (6.16)$$

The coefficient of correlation for these equations is 0.974. These relations are for working electrode length of 10 cm,  $Re$  range (5000-30000), three bulk temperatures (30, 40, and 50 °C), and three heat fluxes (15, 30, and 45 kW/m<sup>2</sup>). The effect of temperature on  $Pr$  is less, and this leads to very slight effect on  $h$  or  $Nu$ , and this is the reason for not using  $Pr_f$  as  $Sc_f$  in the case of mass transfer correlation. In order to study the effect of  $Pr$  on heat transfer rate, the composition of the working solution must be changed. By this way, Friend and Metzner [102] varied  $Pr$  about 12 times (50-600).

#### 6.6.5 Comparison With Other Correlations

Three correlations are available in literature for relating heat transfer data in annular flow of concentric pipes heat exchanger. Monrad and Pelton correlation [15] given in Eq. (2.25), Davis correlation [16] given in Eq. (2.26), and Carpenter et al. correlation [4] given in Eq. (2.27) are used to compare the experimental results obtained in the present work as shown in Fig. 6-56.

In order to know which of the above correlations is more representative to experimental data obtained in the present work, average absolute percentage error is used, which is defined as follows:

Average Absolute Percentage Error (AA%E)

$$= \sum_1^n \left[ \left| \frac{(\text{Nu}_{\text{exp.}} - \text{Nu}_{\text{cal.}})}{\text{Nu}_{\text{exp.}}} \right| \times 100 \right] / n = \sum_1^n (\text{A}\% \text{E}) / n \quad (6.17)$$

Table 6-1 shows that (AA%E) of Davis correlation is less than other correlations, i.e., Davis correlation is better expressive of experimental data.

Table 6-1 Average Absolute Percentage Error (AA%E) for three correlations.

	Monrad and Pelton	Davis	Carpenter et al.
AA%E	8.93	6.46	14.65

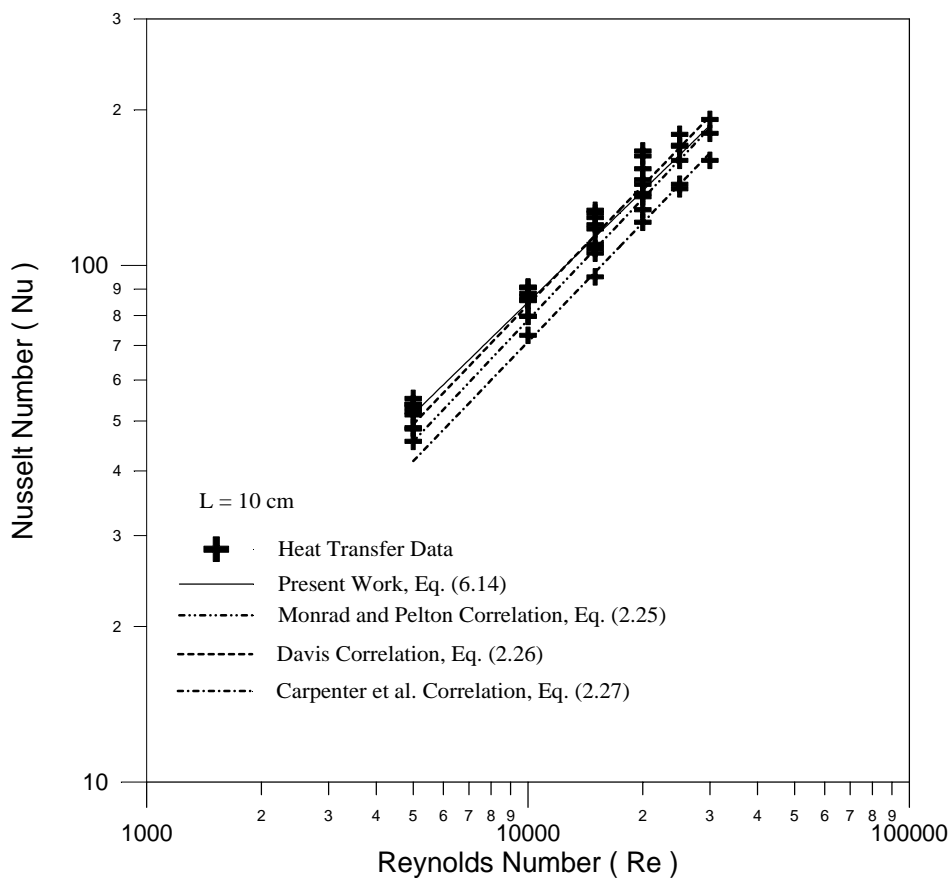


**Figure 6-56** Comparison of experimental Nu with other correlations for  $L=10$  cm.

## 6.7 Analogy Between Heat and Mass Transfer

The analogy between heat and mass transfer can be examined throughout the experimental results of heat and mass transfer obtained in the present work for clean heat transfer surface where no formed corrosion products (i.e.,  $t=0$ ). The Chilton-Colburn analogy is one of the most famous analogies and is given by:

$$J_h = J_m \quad (2.30)$$

Eq. (6.10) for  $J_{mf}$  and Eq. (6.16) for  $J_h$  are plotted in Fig. 6-57, and can be noticed that  $J_h$  is larger than  $J_{mf}$  for all values of Reynolds number, and the deviation increases with increasing Reynolds number. This behavior was also observed in previous literature [19, 76, 103]. Chilton and Colburn in their original study found that  $J_h$  is higher than  $J_m$  for Re range of 1710 to 7450 and the deviation reaches 24%. They considered this analogy is satisfied.

In the present work the deviation is greater (ranges from 43% to 115%) and this may be due to the fact that Prandtl number is much lower than Schmidt number, Pr ranges about (3-6) and Sc ranges (100-350), while Chilton and Colburn used system of close values of Pr and Sc (Pr=0.83, and Sc=0.71). This fact was also stated by Poulson and Robinson [17].

However, the relation between  $J_h$  and  $J_{mf}$  for the present work is obtained by dividing Eq. (6.16) on Eq. (6.10):

$$\frac{J_h}{J_{mf}} = 0.202 \text{Re}^{0.23} \quad (6.18)$$

## 6.8 Corrosion Fouling

Plotting of fouling thermal resistance  $R_f$  against time, as shown in Fig. 6-58, shows that there is a rapid increase in fouling effects at the beginning, and then  $R_f$  tends to approach a constant value. This type of fouling curve is of asymptotic form (see section 3.12.3). The rapid increase in  $R_f$  is due to that

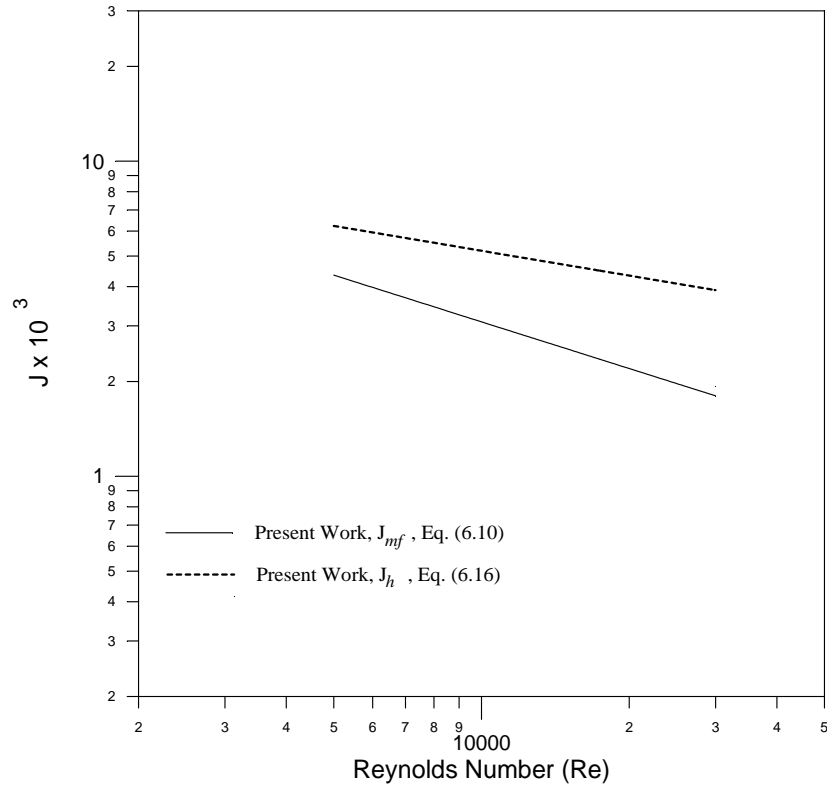


**Figure 6-57** Comparison between  $J_h$  and  $J_{mf}$  for  $L=10$  cm.

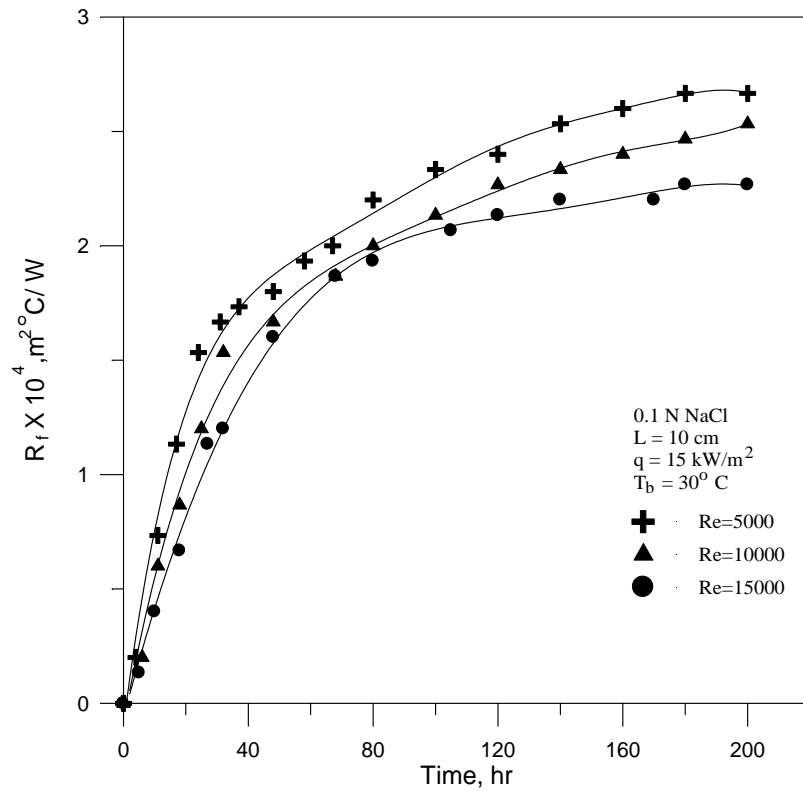


**Figure 6-58** Effect of Reynolds number on  $R_f$ .

deposition rate be predominant to removal rate, until they approach to equal value [79, 82]. The fouling thermal resistance  $R_f$  that developed from deposition of corrosion products on heat transfer surface, has its considerable effect on heat transfer process and on heat transfer coefficient  $h$  as shown in Fig. 6-59, which decreases with time until reaches a constant value.

This behavior of  $R_f$  and  $h$  with time is demonstrated by the behavior of limiting current density  $i_L$  and mass transfer coefficient  $k_m$  with time as shown in Figs. 6-60 and 6-61. At the beginning, there is a rapid decrease in  $i_L$  and  $k_m$ , and then tend to reach constant values with increase in time. In other words, there are also asymptotic form of limiting current density and asymptotic form of mass transfer coefficient but in decreasing direction. The forming of corrosion products on heat transfer surface leads to decrease the amount of oxygen reached to the surface and this leads to decrease the corrosion rate (limiting current density) and mass transfer coefficient.

Two methods are available to observe the effect of corrosion fouling, i.e., surface temperature method, and polarization or limiting current density method. From these two methods, it can be observed:

- 1- Surface temperature provides information about fouling thermal resistance and its effect on heat transport and heat transfer coefficient, while limiting current density provides information about the amount of corrosion involved and mass transfer coefficient.
- 2- More accurate measurement of surface temperature, especially for small changes, can be obtained than the limiting current density.
- 3- With increasing time, the flat plateau of limiting current will be reduced and inclined due to formation of corrosion products and increase the roughness of the surface [18] as shown in Fig. 5.12.

The corrosion potential shifts to more negative values with time as shown in Fig. 6-62. There is a rapid initial change of corrosion potential due

to the high initial corrosion rate, and then approaches a constant value. This behavior was also observed by Mahato et al. [53].

From close examination of fouling deposits forming on surface of carbon steel specimen at the end of fouling experiment, it can be observed that the corrosion products consisted of two layers, the outer layer was red brown in colour and the inner layer was greenish black. From corrosion literature [20, 53, 80], the inner layer consists of mainly ferrous hydroxide  $\text{Fe}(\text{OH})_2$  and the outer layer consists of ferric hydroxide  $\text{Fe}(\text{OH})_3$ .

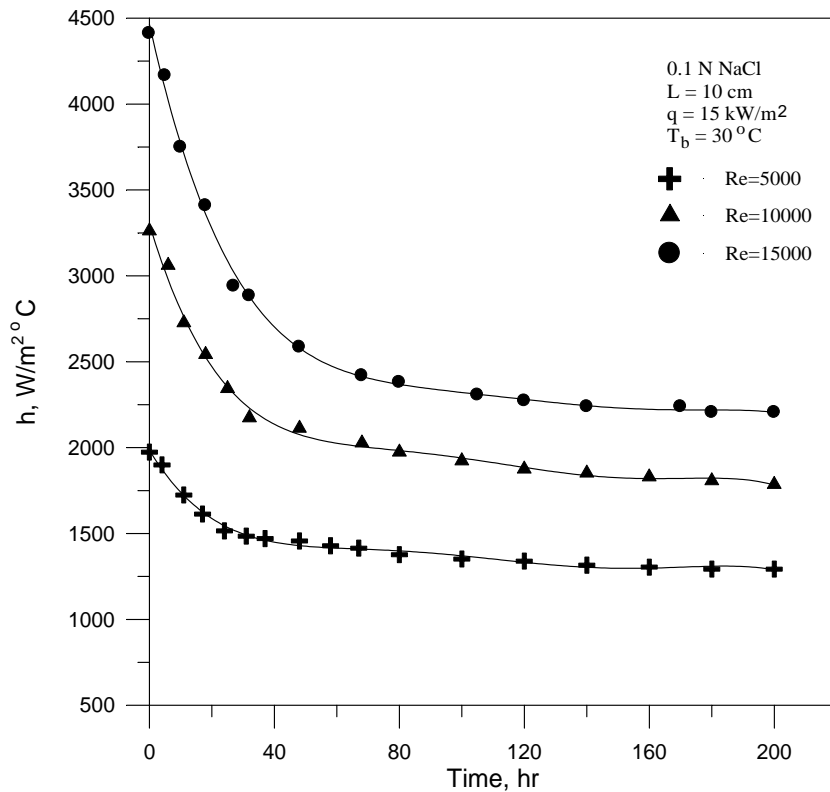


**Figure 6-59** Effect of Reynolds number on heat transfer coefficient.

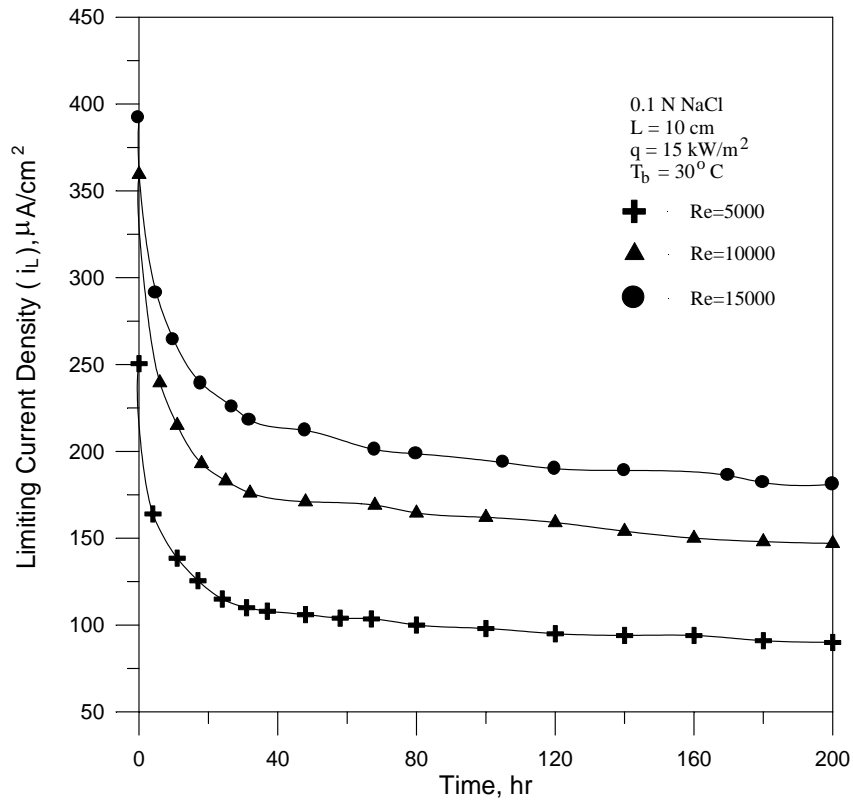


**Figure 6-60** Effect of Reynolds number on limiting current density.

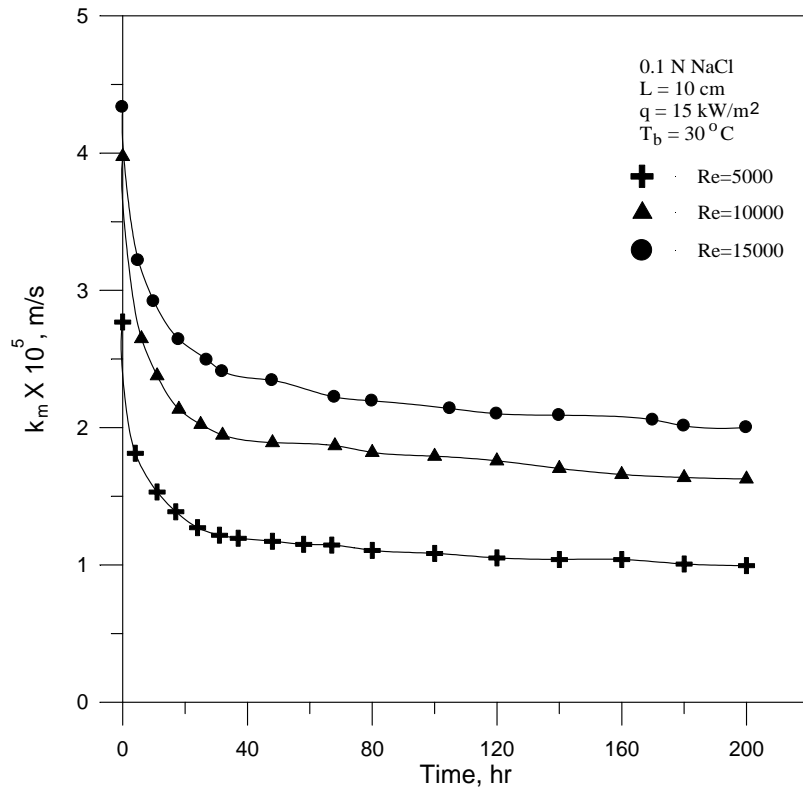


**Figure 6-61** Effect of Reynolds number on mass transfer coefficient.

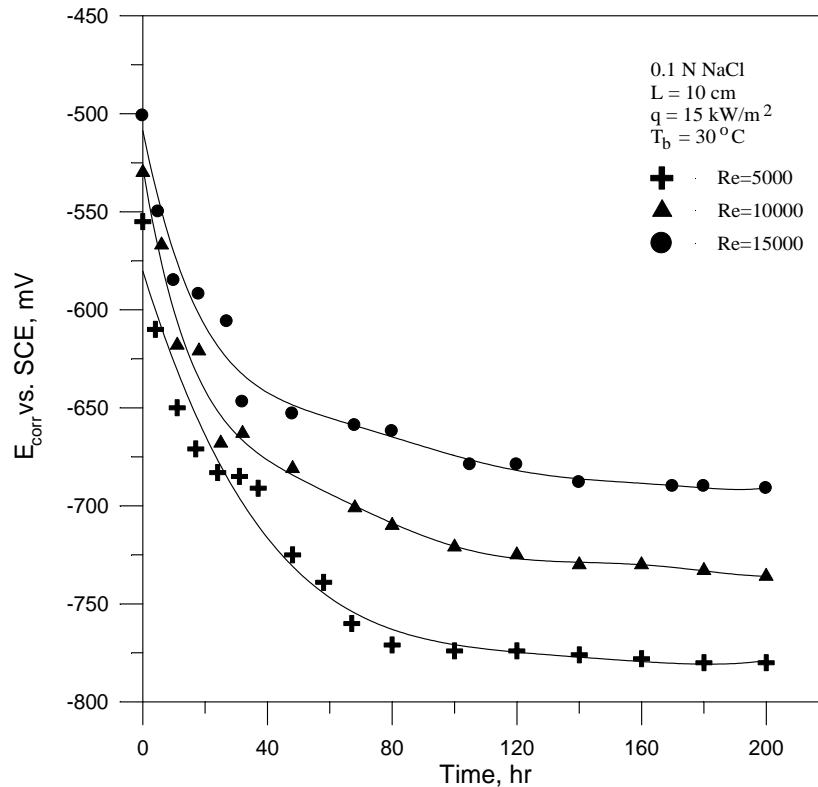


**Figure 6-62** Variation of  $E_{\text{corr}}$  with time at different Reynolds numbers.

### 6.8.1 Effect of Reynolds Number

As it is shown in Tables 5-31 to 5-33 that an increase in Reynolds number at constant bulk temperature leads to reduce the increase in surface temperature ( $T_s - T_{s,0}$ ) as shown in Fig. 6-63, and decrease the fouling thermal resistance  $R_f$  as shown in Fig. 6-58. This means that the effect of corrosion fouling on heat transfer process and heat transfer coefficient values will be reduced with increasing velocity or Reynolds number.

As stated previously that any fouling rate depends on two processes; deposition and removal. With increasing Reynolds number or velocity, the removal rate increases due to decrease in shear strength of the corrosion product deposit and this will tend to decrease the corrosion fouling effects. This decrease in  $R_f$  with increase in velocity was observed by many researchers [68, 89, 90].

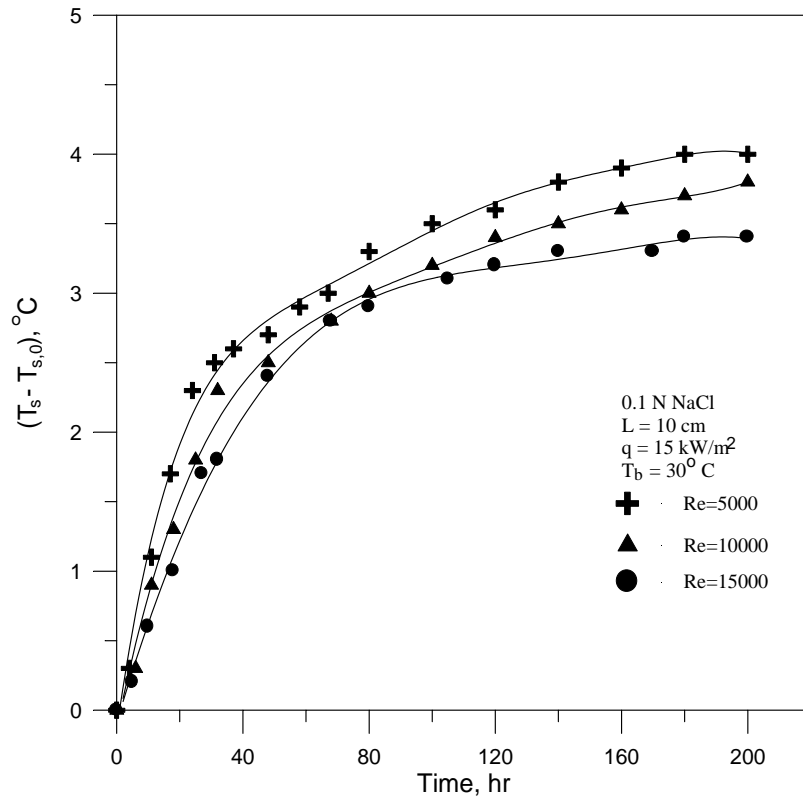


**Figure 6-63** Effect of Reynolds number on  $(T_s - T_{s,0})$ .

In order to understand the effect of velocity or Reynolds number on limiting current density  $i_L$  and mass transfer coefficient  $k_m$  with time, the following expressions are defined:

$$\% i_L \text{ red.} = \frac{i_{L,0} - i_L}{i_{L,0}} \times 100 \quad (6.19)$$

where  $i_L$  is the limiting current density at any time  $t$ .

$i_{L,0}$  is the limiting current density at  $t = 0$ .

$\% i_L \text{ red.}$  is the percentage of decrease in limiting current density with time.

and

$$\% k_m \text{ red.} = \frac{k_{m,0} - k_m}{k_{m,0}} \times 100 \quad (6.20)$$

where  $k_m$  is the mass transfer coefficient at any time  $t$ .

$k_{m,0}$  is the mass transfer coefficient at  $t = 0$ .

$\% k_m \text{ red.}$  is the percentage of decrease in mass transfer coefficient with time.

Since  $k_m$  is directly proportional to  $i_L$  according to Eq. (5.2), so:

$$\% k_m \text{ red.} = \% i_L \text{ red.} \quad (6.21)$$

$\% k_m \text{ red.}$  (or  $\% i_L \text{ red.}$ ) ranges from zero value at  $t=0$  to a final constant asymptotic value in a fashion similar to fouling thermal resistance  $R_f$ . Figure 6-64 shows that an increase in Reynolds number leads to decrease in  $\% i_L \text{ red.}$  (or  $\% k_m \text{ red.}$ ), i.e., the effect of formation of corrosion products on  $i_L$  and  $k_m$  decreases due to increase in removal rate with increasing Re at constant bulk temperature.

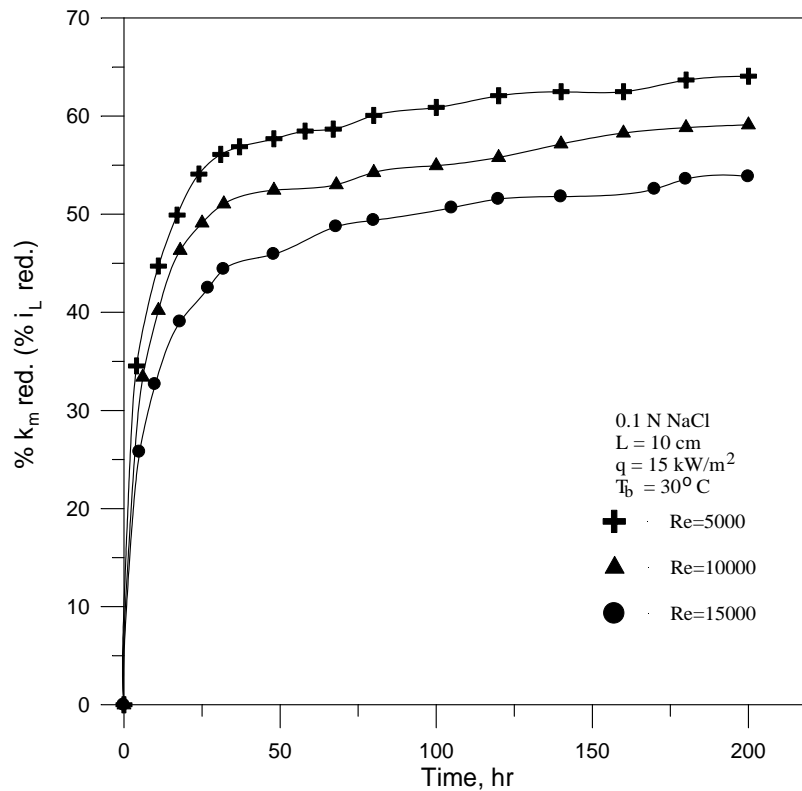


**Figure 6-64** Effect of Reynolds number on  $\% k_m \text{ red.}$  ( $\% i_L \text{ red.}$ ).

### 6.8.2 Effect of Bulk Temperature

The increase in bulk temperature leads to decrease and deteriorate the stability of corrosion layer, and this will decrease the effect of corrosion fouling [70]. On the other hand, increasing bulk temperature at constant

Reynolds number decreases the quantity (flowrate or velocity) of passing solution over the heat transfer surface, and as stated in previous section, this will lead to increase fouling effects and  $R_f$ . As shown in Tables 5-33 to 5-35 or Fig. 6-65 that increasing bulk temperature at constant Re decreases  $R_f$  but slightly. This means that the effect of bulk temperature on stability of corrosion layer is somewhat greater than the decrease in flowrate with increasing bulk temperature.

Also the increase of temperature decreases %  $i_L$  red. (or %  $k_m$  red.) due to reduced effect of corrosion fouling as shown in Fig. 6-66. Decreasing the adhesive force and stability of corrosion layer allows more oxygen to pass to the corroded heat transfer surface which increases corrosion rate. On the other hand, increasing bulk temperature at constant Re leads to decrease the velocity and removal rate of corrosion fouling products and decrease the amount of oxygen reaching the heat transfer surface. It seems that the effect of temperature on stability of corrosion fouling layer is slightly greater than the effect of solution velocity.

### 6.8.3 Correlating and Comparing of Corrosion Fouling Data

As stated previously that the corrosion fouling data obtained in the present work has the asymptotic form. Hence fouling thermal resistance data given in Tables 5-31 to 5-35 can be represented by Eq. (3.55):

$$R_f = R_f^* [1 - \exp(-bt)] \quad (3.55)$$

Table 6-2 shows the values of asymptotic fouling resistance  $R_f^*$  and the values of  $b$  obtained using regression technique.

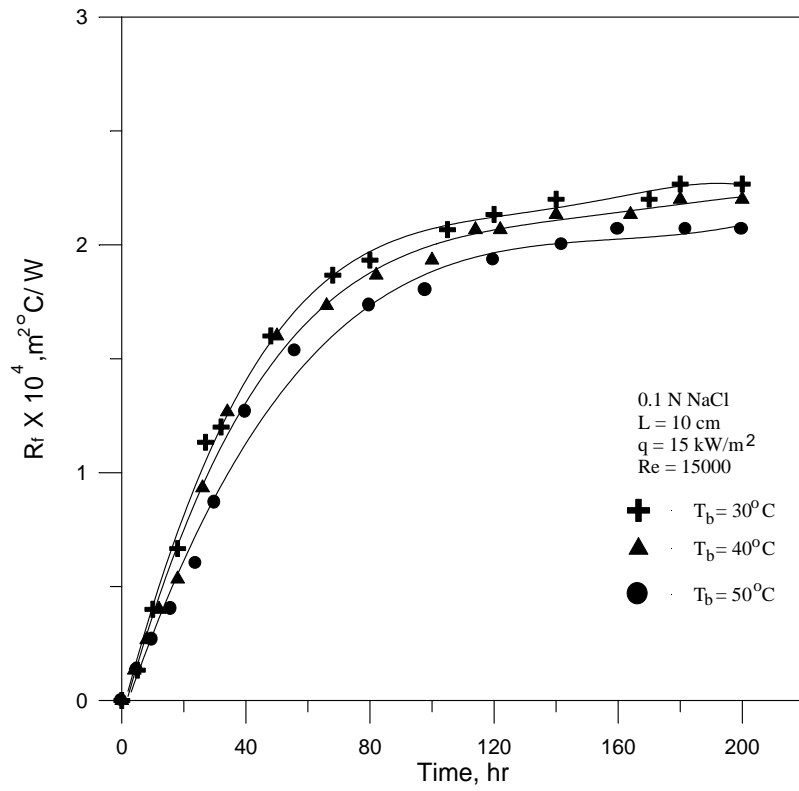


**Figure 6-65** Effect of bulk temperature on  $R_f$ .

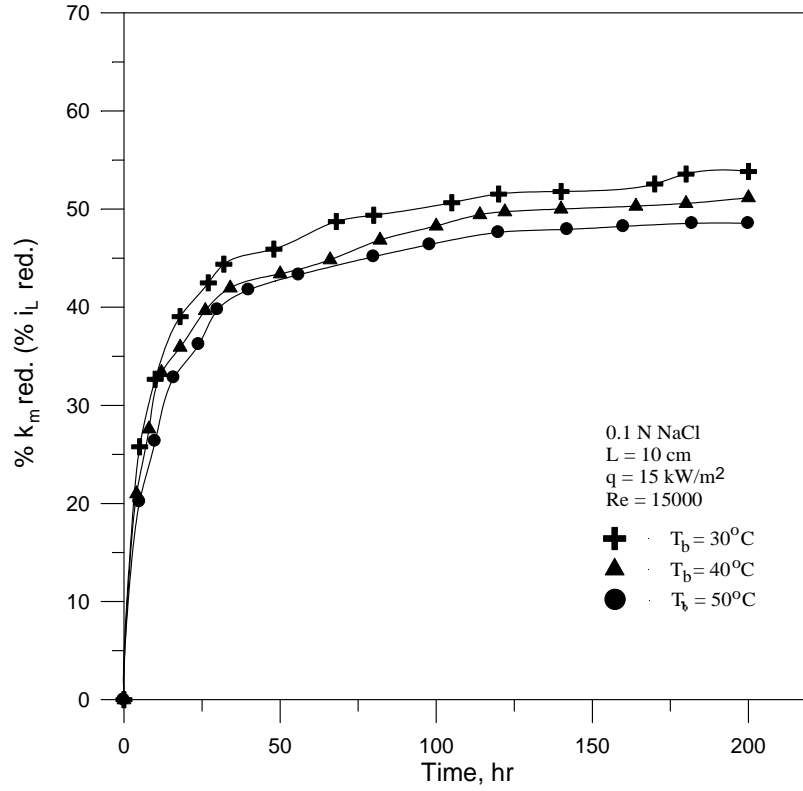


**Figure 6-66** Effect of bulk temperature on %  $k_m$  red. (%  $i_L$  red.).

Table 6-2 Values of  $R_f^*$  and  $b$  obtained using Regression technique.

Re	$T_b$ °C	$R_f^* \times 10^4$ $m^2 \text{ } ^\circ\text{C/W}$	$b$ 1/hr	Coefficient of Correlation
5000	30	2.54	0.0297	0.989
10000	30	2.43	0.0246	0.994
15000	30	2.29	0.0232	0.997
15000	40	2.24	0.0213	0.996
15000	50	2.17	0.0182	0.993

The asymptotic fouling resistance  $R_f^*$  decreases with increasing Reynolds number at constant bulk temperature, and also decreases with increasing bulk temperature at constant Reynolds number. The value of asymptotic fouling resistance  $R_f^*$  (final constant value) ranges ( $2.17 \times 10^{-4}$  -  $2.54 \times 10^{-4}$ )  $m^2 \text{ } ^\circ\text{C/W}$  with 200 hours of exposure time. These values are close to those obtained in literature and as shown in Table 6-3.

Table 6-3 Thermal fouling resistance due to corrosion given in literature<sup>†</sup>.

Reference	Material	Duration of test	$R_f, m^2 \text{ } ^\circ\text{C/W}$
McAllister et al. [68]	90-10 Cu-Ni Aluminum-Brass Admiralty-Brass 304 Stainless Steel	130 days	$3.6 \times 10^{-4}$ $3.2 \times 10^{-4}$ $3.4 \times 10^{-4}$ $6.2 \times 10^{-5}$
Griess et al. [88]	Aluminum alloys	300-500 hr	$7.0 \times 10^{-4}$ (average)
Gutzeit [89]	Admiralty-Brass Aluminum	40 days	$9.0 \times 10^{-3}$
Ritter and Sutor [90]	Copper alloy 706	1000 hr	$1.7 \times 10^{-4}$ $- 5.7 \times 10^{-4}$
Somerscales and Kassemi [80]	1010 Carbon Steel	240 hr	$2.8 \times 10^{-4}$

<sup>†</sup> For more details, see Table 3-2.

From above it can be observed that corrosion produces deposits that have considerable effect on heat transfer process. This means that corrosion fouling is significant as other categories of fouling. This can be concluded from comparing these data of corrosion fouling with values of other types of fouling found in literature. Hence the effect of corrosion fouling should be given consideration in the design of heat transfer equipment.

The values of  $R_f^*$  and  $b$  given in Table 6-2 can be correlated as functions of Reynolds number and bulk temperature by the following equations:

$$R_f^* = 2.855 \times 10^{-4} - 2.5 \times 10^{-9} \text{ Re} - 6.23 \times 10^{-7} T_b \quad (6.22)$$

and 
$$b = 3.862 \times 10^{-2} - 6.2 \times 10^{-7} \text{ Re} - 2.17 \times 10^{-4} T_b \quad (6.23)$$

The coefficient of correlation for the above two equations is 0.999 and 0.981 respectively. Substituting Eqs. (6.22) and (6.23) in Eq. (3.55) yields:

$$R_f = \left( 2.855 \times 10^{-4} - 2.5 \times 10^{-9} \text{ Re} - 6.23 \times 10^{-7} T_b \right) \times \left\{ 1 - \exp \left[ \left( -3.862 \times 10^{-2} + 6.2 \times 10^{-7} \text{ Re} + 2.17 \times 10^{-4} T_b \right) t \right] \right\} \quad (6.24)$$

which gives fouling thermal resistance  $R_f$  in ( $\text{m}^2 \text{ }^\circ\text{C}/\text{W}$ ) as a function of  $\text{Re}$ ,  $T_b$  in  $^\circ\text{C}$ , and  $t$  in hr. Graphical comparison of experimental results with results predicted by the correlation given in Eq. (6.24) is shown in Figs. 6-67 and 6-68.

Hence the value of heat transfer coefficient  $h$  at any time can be calculated using Eq. (3.46):

$$\frac{1}{h} = \frac{1}{h_c} + R_f \quad (3.46)$$

where heat transfer coefficient  $h_c$  for clean surface ( $t=0$ ) is calculated from Eq. (6.14), and  $R_f$  is calculated using Eq. (6.24). Figure 6-69 shows the experimental data of heat transfer coefficient  $h$  and the predicted values using Eq. (3.46).

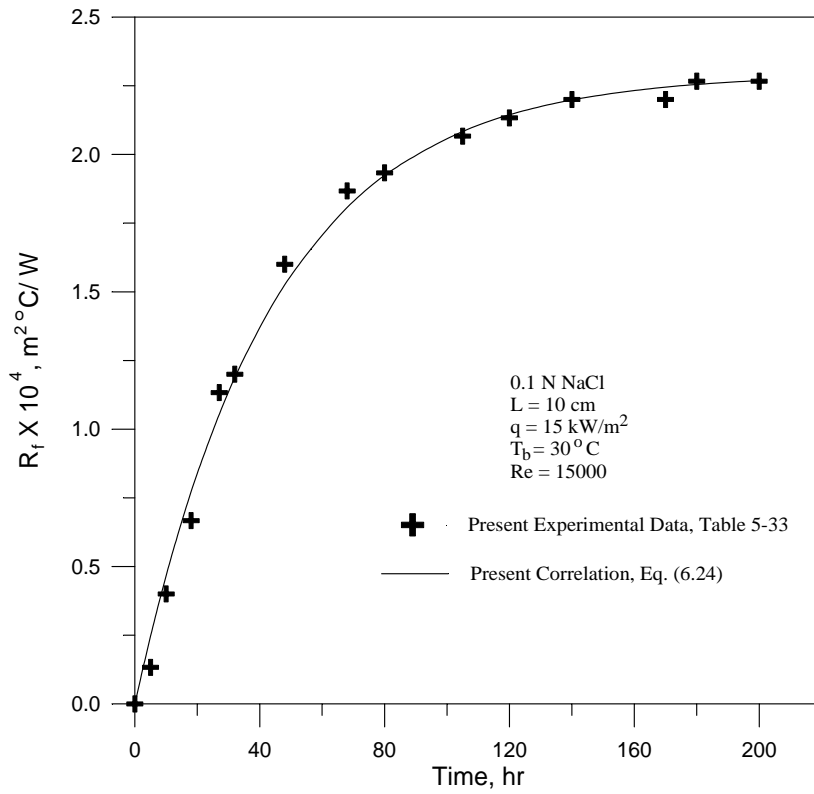


**Figure 6-67** Comparison of predicted  $R_f$  with experimental results for  $Re=15000$ , and  $T_b = 30 \text{ }^\circ\text{C}$ .

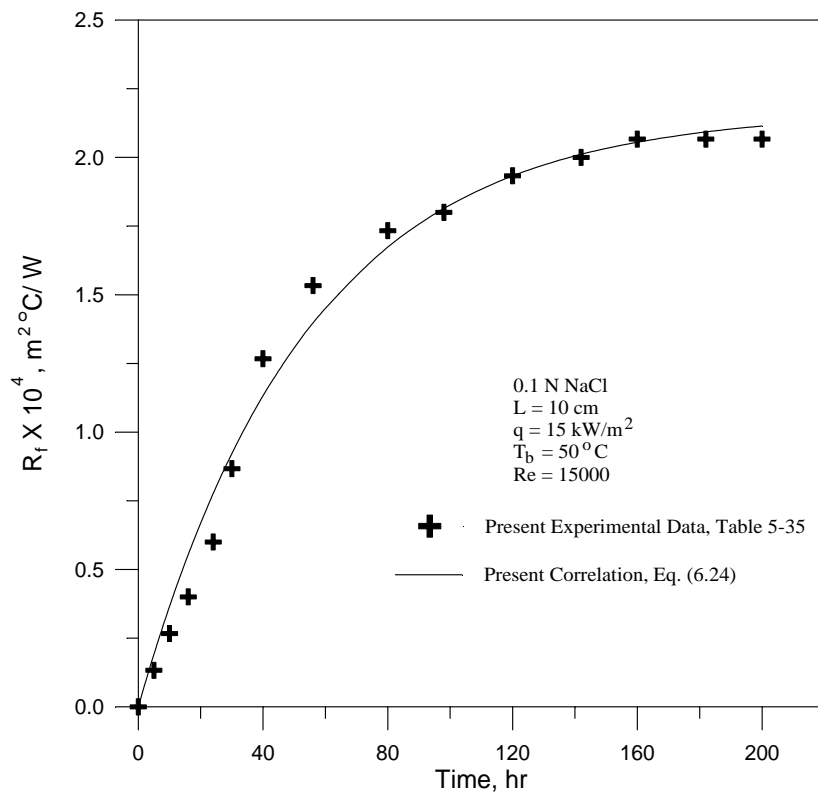


**Figure 6-68** Comparison of predicted  $R_f$  with experimental results for  $Re=15000$ , and  $T_b = 50 \text{ }^\circ\text{C}$ .

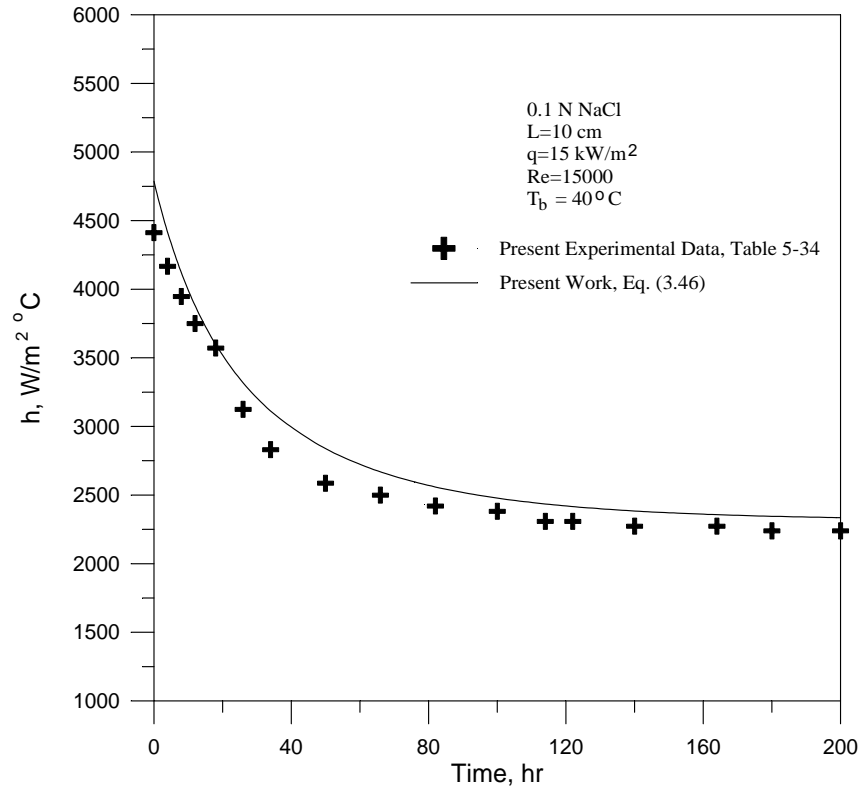


**Figure 6-69** Comparison of predicted  $h$  with experimental results for  $Re=15000$ , and  $T_b = 40$  °C .

The deviation of calculated heat transfer coefficient using Eq. (3.46) from experimental results can be presented by average absolute percentage error (AA%E) as shown in Table 6-4. This deviation is a result of the random error remaining in Eqs. (6.14) and (6.24).

Table 6-4 AA%E of heat transfer coefficient.

Re	$T_b$ , °C	AA%E of $h$
5000	30	10.29
10000	30	9.15
15000	30	8.32
15000	40	5.45
15000	50	7.72

In a similar manner, it can be obtained an asymptotic formula for (%  $k_m$  red.) with time using the following equation:

$$\% k_m \text{ red.} = (\% k_m \text{ red.})^* [1 - \exp(-b_m t)] \quad (6.25)$$

where (%  $k_m$  red.)<sup>\*</sup> is the asymptotic value (constant final value) of percentage reduction in mass transfer coefficient, and  $1/b_m$  is the time constant. The values of these two constants can be obtained using regression technique and as shown in Table 6-5.

Table 6-5 Values of (%  $k_m$  red.)<sup>\*</sup> and  $b_m$  obtained using regression technique.

Re	$T_b$ °C	(% $k_m$ red.) <sup>*</sup>	$b_m$ 1/hr	Coefficient of Correlation
5000	30	59.79	0.1458	0.975
10000	30	55.24	0.1217	0.983
15000	30	50.20	0.0990	0.977
15000	40	47.83	0.0949	0.975
15000	50	46.50	0.0768	0.986

The values of (%  $k_m$  red.)<sup>\*</sup> and  $b_m$  are functions of Reynolds number and bulk temperature, so can be correlated by the following equations:

$$(\% k_m \text{ red.})^* = 70.515 - 9.78 \times 10^{-4} \text{ Re} - 0.1907 T_b \quad (6.26)$$

$$\text{and } b_m = 0.1997 - 4.44 \times 10^{-6} \text{ Re} - 1.078 \times 10^{-3} T_b \quad (6.27)$$

The coefficients of correlation for the above two equations are 0.999 and 0.994 respectively. Substituting Eqs. (6.26) and (6.27) into Eq. (6.25) yields:

$$\% k_m \text{ red.} = \left( 70.515 - 9.78 \times 10^{-4} \text{ Re} - 0.1907 T_b \right) \times \left\{ 1 - \exp \left[ \left( -0.1997 + 4.44 \times 10^{-6} \text{ Re} + 1.078 \times 10^{-3} T_b \right) t \right] \right\} \quad (6.28)$$

Figure 6-70 shows the predicted %  $k_m$  red. using Eq. (6.28) and those of experimental results.

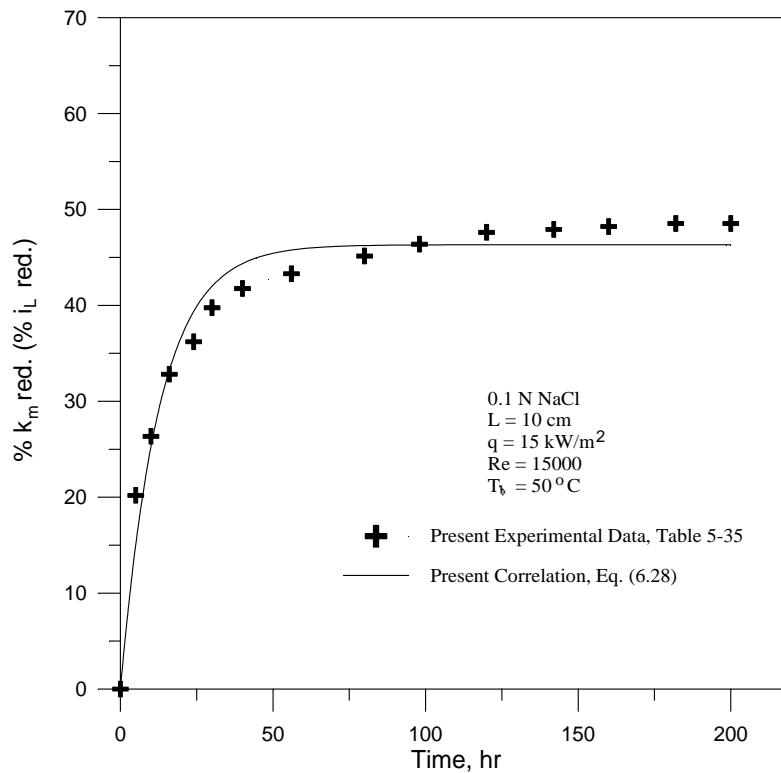


**Figure 6-70** Comparison of predicted %  $k_m$  red. with experimental results for  $Re=15000$ , and  $T_b = 50$  °C .

From Eq. (6.20), the value of mass transfer coefficient  $k_m$  at any time can be calculated as:

$$k_m = k_{m,0} \left[ 1 - \frac{\% k_m \text{ red.}}{100} \right] \quad (6.29)$$

where mass transfer coefficient  $k_{m,0}$  for clean surface ( $t=0$ ) is calculated from Eq. (6.10) or (6.11), and %  $k_m$  red. is calculated using Eq. (6.28).

Figure 6-71 shows the experimental data of mass transfer coefficient  $k_m$  and the predicted values using Eq. (6.29). Table 6-5 shows the deviation of predicted mass transfer coefficient using Eq. (6.29) from experimental results. This deviation is a result of the error remaining from Eqs. (6.10) and (6.29).

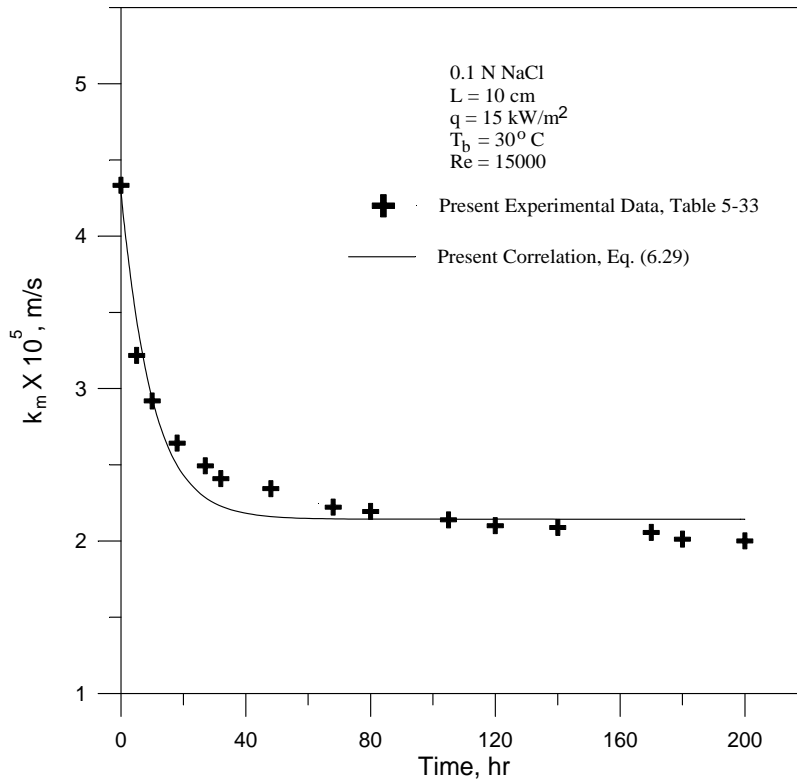


**Figure 6-71** Comparison of predicted  $k_m$  with experimental results for  $Re=15000$ , and  $T_b = 30\text{ }^\circ\text{C}$ .

Table 6-5 AA%E of mass transfer coefficient.

Re	$T_b, \text{ }^\circ\text{C}$	AA%E of $k_m$
5000	30	7.35
10000	30	6.99
15000	30	4.40
15000	40	4.92
15000	50	6.69

Plotting  $R_f^*$  against  $(\% k_m \text{ red.})^*$  and  $b$  against  $b_m$ , linear relations were obtained as shown in Figs. (6.72) and (6.73) and as given by the following equations:

$$R_f^* = 9.35 \times 10^{-5} + 2.7 \times 10^{-6} (\% k_m \text{ red.})^* \quad (6.30)$$

$$b = 0.0065 + 0.157b_m \quad (6.31)$$

The coefficients of correlation for these two equations are 0.996 and 0.982 respectively. Hence, the values of fouling thermal resistance can be predicted from percentage reduction of mass transfer coefficient values and vice versa as shown in Fig 6-74.

This means that a relation is developed for the effect of corrosion on the processes of mass (corrosion rate) and heat transport due to corrosion fouling of heat transfer surfaces. In other words, the heat transfer coefficient at any time can be predicted from mass transfer data, and mass transfer coefficient at any time can be predicted from heat transfer data. Figure 6-75 shows heat transfer coefficient at any time  $h$  predicted from mass data using Eqs. (6.18), (6.30), (6.31), (3.55), and (3.46).

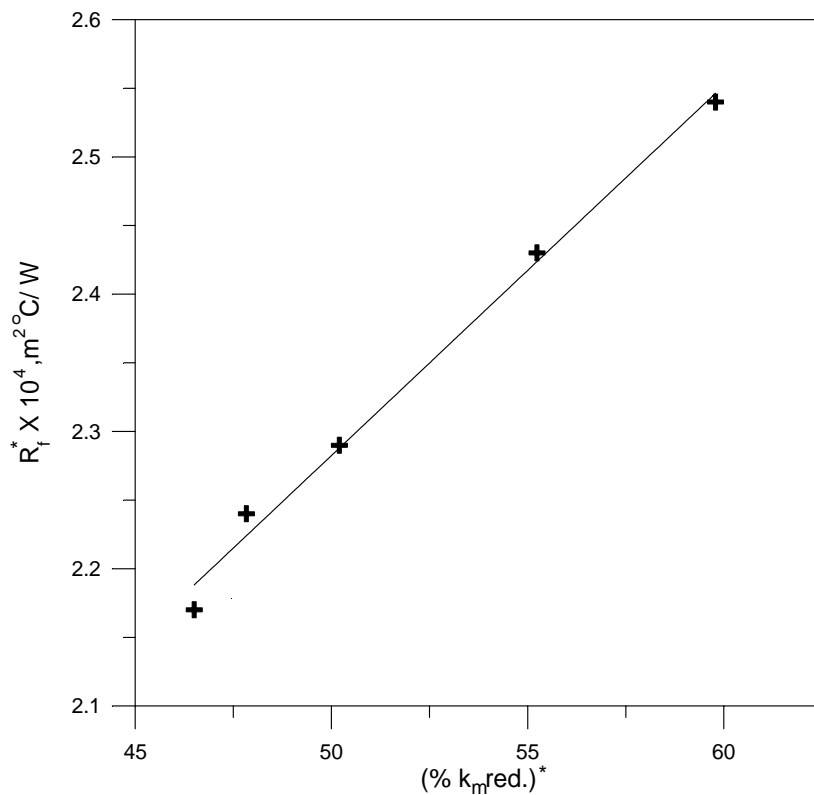


**Figure 6-72** The linear relation between  $R_f^*$  and  $(\% k_m \text{ red.})^*$ .

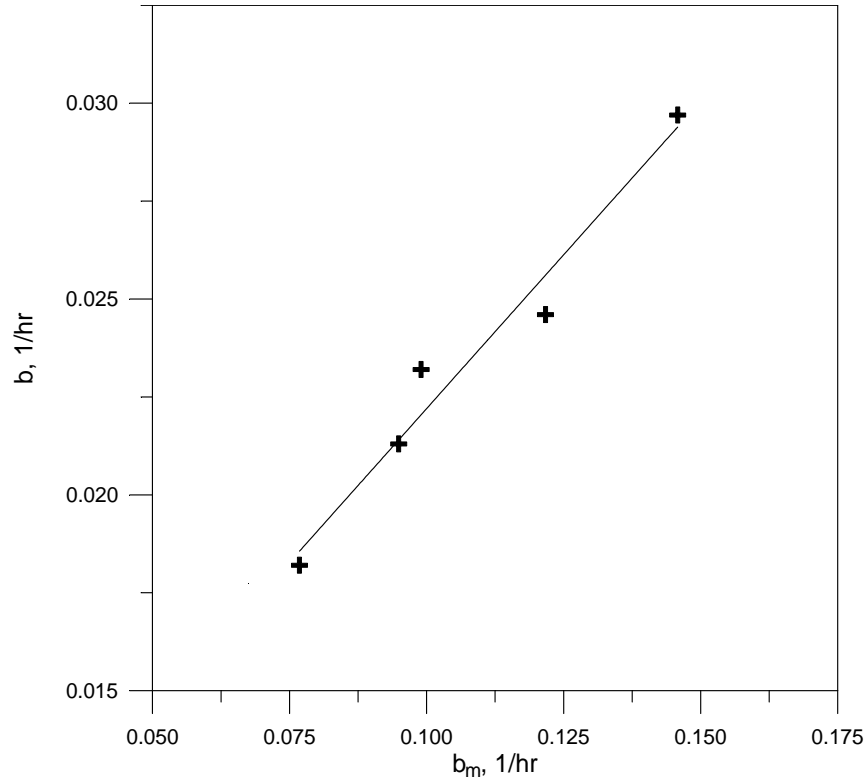


**Figure 6.73** The linear relation between  $b$  and  $b_m$ .

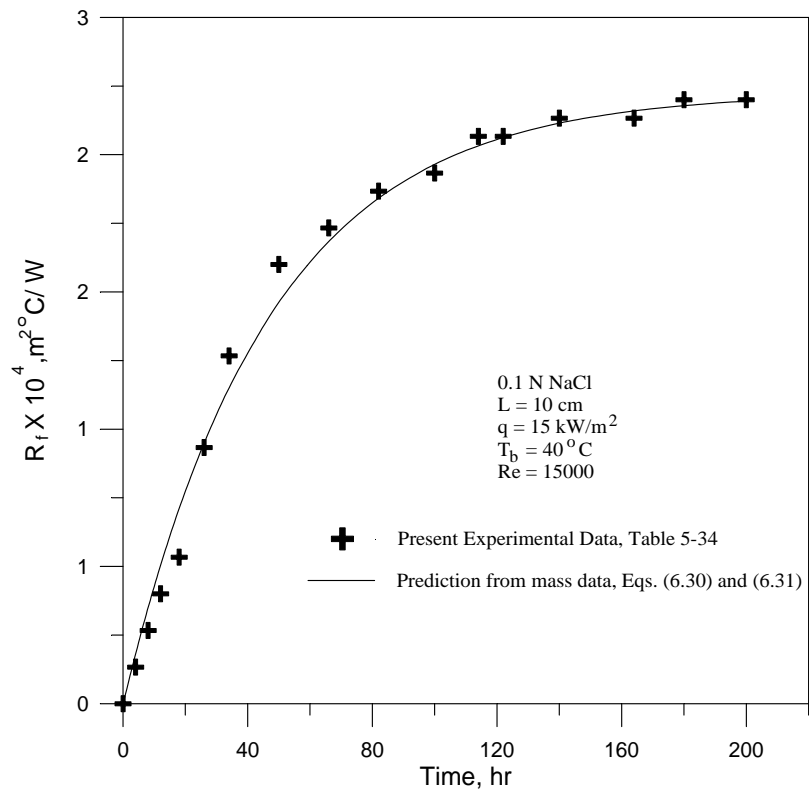


**Figure 6-74** Comparison of predicted  $R_f$  from mass data with experimental results for  $Re=15000$ , and  $T_b = 40$  °C .

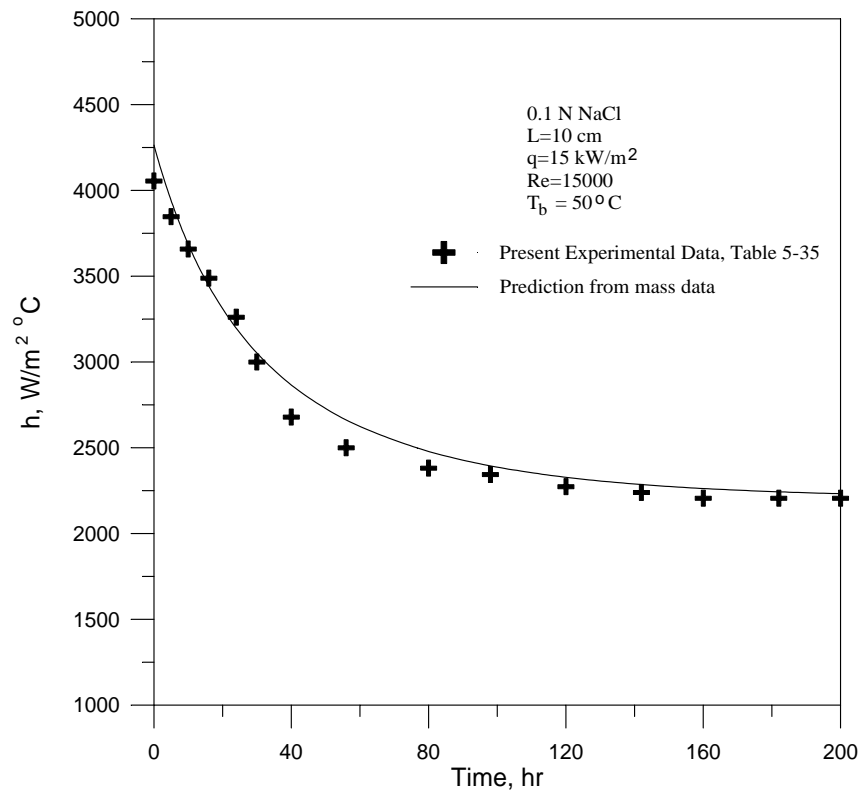


**Figure 6-75** Prediction of  $h$  from mass data for  $Re=15000$ , and  $T_b = 50$  °C .

**CHAPTER SEVEN**

**CONCLUSIONS AND  
RECOMMENDATIONS**

## 7.1 Conclusions

The following points can be concluded from the present work:

- 1- The limiting current density and the corrosion rate increase with increasing Reynolds number or velocity at constant bulk temperature. The corrosion potential level shifts to more noble (less active).
- 2- The limiting current density and corrosion rate decrease with increasing bulk temperature at constant Reynolds number. The corrosion potential level shifts to less noble (more active).
- 3- The limiting current density and corrosion rate decrease with increasing working electrode length at constant Reynolds number and bulk temperature. The corrosion potential values remain approximately close.
- 4- The limiting current density and corrosion rate increase in the presence of heat flux. The corrosion potential level shifts to more negative (more active).
- 5- The results of mass transfer show agreement with Ross and Wragg correlation, and the results of heat transfer show agreement with Davis correlation.
- 6- The analogy between heat and mass transfer was examined by Chilton-Colburn analogy and was found that  $J_h$  is larger than  $J_m$ . This inconsistency was also confirmed in their analogy.
- 7- The effect of corrosion products on heat and mass transfer processes is reduced with increasing velocity or Reynolds number and also with increasing bulk temperature.
- 8- The corrosion potential level shifts to more negative (more active) with increasing effect of corrosion deposits.
- 9- Fouling thermal resistance produced by corrosion of carbon steel surface caused by 0.1 N NaCl solution has an asymptotic form. The mass transfer

coefficient decreases with increasing the time of exposure to solution and also takes the asymptotic form. The effect of corrosion products on heat transfer rate can be predicted from their effect on mass transfer rate and vice versa.

10-Corrosion fouling of heat transfer surfaces produces a thermal resistance that is comparable to that arising from other types of fouling, and should be taken into consideration in the design of heat transfer equipments.

## **7.2 Recommendations**

The following suggestions are recommended for future work:

- 1- Extending the experiments to a range of temperature greater than 50 °C , and heat flux range greater than 45 kW/m<sup>2</sup>.
- 2- Studying the effect of using inhibitor on the corrosion rate under isothermal and heat transfer conditions.
- 3- Changing the electrode length and the radius ratio to study their effect on corrosion rate and on heat transfer process.
- 4- Extending the duration time of fouling experiments to a larger period.
- 5- Performing a detailed physical examination and chemical analysis of the corrosion deposits.

## **REFERENCES**

## References

- 1- Coulson, J. M., and J. F. Richardson, *Chemical Engineering*, Vol. **1**, Butterworth-Heinemann, 5th Edition, (1998).
- 2- Holland, F. A., *Fluid Flow for Chemical Engineers*, Edward Arnold, (1980).
- 3- Geankoplis, C. J., *Transport Processes and Unit Operations*, Prentice Hall, 3rd Edition, (1993).
- 4- Carpenter, E. G., A. P., Colburn, E. M. Schoenborn, and A. Wurster, *Trans. Amer. Inst. Chem. Engrs.*, **42**, 165, (1946).
- 5- Knudsen, J. G., *Amer. Inst. Chem. Engrs.*, J. **8**, 565, (1962).
- 6- Rothfus, R. R., C. C. Monrad, K. G. Sikchi, and W. J. Heideger, *Industr. Engng. Chem.*, **47**, 913, (1955).
- 7- Holman, J. P., *Heat Transfer*, McGraw-Hill Inc., 8th Edition, (1997).
- 8- Treybal, R. E., *Mass Transfer Operation*, McGraw-Hill Inc., 3rd Edition, (1981).
- 9- Schlichting, H., *Boundary Layer Theory*, McGraw-Hill Inc., 6th Edition, (1968).
- 10- Brodkey, R. S., and H. C. Hershey, *Transport Phenomena: A Unified Approach*, McGraw-Hill Inc., (1988).
- 11- Welty, J. R., C. E. Wicks, R. E. Wilson, and G. L. Rorrer, *Fundamentals of Momentum, Heat, and Mass Transfer*, John Wiley and Sons, 4th Edition, (2001).
- 12- Fischer, P., J. W. Sutor, and R. B. Ritter, *Chem. Eng. Progress*, Vol. **71**, No. 7, pp. 66-72, (1975).
- 13- McAdams, W. H., *Heat Transmission*, McGraw-Hill Inc., 3rd Edition, (1954).
- 14- Chapman, A. J., *Heat Transfer*, Macmillan Publishing Company, 4th Edition, (1984).
- 15- Monrad, C. C., and J. F. Pelton, *Trans. Amer. Inst. Chem. Engrs.*, **38**, 165, (1942).
- 16- Davis, E. S., *Trans. Amer. Soc. Mech. Engrs.*, **65**, 755, (1943).
- 17- Poulson, B., and R. Robinson, *Corrosion Science*, Vol. **26**, No. 4, pp. 265-280, (1986).
- 18- Selman, J. R., *AICHE Symposium Series*, 204, *Tutorial Lectures in Electrochemical Engineering and Technology*, Vol. **77**, pp. 88-102, (1981).
- 19- Chilton, T. H., and A. P. Colburn, *Ind. Eng. Chem.*, Vol. **26**, No. 11, pp. 1183-1186, (1934).
- 20- Uhlig, H. H., and R. W. Revie, *Corrosion and Corrosion Control*, John Wiley and Sons, 3rd Edition, (1985).

- 21- Kruger, J., Electrochemistry of Corrosion, Electrochemistry Encyclopedia, (from internet, <http://electrochem.cwru.edu/ed/encycl/>), April (2001).
- 22- Fontana, M. G., and N. D. Greene, Corrosion Engineering, McGraw-Hill Inc., 2nd Edition, (1978).
- 23- Pickett, D. J., Electrochemical Reactor Design, Elsevier Scientific Publishing Company, 2nd Edition, (1979).
- 24- Tobias, C. W., Advances in Electrochemistry and Electrochemical Engineering, Vol. **2**, John Wiley and Sons, (1966).
- 25- Shreir, L. L., Corrosion, Vol. **1**, Newnes-Butterworths, 2nd Edition, (1976).
- 26- Steigerwald, R. F., Corrosion, Vol. **24**, pp. 1-10, (1968).
- 27- Mizushima, T., "The Electrochemical Method in Transport Phenomena," Advances in Heat Transfer, Academic Press Book Company, Vol. **7**, pp. 87-161, (1971).
- 28- Selman, J. R., and C. W. Tobias, "Mass-Transfer Measurements by the Limiting-Current Technique," Advances in Chemical Engineering, Academic Press Book Company, Vol. **10**, pp. 211-318, (1978).
- 29- Lin, C. S., E. B. Denton, H. S. Gaskill, and G. L. Putnam, Ind. Eng. Chem., Vol. **43**, No. 9, pp. 2136-2143, (1951).
- 30- Ross, T. K., and A. A. Wragg, Electrochimica Acta, Vol. **10**, pp. 1093-1106, (1965).
- 31- Wragg, A. A., and T. K. Ross, *ibid.*, Vol. **13**, pp. 2192-2194, (1968).
- 32- ———, *ibid.*, Vol. **12**, pp. 1421-1428, (1967).
- 33- Wragg, A. A., *ibid.*, Vol. **16**, pp. 373-381, (1971).
- 34- Newman, J., Ind. Eng. Chem., Vol. **60**, No. 4, pp. 12-27, (1968).
- 35- Bazan, J. C., and A. J. Arvia, Electrochimica Acta, Vol. **9**, pp. 17-30, (1964).
- 36- ———, *ibid.*, Vol. **9**, pp. 667-684, (1964).
- 37- Coeuret, F., P. LeGoff, and F. Vergnes, Proc. Int. Symp. Fluidization, Eindhoven, **1**, 537, (1967), [Cited in 28].
- 38- Coeuret, F., F. Vergnes, and P. LeGoff, Houille Blanche, 275, (1969), [Cited in 28].
- 39- Carbin, D. C., and D. R. Gabe, Electrochimica Acta, Vol. **19**, 645, (1974).
- 40- ———, *ibid.*, Vol. **19**, 653, (1974).
- 41- Regner, A., and I. Rousar, Coll. Trav. Chim. Tchechoslov., **25**, 1132, (1960), [Cited in 28].
- 42- Jagannadharaju, G. J. V., and C. V. Rao, Indian J. Technol., **3**, 201, (1965).

- 43- Krishna, M. S., G. J. V. Jagannadharaju, and C. V. Rao, *ibid.*, **4**, 8, (1966).
- 44- Krishna, M. S., and G. J. V. Jagannadharaju, *ibid.*, **4**, 97, (1966).
- 45- Krishna, M. S., *ibid.*, **10**, 163, (1972).
- 46- Crittenden, B. D., "Basic Science and Models of Reaction Fouling", *Fouling Science and Technology*, NATO ASI Series, edited by L. F. Melo, T. R. Bott, and C. A. Bernardo, Kluwer Academic Publishers, pp. 293-313, (1988).
- 47- Akimov, G. V., *Corrosion*, Vol. **14**, pp. 463t-483t, (1958).
- 48- West, J. M., *Electrodeposition and Corrosion Processes*, Van Nostrand Reinhold Company, 2nd Edition, (1971).
- 49- Jovancicevic, V., and J. O. M., *J. Electroanal. Chem.*, Vol. **133**, pp. 1797-1807, (1986).
- 50- Anastasijevic, N. A., V. Vesovic, and R. R. Adzic, *ibid.*, Vol. **229**, pp. 305-325, (1987).
- 51- Zecevic, S., D. M. Drazic, and S. Gojkovic, *ibid.*, Vol. **265**, pp. 179-193, (1989).
- 52- Shreir, L. L., *Corrosion*, Vol. **2**, Newnes-Butterworths, 2nd Edition, (1976).
- 53- Mahato, B. K., S. K. Voora, and L. W. Shemilt, *Corrosion Science*, Vol. **8**, pp. 173-193, (1968).
- 54- Evans, U. R., *An Introduction to Metallic Corrosion*, Edward Arnold Ltd., 2nd Edition, (1963).
- 55- Friend, J. N., *J. Iron Steel Inst.*, **11**, 62, 128, (1922), [Cited in 53].
- 56- Evans, U. R., *The Corrosion and Oxidation of Metals*, Edward Arnold Ltd., (1960).
- 57- Speller, F. N., and V. V. Kendall, *Ind. Eng. Chem.*, **15**, 134, (1923).
- 58- Whitman, W. G., *Chem. Rev.*, **2**, 419, (1925), [Cited in 53].
- 59- Cox, C. L., and B. E. Roetheli, *Ind. Eng. Chem.*, **23**, 1012, (1931).
- 60- Cohen, M., *J. Electrochem. Soc.*, **93**, 26, (1948).
- 61- Butler, G., and E. G. Stroud, *J. Appl. Chem.*, **15**, 325, (1965).
- 62- Roetheli, B. E., and R. H. Brown, *Ind. Eng. Chem.*, **23**, 1010, (1931).
- 63- Butler, G., and H. C. K. Ison, *J. Appl. Chem.*, **10**, 80, (1960).
- 64- Mahato, B. K., F. R. Steward, and L. W. Shemilt, *Corrosion Science*, Vol. **8**, pp. 737-749, (1968).
- 65- Butler, G., and E. G. Stroud, *Br. Corrosion J.*, Vol. **1**, pp. 110-119, (1965).
- 66- Wormwell, F., *J. Iron Steel Inst.*, **154**, 219P, (1946).
- 67- Wormwell, F., T. J. Nurse, and H. C. K. Ison, *J. Appl. Chem.*, **3**, 275, (1953).

- 68- McAllister, R. A., D. H. Eastham, N. A. Dougharty, and M. Hollier, *Corrosion*, Vol. **17**, pp. 579t-588t, (1961).
- 69- Bahar, S. S., M.Sc. Thesis, AL-Nahrain University, Baghdad, (2002).
- 70- Ross, T. K., *Br. Corrosion J.*, **2**, 131, (1967).
- 71- Porter, D. T., M. Donimirska, and R. Wall, *Corrosion Science*, Vol. **8**, pp. 833-843, (1968).
- 72- Zarubin, P. I., Doc. Thesis, Moscow, Mos. Inst. Khim. Mash., (1968), [Cited in 74].
- 73- Ashford, J. H., R. Garnsey, and G. M. W. Mann, *Corrosion Science*, Vol. **14**, pp. 515-525, (1974).
- 74- Parshin, A. G., V. S. Pakhomov, and YA. M. Kolotyркиn, *Corrosion Science*, Vol. **22**, No. 9, pp. 845-855, (1982).
- 75- AL-Mashta, S. E., M.Sc. Thesis, AL-Nahrain University, Baghdad, (1996).
- 76- AL-Auasi, B. O. H., Ph.D. Thesis, AL-Nahrain University, Baghdad, (2003).
- 77- Taborek, J., T. Aoki, R. B. Ritter, J. W. Palen, and J. G. Knudsen, *Chem. Eng. Progress*, Vol. **68**, No. 2, pp. 59-67, (1972).
- 78- Pinheiro, Joao De Deus R. S., "Fouling of Heat Transfer Surfaces", *Heat Exchangers; Thermal-Hydraulic Fundamentals and Design*, edited by S. Kakas, A. E. Bergles, and F. Mayinger, Hemisphere Publishing Corporation, pp. 1013-1035, (1981).
- 79- O'callaghan, M. G., "Fouling of Heat Transfer Equipment: Summary Review", *ibid.*, pp. 1037-1047, (1981).
- 80- Somerscales, E. F. C., and M. Kassemi, *Transactions of ASME, J. of Heat Transfer*, Vol. **109**, pp. 267-271, (1987).
- 81- Somerscales, E. F. C., "Corrosion Fouling: Liquid Side", *Fouling Science and Technology*, NATO ASI Series, edited by L. F. Melo, T. R. Bott, and C. A. Bernardo, Kluwer Academic Publishers, pp. 621-635, (1988).
- 82- Collier, J. G., "Heat Exchanger Fouling and Corrosion", *Heat Exchangers; Thermal-Hydraulic Fundamentals and Design*, edited by S. Kakas, A. E. Bergles, and F. Mayinger, Hemisphere Publishing Corporation, pp. 999-1011, (1981).
- 83- Kern, D. Q., and R. E. Seaton, *Br. Chem. Eng.*, Vol. **4**, pp. 258-262, (1959).
- 84- Somerscales, E. F. C., "Fundamentals of Corrosion Fouling", *Experimental Thermal and Fluid Science*, Elsevier Science Inc., **14**, pp. 335-355, (1997).
- 85- ———, *Br. Corrosion J.*, Vol. **34**, No. 2, pp. 109-124, (1999).
- 86- ———, *ibid.*, Vol. **21**, No. 4, pp. 213-220, (1986).

- 87- Somerscales, E. F. C., T. E. Dugan, and S. T. Tse, "Corrosion Fouling on Aluminum Heat Transfer Surface", Condenser Biofouling Control, Proc. Symp., Lake Buena Vista, FL, Electric Power Research Institute, pp. 2-87-2-96, June, Palo Alto, CA, (1985), [Cited in 84, 85].
- 88- Griess, J. C., H. C. Savage, and J. L. English, "Effect of Heat Flux on the Corrosion of Aluminum by Water", Part IV, Report ORNL-3541, US Atomic Energy Commission, Oak Ridge, TN, (1964), [Cited in 84, 85].
- 89- Gutzeit, J., *Materials Protection*, Vol. **4**, pp. 28-34, (1965).
- 90- Ritter, R. B., and J. W. Suitor, "Fouling Research on Copper and its Alloys: Sea Water", Progress Report, Heat Transfer Research Inc., Alhambra, CA, (1976), [Cited in 84, 85].
- 91- Hubbard, D. W., and E. N. Lightfoot, *Ind. Eng. Chem. Fundamentals*, Vol. **5**, No. 3, pp. 370-379, (1966).
- 92- Berger, F. P., and K.-F. F.-L. Hau, *Int. J. Heat Mass Transfer*, Vol. **20**, pp. 1185-1194, (1977).
- 93- Fand, R. M., *ibid.*, Vol. **8**, pp. 995-1010, (1965).
- 94- Quarmby, A., and A. A. M. AL-Fakhri, *ibid.*, Vol. **23**, pp. 463-469, (1980).
- 95- Muller-Steinhagen, H., F. Reif, N. Epstein, and A. P. Watkinson, *Proc. 8th Int. Heat Transfer Conf.*, San Francisco, Vol. **5**, pp. 2555-2560, (1986).
- 96- Hines, J. G., *Br. Corrosion J.*, Vol. **18**, No. 1, pp. 10-14, (1983).
- 97- Gabe D. R., and P. A. Mankanjoula, *EFCF Publication Series*, No. 15, *Electrochemical Engineering*, AIChE Symposium Series, No. 98, pp. 309-318, Pergamon Press, (1986).
- 98- Makrides, A. C., *J. Electrochem. Soc.*, Vol. **107**, pp. 869-877, (1960).
- 99- Von Show, P., L. P. Reiss, and T. J. Hanratty, *AIChE J.*, Vol. **9**, pp. 362-364, (1963).
- 100- Gay, B., N. V. Mackley, and J. D. Jenkins, *Int. J. Heat Mass Transfer*, Vol. **19**, pp. 995-1002, (1976).
- 101- Allen R. W., and E. R. G. Eckert, *J. of Heat Transfer*, *Transactions of the ASME*, August, 301, (1964).
- 102- Friend, W. L., and A. B. Metzner, *AIChE J.*, Vol. **4**, No. 3, 393, (1958).
- 103- Acosta R. E., R. H. Muller, and C. W. Tobias, *ibid.*, Vol. **31**, No. 3, 473, (1985).
- 104- Kentucky Electric Steel Inc., *Carbon Steel Grades*, (2000), Internet: <http://www.Kentuckyelectricsteel.com>.
- 105- Scot Forge, *Carbon Steel Chart*, (2001), Internet: <http://www.scotforge.com>.

- 106- Kurita Handbook of Water Treatment, Kurita Water Industries Ltd., Tokyo, (1985).
- 107- Akgerman, A., and J. L. Gainer, J. Chem. Eng. Data, Vol. **17**, No. 3, pp. 372-377, (1972).
- 108- Hung, G. W., and R. H. Dinius, *ibid.*, Vol. **17**, pp. 449-452, (1972).

# **APPENDICES**

**APPENDIX A**  
**CALIBRATION OF FLOWMETER**

$Q_{\text{flow(ref.)}}$ (l/hr) at 20° C H <sub>2</sub> O	$Q_{\text{flow}}$ (l/hr)		
	30° C	40° C	50° C
500	505	510	512
1000	1020	1025	1031
1500	1536	1550	1560
2000	2045	2060	2076
2500	2551	2555	2560
3000	3063	3072	3080

## APPENDIX B

### CARBON STEEL GRADES

American Iron and Steel Institute (AISI) [104, 105] gives compositions of common carbon steel grades. Compositions given are in weight %.

AISI	C	Mn	P(max.)	S(max.)
1005	0.06 max.	0.35 max.	0.04	0.05
1006	0.08 max.	0.25-0.40	0.04	0.05
1008	0.10 max.	0.30-0.50	0.04	0.05
1010	0.08-0.13	0.30-0.60	0.04	0.05
1011	0.08-0.13	0.60-0.90	0.04	0.05
1012	0.10-0.15	0.30-0.60	0.04	0.05
1013	0.11-0.16	0.50-0.80	0.04	0.05
1015	0.13-0.18	0.30-0.60	0.04	0.05
1016	0.13-0.16	0.60-0.90	0.04	0.05
1017	0.15-0.20	0.30-0.60	0.04	0.05
1018	0.15-0.20	0.60-0.90	0.04	0.05
1019	0.15-0.20	0.70-1.00	0.04	0.05
1020	0.18-0.23	0.30-0.60	0.04	0.05
1021	0.18-0.23	0.60-0.90	0.04	0.05
1022	0.18-0.23	0.70-1.00	0.04	0.05
1023	0.20-0.25	0.30-0.60	0.04	0.05
1025	0.22-0.28	0.30-0.60	0.04	0.05
1026	0.22-0.28	0.60-0.90	0.04	0.05
1029	0.25-0.31	0.60-0.90	0.04	0.05
1030	0.28-0.34	0.60-0.90	0.04	0.05
1034	0.32-0.38	0.50-0.80	0.04	0.05
1035	0.32-0.38	0.60-0.90	0.04	0.05
1037	0.32-0.38	0.70-1.00	0.04	0.05
1038	0.35-0.42	0.60-0.90	0.04	0.05
1039	0.37-0.44	0.70-1.00	0.04	0.05
1040	0.37-0.40	0.60-0.90	0.04	0.05
1042	0.40-0.47	0.60-0.90	0.04	0.05
1043	0.40-0.47	0.70-1.00	0.04	0.05
1044	0.43-0.50	0.30-0.60	0.04	0.05
1045	0.43-0.50	0.60-0.90	0.04	0.05
1046	0.43-0.50	0.70-1.00	0.04	0.05

AISI	C	Mn	P(max.)	S(max.)
1049	0.46-0.53	0.60-0.90	0.04	0.05
1050	0.48-0.55	0.60-0.90	0.04	0.05
1053	0.48-0.55	0.70-1.00	0.04	0.05
1055	0.50-0.60	0.60-0.90	0.04	0.05
1059	0.55-0.65	0.50-0.80	0.04	0.05
1060	0.55-0.65	0.60-0.90	0.04	0.05
1064	0.60-0.70	0.50-0.80	0.04	0.05
1065	0.60-0.70	0.60-0.90	0.04	0.05
1069	0.65-0.75	0.40-0.70	0.04	0.05
1070	0.65-0.75	0.60-0.90	0.04	0.05
1071	0.65-0.75	0.75-1.05	0.04	0.05
1074	0.70-0.80	0.50-0.80	0.04	0.05
1075	0.70-0.80	0.40-0.70	0.04	0.05
1078	0.72-0.85	0.30-0.60	0.04	0.05
1080	0.75-0.88	0.60-0.90	0.04	0.05
1084	0.80-0.93	0.60-0.90	0.04	0.05
1086	0.80-0.93	0.30-0.50	0.04	0.05
1090	0.85-0.98	0.60-0.90	0.04	0.05
1095	0.90-1.03	0.30-0.50	0.04	0.05

## APPENDIX C

### C.1 Physical Properties of Water at Atmospheric Pressure [106]

$T$ °C	$\rho$ kg/m <sup>3</sup>	$\mu \times 10^3$ kg/m.s	$C_P$ kJ/kg.°C	$k$ W/m.°C	Pr
30	995.7	0.801	4.176	0.614	5.448
32	995.1	0.768	4.176	0.616	5.206
34	994.4	0.737	4.176	0.619	4.972
36	993.7	0.709	4.176	0.622	4.760
38	993.0	0.681	4.176	0.625	4.550
40	992.2	0.656	4.176	0.627	4.369
42	991.5	0.632	4.176	0.629	4.196
44	990.1	0.610	4.176	0.632	4.031
46	989.8	0.588	4.180	0.634	3.877
48	989.0	0.568	4.180	0.637	3.727
50	988.1	0.549	4.180	0.640	3.586
52	987.2	0.532	4.180	0.642	3.464
54	986.2	0.515	4.180	0.644	3.343
56	985.3	0.499	4.180	0.647	3.224
58	984.3	0.483	4.184	0.649	3.114
60	983.2	0.469	4.184	0.651	3.014
62	982.2	0.455	4.184	0.654	2.911
64	981.1	0.442	4.184	0.655	2.823
66	980.0	0.429	4.184	0.657	2.732
68	979.0	0.417	4.188	0.659	2.650
70	977.8	0.406	4.188	0.661	2.572

## C.2 Electroconductivity of Sodium Chloride Solution

The electroconductivity of 0.1N NaCl solution was measured using digital electroconductivity meter (Acon Con 6 series Type) at different temperatures.

$T (^{\circ}\text{C})$	30	40	50
E.C. (m mohs/cm)	9.53	11.34	13.29

## C.3 Solubility of Oxygen

The solubility of  $\text{O}_2$  or dissolved oxygen concentration in 0.1 N NaCl solution was measured using dissolved oxygen meter (model 810A plus, Orion).

$T (^{\circ}\text{C})$	30	40	50	60
$C_b$ (mg/l)	7.50	6.35	5.60	4.72

## C.4 Diffusivity of Oxygen

Akgerman and Gainer [107] reported the experimental values of diffusion coefficient of oxygen in water at different temperatures. These values are then corrected for diffusion in 0.1 N NaCl according to the method suggested by Hung and Dinius [108]:

$$D = D_o (1 - K\sqrt{C}) \quad (\text{C.1})$$

where  $D$  and  $D_o$  are the diffusivity of oxygen in the electrolyte solution and in pure water respectively,  $K$  is constant and equal to about 0.482 for range (0.1-

1)  $N$  NaCl, and  $C$  is the normality of NaCl solution. The values of diffusion coefficients of oxygen are tabulated below:

$T (^{\circ}C)$	$D_o \times 10^9 (m^2/s)$ Pure water	$D \times 10^9 (m^2/s)$ 0.1 N NaCl
30	2.80	2.37
37	3.00	2.54
40	3.56	3.02
50	4.20	3.56
55	4.50	3.81
60	5.70	4.83

# APPENDIX D

## D.1 Cathodic Polarization Curves Under Isothermal Conditions

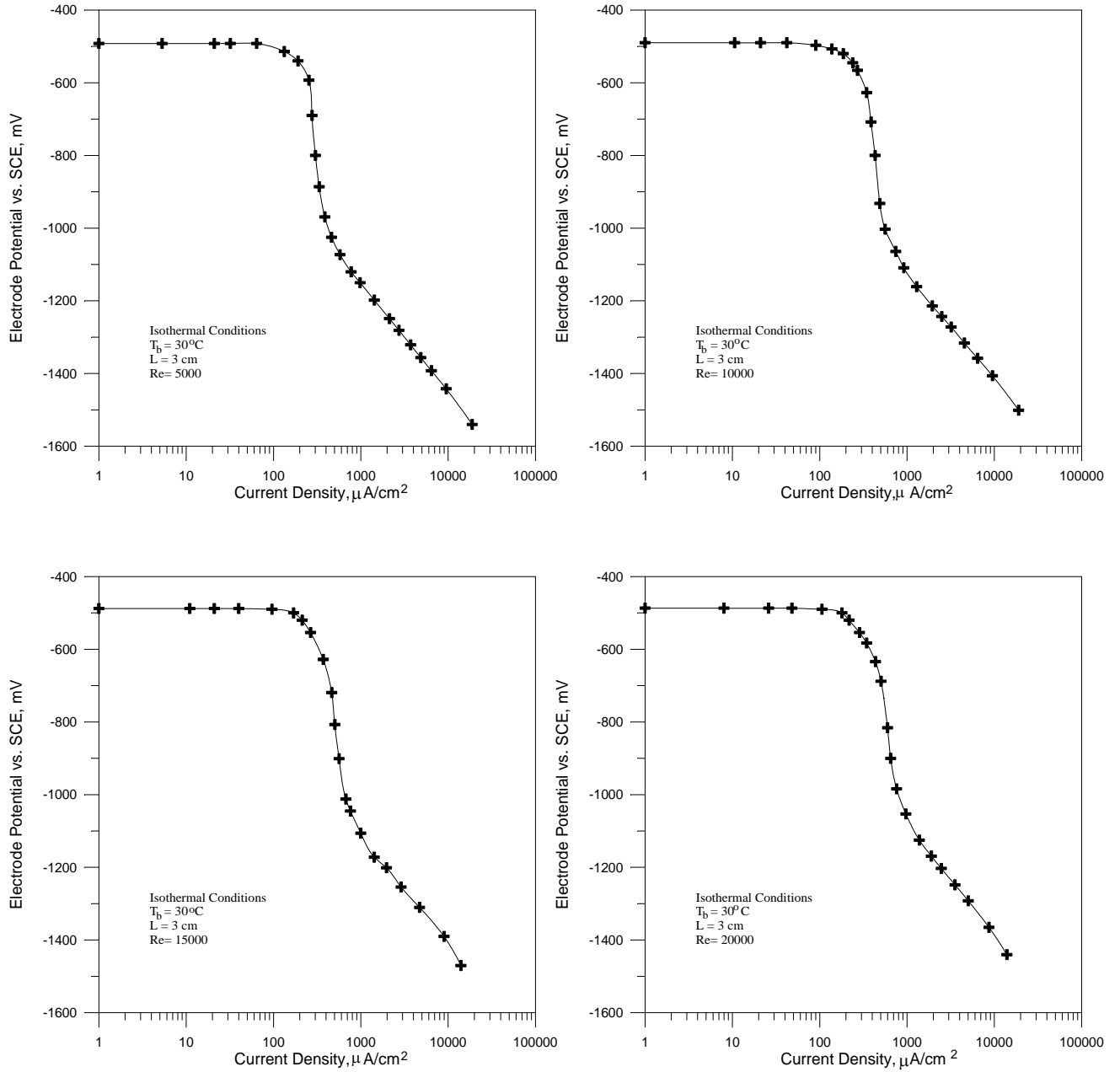


**Figure D1** Cathodic polarization curves under isothermal conditions for  $L=3\text{ cm}$ , and  $T_b=30^\circ\text{C}$  at different  $Re$ .

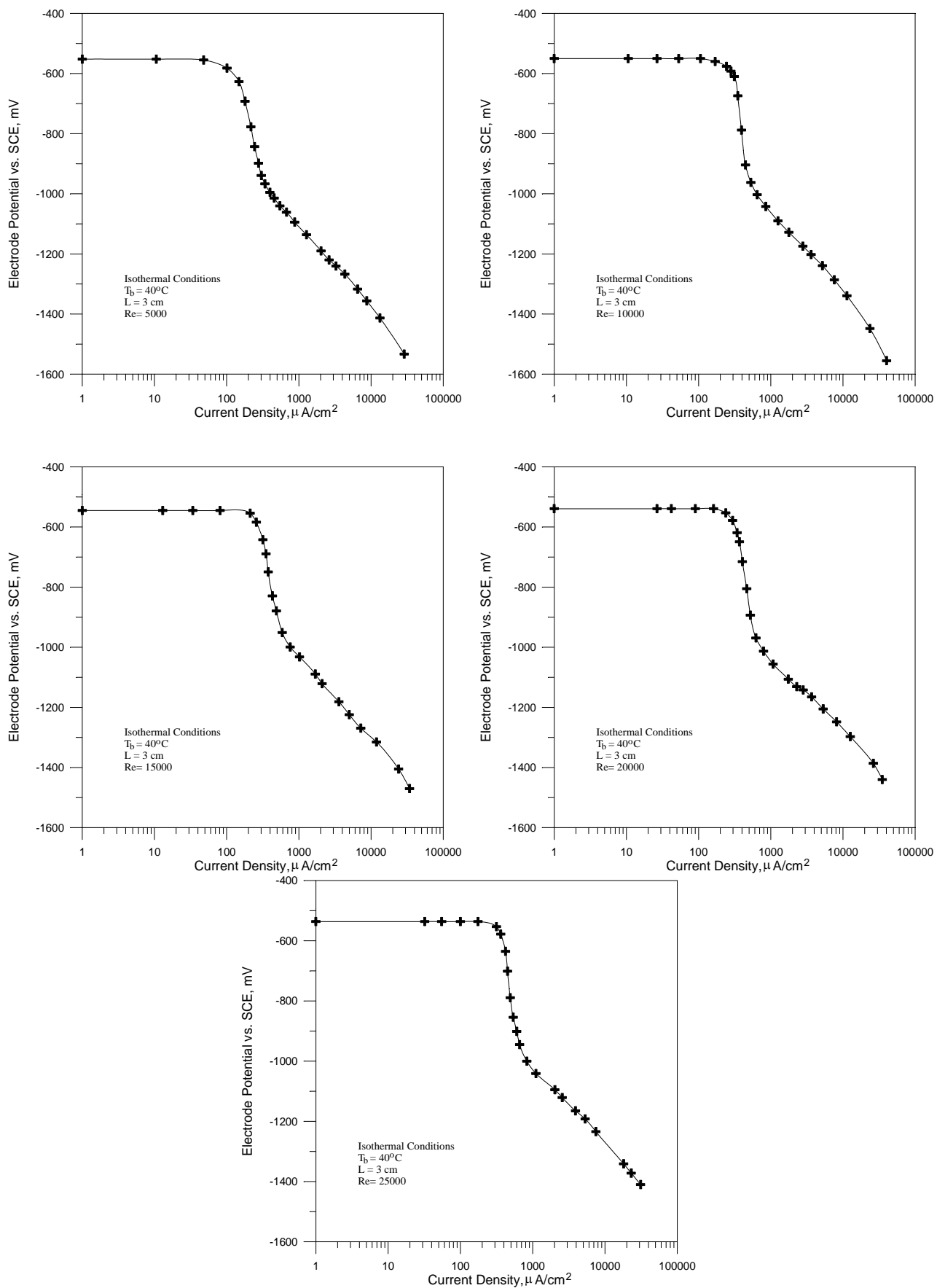


**Figure D2** Cathodic polarization curves under isothermal conditions for  $L=3\text{ cm}$ , and  $T_b=40^\circ\text{C}$  at different  $Re$ .

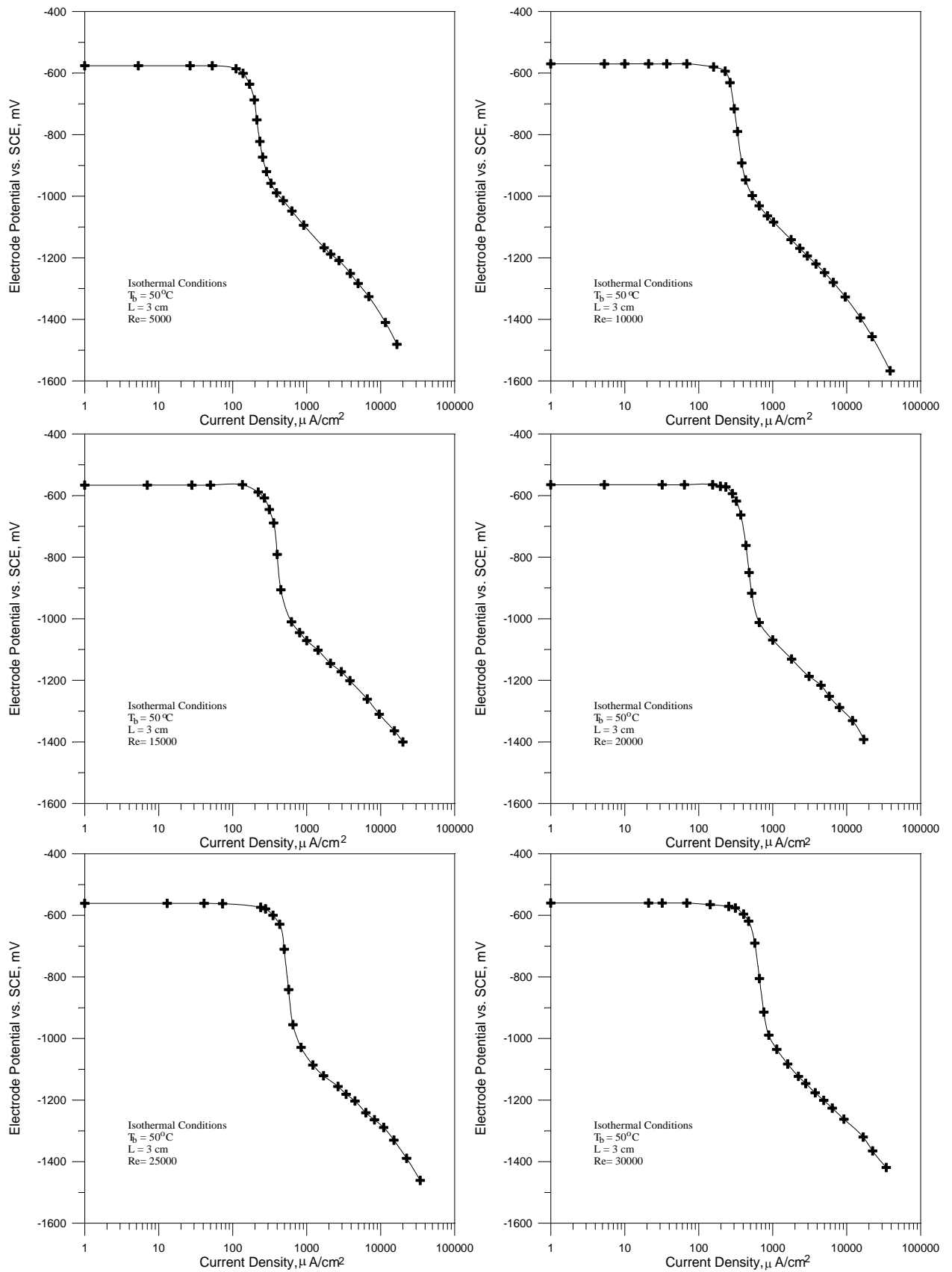


**Figure D3** Cathodic polarization curves under isothermal conditions for  $L=3$  cm, and  $T_b=50$  °C at different Re.

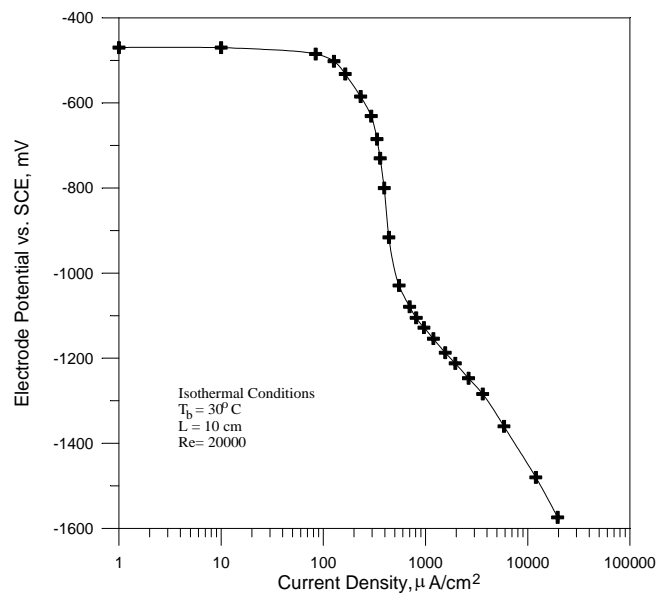
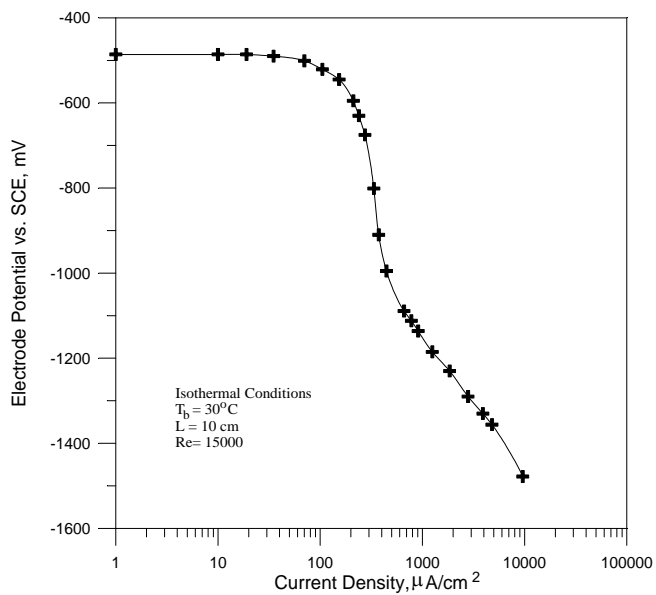
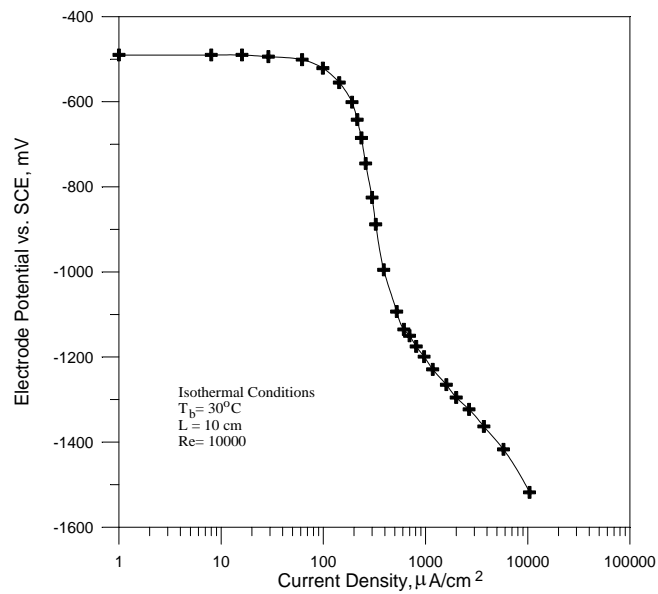
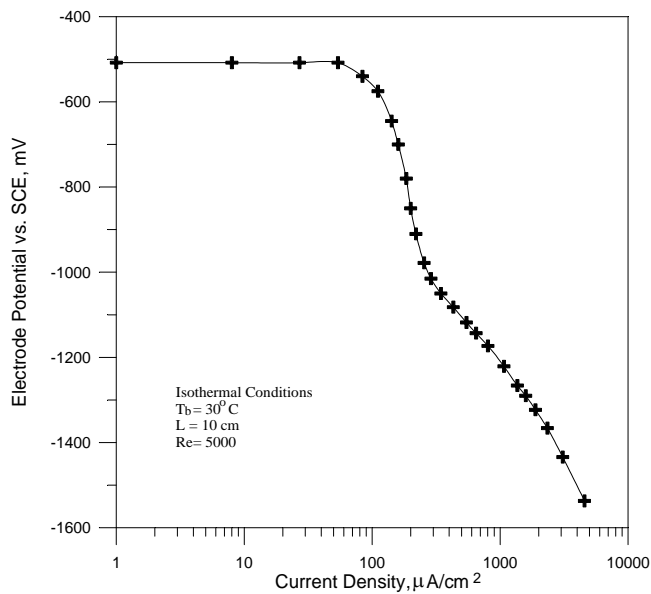


**Figure D4** Cathodic polarization curves under isothermal conditions for  $L=10\text{ cm}$ , and  $T_b=30^\circ\text{C}$  at different  $Re$ .

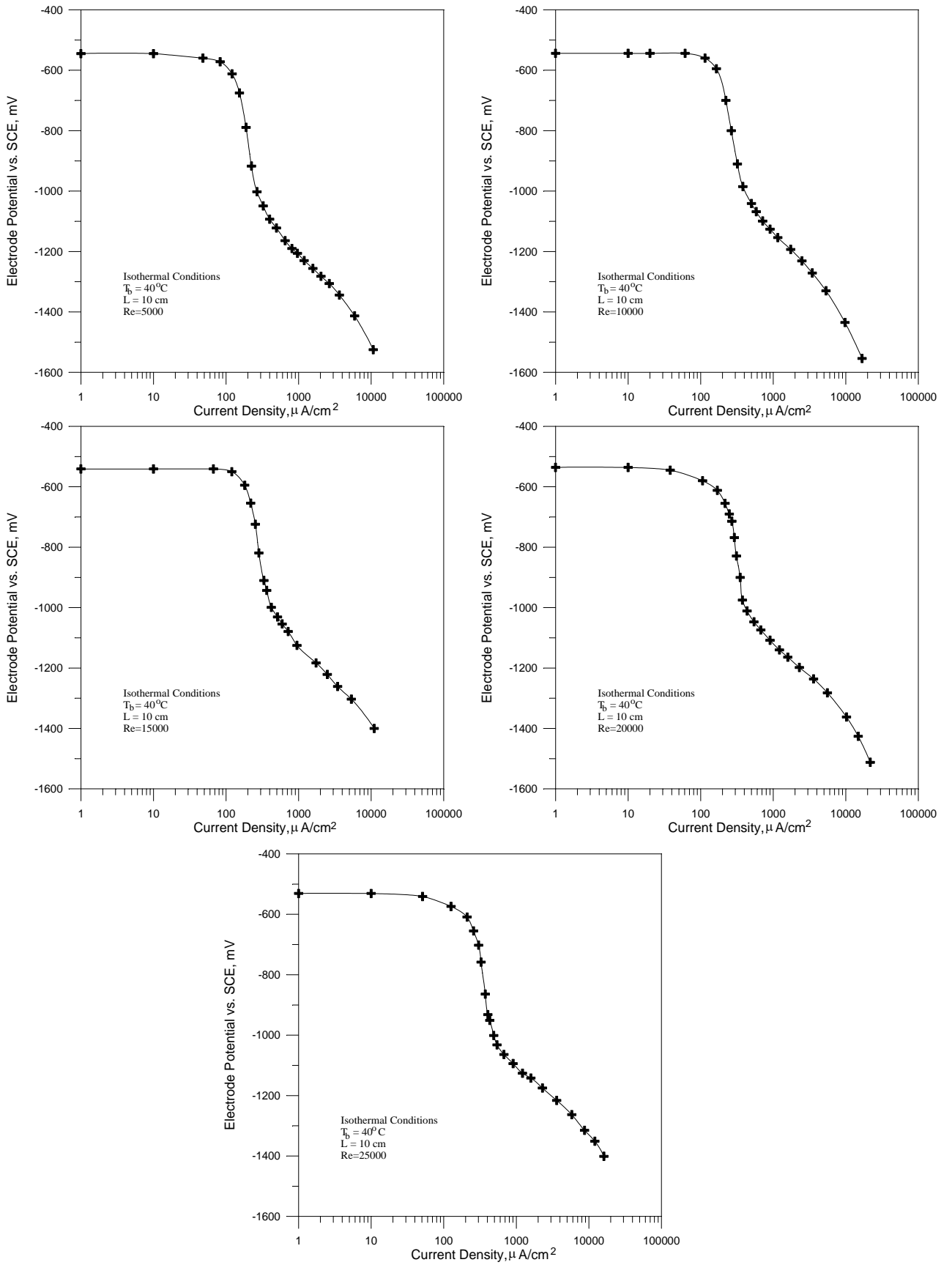


**Figure D5** Cathodic polarization curves under isothermal conditions for  $L=10\text{ cm}$ , and  $T_b=40^\circ\text{C}$  at different Re.

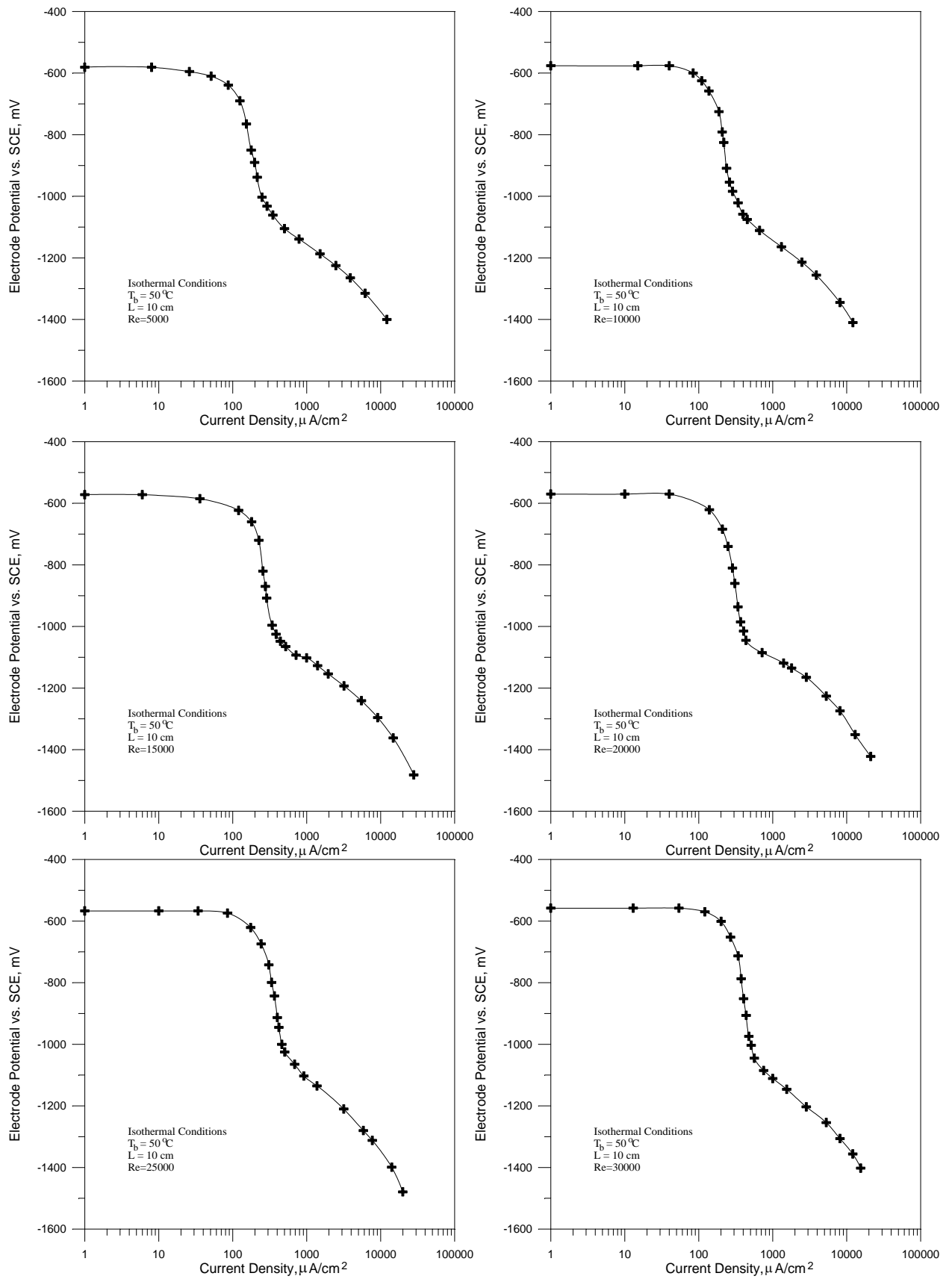


**Figure D6** Cathodic polarization curves under isothermal conditions for  $L=10$  cm, and  $T_b=50$  °C at different Re.

## D.2 Cathodic Polarization Curves Under Heat Transfer Conditions

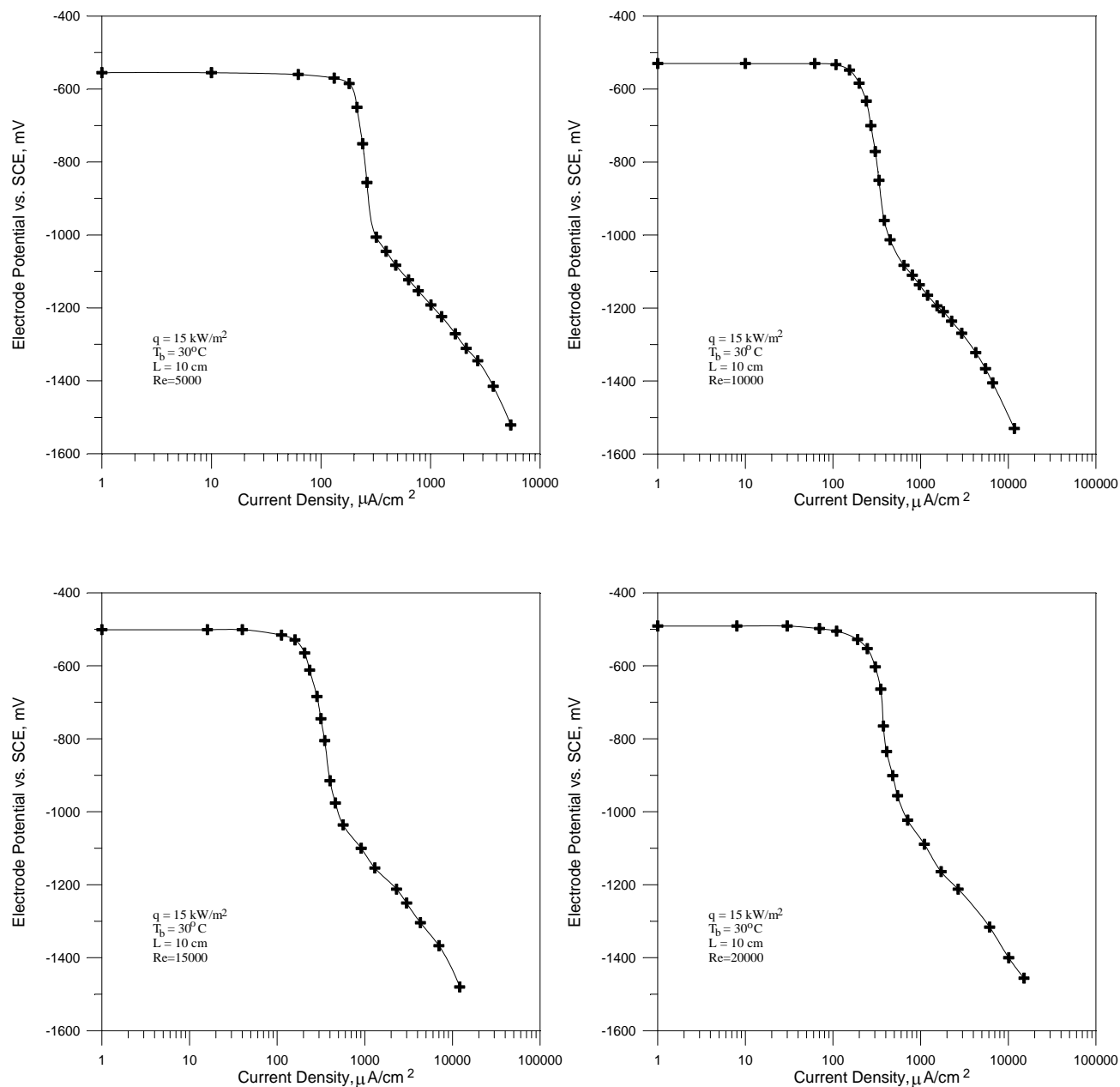


**Figure D7** Cathodic polarization curves for  $q=15 \text{ kW/m}^2$ ,  $L=10 \text{ cm}$ , and  $T_b=30^\circ \text{C}$  at different Re.

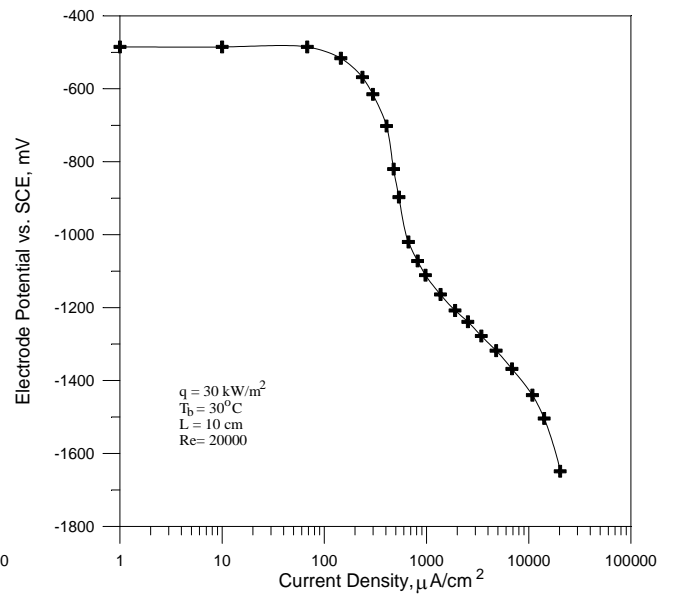
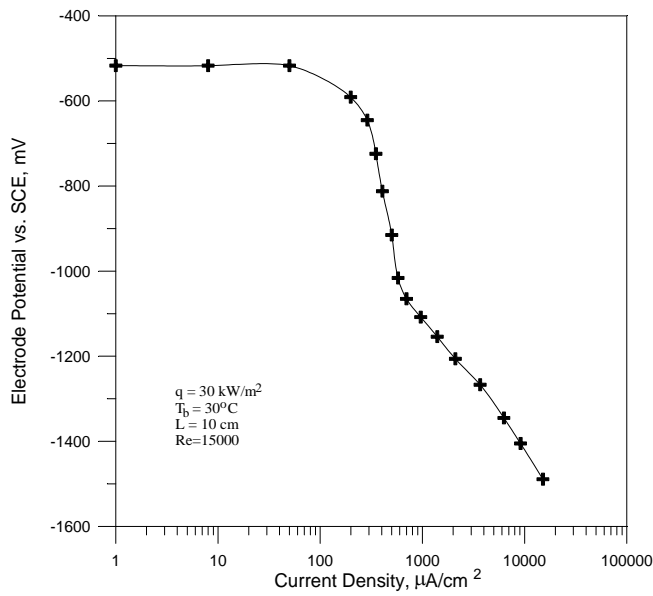
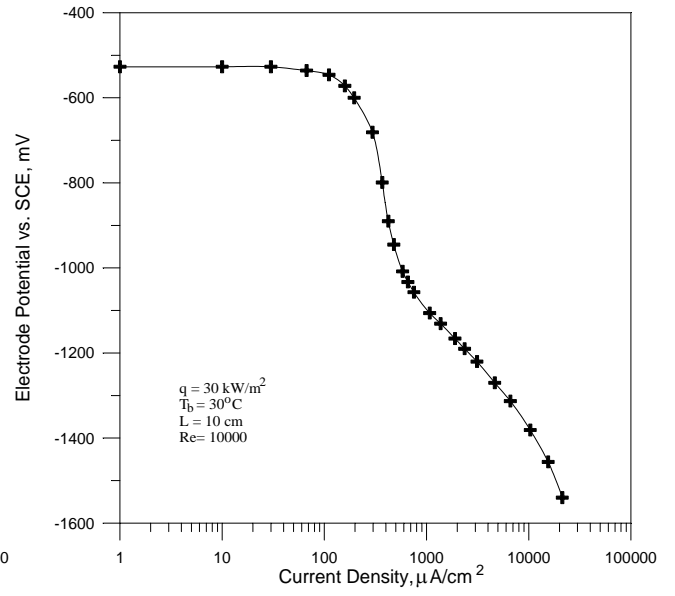
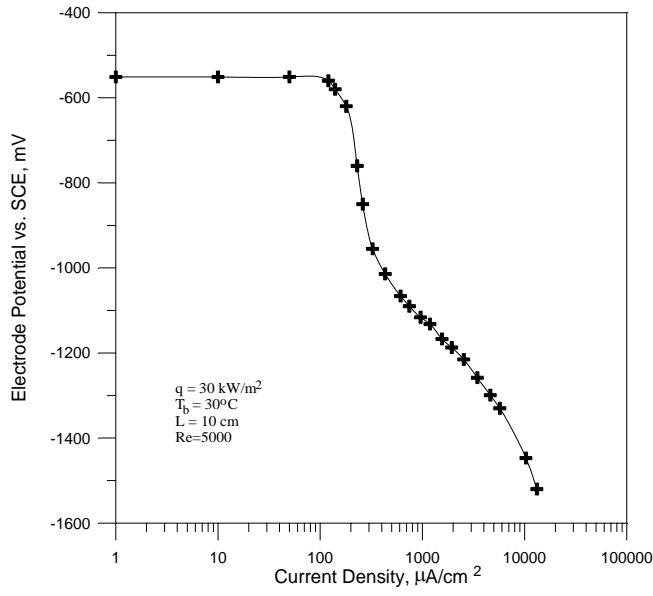


**Figure D8** Cathodic polarization curves for  $q=30 \text{ kW/m}^2$ ,  $L=10 \text{ cm}$ , and  $T_b=30 \text{ }^\circ\text{C}$  at different  $Re$ .

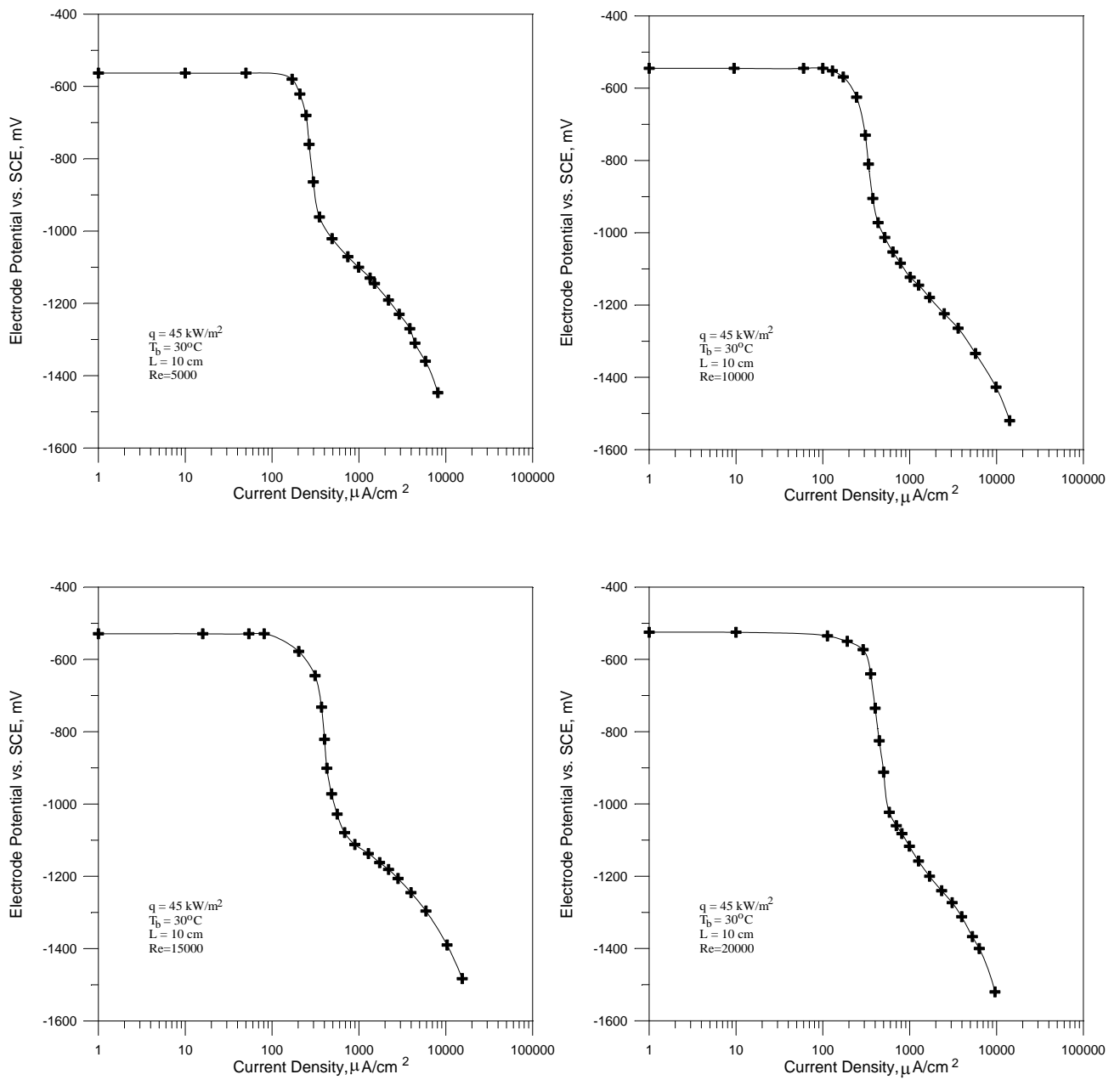


**Figure D9** Cathodic polarization curves for  $q=45 \text{ kW/m}^2$ ,  $L=10 \text{ cm}$ , and  $T_b=30^\circ \text{C}$  at different  $Re$ .

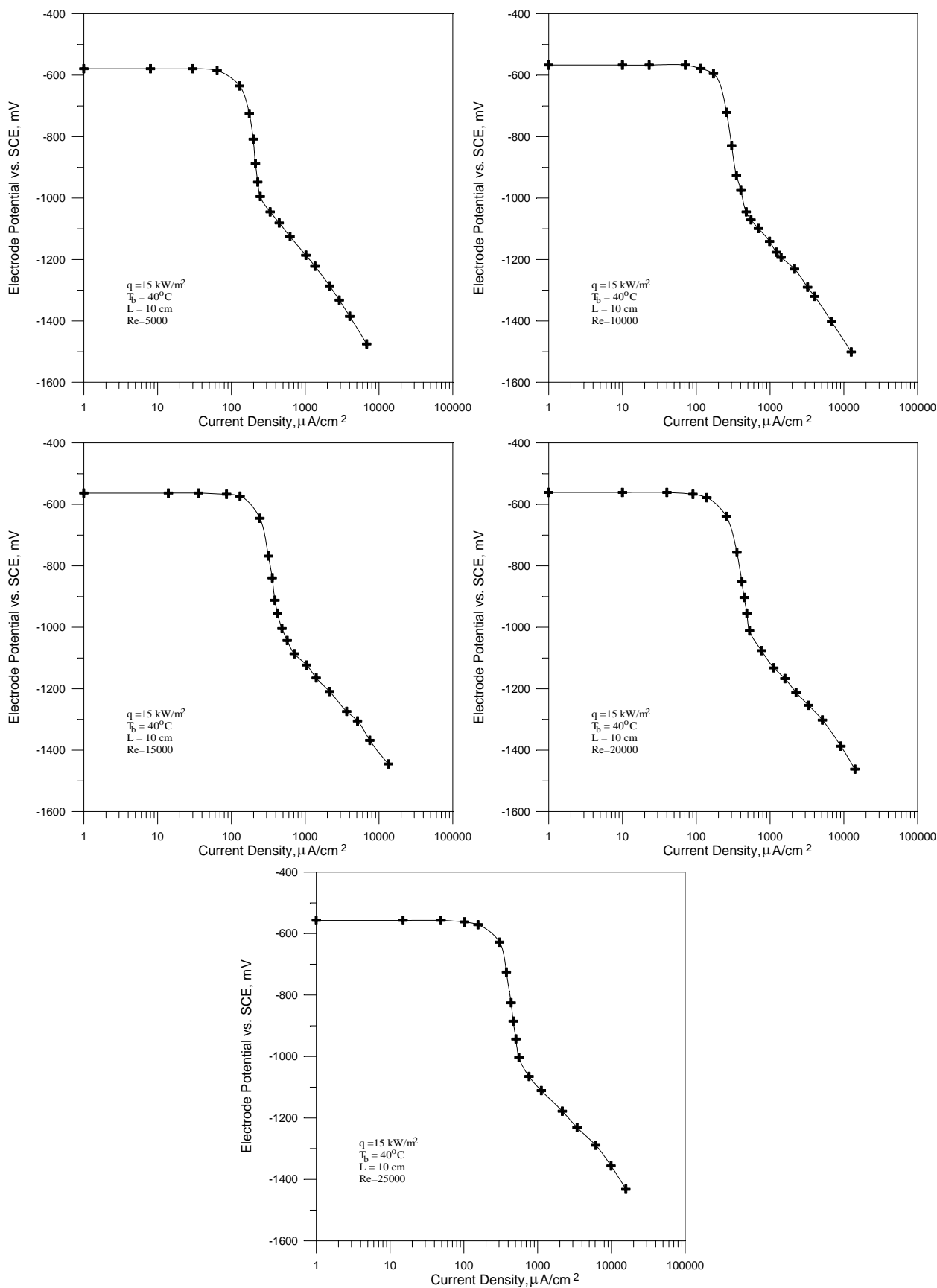


**Figure D10** Cathodic polarization curves for  $q=15 \text{ kW}/\text{m}^2$ ,  $L=10 \text{ cm}$ , and  $T_b=40^\circ\text{C}$  at different  $Re$ .

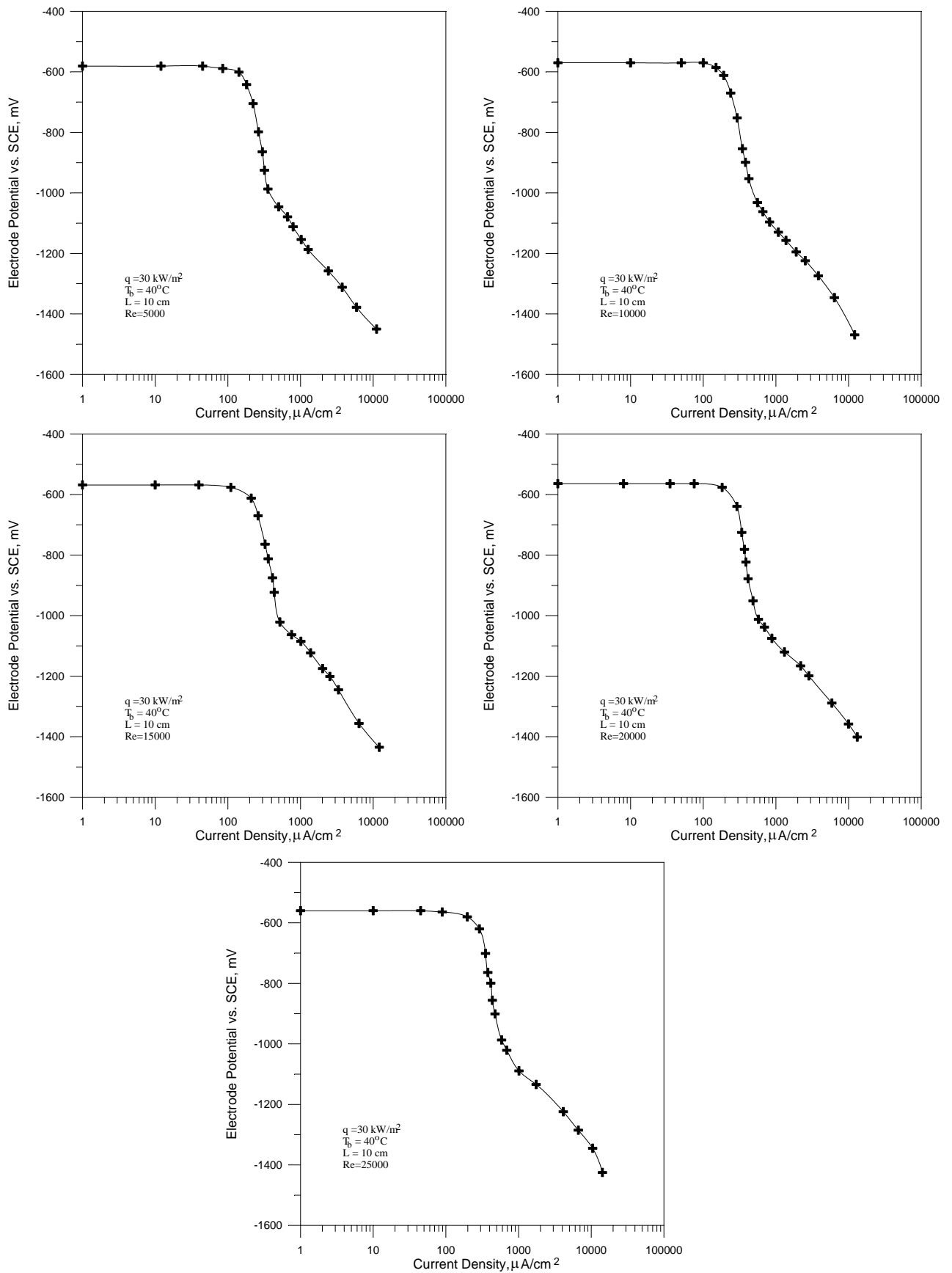


**Figure D11** Cathodic polarization curves for  $q=30 \text{ kW/m}^2$ ,  $L=10 \text{ cm}$ , and  $T_b=40^\circ\text{C}$  at different Re.

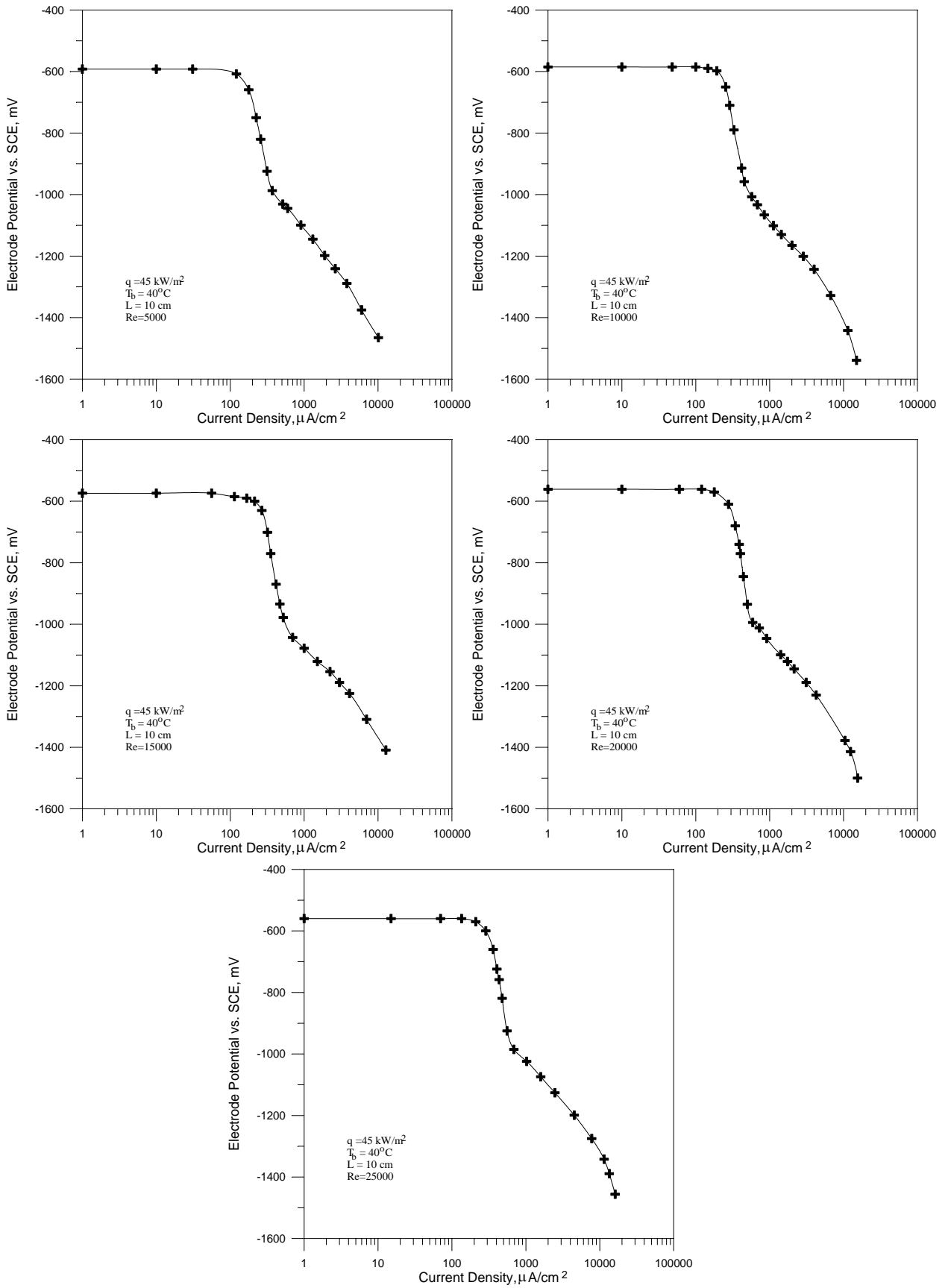


**Figure D12** Cathodic polarization curves for  $q=45 \text{ kW/m}^2$ ,  $L=10 \text{ cm}$ , and  $T_b=40^\circ\text{C}$  at different Re.

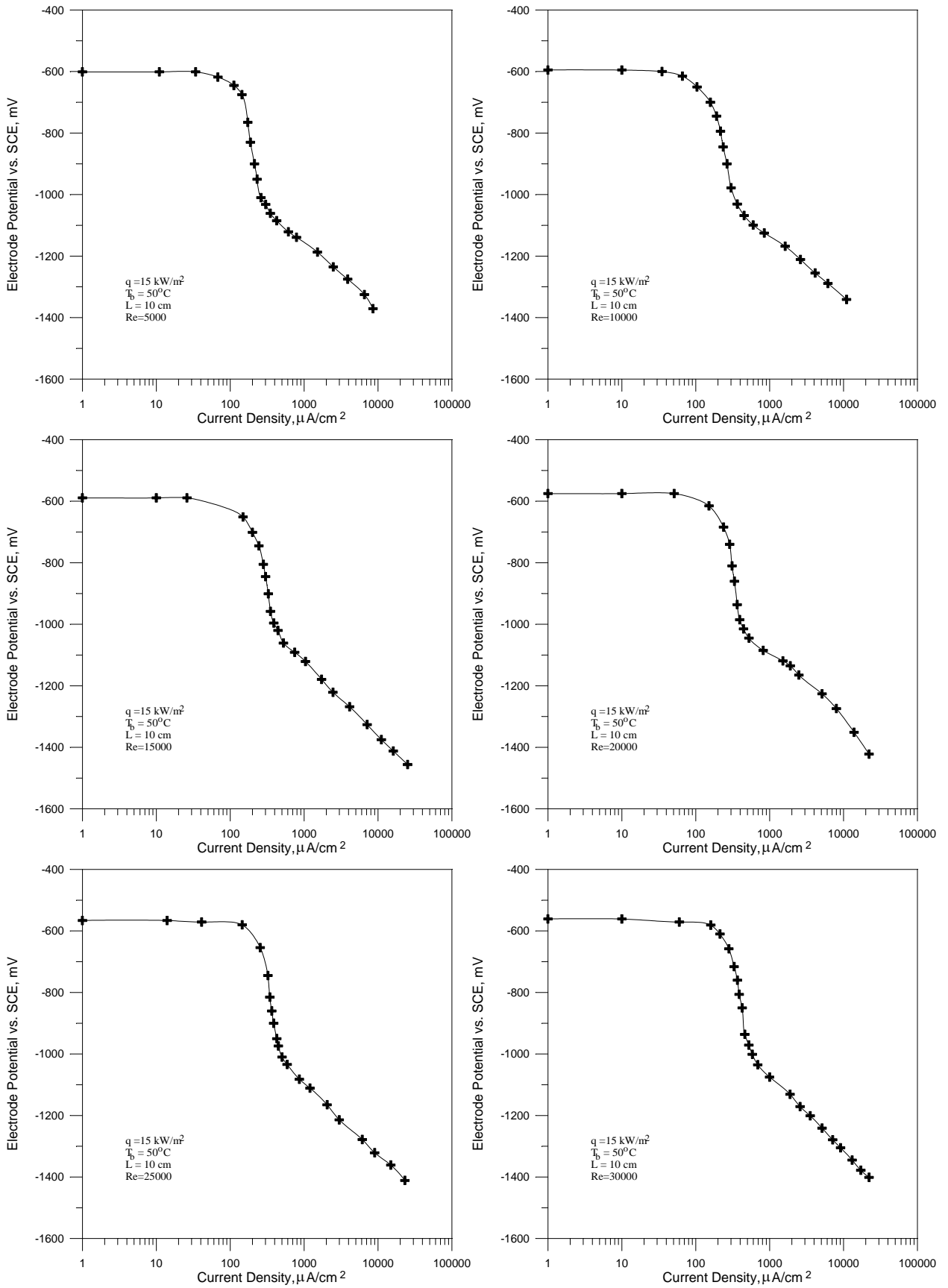


**Figure D13** Cathodic polarization curves for  $q=15 \text{ kW/m}^2$ ,  $L=10 \text{ cm}$ , and  $T_b=50^\circ\text{C}$  at different Re.

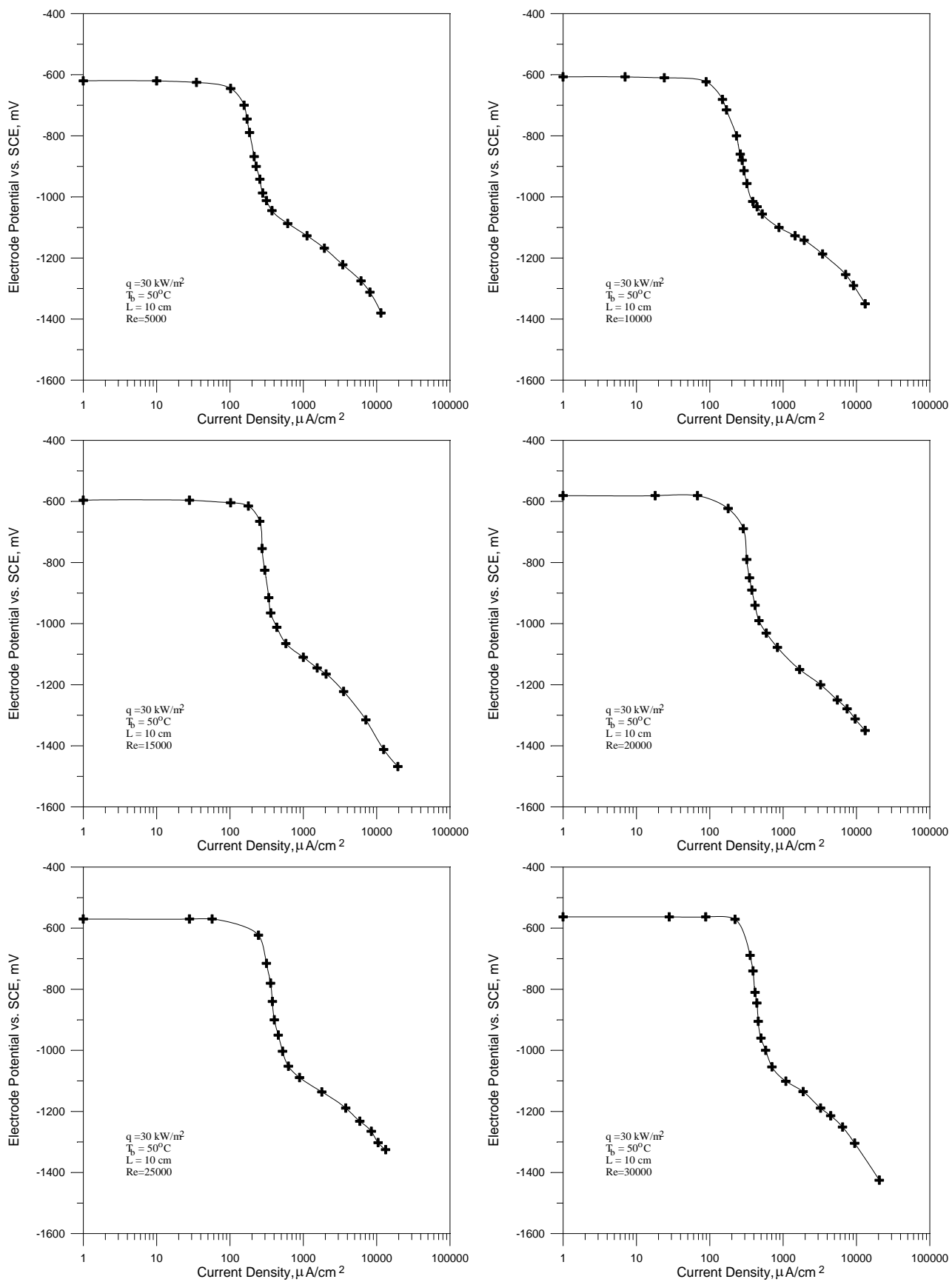


**Figure D14** Cathodic polarization curves for  $q=30 \text{ kW}/\text{m}^2$ ,  $L=10 \text{ cm}$ , and  $T_b=50^\circ\text{C}$  at different  $Re$ .

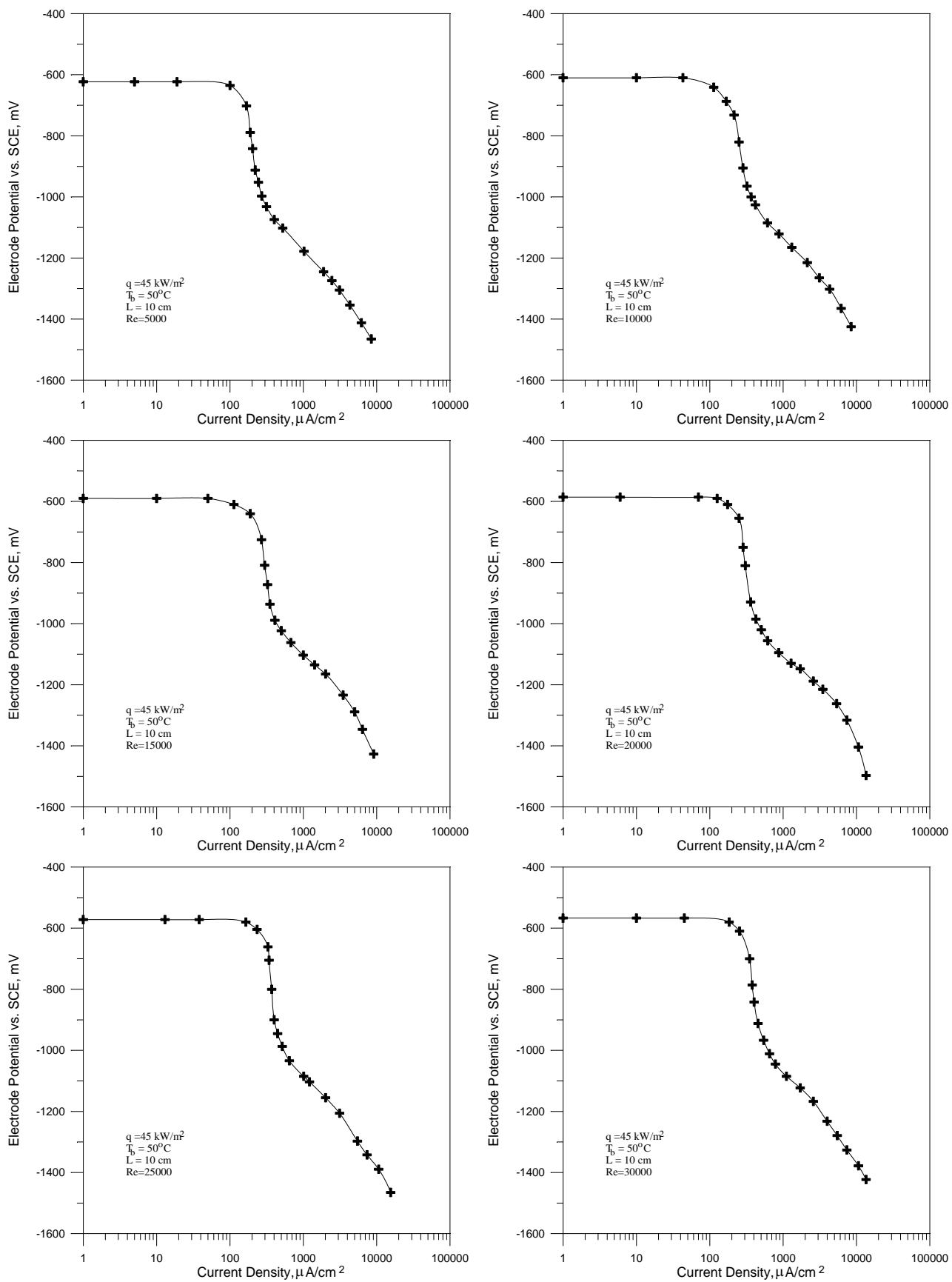


**Figure D15** Cathodic polarization curves for  $q=45 \text{ kW}/\text{m}^2$ ,  $L=10 \text{ cm}$ , and  $T_b=50^\circ\text{C}$  at different  $Re$ .

## شكر وتقدير

أود أن أشكر الأستاذ الدكتور قاسم جبار سليمان لإشرافه وإرشادته ونصائحه العلمية التي ساهمت في إنجاز هذا البحث.  
وأتقدم بالشكر الجزيل الى عائلتي المتمثلة في والدي ووالدتي وأخي ايباد وأخواتي وداد وزينة ودينا لمساندتهم وتشجيعهم لي أثناء مسيرتي العلمية.

## الخلاصة

في هذه الدراسة، تم بحث إنتقال الحرارة من خلال أنبوب من الفولاذ الكربوني معرض للتآكل ضمن مبادل حراري ذوأنبوبين يمر محلول كلوريد الصوديوم ( ٠,١ عياري ) في فجوته الحلقية. تم إجراء التجارب تحت ظروف جريان عشوائي بثبوت درجة الحرارة وبوجود إنتقال للحرارة لمعدل رقم رينولد ( ٥٠٠٠ - ٣٠٠٠٠ ) ودرجات حرارة ( ٣٠ ، ٤٠ ، ٥٠ م° ) وفيض حراري ( ١٥ ، ٣٠ ، ٤٥ كيلو واط/م<sup>٢</sup> ).

تم تحديد معدلات إنتقال الكتلة ( معدلات التآكل ) التي تحدث بسبب تفاعل الاختزال الاوكسجيني ذو السيطرة الانتشارية بواسطة قياس كثافة التيار المحدد، بينما تم تحديد معدلات إنتقال الحرارة بواسطة قياس حرارة السطح. تمت دراسة المخلفات الناتجة من ترسبات التآكل التي تتشكل على السطوح التي يحدث عبرها إنتقال حرارة وتأثيراتها على عمليات إنتقال الحرارة والكتلة من خلال قياس التغيرات التي تحدث على حرارة السطح وعلى كثافة التيار المحدد مع الزمن لفترة ٢٠٠ ساعة.

تم الحصول على المعادلات التالية من بيانات إنتقال الكتلة للسطح النظيف:  
لضروف ثبوت درجة الحرارة

$$J_m = 0.514 \text{Re}^{-0.523} \quad r_2/r_1=1.75, L/d_e=2$$

لضروف ثبوت درجة الحرارة وإنتقال الحرارة

$$J_{mf} = 0.287 \text{Re}^{-0.492} \quad r_2/r_1=1.75, L/d_e=6.7$$

وتم الحصول على المعادلات التالية من بيانات إنتقال الحرارة للسطح النظيف:

$$J_h = 0.058 \text{Re}^{-0.262} \quad r_2/r_1=1.75, L/d_e=6.7$$

ممانعة المخلفات (الترسبات) لإنتقال الحرارة الناتجة من تآكل السطوح التي يحدث عبرها إنتقال حرارة لها الصيغة المقاربة وتتراوح القيمة المقاربة لممانعة المخلفات (الترسبات) لإنتقال الحرارة بين ( ٢,١٧ x ١٠<sup>-٤</sup> - ٢,٥٤ x ١٠<sup>-٤</sup> ) م<sup>٢</sup>/واطلمدة ٢٠٠ ساعة. العلاقة المقاربة هي:

$$R_f = R_f^* [1 - \exp(-bt)]$$

حيث  $R_f^*$  و  $b$  هي دوال لرقم رينولد ودرجة حرارة.

نواتج التآكل التي تتشكل على السطوح التي يحدث عبرها إنتقال حرارة لها تأثير على معامل إنتقال الكتلة الذي يقل مع الزمن أخذاً الصيغة المقاربة. العلاقة المطورة هي:

$$\% k_m \text{red.} = (\% k_m \text{red.})^* [1 - \exp(-b_m t)]$$

حيث  $(\% k_m \text{red.})^*$  و  $b_m$  هي دوال لرقم رينولد ولدرجة حرارة. كذلك تم الحصول على علاقات تربط بين مقادير معادلة ممانعة الترسبات لإنتقال الحرارة و معادلة النقصان في معامل إنتقال الكتلة وكالاتي:

$$R_f^* = 9.35 \times 10^{-5} + 2.7 \times 10^{-6} (\% k_m \text{red.})^*$$

$$b = 0.0065 + 0.157 b_m$$

لذا فإن تأثير ترسبات التآكل على عملية إنتقال الحرارة يمكن التنبؤ به من تأثيرها على عملية إنتقال الكتلة (معدل التآكل) والعكس صحيح. هذا يعني بأن معامل إنتقال الحرارة في أي وقت يمكن التنبؤ به من بيانات إنتقال الكتلة و معامل إنتقال الكتلة يمكن تخمينه من بيانات إنتقال الحرارة.

# إنتقال الحرارة من خلال جدار معدن متآكل لمبادل حراري متحد المركز

أطروحة

مقدمة الى كلية الهندسة في جامعة النهريين  
كجزء من متطلبات نيل درجة دكتوراه فلسفة  
في الهندسة الكيمياوية

من قبل

عماد يوسف منصور عربو

بكلوريوس ١٩٩٤

ماجستير ١٩٩٧

١٤٢٦

٢٠٠٥

ذو القعدة

كانون الأول